frontiers | Research Topics

Drug-drug interactions in pharmacology

Edited by
Francesco Paolo Busardò, Simona Pichini and Oscar Garcia-Algar

Published in
Frontiers in Pharmacology

ISSN 1664-8714
ISBN 978-2-83251-765-9
DOI 10.3389/978-2-83251-765-9

About Frontiers

Frontiers is more than just an open access publisher of scholarly articles: it is a pioneering approach to the world of academia, radically improving the way scholarly research is managed. The grand vision of Frontiers is a world where all people have an equal opportunity to seek, share and generate knowledge. Frontiers provides immediate and permanent online open access to all its publications, but this alone is not enough to realize our grand goals.

Frontiers journal series

The Frontiers journal series is a multi-tier and interdisciplinary set of open-access, online journals, promising a paradigm shift from the current review, selection and dissemination processes in academic publishing. All Frontiers journals are driven by researchers for researchers; therefore, they constitute a service to the scholarly community. At the same time, the *Frontiers journal series* operates on a revolutionary invention, the tiered publishing system, initially addressing specific communities of scholars, and gradually climbing up to broader public understanding, thus serving the interests of the lay society, too.

Dedication to quality

Each Frontiers article is a landmark of the highest quality, thanks to genuinely collaborative interactions between authors and review editors, who include some of the world's best academicians. Research must be certified by peers before entering a stream of knowledge that may eventually reach the public - and shape society; therefore, Frontiers only applies the most rigorous and unbiased reviews. Frontiers revolutionizes research publishing by freely delivering the most outstanding research, evaluated with no bias from both the academic and social point of view. By applying the most advanced information technologies, Frontiers is catapulting scholarly publishing into a new generation.

What are Frontiers Research Topics?

Frontiers Research Topics are very popular trademarks of the *Frontiers journals series*: they are collections of at least ten articles, all centered on a particular subject. With their unique mix of varied contributions from Original Research to Review Articles, Frontiers Research Topics unify the most influential researchers, the latest key findings and historical advances in a hot research area.

Find out more on how to host your own Frontiers Research Topic or contribute to one as an author by contacting the Frontiers editorial office: frontiersin.org/about/contact

Drug-drug interactions in pharmacology

Topic editors

Francesco Paolo Busardò — Marche Polytechnic University, Italy
Simona Pichini — National Institute of Health (ISS), Italy
Oscar Garcia-Algar — Hospital Clinic of Barcelona, Spain

Citation

Busardò, F. P., Pichini, S., Garcia-Algar, O., eds. (2023). *Drug-drug interactions in pharmacology*. Lausanne: Frontiers Media SA. doi: 10.3389/978-2-83251-765-9

Table of contents

frontiers | Frontiers in Pharmacology

TYPE Editorial
PUBLISHED 13 February 2023
DOI 10.3389/fphar.2023.1155738

OPEN ACCESS

EDITED AND REVIEWED BY
Jaime Kapitulnik,
Hebrew University of Jerusalem, Israel

*CORRESPONDENCE
Simona Pichini,
simona.pichini@iss.it

SPECIALTY SECTION
This article was submitted to Drug Metabolism and Transport, a section of the journal Frontiers in Pharmacology

RECEIVED 31 January 2023
ACCEPTED 06 February 2023
PUBLISHED 13 February 2023

CITATION
Pichini S, Di Trana A, García-Algar O and Busardò FP (2023), Editorial: Drug-drug interactions in pharmacology. *Front. Pharmacol.* 14:1155738. doi: 10.3389/fphar.2023.1155738

Editorial: Drug-drug interactions in pharmacology

Simona Pichini[1]*, Annagiulia Di Trana[1], Oscar García-Algar[2] and Francesco Paolo Busardò[3]

[1]National Centre on Addiction and Doping, Istituto Superiore di Sanità, Rome, Italy, [2]Neonatology Unit, Hospital Clinic-Maternitat, ICGON, BCNatal, Barcelona, Spain, [3]Department of Excellence-Biomedical Sciences and Public Health, Università Politecnica Delle Marche, Ancona, Italy

KEYWORDS

drug-drug interaction, pharmacology, pharmacokinetics, pharmacodinamics, ADME cycle

Editorial on the Research Topic
Drug-drug interactions in pharmacology

In pharmacology, drug-drug interactions result in unintended reactions, toxic side effects, or a lack of clinical efficacy in an individual body when multiple medications are simultaneously administered for one or more diseases (Molenaar-Kuijsten et al., 2021). These are usually considered in terms of two principal classes of underlying mechanisms: pharmacodynamics and pharmacokinetics (Nguyen et al., 2020). Indeed, the pharmacological effect of one or both drugs may be enhanced or suppressed, or a new and unanticipated adverse effect may occur, even leading to fatal consequences (Barbera et al., 2013; Karch et al., 2016).

Concerning pharmacokinetics, drug absorption, distribution, metabolism, and excretion (ADME cycle) variations may result in a plasma concentration fluctuation, influencing drug bioavailability. Interactions between drugs at the metabolic level can modify the metabolic enzymes altering drug activation or inactivation. If the metabolism is inhibited, it will remain longer in the body, so its concentration will increase, potentially causing secondary toxic effects. Conversely, metabolism enhancement can decrease plasma concentration and hence its bioavailability.

Pharmacodynamically, drugs can interact by binding to the same receptor. Two receptor agonists or two antagonists would increase the pharmacological actions of both, whereas an agonist and an antagonist would decrease each other's pharmacological effects. In some interactions, drugs may produce biochemical changes that alter the sensitivity to toxicities produced by other drugs. Finally, whereas in the majority of cases, drug-drug interactions can cause toxic adverse effects (e.g., beta-blockers and bronchodilators; diuretics and steroids or digoxin; rifampicin and verapamil or carbamazepine), there are also several therapeutically beneficial drug interactions (e.g., docetaxel and piperine; resveratrol and diclofenac; ivermectin and lopinavir or saquinavir).

This Research Topic aims to provide original investigations, brief reports, and review papers concerning the latest insights into drug-drug interactions in pharmacology.

Recently, physiologically based pharmacokinetic (PBPK) models have been widely applied for the computational description of drug-drug interaction, since regulatory agencies have progressively accepted the model as predictive. To this concern, Chen et al. investigated the influence of triazoles antifungal drugs on the pharmacokinetics of zanubrutinib and acalabrutinib, two Bruton's tyrosine kinase inhibitors commonly used in

the therapy of B-cell malignancies. The PBPK models were computed by software and validated using clinically observed plasma concentrations reported in published studies. The authors successfully described the zanubrutinib and acalabrutinib area under the curve (AUC) increase due to the concurrent oral administration of voriconazole, fluconazole, and itraconazole at different dosages. The *in silico* prediction of drug-drug interaction using a PBPK model was performed by Granana-Castillo et al. to assess the possible pharmacokinetic interaction between rifapentine and rilpivirine. Rilpivirine bioavailability variation was observed in both the administration regimens simulated, with a higher decrease of AUC_{0-24} in the simulation of concomitant administration of rifapentine with rilpivirine at the steady state. The obtained results suggested avoiding the coadministration of the two drugs. Furthermore, the olverembatinib drug-drug interaction was investigated by Yu et al. applying a PBPK model to evaluate the possible pharmacokinetic interaction CYP450 mediated. The used model allowed for the successful prediction that CYP3A4 inhibitors may increase olverembatinib plasma concentrations, while the CYP3A4 inducers may decrease its AUC. Conversely, the impact on other CYP450 isoforms was negligible.

Considering the importance of single CYP450 isoforms in drug metabolism, the polymorphism of such enzymes may play a crucial role. To this concern, Ye et al. investigated the influence of CYP2D6 variations on fluvoxamine pharmacokinetics and the drug-drug interaction with apatinib in an *in vivo* model, using Sprague Dawley rats. The study showed that apatinib inhibits fluvoxamine metabolism according to a mixed mechanism and the gene polymorphisms can remarkably affect plasma availability. Similarly, the genetic variability of CYP3A4 may affect pyrotinib pharmacokinetics as elucidated by Zhang et al. The authors applied a PKPB model to evaluate the potential risk of pyrotinib coadministration with strong inhibitors and to quantitatively estimate potential drug-drug interaction for CYP3A4 modulators. Moreover, ketoconazole, fluconazole, and itraconazole may reduce the clearance of pyrotinib *in vitro* and *in vivo* model, as reported by Wang et al.

The growing interest in natural active principles pushed the scientific community to investigate the possible drug-drug interactions with the most used pharmaceutical drugs. Differently from synthetic pharmaceutical drugs, natural remedies from traditional medicine are composed of different active principles, which produce therapeutic effects acting in synergy. The pharmacokinetic herb-drug interactions (HDI) between *Polygonum capitatum* Buch.-Ham. ex D. Don extract and ciprofloxacin were investigated by Li et al., according to a randomized, three-period, crossover trial in healthy humans. Furthermore, the tissue distribution was evaluated in rats. Multiple transporter-mediated HDI contributes to the effects of *P. capitatum* on the reduced systemic exposure and altered tissue distribution of ciprofloxacin. The natural active principle *Epimedium sagittatum* interaction with CYP3A4 was investigated by Li et al. to evaluate the possible drug-drug interaction with corticosteroids. Epimedium resulted to inhibit CYP3A4 activity according to a dose-dependent mechanism in the HepG2 cells model, enhancing the corticosteroids' anti-inflammatory effect.

The molecular mechanism of action of the natural active principle Ginkgolide B was the focus of Cao et al., who studied the inhibition function of Ginkgolide B on neuronal apoptosis after cerebral ischemia in an *in vivo* rat model and *in vitro* cultured SH-SYS5Y cells model. The results suggest that the natural active principle may reduce neuronal apoptosis preventing ischemic stroke. An innovative computational approach was applied by Yuan et al. to construct a protein-protein interaction network in order to study the effect of Xuefu Zhuyu Decoction in the treatment of atherosclerosis**.** A similar computational approach was applied by Zhou et al. to construct molecular subtypes of colon cancer and subsequently explore prognostic genes with GEPIA2. The machine learning-based study allowed proposing new colon cancer prognostic markers.

Analytical methods represent an important aspect of drug-drug interaction pharmacokinetic studies. To this concern, Tang et al. developed and validated a UHPLC-MS/MS method to quantify almonertinib in rat plasma. The method was successfully applied to study the pharmacokinetic interaction between paxlovid and almonertinib in an *in vivo* rat model.

Finally, drug-drug interaction studies may elucidate important aspects of polytherapy-induced drug resistance. Ghosh et al. examined the interactions of antiseizure drugs in isolated brain cells from patients with drug-resistant epilepsy, highlighting that antiseizure drugs modulate pro- and anti-apoptotic protein levels *via* a CYP-mediated mechanism.

In conclusion, this Research Topic is providing updated studies concerning drug-drug interactions between new drugs, natural drugs, and polydrug treatments, proposing new promising computational approaches.

Author contributions

All authors listed have made a substantial, direct, and intellectual contribution to the work, and approved it for publication.

Acknowledgments

The Research Topic Editors express their gratefulness to all the contributors for submitting their work to this Research Topic, to the Review Editors and external Reviewers who participated in the review process, and to the Editorial and Production teams of Frontiers for their valuable assistance through the various stages of the publication process.

Conflict of interest

The authors declare that the research was conducted in the absence of any commercial or financial relationships that could be construed as a potential conflict of interest.

Publisher's note

References

Barbera, N., Busardò, F. P., Indorato, F., and Romano, G. (2013). The pathogenetic role of adulterants in 5 cases of drug addicts with a fatal outcome. *Forensic Sci. Int.* 227, 74–76. doi:10.1016/j.forsciint.2012.08.041

Karch, S. B., Busardò, F. P., Vaiano, F., Portelli, F., Zaami, S., and Bertol, E. (2016). Levamisole adulterated cocaine and pulmonary vasculitis: Presentation of two lethal cases and brief literature review. *Forensic Sci. Int.* 265, 96–102. doi:10.1016/J.FORSCIINT.2016.01.015

Molenaar-Kuijsten, L., Van Balen, D. E. M., Beijnen, J. H., Steeghs, N., and Huitema, A. D. R. (2021). A review of CYP3A drug-drug interaction studies: Practical guidelines for patients using targeted oral anticancer drugs. *Front. Pharmacol.* 12, 670862. doi:10.3389/fphar.2021.670862

Nguyen, T., Liu, X., Abuhashem, W., Bussing, R., and Winterstein, A. G. (2020). Quality of evidence supporting major psychotropic drug-drug interaction warnings: A systematic literature review. *Pharmacotherapy* 4, 455–468. doi:10.1002/phar.2382

frontiers | Frontiers in Pharmacology

ORIGINAL RESEARCH
published: 28 June 2022
doi: 10.3389/fphar.2022.941094

Ginkgolide B Protects Against Ischemic Stroke *via* Targeting AMPK/PINK1

Yile Cao[1], *Lei Yang*[2]* *and Hong Cheng*[3]*

[1]Department of Clinical Medicine, School of Medicine, Yangzhou University, Yangzhou, China, [2]Department of Orthopedics, Taizhou People's Hospital, Taizhou, China, [3]Medical College, Yangzhou University, Yangzhou, China

Introduction: Ginkgolide B (GB), which is an active constituent derived from Ginkgo biloba leaves, has been reported to ameliorate Alzheimer's disease (AD), ischemic stroke, as well as other neurodegenerative diseases due to its viable immunosuppressive and anti-inflammatory functions. However, it has yet to be proven whether GB inhibits neuronal apoptosis in ischemic stroke.

Methods: In the present research, the inhibition function of GB on neuronal apoptosis and its underpinning process(s) after cerebral ischemia were studied through transient middle cerebral artery occlusion (t-MCAO) in an *in vivo* rat model as well as in cultured SH-SY5Y cells subjected to oxygen and glucose deprivation (OGD)/reoxygenation *in vitro*. The neurological score was calculated and Nissl and TUNEL staining were performed to evaluate the stroke outcome, neuronal loss, and neuronal apoptosis. Subsequently, the western blot was utilized to detect Bcl2 and p-AMPK/AMPK expression.

Results: Compared to t-MCAO rats, rats receiving GB treatment showed a significant reduction of neuronal loss and apoptosis and improved neurological behavior at 72 h after MCAO. GB treatment also upregulated the expression of Bcl2 and p-AMPK. *In vitro*, GB suppressed the apoptosis in OGD/reoxygenation-challenged neuronal SH-SY5Y cells through AMPK activation.

Conclusions: Our observations suggest that GB enhanced AMPK activation in neural cells, reducing neuronal apoptosis, thus eventually preventing ischemic stroke.

Keywords: stroke, apoptosis, AMPK, PINK1, OGD, t-MCAO, ginkgolide B

OPEN ACCESS

Edited by:
Francesco Paolo Busardò, Marche Polytechnic University, Italy

Reviewed by:
Angelo Montana, University of Catania, Italy
Barcelo Bernardino, Hospital Universitario Son Espases, Spain

***Correspondence:**
Lei Yang
leiyang@njmu.edu.cn
Hong Cheng
hcheng@yzu.edu.cn

Specialty section:
This article was submitted to Drug Metabolism and Transport, a section of the journal Frontiers in Pharmacology

Received: *11 May 2022*
Accepted: *13 June 2022*
Published: *28 June 2022*

Citation:
Cao Y, Yang L and Cheng H (2022) Ginkgolide B Protects Against Ischemic Stroke via Targeting AMPK/PINK1. Front. Pharmacol. 13:941094. doi: 10.3389/fphar.2022.941094

INTRODUCTION

Ischemic stroke is a kind of brain damage induced by a rapid reduction in cerebral blood flow (CBF) and a subsequent shortage of oxygen and glucose in the blood supply to the brain (Siniscalchi et al., 2014). The impairment caused by ischemia to the brain could be partly restored if the patient receives suitable therapy with thrombolytics during a specified time limit (about 3–4.5 h) (Drieu et al., 2018). Although effective, thrombolytics, including tissue-type plasminogen activator (t-PA), are restricted in their use due to their adverse impacts and relatively limited treatment timeframe (Zhang et al., 2005; Khan et al., 2007). Therefore, finding a successful stroke treatment method is in urgent need in clinical practice (Amani et al., 2019).

Both mitochondrial function and the glucose metabolic pathway are combined with redox signaling and are remarkably responsive to cerebral ischemia. It is the redox signaling system that regulates the generation of mitochondrial oxidant hyperoxia under normal physiological states (Hu et al., 2016; Yang and Long, 2018; Chen et al., 2019). Disturbances in glucose metabolism result in cerebral ischemia damaging mitochondrial transfer proteins (depolarized mitochondria), resulting in the presence and progression of hydrogen peroxide and superoxide at an unregulated rate (Akhmedov et al., 2015; Yang et al., 2019; Zuurbier et al., 2020). Eventually, these factors contribute to neuronal apoptosis.

PINK1 is a mitochondrial threonine/serine kinase stably located on the outer membrane of mitochondria that have suffered from damage. The substrates of PINK1 include the E3 ubiquitin ligase Parkin and ubiquitin itself. The phosphorylation of Parkin and ubiquitin cause the unnecessary depolarization of mitochondria, ubiquitinating them for selective degradation (Kim et al., 2008; Kane et al., 2014; Koyano et al., 2014). Therefore, PINK1 has an important role in mitochondria quality control. In addition, some studies have also shown that the mitogen-activated protein kinase (MAPK) pathway is essential for PINK1-dependent neuroprotection (Hang et al., 2015; Cao et al., 2020; Seabright and Lai, 2020).

Ginkgolide B (GB) isolated from *Ginkgo biloba* leaves was revealed to have anti-inflammation and antioxidant effects in ischemic stroke (Chi et al., 2015; Shu et al., 2016; Feng et al., 2019; Liu et al., 2019). There is evidence that GB ameliorates oxidative stress responses related to AMPK activation (Jiang et al., 2020; Wang et al., 2021). However, whether the activation of AMPK caused by GB treatment can protect mitochondrial function and attenuate neuronal apoptosis during stroke remains uncertain.

MATERIALS AND METHODS

Animals and Drug Treatment

The APExBIO Technology LLC (Houston, TX, United States) supplied Ginkgolide B (Cas No. 15291-77-7) that was dissolved in DMSO and had a 99.5 percent purity. Sprague Dawley (SD) male rats (220–300 g) (Beijing Vital River Laboratory Animal Technology Co., Ltd., Beijing, China) were utilized in the present research. The rats were kept in standard conditions (12 h darkness-light light-dark cycle and ambient temperature at 23 ± 2°C). Then, all rats were housed for at least 1 week before surgery. Subsequently, the rats were classified at random into four experimental cohorts (n = 10 for each cohort), namely MCAO cohort, Sham-treated cohort, GB-treated cohort, and GB treated/MCAO cohort. The operation for Middle Cerebral Artery Occlusion (MCAO) was carried out in the same manner as discussed previously (Bai et al., 2016). Specifically, the rats were placed in a supine posture after being anesthetized using isoflurane. Then, the internal carotid artery (ICA), external carotid artery (ECA), and right common carotid artery (CCA) were dissected *via* a midline neck cut. The MCA was subjected to blocking by introducing an intraluminal silicone coating filament (Cinon Tech Co. Ltd., Beijing, China) into the CCA lumen and gradually advancing it into the ICA until it reached a location about 18 mm distal to the branching of the carotid artery. The filament was kept intact for 90 min before being slowly drawn back for a short duration to enable the restoration of blood flow in anticipation of reperfusion. The sham cohort was subsequently subjected to the identical experimental protocol, with the exception of the filament placement. One hour following surgery, GB (4 mg/kg) was administered intraperitoneally to the rats twice per day for three consecutive days following MCAO. A total of 10 rats died as a result of the surgical operations, with 5 from the MCAO cohort and another 5 from the GB treated/MCAO cohort dying during the process. An equivalent volume of saline instead of GB was injected into the rats from the sham and MCAO cohorts. The surgical operations led to the deaths of eight rats, with four from the MCAO cohort and another four from the MCAO + GB cohort. Once 72 h had elapsed following reperfusion, the rats were subjected to decapitation and their brains were harvested for analysis. In accordance with the National Institutes of Health's Guide for the Care and Use of Laboratory Animals, all protocols utilized in the present research were subjected to approval by the Ethics Committee for the Use of Experimental Animals of Jiangsu Kanion Pharmaceutical Co. Ltd. State Key Laboratory of New Pharmaceutical Process for Traditional Chinese Medicine.

Neurobehavioral Testing

A composite neuro score of 28 points was utilized to assess the sensory and motor capabilities of the rats receiving MCAO (Encarnacion et al., 2011). Specifically, this neural score was comprised of 11 assessments with a total combined score of 28, where a total score of 0 denoted significant neurological dysfunction, whereas a total score of 28 showed normal function without neurological impairment. The 11 tests were listed below (Siniscalchi et al., 2014) circling (maximum 4 points), (Drieu et al., 2018) motility (maximum 3 points), (Zhang et al., 2005) general condition (maximum 3 points), (Khan et al., 2007) righting reflex when placed on back (maximum 1 point), (Amani et al., 2019) paw placement of each paw onto a table top (maximum 4 points), (Hu et al., 2016) ability to pull self up on a horizontal bar (maximum 3 points), (Yang and Long, 2018) climbing on an inclined platform (maximum 3 points), (Chen et al., 2019) grip strength (maximum 2 points), (Akhmedov et al., 2015) contralateral reflex (maximum 1 point) and (Yang et al., 2019) contralateral rotation when held by the base of tail (maximum 2 points), and (Zuurbier et al., 2020) visual forepaw reaching (maximum 2 points).

Nissl Staining

The brains of rats from each respective cohort were harvested, followed by fixing in a 10% buffered neutral formalin solution. After standard paraffin embedding, cresyl violet (Nissl staining) was utilized to stain segments. Specifically, dehydration of the sections was performed utilizing increasing concentrations of ethanol in water (30, 50, 75, 95, and 100%), followed by rehydration using decreasing concentrations of the same solution (95, 75, 50, and 30%). Subsequently, the sections were subjected to staining for

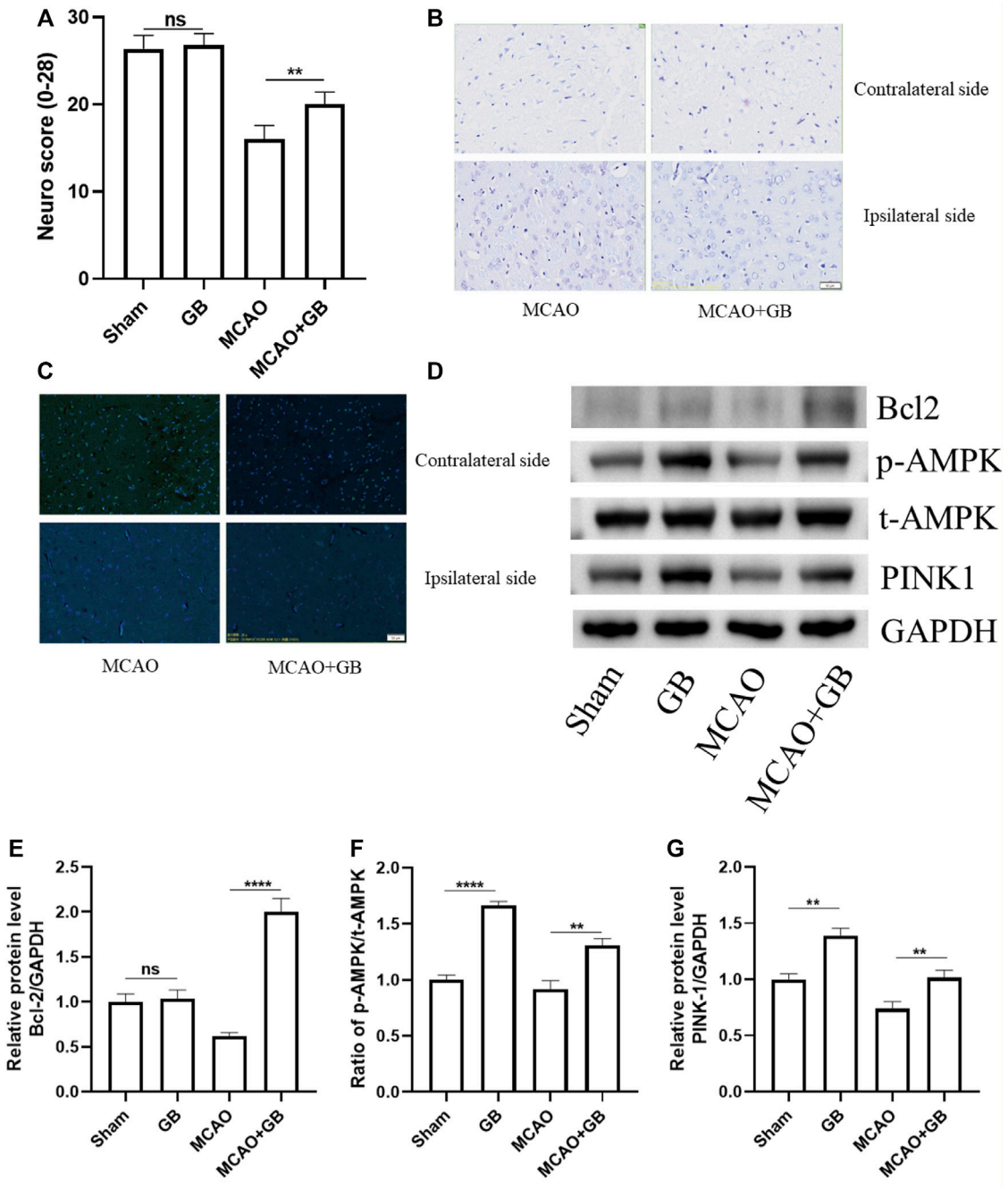

FIGURE 1 | (A) The 28-point composite scoring system for neural behavior. Data are expressed as mean ± SEM and evaluated by means of one-way ANOVA ($n = 6$ per cohort). **(B)** Images of Nissl staining in the dorsal striatum following mild focal ischemia. Scale bar, 50 μm. **(C)** Images of the TUNEL staining in the dorsal striatum following mild focal ischemia. Scale bar, 50 μm. **(D–G)** Representative western blots of Bcl-2, AMPK, and PINK1 in rats exposed to MCAO treatment. (ns, no significant difference, $^{**}p < 0.01$, $^{****}p < 0.0001$).

30 min utilizing cresyl violet solution (0.25 percent) at ambient temperature, followed by stepwise dehydration with 95 and 100% ethanol in water, and clearing using xylene. A fluorescent microscope (Nikon Eclipse 80i, Tokyo, Japan) was utilized to capture microscopy pictures for the purpose of detecting the neuronal loss and the images were subsequently evaluated utilizing NIS-Elements D (version 5.0). Enumeration of the number of neurons was performed from the ipsilateral and contralateral sides of the cerebral cortex and striatum under x400 magnification (Miyajima et al., 2018). Six rats were used to acquire data for two fields in each section.

TdT-Mediated dUTP Nick End Labeling Staining

To determine neuronal apoptosis, TUNEL (TdT-mediated dUTP nick end labeling) staining was performed utilizing a Roche *in Situ* Cell Death Detection Kit in accordance with the guidelines stipulated by the manufacturer. Microscopy images were obtained using a fluorescence microscope (Nikon, Tokyo, Japan) and were evaluated utilizing the NIS-Elements D (version 5.0). Enumeration of the number of positive cells was performed from the ipsilateral and contralateral sides of the cerebral cortex and striatum under x400 magnification. Six rats were used to acquire data for two fields in each section.

Cell Culture

The Cell Bank of the Chinese Academy of Sciences (no. CRL-2266) supplied the SH-SY5Y cells, which were used to culture a high glucose DMEM (Thermo Fisher Scientific, Waltham, MA, United States) comprising 10 percent fetal bovine serum (FBS) (Thermo Fisher Scientific, Waltham, MA, United States) and 1%

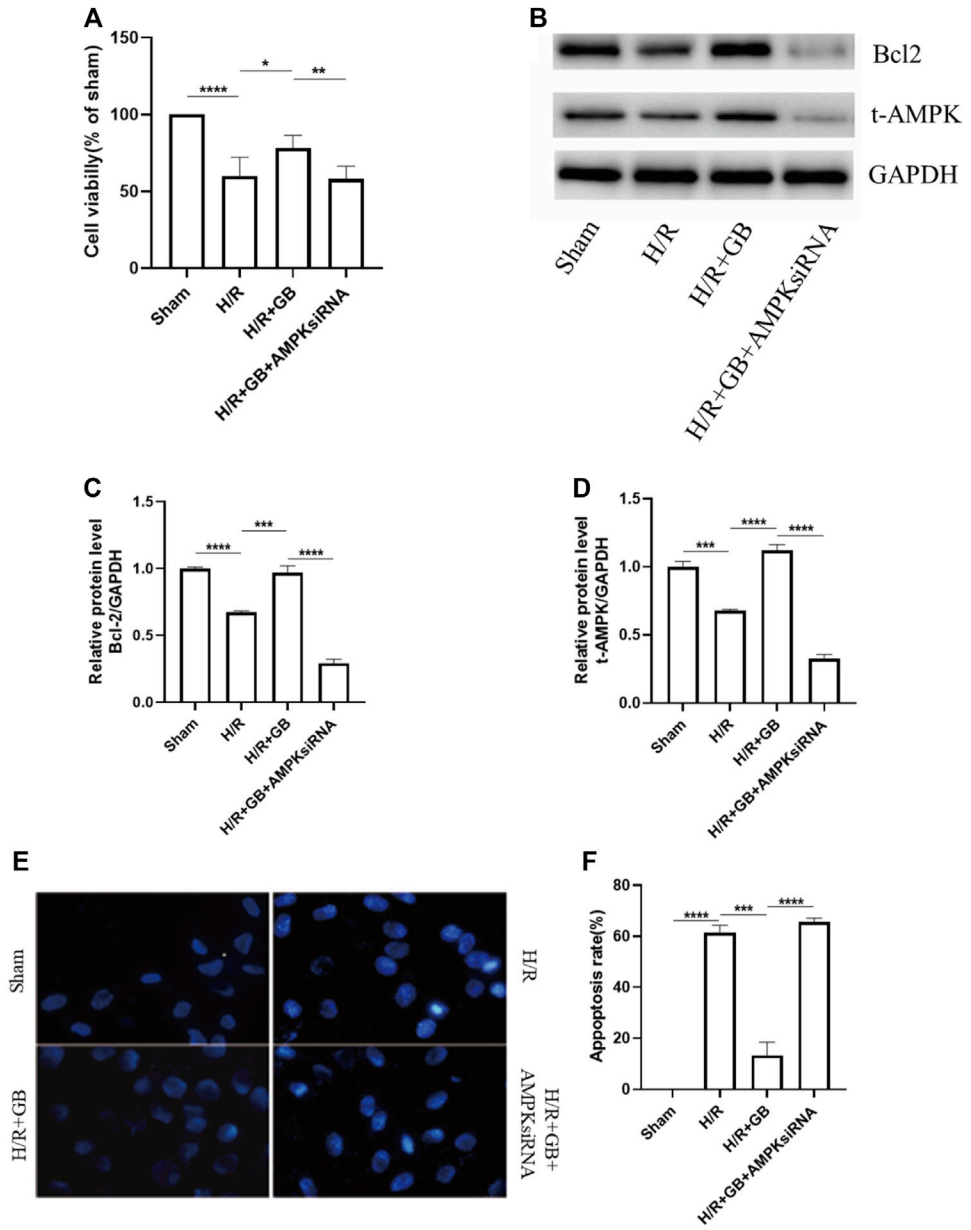

FIGURE 2 | (A) MTT assay was utilized to evaluate cell viability. Data are expressed as mean ± SEM and are representative of 3 separate experimentations. **(B–D)** Western blot images of Bcl-2, AMPK in SH-SY5Y cells subjected to H/R and treated with or without GB. **(E,F)** Hoechst 33342 staining representative images **(E)**. Bar graphs illustrating the apoptosis rate of the cells subjected to various treatments **(F)**. Data are expressed as mean ± SEM and represent 3 distinct experiments. (***p < 0.001, ****p < 0.0001).

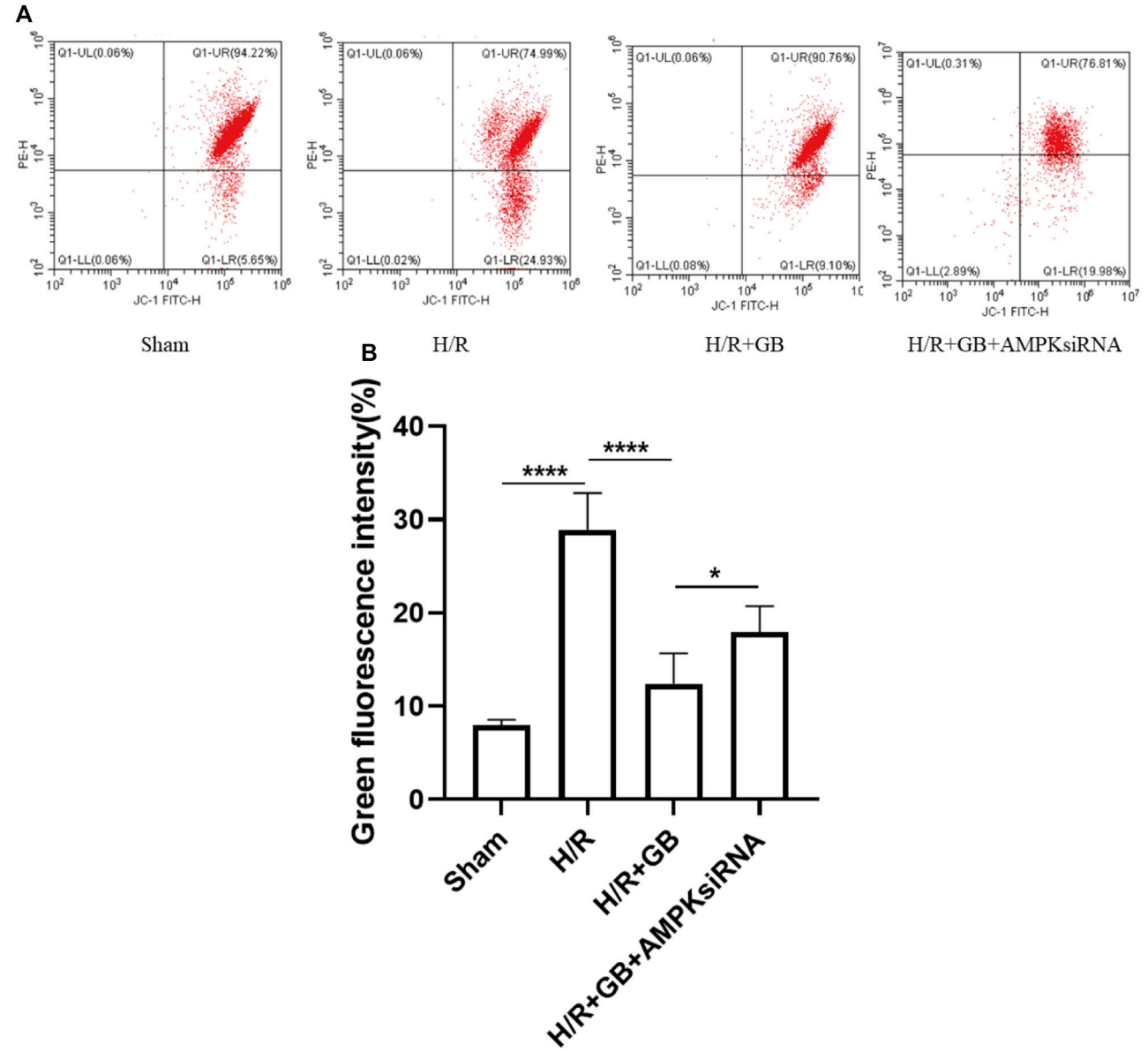

FIGURE 3 | MMP measured *via* FACS **(A)**. Bar graphs showing the ratio of green/red rate in the cells subjected to various treatments **(B)**. Data are expressed as the mean ± SEM and represent 3 distinct experiments. (*$p < 0.05$, ****$p < 0.0001$).

penicillin-streptomycin. Subsequently, the cell culture media was replenished every 2 days. The cells were kept at 37°C in a humid chamber containing 5 percent CO_2

Hypoxia/Reoxygenation

The cells were exposed to H/R as previously reported (Miglio et al., 2004) after being treated for 6 h in the presence or absence of 100 μM GB (Liu et al., 2019). Briefly, the culture media was substituted with OGD buffer (pH 7.4; 2.3 mM $CaCl_2$; 3.6 mM $NaHCO_3$; 5.0 mM HEPES; 5.6 mM KCl; and 154 mM NaCl) and was then put into an airtight chamber where the samples were gassed for 10 min with 95% N_2–5% CO_2. The compartment was completely sealed, which was then moved to a humified incubator at 37°C containing 5 percent CO_2 for 16 h 24 h prior to subsequent experiments, the chamber was opened to initiate reoxygenation and restore the cells to their previous normal culture states.

Transient Transfection With Small Interfering RNA

SH-SY5Y cells were subjected to transient transfection with 100 nM siRNAs targeting AMPKα1/α2 (sc-29673 and sc-38923) or non-silencing control siRNA (scram) (sc-37007) (Santa Cruz Biotechnology, Santa Cruz, CA, United States) for the purpose of knocking down endogenous AMPK.

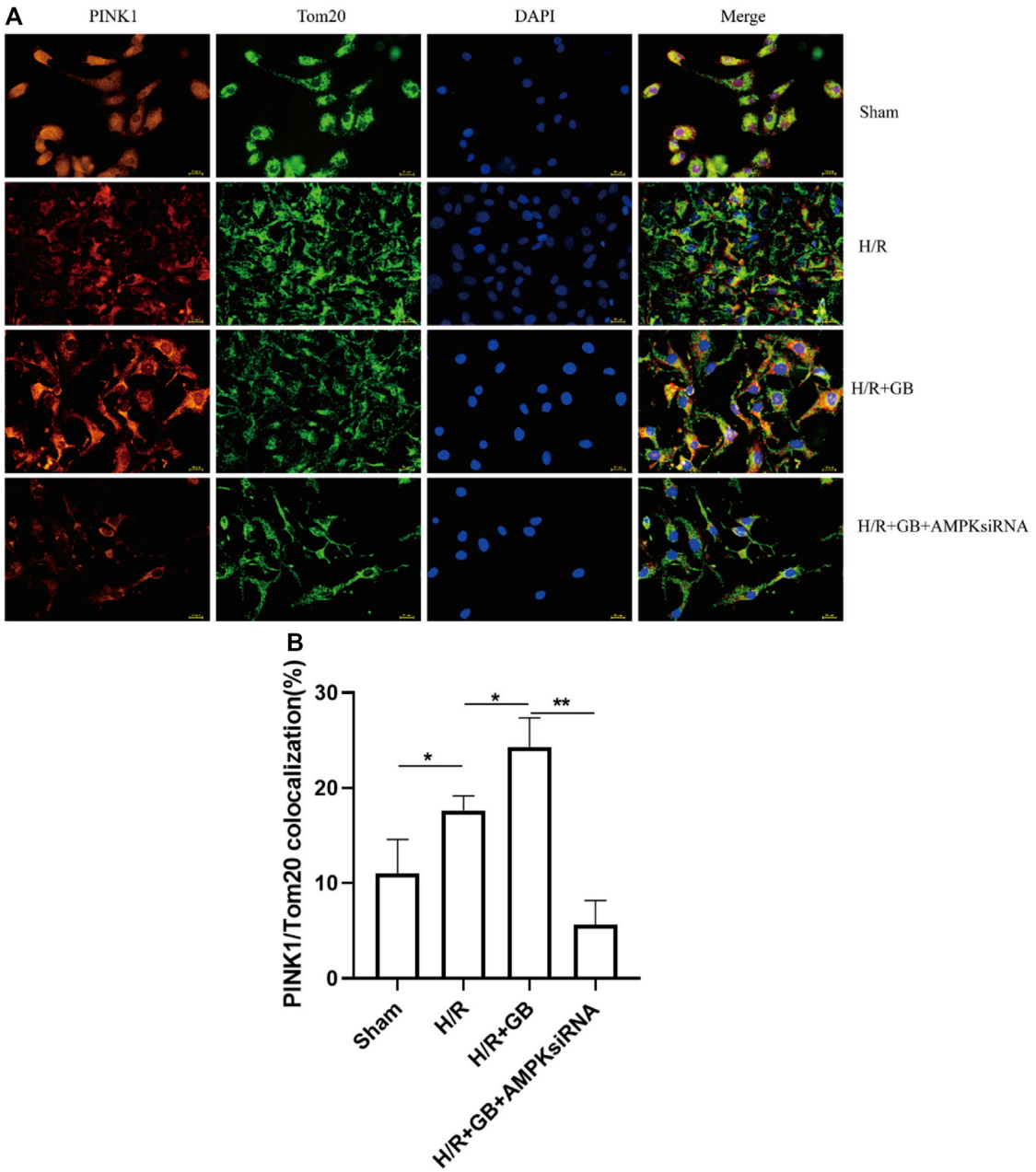

FIGURE 4 | Representative images of PINK1 located on the outer mitochondrial membrane **(A)**. Bar graphs showing the ratio of PINK1/Tom20 co-localization in the cells subjected to various treatments **(B)**. Data are expressed as mean ± SEM and represent 3 separate experiments. (*$p < 0.05$, **$p < 0.01$).

Lipofectamine™ RNAiMAX (Thermo Fisher Scientific, Waltham, MA, United States) was employed as the transfection agent, and the cells were maintained in a culture media in the absence of antibiotics in accordance with the guidelines stipulated by the manufacturer.

Cellular Viability Assessment

As noted earlier, Taveira et al. (2014) the viability of cells was determined using an MTT assay. An ELISA microplate reader (Molecular Devices, Sunnyvale, CA, United States) was utilized for the purpose of measuring the absorption spectrum of produced formazan crystals at 570 nm. The findings are then presented as a percentage of the obtained control cell values.

Hoechst 33342 Staining

Seeding of the SH-SY5Y cells was performed at a density of 2×10^5 cells/well in 6-well plates. After conducting various forms of treatment, the cells were rinsed using PBS before loading them with Hoechst 33342 dye (10 μg/ml, Sigma-Aldrich, St. Louis, MO, United States) for 15 min. Images were obtained using a

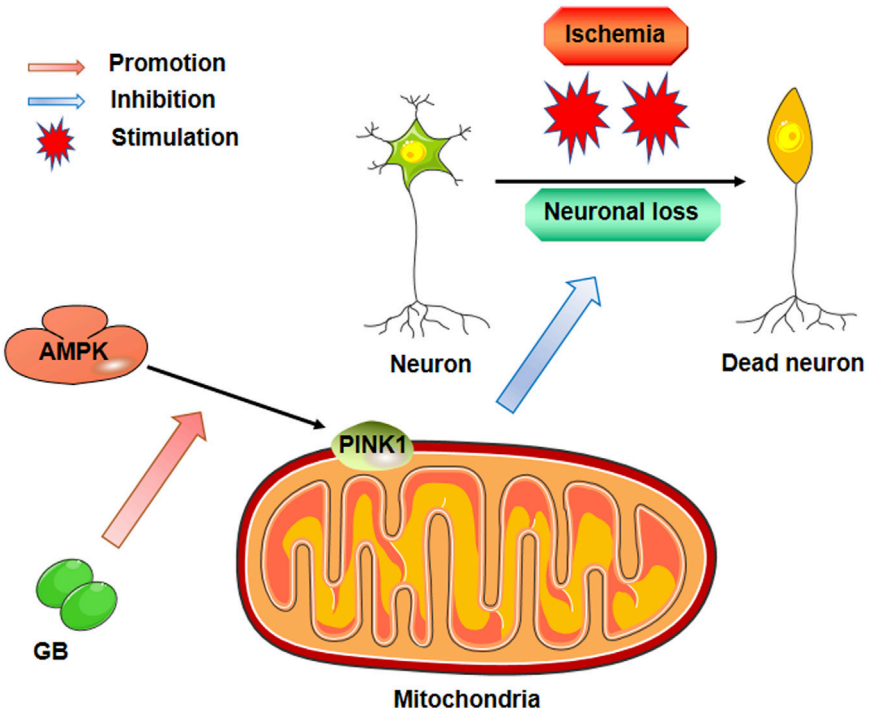

FIGURE 5 | Pharmacological mechanism of Ginkgolide B against neuronal loss post ischemic stroke.

fluorescence microscope (Nikon, Tokyo, Japan) and were evaluated utilizing NIS-Elements D (version 5.0). Subsequently, the isolated nuclei were examined at a magnification of x400 to differentiate the typical homogeneous nuclear pattern from the apoptotic cells' compacted merged chromatin pattern. With respect to the quantification of cell apoptosis, 200 nuclei were examined from six randomly chosen microscopic views. The total number of apoptotic cells in each section was derived and presented as the percentage of the total cell number. Three individual sections were evaluated.

Mitochondrial Membrane Potential Measurement

A mitochondrial membrane potential assay kit (C2006, Beyotime Biotechnology, Shanghai, China) was utilized to measure the MMP of cells. After treatment, SH-SY5Y cells were subjected to incubation for 20 min in darkness with a JC-1 staining solution. Thus, ΔΨm was expressed by the ratio of green (monomeric form, demonstrating depolarized/low MMP) over red (aggregated form, signifying polarized/normal MMP) determined with the aid of the Becton-Dickinson FACS Calibur system (BD Biosciences, Franklin Lakes, NJ, United States).

Immunofluorescence Staining

To evaluate the expression of PINK1 in the outer mitochondrial membrane, incubation of the SH-SY5Y cells was performed in a glass chamber slide (Thermo Fisher Scientific, Waltham, MA, United States) and treated with or without GB under hypoxia/reoxygenation conditions. Subsequently, the cells were subjected to 15 min of fixing using 4 percent paraformaldehyde at ambient temperature, followed by permeabilization of the cells using 0.1 percent Triton X-100 and blocking using 10 percent goat serum. Then, the cells were subjected to incubation with anti-PINK1 (23274-1-AP, 1:200, Proteintech, Wuhan, China) and 488-conjugated mouse anti-Tom 20 antibody (sc-17764 AF488, 1: 100, Santa Cruz Biotechnology, Santa Cruz, CA, United States) over the night at a temperature of 4°C and 594-conjugated donkey anti-rabbit antibody (Thermo Fisher Scientific, Waltham, MA, United States) at ambient temperature for 1 h. Eventually, the slides were mounted, followed by imaging with the aid of a fluorescence microscope (Nikon, Tokyo, Japan).

Western Blotting

Protein concentrations obtained from the infarcted brain tissues or SH-SY5Y cells were assessed utilizing a BCA Protein Assay Kit (KeyGEN BioTECH, Nanjing, China). Specifically, proteins in identical quantities were treated to sodium dodecyl sulfate-polyacrylamide gel electrophoresis (SDS-PAGE) with 30 ug proteins added into per lane for the electrophoresis, followed by loading onto polyvinylidene fluoride (PVDF) membranes (Millipore, Billerica, MA, United States). Once the membranes had been blocked, incubation of the membranes using primary antibodies at 4°C throughout the night was performed, followed by another incubation using HRP-conjugated secondary antibodies at ambient temperature for 1 h. The membranes were then exposed and analyzed utilizing an ECL system

(Tanon, Shanghai, China). The following were the primary antibodies that were employed in the protocol: anti-AMPK (ab32047), p-AMPK (ab133448), PINK1 (ab186303), Bcl-2 (ab196495), and Bax (ab32503). The secondary antibody used was an HRP-conjugated anti-GAPDH monoclonal antibody (HRP-60004, 1:5000, Proteintech, Rosemont, IL, United States).

Statistical Analysis

The findings were analyzed using the Statistical Product and Service Solutions (SPSS) software (version: 22.0) (IBM, Armonk, NY, United States) and data were expressed as the means ± SEM. When comparing the different experimental cohorts, one-way ANOVA was utilized and Tukey's *post hoc* analysis was performed for multiple range tests. Statistical significance was deemed to have been attained at $p < 0.05$.

RESULTS

Ginkgolide B Treatment Improved the Composite Neuro Score and Attenuated Neuronal Loss and Apoptosis in Rats After Middle Cerebral Artery Occlusion

We utilized a 28-point composite neuro score to validate the neuroprotective effect of GB on sensorimotor dysfunction in rats following MCAO. We observed that there was a decrease in the scores of MCAO rats as opposed to the sham-operated controls, whereas neuronal loss and apoptosis showed an evident elevation in scores. It was also observed that GB treatment significantly reversed these changes (**Figures 1A–C**). The results of the western blot assay indicated that the decreased neuronal apoptosis in GB-treated MCAO rats was accompanied by an elevation in PINK1 and p-AMPK levels (**Figures 1D–G**). These results suggest that GB treatment could alleviate sensorimotor dysfunction following MCAO and could be AMPK/PINK1-dependent.

Ginkgolide B Treatment Decreased Oxygen and Glucose Deprivation-R-Induced SH-SY5Y Apoptosis and was AMPK-Dependent

We used SH-SY5Y human neuroblastoma cells that had been cultured under the OGD-R circumstance as a model of ischemia-reperfusion damage for the purpose of investigating the protection impact of GB-related on neuronal cell death following ischemia. As shown in **Figure 2A**, there was a remarkably decreased viability in OGD-R treated cells as evaluated by the MTT assay. However, it was observed that GB treatment significantly reversed this decrease. AMPKα1/α2 siRNA effectively decreased AMPKα protein levels (**Figures 2B–D**) and led to a significant decrease in cell viability of GB-treated cells under OGD-R conditions. Similar results were found in SH-SY5Y cell apoptosis, as evidenced by the results of Hoechst 33342 staining (**Figures 2E,F**). These results suggest that GB treatment decreased SH-SY5Y cells apoptosis induced by OGD-R and was AMPK-dependent.

Ginkgolide B Improved Oxygen and Glucose Deprivation-R-Induced SH-SY5Y Mitochondrial Damage and was AMPK-Dependent

The mitochondrial membrane potential (MMP) is an index that can be used to measure the extent of mitochondrial damage. The protective properties of GB in relation to mitochondrial damage were explored in SH-SY5Y cells following ischemia, as evaluated through JC-1 staining. The intensity of green fluorescence was substantially elevated following OGD-R treatment, demonstrating that the MMP of cells was attenuated. However, this decreasing trend was reversed upon treatment with GB. AMPK knockdown using AMPKα1/α2 siRNA abrogated the GB treatment-induced improvement of MMP in H/R-treated cells (**Figure 3**). These findings illustrated that GB could perform a function in reducing the mitochondrial damage response to OGD-R stress and that AMPK performs a critical function in this process. These results also indicated that the OGD-R-stimulated neuronal apoptosis was dependent on the mitochondrial apoptosis pathway. The level of Bcl-2 expression in OGD-R treated cells confirmed this finding.

Ginkgolide B Upregulates the Expression of PINK1 in Response to Ischemia and was AMPK-Dependent

The stable expression of PINK1 on the outer mitochondrial membrane performs a critical function in reducing mitochondrial damage. To explore the effect of GB treatment on the mitochondrial damage in SH-SY5Y cells following ischemia, the localization of PINK1 on the outer mitochondrial membrane in OGD-R cells was evaluated upon treatment with GB, as evidenced by the results of the double immunofluorescence staining. As shown in **Figure 4**, co-localization was slightly enhanced in cells treated with OGD-R compared to the sham control and was enhanced upon GB treatment. Moreover, this enhancing trend was abrogated upon treatment with AMPK siRNA. These results suggest that the increased PINK1 expression in the outer mitochondrial membrane upon GB treatment was AMPK-dependent.

DISCUSSION

Rat focal cerebral ischemia models induced *via* transient middle cerebral artery occlusion (t-MCAO) could produce a reliable infarct that strongly resembles human ischemic stroke (Fluri et al., 2015). This model was then widely used in studies focusing on ischemic pathophysiological processes and related neuroprotective strategies (Shah et al., 2019). In the present research, we examined the protection ability of GB against stroke and its specific mechanism using a rat t-MCAO model. It was observed that the neuroprotective functions of GB in

MCAO rats resulted in a decrease in neuronal apoptosis, which was associated with the upregulated expression of PINK1 that was dependent on the activation of the AMPK pathway.

Neuronal apoptosis is a major pathological process following ischemia, and complex mechanisms are responsible for this mechanism. In the present research, we focused on exploring the neuroprotective effect of Ginkgolide B, a widely used compound in treating ischemic stroke, in relation to neuronal apoptosis. In MCAO rats, GB treatment significantly decreased neuronal loss and apoptosis and was accompanied by increased PINK1 expression and AMPK activation. These results suggest a potential novel link between GB and a mitochondrial damage response to cerebral ischemia. To delve into the underlying mechanism, SH-SY5Y human neuroblastoma cells that had been cultured based on the OGD-R circumstance were used to construct a model of ischemia-reperfusion damage (Miglio et al., 2004; Fallarini et al., 2009). Using this *in vitro* model, we showed that GB reduced mitochondrial damage by upregulating the expression of PINK1 in the outer mitochondrial membrane and that the observed upregulation of PINK1 prevents mitochondrial apoptosis. Meanwhile, to prevent the non-specific impacts of pharmacologic approaches with regard to the correlation between AMPK signaling pathways and GB, a genetic approach using AMPKα1/α2 siRNA was employed to silence AMPK. The results demonstrated that the protective function of GB on mitochondrial damage and apoptosis is dependent on AMPK activation. As far as we know, the present research is the first investigation to explore the role of GB on mitochondrial apoptosis in cerebral ischemia.

GB has been widely used to treat stroke (Chi et al., 2015; Feng et al., 2019) because of its anti-inflammatory (Gu et al., 2012; Shu et al., 2016; Li et al., 2020), metabolic, and neurotrophic effects (Nabavi et al., 2015; Yu et al., 2018; Xin et al., 2020; Yang et al., 2021). However, in clinical practice, neuro progresses to irreversible ischemic injury after stroke occlusion within a few minutes. The substances released from damaged nerve cells in such a short-time window induce the inflammatory response after stroke. As consequence, the anti-apoptotic properties of GB might have an integral function in stroke treatment although such a role is rarely reported. In the present research, the anti-apoptotic impact of GB on cerebral ischemia was confirmed by *in vivo* and *in vitro* experiments. Furthermore, our results corroborate that the AMPK pathway performs a key function in mitochondrial function and apoptosis (**Figure 5**). In summary, our study provided a novel possibility for stroke treatment that needs to be further studied.

DATA AVAILABILITY STATEMENT

The original contributions presented in the study are included in the article/supplementary material, further inquiries can be directed to the corresponding authors.

ETHICS STATEMENT

The animal study was reviewed and approved by the Ethics Committee for the Use of Experimental Animals of Jiangsu Kanion Pharmaceutical Co. Ltd. State Key Laboratory of New Pharmaceutical Process for Traditional Chinese Medicine.

AUTHOR CONTRIBUTIONS

YC, LY, and HC conceived and designed the experiments. YC performed the experiments, analyzed the data and prepared the manuscript. LY and HC supervised the research. All authors approved the final version of this manuscript.

FUNDING

The study was supported the Funding from the Science and Technology Innovation Foundation of Yangzhou University (X20200746).

REFERENCES

Akhmedov, A. T., Rybin, V., and Marín-García, J. (2015). Mitochondrial Oxidative Metabolism and Uncoupling Proteins in the Failing Heart. *Heart Fail Rev.* 20 (2), 227–249. doi:10.1007/s10741-014-9457-4

Amani, H., Mostafavi, E., Alebouyeh, M. R., Arzaghi, H., Akbarzadeh, A., Pazoki-Toroudi, H., et al. (2019). Would Colloidal Gold Nanocarriers Present an Effective Diagnosis or Treatment for Ischemic Stroke? *Int. J. Nanomedicine* 14, 8013–8031. doi:10.2147/IJN.S210035

Bai, S., Hu, Z., Yang, Y., Yin, Y., Li, W., Wu, L., et al. (2016). Anti-Inflammatory and Neuroprotective Effects of Triptolide *via* the NF-Kb Signaling Pathway in a Rat MCAO Model. *Anat. Rec. Hob.* 299 (2), 256–266. doi:10.1002/ar.23293

Cao, S., Wang, C., Yan, J., Li, X., Wen, J., and Hu, C. (2020). Curcumin Ameliorates Oxidative Stress-Induced Intestinal Barrier Injury and Mitochondrial Damage by Promoting Parkin Dependent Mitophagy through AMPK-TFEB Signal Pathway. *Free Radic. Biol. Med.* 147, 8–22. doi:10.1016/j.freeradbiomed.2019.12.004

Chen, X., Wang, Q., Shao, M., Ma, L., Guo, D., Wu, Y., et al. (2019). Ginsenoside Rb3 Regulates Energy Metabolism and Apoptosis in Cardiomyocytes *via* Activating PPARα Pathway. *Biomed. Pharmacother.* 120, 109487. doi:10.1016/j.biopha.2019.109487

Chi, C. L., Shen, D. F., Wang, P. J., Li, H. L., and Zhang, L. (2015). Effect of Ginkgolide B on Brain Metabolism and Tissue Oxygenation in Severe Haemorrhagic Stroke. *Int. J. Clin. Exp. Med.* 8 (3), 3522–3529.

Drieu, A., Levard, D., Vivien, D., and Rubio, M. (2018). Anti-inflammatory Treatments for Stroke: from Bench to Bedside. *Ther. Adv. Neurol. Disord.* 11, 1756286418789854. doi:10.1177/1756286418789854

Encarnacion, A., Horie, N., Keren-Gill, H., Bliss, T. M., Steinberg, G. K., and Shamloo, M. (2011). Long-term Behavioral Assessment of Function in an Experimental Model for Ischemic Stroke. *J. Neurosci. Methods* 196 (2), 247–257. doi:10.1016/j.jneumeth.2011.01.010

Fallarini, S., Miglio, G., Paoletti, T., Minassi, A., Amoruso, A., Bardelli, C., et al. (2009). Clovamide and Rosmarinic Acid Induce Neuroprotective Effects in *In Vitro* Models of Neuronal Death. *Br. J. Pharmacol.* 157 (6), 1072–1084. doi:10.1111/j.1476-5381.2009.00213.x

Feng, Z., Sun, Q., Chen, W., Bai, Y., Hu, D., and Xie, X. (2019). The Neuroprotective Mechanisms of Ginkgolides and Bilobalide in Cerebral Ischemic Injury: a Literature Review. *Mol. Med.* 25 (1), 57. doi:10.1186/s10020-019-0125-y

Fluri, F., Schuhmann, M. K., and Kleinschnitz, C. (2015). Animal Models of Ischemic Stroke and Their Application in Clinical Research. *Drug Des. Devel Ther.* 9, 3445–3454. doi:10.2147/DDDT.S56071

Gu, J. H., Ge, J. B., Li, M., Wu, F., Zhang, W., and Qin, Z. H. (2012). Inhibition of NF-Kb Activation Is Associated with Anti-inflammatory and Anti-apoptotic Effects of Ginkgolide B in a Mouse Model of Cerebral Ischemia/reperfusion Injury. *Eur. J. Pharm. Sci.* 47 (4), 652–660. doi:10.1016/j.ejps.2012.07.016

Hang, L., Thundyil, J., and Lim, K. L. (2015). Mitochondrial Dysfunction and Parkinson Disease: a Parkin-AMPK Alliance in Neuroprotection. *Ann. N. Y. Acad. Sci.* 1350, 37–47. doi:10.1111/nyas.12820

Hu, M., Ye, P., Liao, H., Chen, M., and Yang, F. (2016). Metformin Protects H9C2 Cardiomyocytes from High-Glucose and Hypoxia/Reoxygenation Injury *via* Inhibition of Reactive Oxygen Species Generation and Inflammatory Responses: Role of AMPK and JNK. *J. Diabetes Res.* 2016, 2961954. doi:10.1155/2016/2961954

Jiang, Y. X., Li, W., Wang, J., and Wang, G. G. (2020). Cardiac Dysfunction Is Attenuated by Ginkgolide B *via* Reducing Oxidative Stress and Fibrosis in Diabetic Rats. *Iran. J. Basic Med. Sci.* 23 (8), 1078–1084. doi:10.22038/ijbms.2020.44210.10358

Kane, L. A., Lazarou, M., Fogel, A. I., Li, Y., Yamano, K., Sarraf, S. A., et al. (2014). PINK1 Phosphorylates Ubiquitin to Activate Parkin E3 Ubiquitin Ligase Activity. *J. Cell Biol.* 205 (2), 143–153. doi:10.1083/jcb.201402104

Khan, M., Elango, C., Ansari, M. A., Singh, I., and Singh, A. K. (2007). Caffeic Acid Phenethyl Ester Reduces Neurovascular Inflammation and Protects Rat Brain Following Transient Focal Cerebral Ischemia. *J. Neurochem.* 102 (2), 365–377. doi:10.1111/j.1471-4159.2007.04526.x

Kim, Y., Park, J., Kim, S., Song, S., Kwon, S. K., Lee, S. H., et al. (2008). PINK1 Controls Mitochondrial Localization of Parkin through Direct Phosphorylation. *Biochem. Biophys. Res. Commun.* 377 (3), 975–980. doi:10.1016/j.bbrc.2008.10.104

Koyano, F., Okatsu, K., Kosako, H., Tamura, Y., Go, E., Kimura, M., et al. (2014). Ubiquitin Is Phosphorylated by PINK1 to Activate Parkin. *Nature* 510 (7503), 162–166. doi:10.1038/nature13392

Li, X., Huang, L., Liu, G., Fan, W., Li, B., Liu, R., et al. (2020). Ginkgo Diterpene Lactones Inhibit Cerebral Ischemia/reperfusion Induced Inflammatory Response in Astrocytes *via* TLR4/NF-Kb Pathway in Rats. *J. Ethnopharmacol.* 249, 112365. doi:10.1016/j.jep.2019.112365

Liu, Q., Jin, Z., Xu, Z., Yang, H., Li, L., Li, G., et al. (2019). Antioxidant Effects of Ginkgolides and Bilobalide against Cerebral Ischemia Injury by Activating the Akt/Nrf2 Pathway *In Vitro* and *In Vivo*. *Cell Stress Chaperones* 24 (2), 441–452. doi:10.1007/s12192-019-00977-1

Miglio, G., Varsaldi, F., Francioli, E., Battaglia, A., Canonico, P. L., and Lombardi, G. (2004). Cabergoline Protects SH-Sy5y Neuronal Cells in an *In Vitro* Model of Ischemia. *Eur. J. Pharmacol.* 489 (3), 157–165. doi:10.1016/j.ejphar.2004.03.006

Miyajima, N., Ito, M., Rokugawa, T., Iimori, H., Momosaki, S., Omachi, S., et al. (2018). Detection of Neuroinflammation before Selective Neuronal Loss Appearance after Mild Focal Ischemia Using [18F]DPA-714 Imaging. *Ejnmmi Res.* 8 (1), 43. doi:10.1186/s13550-018-0400-x

Nabavi, S. M., Habtemariam, S., Daglia, M., Braidy, N., Loizzo, M. R., Tundis, R., et al. (2015). Neuroprotective Effects of Ginkgolide B against Ischemic Stroke: A Review of Current Literature. *Curr. Top. Med. Chem.* 15 (21), 2222–2232. doi:10.2174/1568026615666150610142647

Seabright, A. P., and Lai, Y. C. (2020). Regulatory Roles of PINK1-Parkin and AMPK in Ubiquitin-dependent Skeletal Muscle Mitophagy. *Front. Physiol.* 11, 608474. doi:10.3389/fphys.2020.608474

Shah, F. A., Li, T., Kury, L. T. A., Zeb, A., Khatoon, S., Liu, G., et al. (2019). Pathological Comparisons of the Hippocampal Changes in the Transient and Permanent Middle Cerebral Artery Occlusion Rat Models. *Front. Neurol.* 10, 1178. doi:10.3389/fneur.2019.01178

Shu, Z. M., Shu, X. D., Li, H. Q., Sun, Y., Shan, H., Sun, X. Y., et al. (2016). Ginkgolide B Protects against Ischemic Stroke *via* Modulating Microglia Polarization in Mice. *Cns Neurosci. Ther.* 22 (9), 729–739. doi:10.1111/cns.12577

Siniscalchi, A., Gallelli, L., Malferrari, G., Pirritano, D., Serra, R., Santangelo, E., et al. (2014). Cerebral Stroke Injury: the Role of Cytokines and Brain Inflammation. *J. Basic Clin. Physiol. Pharmacol.* 25 (2), 131–137. doi:10.1515/jbcpp-2013-0121

Taveira, M., Sousa, C., Valentão, P., Ferreres, F., Teixeira, J. P., and Andrade, P. B. (2014). Neuroprotective Effect of Steroidal Alkaloids on Glutamate-Induced Toxicity by Preserving Mitochondrial Membrane Potential and Reducing Oxidative Stress. *J. Steroid Biochem. Mol. Biol.* 140, 106–115. doi:10.1016/j.jsbmb.2013.12.013

Wang, J., Ding, Y., Zhuang, L., Wang, Z., Xiao, W., and Zhu, J. (2021). Ginkgolide B-induced AMPK P-athway A-ctivation P-rotects A-strocytes by R-egulating E-ndoplasmic R-eticulum S-tress, O-xidative S-tress and E-nergy M-etabolism I-nduced by Aβ1-42. *Mol. Med. Rep.* 23 (6), 23. doi:10.3892/mmr.2021.12096

Xin, C., Zhang, Z., Gao, G., Ding, L., Yang, C., Wang, C., et al. (2020). Irisin Attenuates Myocardial Ischemia/Reperfusion Injury and Improves Mitochondrial Function through AMPK Pathway in Diabetic Mice. *Front. Pharmacol.* 11, 565160. doi:10.3389/fphar.2020.565160

Yang, H., Li, G. P., Liu, Q., Zong, S. B., Li, L., Xu, Z. L., et al. (2021). Neuroprotective Effects of Ginkgolide B in Focal Cerebral Ischemia through Selective Activation of Prostaglandin E2 Receptor EP4 and the Downstream Transactivation of Epidermal Growth Factor Receptor. *Phytotherapy Res.* 35, 2727–2744. doi:10.1002/ptr.7018

Yang, Q., and Long, Q. (2018). PPARδ, a Potential Therapeutic Target for Heart Disease. *Nucl. Recept. Res.* 5, 1072–1084. doi:10.32527/2018/101375

Yang, Y., Zhao, M., Yu, X. J., Liu, L. Z., He, X., Deng, J., et al. (2019). Pyridostigmine Regulates Glucose Metabolism and Mitochondrial Homeostasis to Reduce Myocardial Vulnerability to Injury in Diabetic Mice. *Am. J. Physiol. Endocrinol. Metab.* 317 (2), E312–E326. doi:10.1152/ajpendo.00569.2018

Yu, J., Li, X., Matei, N., McBride, D., Tang, J., Yan, M., et al. (2018). Ezetimibe, a NPC1L1 Inhibitor, Attenuates Neuronal Apoptosis through AMPK Dependent Autophagy Activation after MCAO in Rats. *Exp. Neurol.* 307, 12–23. doi:10.1016/j.expneurol.2018.05.022

Zhang, W., Potrovita, I., Tarabin, V., Herrmann, O., Beer, V., Weih, F., et al. (2005). Neuronal Activation of NF-kappaB Contributes to Cell Death in Cerebral Ischemia. *J. Cereb. Blood Flow. Metab.* 25 (1), 30–40. doi:10.1038/sj.jcbfm.9600004

Zuurbier, C. J., Bertrand, L., Beauloye, C. R., Andreadou, I., Ruiz-Meana, M., Jespersen, N. R., et al. (2020). Cardiac Metabolism as a Driver and Therapeutic Target of Myocardial Infarction. *J. Cell Mol. Med.* 24 (11), 5937–5954. doi:10.1111/jcmm.15180

Conflict of Interest: The authors declare that the research was conducted in the absence of any commercial or financial relationships that could be construed as a potential conflict of interest.

Publisher's Note: All claims expressed in this article are solely those of the authors and do not necessarily represent those of their affiliated organizations, or those of the publisher, the editors and the reviewers. Any product that may be evaluated in this article, or claim that may be made by its manufacturer, is not guaranteed or endorsed by the publisher.

frontiers | Frontiers in Pharmacology

ORIGINAL RESEARCH
published: 22 July 2022
doi: 10.3389/fphar.2022.960311

Development and Validation of a UHPLC–MS/MS Method for Quantitation of Almonertinib in Rat Plasma: Application to an *in vivo* Interaction Study Between Paxlovid and Almonertinib

Peng-fei Tang[1], *Su-su Bao*[1], *Nan-yong Gao*[2], *Chuan-feng Shao*[1], *Wei-fei Xie*[1], *Xue-meng Wu*[3], *Le-ping Zhao*[1]* and *Zhong-xiang Xiao*[1]*

[1]*Affiliated Yueqing Hospital, Wenzhou Medical University, Wenzhou, China,* [2]*Department of Pharmacology, School of Pharmacy of Wenzhou Medical University, Wenzhou, China,* [3]*Market Supervision Administration of Yueqing City, Wenzhou, China*

OPEN ACCESS

Edited by:
Simona Pichini,
National Institute of Health (ISS), Italy

Reviewed by:
Alberto Salomone,
University of Turin, Italy
Zheng Han,
Shanghai Academy of Agricultural Sciences, China

***Correspondence:**
Le-ping Zhao
z13587773853@163.com
Zhong-xiang Xiao
xiangzi198155@163.com

Specialty section:
This article was submitted to Drug Metabolism and Transport, a section of the journal Frontiers in Pharmacology

Received: *02 June 2022*
Accepted: *23 June 2022*
Published: *22 July 2022*

Citation:
Tang P-f, Bao S-s, Gao N-y, Shao C-f, Xie W-f, Wu X-m, Zhao L-p and Xiao Z-x (2022) Development and Validation of a UHPLC–MS/MS Method for Quantitation of Almonertinib in Rat Plasma: Application to an in vivo Interaction Study Between Paxlovid and Almonertinib. Front. Pharmacol. 13:960311. doi: 10.3389/fphar.2022.960311

Almonertinib was approved for the first-line treatment of advanced NSCLC patients with EGFR-TKI-sensitive genetic mutations by National Medical Products Administration (NMPA) in 2021.The purpose of this study was to establish and validate a fast, accurate, stable and facile ultra-performance liquid chromatography-tandem mass spectrometry method for the quantification of almonertinib in rat plasma, it was employed to explore the effect of Paxlovid on the pharmacokinetics of almonertinib in rats. Zanubrutinib was used as an internal standard (IS), and the plasma samples were prepared by the protein precipitation method using acetonitrile. Chromatographic separation was carried out on a Shimadzu LC-20AT ultra-performance liquid chromatography system using a Shim-pack velox C18 (2.1× 50 mm, 2.7 μM) column. The mobile phase consisted of methanol and 0.1% formic acid-water. Mass spectrum analysis was executed using Shimadzu 8040 Triple quadrupole mass spectrometry. The precursor and product ions of the analyte and internal standard were detected in multiple reaction monitoring (MRM) mode. The typical fragment ions were *m/z 526.20 → 72.10* for almonertinib and *m/z 472.15 → 290.00* for zanubrutinib (IS). The method was validated to have good linearity for quantifying almonertinib in rat plasma from 0.1–1000 ng/ml (R^2 = 0.999), and the LLOQ was 0.1 ng/ml. The validity of this method was sufficiently verified for selectivity, specificity, extraction recovery, matrix effect, accuracy, precision and stability. The validated UHPLC–MS/MS method was successfully applied to the drug interaction study of almonertinib with Paxlovid in rats. Paxlovid significantly inhibits the metabolism of almonertinib and increased the exposure of almonertinib. This study can help us to understand the metabolic profile of almonertinib better, and further human trials should be conducted to validate the results.

Keywords: almonertinib, drug-drug interaction, UHPLC-MS/MS, Paxlovid, pharmacokinetics

1 INTRODUCTION

Almonertinib is a new type of irreversible third-generation EGFR inhibitor, that is, highly selective for EGFR-TKI-sensitive genetic mutations and T790 M drug-resistant gene mutations (Nagasaka et al., 2021). Almonertinib was approved for the treatment of patients with advanced NSCLC following progression on prior EGFR-TKIs and having a T790M drug-resistance mutation by the National Medical Products Administration (NMPA) in 2020 (Lu et al., 2021). It was subsequently approved for the first-line treatment of advanced NSCLC patients with EGFR-TKI-sensitive genetic mutations by NMPA in 2021 based on the AENEAS trial (Lu, 2021). In contrast to earlier generations of EGFR-TKIs, almonertinib is a small molecular drug that uses pyrimidine as a structural basis and retains the acrylamide structure; it exerts antitumor effects by covalently binding cysteine 797 at the ATP binding site of the TK domain (Yang et al., 2020). (**Figure 1**) Compared with the first-generation EGFR-TIK gefitinib, almonertinib has shown obvious advantages in progression-free survival (PFS), duration of response (DOR) and objective response rate (ORR) for first-line therapy (Lu, 2021). The higher selectivity for EGFR-TKI-sensitive genetic mutations and relatively lower off-target effects for other wild-type EGFRs mean that almonertinib shows better security than previous generations (Lu, 2021; Shirley and Keam, 2022). The AENEAS results show that the incidence of drug-related adverse reactions was lower with almonertinib than with gefitinib for mild adverse events, such as rash (23.4% vs. 41.4%), diarrhea (16.4% vs. 35.8%), liver damage (29.9% vs. 54.0%) and serious adverse events (4.2% vs. 11.2%) (Lu, 2021).

Beginning in 2019, COVID-19 caused by the SARS-CoV-2 pose a constant threat to global people's health (Pollard et al., 2020). Paxlovid was approved for the treatment of adults and pediatric patients with mild-to-moderate COVID-19 by the FDA emergency use authorization in December 2021 (Saravolatz et al., 2022). Paxlovid consist of nirmatrelvir, an antiviral active compound against SARS-CoV-2 and ritonavir, a CYP3A4 inhibitor (Owen et al., 2021). For the patient with both NSCLC and COVID-19, drug therapy requires the combination of almonertinib and Paxlovid (Passaro et al., 2021). The results of *in vitro* experiments show that almonertinib is primarily metabolized to N-demethylation metabolite through CYP3A4 (Liu et al., 2022a). In clinical study, the combination of almonertinib and CYP3A4 inducers or inhibitors could have affected plasma concentration of almonertinib and thus influences clinical effect and adverse reactions of almonertinib (Liu et al., 2022a). Therefore, it is necessary to establish a technique for the fast and accurate determination of almonertinib concentrations in plasma, which will help to evaluate the change of pharmacokinetics parameters and discover potential drug interactions during combined administration.

To our knowledge, only one analytical method to quantify almonertinib in biological sample have been reported (Liu et al., 2022b). This method is less than perfect for a number of reasons. For example, it is only applicable in human plasma, has a narrow linear range, and lacks sufficient experimental data validated by other laboratories. Thus, this UHPLC-MS/MS method can't fulfill the requirements of the preclinical drug-drug interaction studies. Therefore, the purpose of this study was to establish and validate a fast, accurate, stable UHPLC-MS/MS method for the quantification of almonertinib in rat plasma. The feasibility and accuracy of this method are verified by selectivity, specificity, extraction

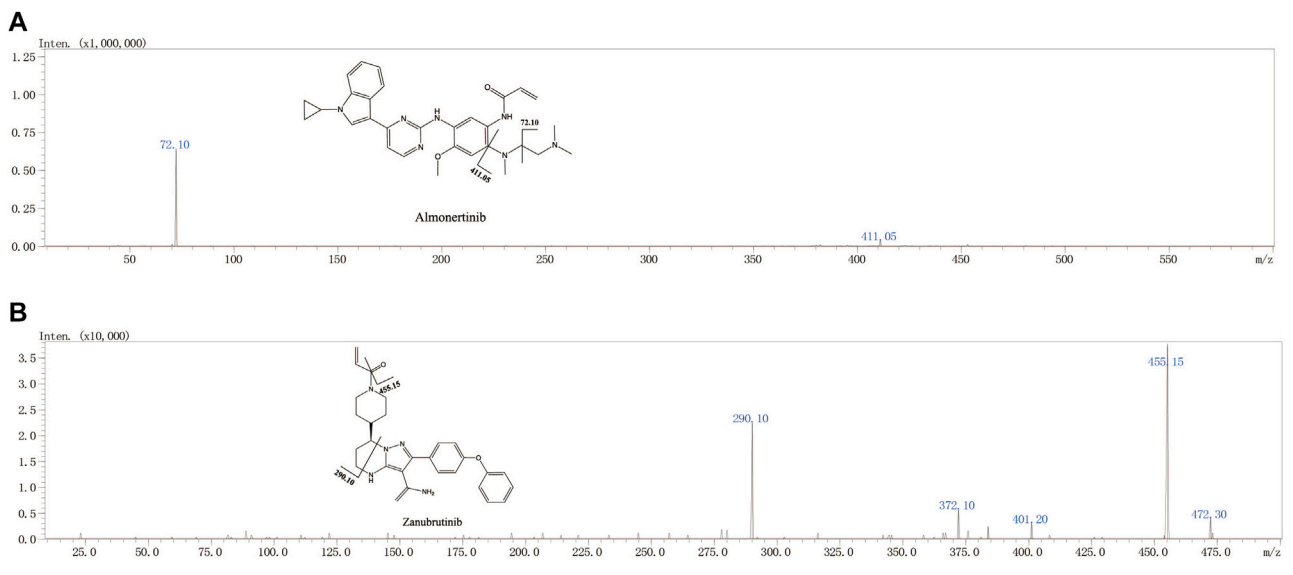

FIGURE 1 | The chemical structures and Mass spectra of almonertinib and IS in the present study.

recovery, matrix effect, accuracy, precision and stability experiments. Finally, the effects of Paxlovid on drug exposure and pharmacokinetic parameters of almonertinib were assessed using established methods.

2 MATERIALS AND METHODS

2.1 Chemicals and Reagents

Almonertinib (over 99% purity), Nirmatrelvir (purity 99.0%), Ritonavir (purity 99.0%) and the internal standard (IS) Zanubrutinib (purity 99.0%) were purchased from Toronto Research Chemicals Inc. (Toronto, Ontario, Canada). Analytical-grade methanol, acetonitrile, water and formic acid for mass spectrometry were obtained from Honeywell Burdick & Jackson (Muskegon, Michigan, United States). Other reagents used were purchased from J&K Scientific Ltd. (Shanghai, China).

2.2 UHPLC–MS/MS Detection Method

Sample chromatographic separation was carried out on a Shimadzu LC-20AT ultra-performance liquid chromatography system (Shimadzu Corp., Tokyo, Japan), which was equipped with a vacuum degas unit, an infusion pump, an autosampler and a column oven. A Shim-pack velox C18 (2.1× 50 mm, 2.7 μM) column at 40°C was used to perform the separation process. After a long period of exploration, 0.1% formic acid-water (A) and methanol (B) compose the mobile phase. The whole analysis process adopts gradient elution mode, and the elution procedure was used as follows: the first 0–0.5 min maintained at 10% B, the next 0.5–0.51 min linear increase to 80% B, 0.51–1.5 min maintained at 80% B, 1.5–2.0 min linear decrease to 10%, and the last 2.0–3 min maintained at 10%. The total running time of each injection was 3 min. During the analysis process, the flow rate was maintained at 0.4 ml/min, and the sample injection volume was set to 2 μl. Good separating efficacy of almonertinib and zanubrutinib (IS) was observed under the above test conditions, and their retention times were 2.08 and 2.35 min, respectively.

Sample detection was executed using Shimadzu 8040 Triple quadrupole mass spectrometry (Shimadzu Corp., Tokyo, Japan). The instrument was equipped with electrospray ionization (ESI) and dedicated data acquisition workstations. The various parameters of the instrument were set as follows: the detector voltage was set to 4.5 kV, the heating block temperature was set to 400°C, and the flow of atomizing gas and drying gas was 3 L/min and 5 L/min, respectively. The precursor and product ions of the analyte and internal standard were detected in multiple reaction monitoring (MRM) mode. To ensure the specificity of the detection, we used the fragment with the highest signal strength as the quantitation, and the second strength product ions were used for qualification. In addition to specific parent and product ions, the retention time of the analyte and IS was also used to improve the specificity of detection. Detailed MS parameters information for almonertinib and zanubrutinib are listed in **Table 1**.

2.3 Calibration Solution and Quality Control Samples Preparation

Stock solutions (1 mg/ml) of almonertinib and IS (zanubrutinib) were prepared by dissolving the respective standards in methanol. The stock solution was diluted with methanol by multiple grades, and various concentrations of working solutions were obtained. Sample preparation for each standard curve point and quality control (QC) were performed by adding 10 μl of the corresponding almonertinib working solution to 90 μl of blank rat plasma. The concentrations of all points of the standard curve were finally determined to be 0.1, 0.5, 1, 5, 10, 50, 100, 500, and 1000 ng/ml. The working solution of the IS (internal standard) was prepared by diluting the stock solution with methanol to a final concentration of 400 ng/ml. Quality control (QC) samples of three concentrations (0.3, 100, and 800 ng/ml) were prepared the same way. All samples and solutions were placed in a medical freezer for cold storage at −20°C and transferred to room temperature before determination.

2.4 Sample Preparation

The rat plasma samples were transferred from a −80°C medical refrigerator to room temperature for thawing before preparation. Then, 100 μl plasma and 40 μl internal standard were added to a 1.5 ml centrifuge tube, and 200 μl acetonitrile was added for protein precipitation. The centrifuge tube was placed on the vortex for 2 min to achieve perfect mixing. The mixture was centrifuged at 12,000 g for 10 min, and then 100 μl supernatant was transferred to a new centrifuge tube containing 100 μl ultrapure water. After gently mixing the centrifuge tube for 30 s, the mixture was used for UHPLC–MS/MS analysis.

2.5 Method Validation

Before using the present method for detection, the linearity, stability, selectivity, recovery, accuracy, matrix effect and

TABLE 1 | MS parameters of almonertinib and zanubrutinib.

Analytes	Precursor ion (*m/z*)	Product ion 1 (*m/z*)	Collision energy 1 (V)	Product ion 2 (*m/z*)	Collision energy 2 (V)
Almonertinib	526.20	72.10	35	411.05	32
Zanubrutinib	472.15	290.00	40	455.15	36

precision of the method were verified according to FDA method validation guidance (U.S. Department of Health and Human Services Food and Drug Administration et al., 2018).

2.5.1 Selectivity and Specificity

Selectivity is the ability of the analytical method to distinguish and accurately quantify the target compound in a mixture. The selectivity of the method was determined by comparing the test results of blank plasma from six different rats, blank plasma containing almonertinib and IS, and rat plasma samples after oral administration.

2.5.2 Linearity, Low Limit of Detection and Lower Limit of Quantification

Standard curves were established by testing standard samples at nine various concentrations (0.1–1000 ng/ml) on three different days. Data from the regression line of the peak area ratios against concentrations can provide mathematical estimates of the degree of linearity. The low limit of detection (LLOD) is the lowest concentration of an analyte that an analytical method can reliably measure above that of a blank at the 99% confidence level. LLOD was evaluated based on the signal-to-noise ratio of at least 3:1. The lower limit of quantification (LLOQ) is the lowest amount of almonertinib that can be quantitatively determined with acceptable precision and accuracy. The LLOQ was evaluated based on the signal to noise ratio of at least 10:1.

2.5.3 Extraction Recovery and Matrix Effect

Extraction recovery and matrix effects were evaluated using blank plasma from six different rats and three different concentrations (0.3, 100 and 800 ng/ml) of almonertinib QC standards. The comparison of the peak areas of QC samples pre-spiked in blank plasma with those of post-extracted blank plasma spiked samples was defined to evaluate the extraction recovery of almonertinib from rat plasma at the same concentrations. Matrix effects were evaluated by comparing the slope of the standard addition plot with the slope of standard calibration plot.

2.5.4 Accuracy and Precision

Rat plasma QC samples at three different concentration levels (0.3, 100 and 800 ng/ml) were measured by the present method on a single day or three different days. The relative error (RE%) and relative standard deviation (RSD%) of the test results should be calculated to determine whether they are within the specified range (15%) and used to evaluate the precision of the present method. The apparent recoveries should be calculated by dividing the measured almonertinib concentrations to the nominal spiked values in the blank matrix to assess accuracy, and the values of apparent recoveries should be between 85% and 115%.

2.5.5 Stability

Rat plasma QC samples at three different concentration levels (0.3, 100,and 800 ng/ml) under various storage conditions were determined in six replicates to study the stability of the method. These studies reflect the stability of QC samples during storage and analysis, including stability in the analysis experiment (4 h at room temperature), short-term storage (4°C for 24 h), long-term storage (−80°C for a month) and freezing-thawing cycles (three times). The RSD% and RE% of the testing results were calculated, and values below 15% and ±15% were thought to be stable.

2.6 DDI Study

Twelve male Sprague–Dawley (SD) rats (200 ± 20 g) were supplied by the Animal Experiment Center of Wenzhou Medical University. All animal-related experimental procedures complied with the Guide for Care and Use of Laboratory Animals and were approved by the Animal Research Ethics Committee of Wenzhou Medical University (Ethics approval number: wydw 2021-0019). Before the start of the experiment, all SD rats were raised on a SPF level lab, and received sufficient food and water. Almonertinib, nirmatrelvir and ritonavir were dissolved in 0.5% carboxymethyl cellulose sodium (CMC-Na) solution. The rats were fasted for 12 hours before the pharmacokinetics experiment but not banned from drinking water. All SD rats were split at random into two groups of 6. Group B (experimental group) were given 55 mg/kg nirmatrelvir and 20 mg/kg ritonavir by gavage administration, and Group A (control group) were given the same dose 0.5% CMC-Na. After half an hour, we infused 10 mg/kg almonertinib into the stomach of each rat and then obtained 0.3mlblood from the caudal vein of each rat at different time points (0.25 h, 1 h, 2 h, 3 h, 4 h, 5 h, 6 h, 7 h, 8 h, 10 h, 12 h and 24 h). Blood samples were collected in heparin tubes, and centrifuged at 13,000 g for 10 min at 4°C. Then, plasma was transferred to sterile tubes and stored in a −80°C refrigerator until the testing process.

The pharmacokinetic parameters of almonertinib were calculated by DAS 3.0 software using the noncompartment model. The critical pharmacokinetic parameters of the two groups were conducted in One-way ANOVA and Dunnett's test by using software SPSS version 17.0. A p value less than 0.05 indicates a significant difference between the two groups.

3 RESULTS AND DISCUSSION

3.1 Method Development and Optimization

3.1.1 Chromatographic Condition Development Optimization

The mobile phase composition, elution mode, types of separation columns and temperature of the column were optimized to achieve high-efficiency separation of almonertinib and IS, which facilitates the present method carrying higher sensitivity, specificity, shorter running time and more perfect peak shapes. Performance tests were carried out for different types of columns, such as different column lengths, different particle sizes and different packing materials. A Shim-pack velox C18 (2.1× 50 mm, 2.7 μM) column showed a better chromatographic peak form, retained value and separation. A comprehensive assessment of different mobile phase compositions, such as acetonitrile, methanol, water containing or without 0.1% formic acid or other inorganic salts, was performed. The mobile phase composed of methanol and water containing 0.1% formic acid implemented high

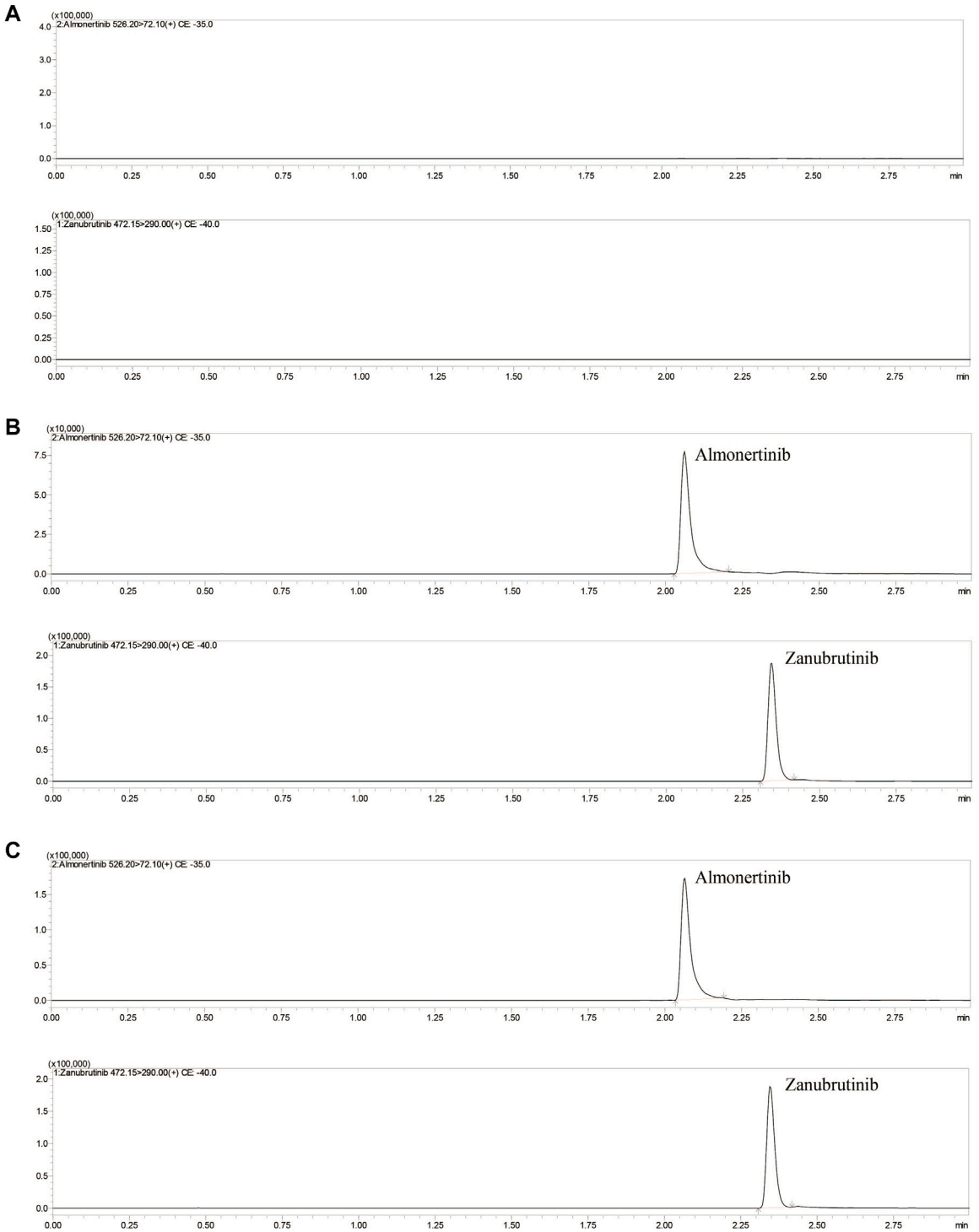

FIGURE 2 | Representative UHPLC–MS/MS chromatograms of almonertinib and zanubrutinib (IS). **(A)** blank plasma; **(B)** a blank plasma sample spiked with almonertinib and IS; **(C)** a rat plasma sample obtained 1 h after oral administration of almonertinib.

separation and a better peak shape. Isocratic or gradient elution, flow rate 0.3–0.5 ml/min and column temperature 20–40°C were tested. Through comparative analyses, suitable types of programs and parameters for the method are selected. Finally, methanol and 0.1% formic acid-water were selected as the mobile phase, and gradient elution was

performed under a flow rate of 0.4 ml/min and column temperature of 40°C. The mobile phase ratio was methanol and 0.1% formic acid-water (10:90) at the beginning of the gradient elution program, and then the methanol volume percentage rises to 80% at 0.5 min. Keep the methanol volume percentage at 80% until 1.5 min, and then the percentage of methanol dropped to 10% within half a minute, and finally maintain this ratio until the program finished at 3 min. The total run time of method was 3 min, and retention times of almonertinib and IS were 2.08 and 2.35 min, respectively. **Figure 2** shows characteristic chromatograms of blank control, blank rat plasma containing almonertinib and IS standard, and rat plasma after intragastric administration.

3.1.2 Mass Spectrometer Condition Optimization

The running parameters of the mass spectrometer, such as CE (collision energy), detection modes, atomizing gas and drying gas flow rate, and CID (collision-induced dissociation) gas pressure, were optimized to obtain optimal performance for the detection of almonertinib and IS. The optimized parameters should look like this: atomizing gas and drying gas flow rate 3 and 15 L/min, CID gas pressure 17 kPa, DL temperature 250°C. In positive ion mode, CE values are shown in **Table 1**.

3.1.3 Optimization of Sample Preparation and Internal Standard

The most common methods used for the extraction of compounds in biological samples were the protein precipitation method and solvent extraction. By analyzing and comparing the above two technologies, we found the most suitable method to extract almonertinib and IS. The results reveal that among various kinds of compound extraction methods, acetonitrile-based protein precipitation showed a higher extraction recovery (95.5%–98.0%) and was a simpler and more convenient method. Compared with other precipitants, such as methanol, perchloric acid, ethanol and dimethyl sulfoxide, acetonitrile exhibited better protein precipitation results and more stable chemical properties. For the reasons presented above, we decided to use the acetonitrile precipitation method for sample pretreatment.

To explore the more appropriate IS, classic internal standards (dextromethorphan and nifedipine) and analog internal standards (zanubrutinib and gefitinib) were tested. The results showed that zanubrutinib not only had remarkable stability and sensitivity but also showed similar chemistry and retention time to almonertinib. More importantly, they are all appropriate for the positive ion monitoring mode.

3.2 Method Validation

3.2.1 Selectivity and Specificity

Figure 2 shows the chromatograms of blank plasma, blank plasma containing standard preparations of almonertinib and IS, and rat plasma samples after oral administration. The relative retention times were approximately 2.08 min for almonertinib and 2.35 min for IS. The detection method was not interfered with by endogenous substances and commonly used chemicals.

3.2.2 Linearity and Lower Limit of Quantification

Linear regression analysis was performed on the relative peak area (almonertinib/IS) and corresponding serum concentration by the least squares method. L The regression parameters were calculated for the calibration curves. The STEYX of almonertinib was 0.0072. The S_a and S_b values of almonertinib were 1.4×10^{-6} and 3.2×10^{-6}, respectively. STEYX is the standard error of estimation, S_a is the standard deviation of the intercept, S_b is the standard deviation of the slope. The LLOQ of the almonertinibwas 0.1 ng/ml, and the corresponding RSD and RE were <9.92% and within 0.74%, respectively. The LLOD of our detection method was 0.03 ng/ml. The linearity of the calibration curves was validated by acceptable values of STEYX, S_b, S_a, LLOD and LLOQ.

3.2.3 Extraction Recovery and Matrix Effect

The extraction recovery and matrix effects (MEs) of almonertinib QC samples at high, medium and low concentrations (0.3, 100 and 800 ng/ml) are shown in **Table 2**. The average extraction recoveries of almonertinib at concentrations of 0.3, 100 and 800 ng/ml were 95.7%, 94.1%, and 97.2%, respectively, and the MEs were 98.8%, 99.3%, and 99.0%, respectively. The results of the QC sample test have shown that the detection method has high recovery and that the matrix effects can be ignored in daily determination.

3.2.4 Accuracy and Precision

Accuracy and precision evaluation of the method was carried out by calculating the apparent recoveries, RE% and RSD% for three concentration levels of QC samples and LLOQ. The end experimental results are displayed in **Table 3**. The apparent recoveries were between 96.0% and 98.7% at different concentrations. The intra- and interday RSD% values were lower than 10.7% and 6.4%, respectively, and the corresponding RE% values were in the ranges of −5.9% −3.5% and −0.8% −3.0%, respectively. Excellent accuracy and reproducibility of the method have been revealed by experimental data.

3.2.5 Stability

Long- and short-term stability tests of the analytes were carried out by calculating the RE% and RSD% of QC samples under four different storage conditions. The stability test results for almonertinib are displayed in **Table 4**. Under different storage conditions, the RSD% is less than 13.1%, and the RE% is less than ± 11.3%. Based on the experimental results, almonertinib in plasma was stable under various circumstances (room temperature, 4°C refrigeration, freeze thawing and long-term cryopreservation).

3.3 DDI Study

The established UHPLC-MS/MS method was successfully used in the study of drug-drug interaction between almonertinib and Paxlovid in rats. The average plasma concentration curves of two groups at different time points after gavage administration of almonertinib (10 mg/kg) are presented in **Figure 3**. The main pharmacokinetic parameters of two groups are presented in **Table 5**.

There are reports that co-administration of itraconazole 200 mg twice daily and single dose of 110 mg almonertinib significantly inhibited the metabolism of almetinib in healthy

TABLE 2 | Extraction recovery and matrix effect of almonertinib in rat plasma (n = 6).

Analyte	Concentration (ng/ml)	Extraction recovery (%)		Matrix effect (%)	
		Mean ± SD	RSD (%)	Mean ± SD	RSD (%)
Almonertinib	0.3	95.7 ± 5.4	5.6	98.8 ± 8.3	8.4
	100	94.1 ± 5.1	5.4	99.3 ± 6.4	6.5
	800	97.2 ± 4.3	4.5	99.0 ± 10.4	10.5

TABLE 3 | Precision and accuracy for almonertinib of QC samples in rat plasma (n = 6).

Analyte	Concentration (ng/ml)	Intra-day			Inter-day			Apparent recovery (%)
		Mean ± SD	RSD (%)	RE (%)	Mean ± SD	RSD (%)	RE (%)	
Almonertinib	0.1	0.10 ± 0.01	9.9	−0.5	0.10 ± 0.01	6.4	−0.7	97.3
	0.3	0.30 ± 0.03	9.7	1.5	0.30 ± 0.01	3.40	0.6	96.3
	100	94.14 ± 8.49	9.0	−5.9	99.23 ± 5.65	5.8	−0.8	96.0
	800	828.35 ± 88.76	10.7	3.5	824.18 ± 6.51	0.8	3.0	98.7

TABLE 4 | Summary of the stability of almonertinib in rat plasma under different storage conditions (n = 6).

Analyte	Concentration (ng/ml)	Room temperature		4°C		Three freeze-thaw		−80°C	
		RE (%)	RSD (%)	RE (%)	RSD (%)	RE (%)	RSD (%)	RE (%)	RSD (%)
Almonertinib	0.3	−7.2	12.9	11.3	9.4	4.6	7.1	−2.4	9.1
	100	4.1	13.1	−5.9	6.6	−5.5	5.9	−0.5	8.9
	800	−4.0	8.8	2.1	7.3	3.0	6.9	1.9	10.4

TABLE 5 | The main pharmacokinetic parameters of almonertinib in different treatment groups of rats. Group A: the control group (0.5% CMC-Na) and Group B: 55 mg/kg nirmatrelvir and 20 mg/kg ritonavir. (n = 6, Mean ± SD).

Parameters	Unit	Group A	Group B
$AUC_{(0-t)}$	μg/L*h	385.33 ± 20.26	777.14 ± 47.80*
$AUC_{(0-\infty)}$	μg/L*h	389.85 ± 20.78	788.25 ± 50.22*
$MRT_{(0-t)}$	h	6.92 ± 0.09	7.72 ± 0.22
$MRT_{(0-\infty)}$	h	7.30 ± 0.16	8.05 ± 0.20
$t_{1/2}$	h	3.15 ± 0.82	3.40 ± 0.26
T_{max}	h	5.00 ± 0.00	5.17 ± 0.41
CLz/F	L/h/kg	0.86 ± 0.65	2.23 ± 0.55*
C_{max}	μg/L	63.23 ± 9.39	111.39 ± 16.12*

volunteers (Liu et al., 2022a). Itraconazole has been shown to be a potent CYP3A4 inhibitor (Brüggemann et al., 2009). The Paxlovid contains ritonavir, one kind of powerful CYP3A4 inhibitor (Sevrioukova and Poulos, 2014). Therefore, Paxlovid was chosen in combination with almonertinib to determine whether it would affect pharmacokinetics of almonertinib in rat. The results show that compared with the control group, the pharmacokinetic parameters of almonertinib, such as $AUC_{(0-t)}$, $AUC_{(0-\infty)}$, CLz/F, and C_{max}, were significantly increased ($p < 0.05$) when concomitantly used with Paxlovid. It shows that Paxlovid has obvious inhibiting effect on the metabolism of almonertinib, resulting in a significant increase in total systemic exposure to almonertinib. Therefore, extreme caution should be exercised when using almonertinib in combination with Paxlovid, the patients are more prone to severe adverse reactions due to elevated plasma levels of almonertinib. If the combination of the two drugs is inevitable, our results suggest that the dose of almonertinib should be reduced. Since the interaction study of almonertinib and Paxlovid was performed in a small

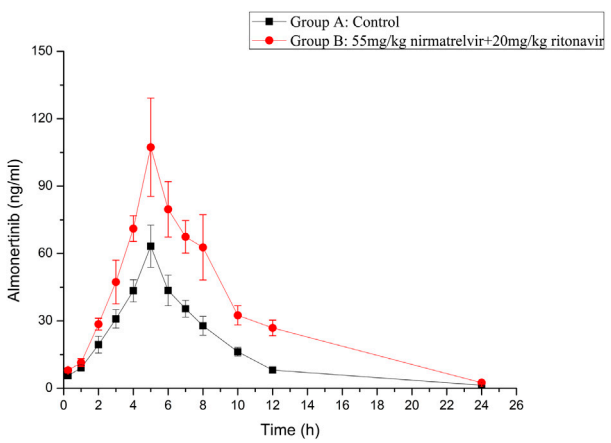

FIGURE 3 | Mean plasma concentration-time curve of almonertinib in different treatment groups of rats. Group A: the control group (0.5% CMC-Na) and Group B: 55 mg/kg nirmatrelvir and 20 mg/kg ritonavir (n = 6, Mean ± SD).

number of rats, all results need to be validated in subsequent clinical trials.

4 CONCLUSION

This study established a fast, accurate, stable and facile ultra-performance liquid chromatography-tandem mass spectrometry method for the determination of almonertinib in rat plasma. The new method has been successfully applied to the drug interaction study of almonertinib and Paxlovid in rats. Paxlovid has a marked inhibitory effect on the metabolism of almonertinib, increasing the exposure of almonertinib. Considering the complexity of cancer patients, further human trials should be performed to verify the accuracy of animal studies.

DATA AVAILABILITY STATEMENT

The original contributions presented in the study are included in the article/supplementary material, further inquiries can be directed to the corresponding authors.

ETHICS STATEMENT

The animal study was reviewed and approved by Wenzhou Medical University.

AUTHOR CONTRIBUTIONS

Conceptualization, P-fT, N-yG, and S-sB; methodology, P-fT, N-yG, and Z-xX; formal analysis, P-fT and W-fX; investigation, N-yG and X-mW; writing—original draft preparation, P-fT, N-yG, L-pZ, and C-fS; writing—review and editing, Z-xX and W-fX; visualization, L-pZ; project administration, C-fS; funding acquisition, L-pZ and C-fS All authors have read and agreed to the published version of the manuscript.

FUNDING

This work was supported by the National Natural Science Foundation of China (NSFC 81973397).

REFERENCES

Brüggemann, R. J., Alffenaar, J. W., Blijlevens, N. M., Billaud, E. M., Kosterink, J. G., Verweij, P. E., et al. (2009). Clinical Relevance of the Pharmacokinetic Interactions of Azole Antifungal Drugs with Other Coadministered Agents. *Clin. Infect. Dis.* 48, 1441–1458. doi:10.1086/598327

Liu, L., Li, W., Yang, L., Guo, Z. T., Xue, H., Xie, N. J., et al. (2022a). Itraconazole and Rifampicin, as CYP3A Modulators but Not P-Gp Modulators, Affect the Pharmacokinetics of Almonertinib and Active Metabolite HAS-719 in Healthy Volunteers. *Acta Pharmacol. Sin.* 43, 1082–1090. doi:10.1038/s41401-021-00710-8

Liu, L., Yang, L., Li, W., and Chen, X. (2022b). Simultaneous Determination of Almonertinib and its Active Metabolite HAS-719 in Human Plasma by LC-MS/MS: Evaluation of Pharmacokinetic Interactions. *J. Chromatogr. B Anal. Technol. Biomed. Life Sci.* 1197, 123231. doi:10.1016/j.jchromb.2022.123231

Lu, S. (2021). "Randomized phase III trial of aumolertinib(HS-10296, Au) versus gefitinib (G) as first-line treatment of patients withlocally advanced or metastatic non-small cell lung cancer (NSCLC) and EGFR exon19 del or L858R mutations (EGFRm)," in *ASCO*. doi:10.1200/jco.2021.39.15_suppl.9013

Lu, S., Wang, Q., Zhang, G., Dong, X., Yang, C. T., Song, Y., et al. (2021). Efficacy of Aumolertinib (HS-10296) in Patients with Advanced EGFR T790M+ NSCLC: Updated Post-National Medical Products Administration Approval Results from the APOLLO Registrational Trial. *J. Thorac. Oncol.* 17(3):411-422.doi:10.1016/j.jtho.2021.10.024

Nagasaka, M., Zhu, V. W., Lim, S. M., Greco, M., Wu, F., and Ou, S. I. (2021). Beyond Osimertinib: The Development of Third-Generation EGFR Tyrosine Kinase Inhibitors for Advanced EGFR+ NSCLC. *J. Thorac. Oncol.* 16, 740–763. doi:10.1016/j.jtho.2020.11.028

Owen, D. R., Allerton, C. M. N., Anderson, A. S., Aschenbrenner, L., Avery, M., Berritt, S., et al. (2021). An Oral SARS-CoV-2 Mpro Inhibitor Clinical Candidate for the Treatment of COVID-19. *Science* 374, 1586–1593. doi:10.1126/science.abl4784

Passaro, A., Bestvina, C., Velez Velez, M., Garassino, M. C., Garon, E., and Peters, S. (2021). Severity of COVID-19 in Patients with Lung Cancer: Evidence and Challenges. *J. Immunother. Cancer* 9. doi:10.1136/jitc-2020-002266

Pollard, C. A., Morran, M. P., and Nestor-Kalinoski, A. L. (2020). The COVID-19 Pandemic: a Global Health Crisis. *Physiol. Genomics* 52, 549–557. doi:10.1152/physiolgenomics.00089.2020

Saravolatz, L. D., Depcinski, S., and Sharma, M. (2022). Molnupiravir and Nirmatrelvir-Ritonavir: Oral COVID Antiviral Drugs. *Clin. Infect. Dis.*, ciac180. doi:10.1093/cid/ciac180

Sevrioukova, I. F., and Poulos, T. L. (2014). Ritonavir Analogues as a Probe for Deciphering the Cytochrome P450 3A4 Inhibitory Mechanism. *Curr. Top. Med. Chem.* 14, 1348–1355. doi:10.2174/1568026614666140506120647

Shirley, M., and Keam, S. J. (2022). Aumolertinib: A Review in Non-small Cell Lung Cancer. *Drugs* 82, 577–584. doi:10.1007/s40265-022-01695-2

U.S. Department of Health and Human Services Food and Drug Administration (2018). *Center for Drug Evaluation and Research (Cder), and Center for Veterinary Medicine (Cvm)*. Washington, DC: Bioanalytical Method Validation Guidance for Industry.

Yang, J. C., Camidge, D. R., Yang, C. T., Zhou, J., Guo, R., Chiu, C. H., et al. (2020). Safety, Efficacy, and Pharmacokinetics of Almonertinib (HS-10296) in Pretreated Patients with EGFR-Mutated Advanced NSCLC: A Multicenter, Open-Label, Phase 1 Trial. *J. Thorac. Oncol.* 15, 1907–1918. doi:10.1016/j.jtho.2020.09.001

Conflict of Interest: The authors declare that the research was conducted in the absence of any commercial or financial relationships that could be construed as a potential conflict of interest.

Publisher's Note: All claims expressed in this article are solely those of the authors and do not necessarily represent those of their affiliated organizations, or those of the publisher, the editors and the reviewers. Any product that may be evaluated in this article, or claim that may be made by its manufacturer, is not guaranteed or endorsed by the publisher.

frontiers | Frontiers in Pharmacology

TYPE Original Research
PUBLISHED 22 August 2022
DOI 10.3389/fphar.2022.983233

OPEN ACCESS

EDITED BY
Simona Pichini,
National Institute of Health (ISS), Italy

REVIEWED BY
Stéphen Manon,
CNRS, UMR5095, France
Antonio Leo,
Scuola di Medicina e Chirurgia,
Università Magna Grecia di Catanzaro,
Italy

*CORRESPONDENCE
Chaitali Ghosh,
GHOSHC@ccf.org

SPECIALTY SECTION
This article was submitted to Drug Metabolism and Transport, a section of the journal Frontiers in Pharmacology

RECEIVED 30 June 2022
ACCEPTED 29 July 2022
PUBLISHED 22 August 2022

CITATION
Ghosh C, Westcott R, Perucca E, Hossain M, Bingaman W and Najm I (2022), Cytochrome P450-mediated antiseizure medication interactions influence apoptosis, modulate the brain BAX/Bcl-X_L ratio and aggravate mitochondrial stressors in human pharmacoresistant epilepsy. *Front. Pharmacol.* :983233. doi: 10.3389/fphar.2022.983233

Cytochrome P450-mediated antiseizure medication interactions influence apoptosis, modulate the brain BAX/Bcl-X_L ratio and aggravate mitochondrial stressors in human pharmacoresistant epilepsy

Chaitali Ghosh[1,2]*, Rosemary Westcott[1], Emilio Perucca[3,4], Mohammed Hossain[1], William Bingaman[5] and Imad Najm[5]

[1]Department of Biomedical Engineering, Cerebrovascular Research, Lerner Research Institute, Cleveland Clinic, Cleveland, OH, United States, [2]Department of Biomedical Engineering and Molecular Medicine, Cleveland Clinic Lerner College of Medicine of Case Western Reserve University, Cleveland, OH, United States, [3]Department of Medicine (Austin Health), The University of Melbourne, Melbourne, VIC, Australia, [4]Australia and Department of Neuroscience, Monash University, Melbourne, VIC, Australia, [5]Charles Shor Epilepsy Center, Neurological Institute, Cleveland Clinic, Cleveland, OH, United States

Polytherapy with antiseizure medications (ASMs) is often used to control seizures in patients suffering from epilepsy, where about 30% of patients are pharmacoresistant. While drug combinations are intended to be beneficial, the consequence of CYP-dependent drug interactions on apoptotic protein levels and mitochondrial function in the epileptic brain remains unclear. We examined the interactions of ASMs given prior to surgery in surgically resected brain tissues and of three ASMs (lacosamide, LCM; oxcarbazepine, OXC; levetiracetam LEV) in isolated brain cells from patients with drug-resistant epilepsy (n = 23). We divided the patients into groups–those who took combinations of NON-CYP + CYP substrate ASMs, NON-CYP + CYP inducer ASMs, CYP substrate + CYP substrate or CYP substrate + CYP inducer ASMs–to study the 1) pro- and anti-apoptotic protein levels and other apoptotic signaling proteins and levels of reactive oxygen species (reduced glutathione and lipid peroxidation) in brain tissues; 2) cytotoxicity at blood-brain barrier epileptic endothelial cells (EPI-ECs) and subsequent changes in mitochondrial membrane potential in normal neuronal cells, following treatment with LCM + OXC (CYP substrate + CYP inducer) or LCM + LEV (CYP substrate + NON-CYP-substrate) after blood-brain barrier penetration, and 3) apoptotic and mitochondrial protein targets in the cells, pre-and post-CYP3A4 inhibition by ketoconazole and drug treatments. We found an increased BAX (pro-apoptotic)/Bcl-X_L (anti-apoptotic) protein ratio in epileptic brain tissue after treatment with CYP substrate + CYP substrate or inducer compared to NON-CYP + CYP substrate or inducer, and subsequently decreased glutathione and elevated lipid peroxidation levels. Further, increased cytotoxicity and Mito-ID

levels, indicative of compromised mitochondrial membrane potential, were observed after treatment of LCM + OXC in combination compared to LCM + LEV or these ASMs alone in EPI-ECs, which was attenuated by pre-treatment of CYP inhibitor, ketoconazole. A combination of two CYP-mediated ASMs on EPI-ECs resulted in elevated caspase-3 and cytochrome c with decreased SIRT3 levels and activity, which was rescued by CYP inhibition. Together, the study highlights for the first time that pro- and anti-apoptotic proteins levels are dependent on ASM combinations in epilepsy, modulated via a CYP-mediated mechanism that controls free radicals, cytotoxicity and mitochondrial activity. These findings lead to a better understanding of future drug selection choices offsetting pharmacodynamic CYP-mediated interactions.

KEYWORDS

cytochrome P450, blood-brain barrier, epilepsy, drug interaction, apoptotic signaling, pharmacodynamics, SIRT3

1 Introduction

Multiple antiseizure medications (ASMs) are frequently used to control difficult-to-treat seizures in patients with epilepsy (Kwan et al., 2011). When polytherapy is used, clinically important drug-drug interactions can occur, many of which involve inhibition or induction of cytochrome P450 (CYP) isoenzymes (Patsalos et al., 2002; Perucca, 2005a; Perucca, 2005b; Perucca and Meador, 2005; Zaccara and Perucca, 2014). It is generally assumed that clinically relevant metabolic drug interactions occur in the liver and other major organs responsible for drug clearance. However, there increasing evidence that CYP enzymes in the brain also have significant biological consequences (Miksys and Tyndale, 2002; Ghosh et al., 2016). Unlike in the liver, brain CYP is concentrated near ASM targets, and can influence drug metabolism locally (Miksys and Tyndale, 2002; Gervasini et al., 2004; Ferguson and Tyndale, 2011; Anna Haduch et al., 2013; Ghosh et al., 2016; Williams et al., 2019). Many ASMs are either CYP substrates (i.e., lacosamide) or CYP inducers (i.e., oxcarbazepine), while others are not mediated by CYP at all (i.e., levetiracetam) (Contin et al., 2004; Andreasen et al., 2007; Cawello et al., 2012; McGrane et al., 2018). This poses a risk for drug-drug interactions between co-prescribed ASMs based on their involvement with CYP enzymes.

One promising third-generation ASM, for example, is lacosamide (LCM), which is metabolized by CYP enzymes. When administered alone, LCM has been shown to be neuroprotective, reduce oxidative stress and neuroinflammation, and decrease inflammation-induced cortical apoptosis in aged rats (Savran et al., 2019). Although, it is often co-prescribed with other ASMs for the treatment of epilepsy. In 2008, LCM was approved as an adjunctive therapy in adults or adolescents with epilepsy for the treatment of partial-onset seizures with or without secondary generalization in the United States and European Union (Bauer et al., 2017) and LCM monotherapy was approved as a treatment for focal epilepsy. LCM has been found to be a relatively well-tolerated medication in these patients, and the pharmacokinetic interactions of LCM with other ASMs has been described in the past years (Shandra et al., 2013; Markoula et al., 2014). However, the pharmacodynamic effects of LCM polytherapy with other ASMs, including CYP inducers and those not mediated by CYP, have not yet been described.

In general, CYP inhibition is commonly known to elevate the blood level of concomitant drugs, which can result in serious adverse reactions to the medications (Markoula et al., 2014; Sun et al., 2020). In contrast, CYP induction with combination therapy could cause decreased levels of drug in the blood, often reducing drug efficacy (Markoula et al., 2014; Sun et al., 2020); although, not much is known about the pharmacodynamic consequences elicited by interactions between CYP inducers and substrates. One case report describing the effects of oxcarbazepine (OXC), although reported to cause mild hepatic CYP induction, co-administered with other CYP substrate to treat mood disorders exhibited some worsening of psychiatric symptoms after the inducing agent was added (Baird, 2002). Another study in rats showed that combination therapy of diazepam (CYP substrate) with either phenobarbital (CYP inducer) or phenytoin (CYP inducer) caused increased neuronal apoptosis compared to monotherapy with any of these medications (Bittigau et al., 2002). ASMs can also interact with various mitochondrial pathways, structures, or functions (Berger et al., 2010; Finsterer and Scorza, 2017), affect enzymatic cascades, such as the respiratory chain, oxidative phosphorylation, or non-respiratory chain pathways, including the tricarboxic cycle or the β-oxidation pathways, and influence apoptosis associated with changes in cellular dynamics (Finsterer and Scorza, 2017). These evidences provide a glimpse into the possibility of harmful pharmacodynamic effects of ASM polytherapy, like increased apoptosis, relating to CYP involvement, which needs to be further elucidated.

Our previous *in vitro* work with endothelial cells from human epileptic brain tissue showed changes in CYP activity could result in a wide-array of molecular and cellular changes, including changes in the permeability of the blood-brain barrier (BBB) (Ghosh et al., 2015). In studies conducted in surgically resected brain specimens from patients with medically intractable epilepsy, we also found that brain CYP3A4 activity varied depending on type of ASM combinations taken by the patients, and that these changes correlated with seizure frequency (Williams et al., 2019). In the current study, we investigated resected brain tissues and isolated brain cells from medically refractory epilepsy patients treated with different ASM combinations before surgery, to identify comparative treatment effects on 1) pro-apoptotic (BAX) and anti-apoptotic (Bcl-X_L) protein levels and other apoptotic signaling proteins and mitochondrial function implicated in cellular stress (e.g., ERK, phospho-ERK, BAD, caspase-3, cytochrome c and SIRT3) and reactive oxygen species (e.g., reduced glutathione and lipid peroxidation) in epileptic brain tissues; 2) cytotoxicity in endothelial cells from human epileptic brain tissue (EPI-ECs) and in human epileptic BBB *in vitro*, and changes in mitochondrial membrane potential in the neuronal cultures post-treatment; 3) mechanisms of mitochondrial oxidative stress in EPI-ECs focusing on the activity of SIRT3, a nicotinamide adenine dinucleotide-dependent deacetylase and a key component of mitochondria. We further assessed apoptotic and mitochondrial protein targets in EPI-ECs and normal human neuronal cells, pre- and post-CYP3A4 inhibition by ketoconazole with ASM treatments to determine the involvement of CYP enzymes in the process.

2 Materials and methods

2.1 Human subjects

Brain tissue specimens from individuals (n = 23) with pharmacoresistant epilepsy were obtained following focal surgical resections, using a protocol approved by the Cleveland Clinic Institutional Review Board (IRB 07-322) in compliance with the principles outlined in the Declaration of Helsinki. The epileptic nature of the resected brain tissue was identified based on prior noninvasive (scalp video-EEG monitoring, magnetic resonance imaging, positron emission tomography) and invasive (stereo-electroencephalography) investigations. Demographic details and information on seizure frequency, duration of epilepsy, age, gender, localization of the resected epileptic tissue, underlying ASM treatment, and pathology of each specimen is provided in Supplementary Table S1. Results of tests conducted on resected human epileptic brain tissues were compared based on type of ASMs taken patients at the time of surgery and at least 3 months prior to surgery. These are either ASMs as combinations of NON-CYP + CYP substrate, NON-CYP + CYP inducer, CYP substrate + CYP substrate or CYP substrate + CYP inducer. The experimental design is outlined in Supplementary Figure S1.

2.1 Protein isolation and Western blot analysis

Small portions of the snap-frozen resected epileptic brain tissue were homogenized in radioimmunoprecipitation assay buffer (Sigma-Aldrich, United States) with protease inhibitor (Sigma-Aldrich, United States). The tissue suspension was centrifuged at 14000G (Avanti-J25I, Beckman Coulter, United States), the supernatant was collected and the concentration of protein was measured by the Bradford method. BAX, Bcl-X_L, ERK1/2, Phospho-ERK (Thr980), SIRT3, BAD, cytochrome c and caspase-3 were separated by 10% sodium dodecyl sulfate polyacrylamide gel electrophoresis and later transferred to polyvinylidene fluoride (PVDF) membranes (EMD Millipore Corp., Billerica, MA, United States) in semi-dry transfer (trans-Blot™ SD, Bio-Rad, United States) and blocked for 4 h at room temperature. In brief, the membranes were incubated overnight with primary antibody (see target proteins listed in Supplementary Table S2A) and subsequently probed with the appropriate secondary antibody (Supplementary Table S2B) as previously described (Williams et al., 2019; Hossain et al., 2020). For the target proteins, the PVDF membranes were incubated in stripping buffer at room temperature for 30 min followed by blocking, or a fresh gel was simultaneously repeated with the samples. Western blots were run in duplicates. In each case, the protein expression was normalized by β-actin (as a loading control) and quantified by ImageJ software.

2.3 Reduced glutathione assay

Reduced glutathione (GSH) was measured using a Glutathione Assay kit from Abnova (catalog KA1649) according to the manufacturer's instructions. In this assay, 5, 5′-dithiobis (2-nitrobenzoic acid) reacts with reduced glutathione to form a yellow product. The optical density, measured at 412 nm, is directly proportional to the glutathione concentration in the sample. GSH in tissue extracts was quantified from calibration curves generated using a standard. All standards and samples were measured in duplicate. Data were normalized for protein content (Lindenmaier et al., 2005; Ghosh et al., 2015).

2.4 Lipid peroxidation malondialdehyde assay

Oxidative stress was assessed by quantifying lipid peroxidation with a malondialdehyde (MDA) Assay Kit, Abnova (catalog KA3736), according to the manufacturer's instructions. Lipid peroxidation forms MDA and 4-hydroxynonenal, with the end products of the reaction

providing a widely accepted measure of oxidative damage. MDA in tissue samples reacts with thiobarbituric acid to generate the MDA-thiobarbituric acid adduct which is analyzed colorimetrically (λ = 532 nm). MDA in tissue extracts was quantified from calibration curves generated using a standard (Lin et al., 2021), and data were normalized for protein content.

2.5 Cell culture

2.5.1 Human epileptic brain endothelial cells

Primary epileptic endothelial cells were obtained from brain specimens resected from patients with drug-resistant epilepsy (n = 10) mostly due to focal cortical dysplasia, according to a previously described procedure (Ghosh et al., 2018; Hossain et al., 2020). Briefly, surgical specimens were incubated with collagenase type II (2 mg/ml; Worthington Biochemical Corp., Lakewood, NJ, United States) at 37°C for 20 min to dissociate the endothelial cells. The collagenase was then washed off with medium (1.5 g/100 ml, MCDB 105 supplemented with endothelial cells growth supplement 15 mg/100 ml, heparin 800 U/100 ml, 10% fetal bovine serum, and 1% penicillin/streptomycin). Cells were stained positive for von Willebrand factor and negative for glial fibrillary acidic protein (data not shown). EPI-ECs were initially expanded in 75 cm^2 flasks pre-coated with fibronectin, 3 μg/cm^2 (Ghosh et al., 2018; Hossain et al., 2020).

2.5.2 Human astrocytes and neuronal cell culture

Normal human astrocytes (catalog 1800) were purchased from ScienCell Research Laboratories, Inc. (Carlsbad, California) and cultured in poly-D-lysine pre-coated flasks (3 μg/cm^2) with appropriate media (Ghosh et al., 2018; Hossain et al., 2020). Human dopaminergic neuronal cells (DAN) derived from fetal brain tissues were purchased from ClonExpress (catalog number: DAN 020; Gaithersburg, MD, United States) using the culture media recommended by the manufacturer (Ghosh et al., 2015; Ghosh et al., 2022). The neuronal cultures were characterized with anti-human microtubule associated protein 2 (MAP-2) immunohistochemistry (data not shown).

2.5.3 Blood-brain barrier *in vitro* system for direct evaluation of antiseizure medication access to cultured neurons

The *in vitro* BBB setup was established using flow-based *in vitro* modules (FiberCell Systems Inc., New Market, Maryland; catalog C2025) as previously described (Ghosh et al., 2018; Hossain et al., 2020). In the FiberCell polysulfide plus cartridge, each module contains 20 hollow-fiber capillaries embedded inside a clear plastic chamber, which is attached to a reservoir for media circulation and connected to a pulsatile pump. EPI-ECs (4×10^6/device) were seeded in the luminal side in different devices. Astrocytes (3×10^6/device) were co-cultured in the abluminal side of the *in vitro* device. BBB formation was evaluated by trans-endothelial electrical resistance measurement (Supplementary Figure S2). Different ASMs combinations were perfused through the capillaries and their effects following their passage across the BBB were directly tested on the neuronal culture present in the chamber. Specifically, passage across the BBB and subsequent effects was tested after perfusion with the non-CYP substrate levetiracetam (LEV) alone, and the CYP substrate lacosamide (LCM) alone and in combination with LEV or with a CYP inducer (oxcarbazepine, OXC). These drug treatments were chosen based on the drug regimen of this cohort of patients (see Figure 2D). The overall experimental design is outlined in Supplementary Figure S1.

The neuronal cultures exposed to ASMs through the BBB were subsequently evaluated to determine: 1) cytotoxicity by adenylate kinase measurement; 2) mitochondrial membrane potential by Mito-ID analysis; 3) levels of apoptosis and mitochondrial protein targets such as BAX, Bcl-X_L, ERK1/2, phospho-ERK (Thr980), SIRT3, cytochrome c in the neuronal cell lysates by 10% gel electrophoresis and analyzed by Western blot. Parallel evaluations were performed to test the effects of the ASMs on EPI-ECs derived from epileptic brain tissue to determine: 1) cytotoxicity by adenylate kinase measurement; 2) mitochondrial SIRT3 activity; and 3) the apoptotic and mitochondrial protein targets such as BAX, Bcl-X_L, ERK1/2, phospho-ERK (Thr980), SIRT3, cytochrome c, caspase-3 separated by 10% gel electrophoresis and analyzed by Western blot.

2.6 Adenylate kinase/toxilight cytotoxicity assay

Cytotoxicity was assessed in EPI-ECs and neuronal cells (DAN) by measuring the levels of adenylate kinase in the supernatant. This highly sensitive assay measures adenylate kinase (catalog number: LT07-217; Lonza) released from damaged mammalian cells and provides an accurate determination of the degree of cytolysis (Ghosh et al., 2015). Bioluminescent adenylate kinase is present in all cells, and loss of cell integrity through damaged membrane results in its leakage into the surrounding medium. Adenylate kinase measurements are plotted as relative luminescent units, so that approximately equal numbers of cells (6×10^5 cells/per chamber) exposed to different drug exposures can be compared with the control and the 0 h time point. Cytotoxicity measurements were made with and without pretreatment with the CYP3A4 inhibitor ketoconazole (KCZ, 10 μM) for 2 h, followed by exposure to ASMs alone or in combination (LCM, LEV, LCM + LEV, LCM + OXC).

2.7 Mitochondrial membrane potential

Mitochondria play a central role in cellular metabolism, bioenergetics and apoptosis (Zorova et al., 2018). The Mito ID® Membrane Potential Cytotoxicity Kit measures

fluctuations in mitochondrial membrane potential utilizing a cationic dual-emission dye that exists as green fluorescent monomers in the cytosol, and accumulates as orange fluorescent J-aggregates in the mitochondria. The formation of JC-1 monomers and their fluorescence are linearly correlated with the decrease in membrane potential. Briefly, neuronal cells were incubated with JC-1 at 37°C for 15 min. The Mito ID kit (catalog ENZ-51019-KP002, Enzo Life Sciences Inc., NY, United States) was used for the assay. Mitochondria having a low membrane potential accumulate low concentrations of dye and exhibit a green fluorescence, while more highly polarized mitochondria produce an orange signal. The effect of ASMs alone (LCM; LEV) and combined (LCM + OXC; LCM + LEV) were tested to evaluate mitochondrial membrane potential changes ($\Delta\Psi m$) in the neuronal cells. Carbonyl cyanide m-chlorophenylhydrazone (CCCP) was used as positive control to determine uncoupled mitochondria. The Bio-Tek Synergy fluorescence microplate reader was used to measure the signal. This photophysical property is due to the reversible formation of J-aggregates upon membrane polarization that causes shifts in emitted light from ~530 nm (the emission of the monomeric dye) to 590 nm (the emission of the J-aggregate form) when excited at 490 nm. The percentage mitochondrial membrane potential signal was compared with a 4 μM CCCP concentration as recommended by the manufacturer.

2.8 SIRT3 activity assay

The deacetylase activity of SIRT3 in EPI-ECs (n = 3) exposed to ASMs alone (LCM or LEV) or combined (LCM + OXC; LCM + LEV) was measured by a fluorometric method using the SIRT3 Activity Assay Kit (catalog ab156067, Abcam, Waltham, MA United States). The manufacturer's protocol and recommendations were followed. We tested in the same EPI-ECs (n = 3) the effect of CYP inhibition SIRT3 activity after exposure to the ASM alone and combined. Briefly, the enzymatic reaction was initiated by incubating 15 μg of protein from test samples (prepared without using protease inhibitor) with 20 μM of a SIRT3 specific fluoro-substrate peptide, 200 μM of NAD and 5 μL of developer solution. Three control experiments were performed, one without cell lysate, one without the recombinant enzyme and one without NAD. A standard curve for SIRT3 expression was fitted using 0, 400, 800 and 1,000 ng of recombinant SIRT3. Deacetylase activity was evaluated by measuring the fluorescence at 2 min time intervals for 60 min using a CYTATION/5 Microplate reader (BioTek Instruments, United States) (Michalak et al., 2017; Yi et al., 2019). Fluorescent intensity was plotted against each time-point to follow the enzyme activity, and relative SIRT3 activity was determined by the mean end-point measurements and compared between the groups.

2.9 Protein isolation from cell lysate and Western blot after antiseizure medication treatment post-CYP inhibition

Both cell types (EPI-ECs and DAN) in each treatment group were cultured separately in 100 mm Petri dishes in standard/recommended medium. At 80% confluency, cells were exposed to ASMs alone (LCM; LEV) and combined (LCM + OXC; LCM + LEV), with and without 2 h-KCZ pre-treatment. After 24 h of ASM exposure, cells were lysed using lysis buffer with protease inhibitor cocktail for Western blot analysis. Cell lysates were separated through a 10% SDS gel and transferred onto PVDF membranes. The membranes were blocked and incubated with primary antibodies against BAX, Bcl-X_L, BAD, ERK1/2, Phospho-ERK (Thr980), SIRT3, cytochrome c, caspase-3 or β-actin overnight at 4°C. The next day, the membranes were incubated with specific secondary antibodies for 1 h at room temperature as described previously (Ghosh et al., 2015; Williams et al., 2019). The antibody details are provided in Supplementary Table S2.

2.10 Statistical analysis

All data are expressed as mean ± standard error of the mean (SEM). The statistical analysis were conducted based on the applied test for comparison of data sets as appropriate by two-sample t-test. One-way or two-way analysis of variance (ANOVA) followed by a Tukey post hoc test was used for multiple comparison. A p value of <0.05 was considered statistically significant. Origin 9.0 software (OriginLab Corp., Northampton, MA, United States) was used for the statistical analyses.

3 Results

3.1 BAX and Bcl-X_L imbalance in epileptic brain tissue based on type of antiseizure medication exposure

We analyzed the samples from a patient cohort categorized by type of ASM treatment taken and evaluated the pre-characterized epileptic tissue by histopathological (post-resection) staining as described previously (Williams et al., 2019). The snap-frozen epileptic brain tissues from twenty patients divided into four groups based on their ASM treatment regimen before surgery: NON-CYP + CYP substrate, NON-CYP + CYP inducer, CYP substrate + CYP substrate and CYP substrate + CYP inducer. The western blot analysis showed that in the CYP substrate + CYP substrate (*p = 0.022; *p = 0.023) and CYP substrate

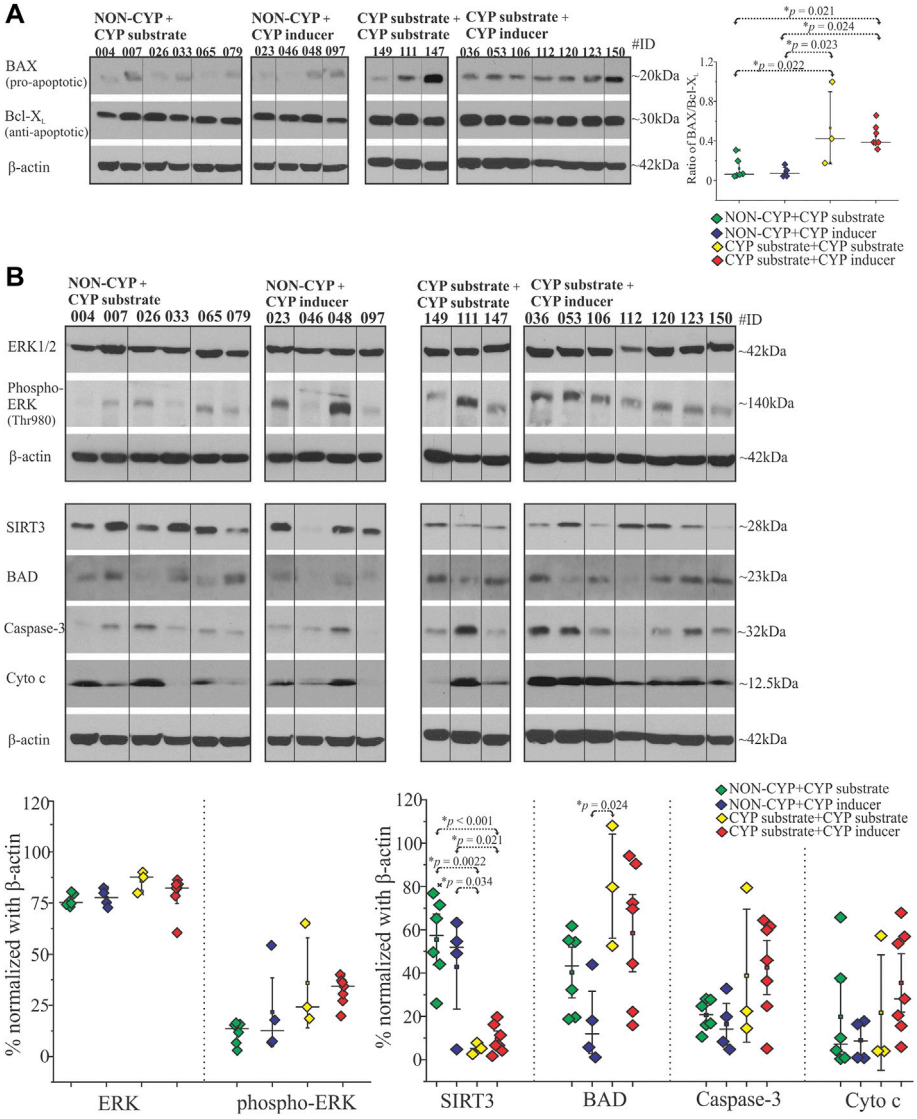

FIGURE 1
Antiseizure medications as CYP-substrates or inducers or in combination with NON-CYP-mediated ASMs alters the BAX and Bcl-X_L levels, affects other apoptotic and mitochondrial target proteins in epileptic brain. **(A)** BAX (pro-apoptotic) and Bcl-X_L (anti-apoptotic) analysis of the brain tissue shown by a representative western blots (n = 10 subjects/group) and the densitometric quantification normalized with β-actin were used to depict the ratio of BAX/Bcl-X_L levels plotted to compare within the groups. **(B)** A significant decrease in mitochondrial deacetylase SIRT3 levels was observed in the CYP substrate + CYP substrate or CYP inducer groups compared to the NON-CYP + CYP substrate or CYP inducer groups in epileptic brain tissues (total n = 20 subjects). BAD protein levels are significantly increased in the CYP substrate + CYP substrate group compared to the NON-CYP + CYP inducer group. Data are normalized with β-actin. Results are expressed as mean ± SEM by ANOVA.

+ CYP inducer (*p = 0.021; *p = 0.024) groups the BAX (pro-apoptotic) to Bcl-X_L (anti-apoptotic) ratio were significantly elevated compared to the NON-CYP + CYP substrate and NON-CYP + CYP inducer groups, respectively (Figure 1A). This finding is indicative of higher pro-apoptotic condition in epileptic brain tissue of patients receiving a combination of CYP substrates or CYP substrates with CYP inducers. The full blots are shown in Supplementary Figure S3.

3.2 Alterations in apoptotic and mitochondrial signaling proteins based on type of antiseizure medication exposure

Beside BAX and Bcl-X_L, other key apoptotic and mitochondrial signaling proteins were assayed in epileptic brain tissue obtained from patients in the NON-CYP + CYP substrate, NON-CYP + CYP inducer, CYP substrate + CYP substrate and CYP substrate + CYP inducer groups and compared. ERK1/2 expression did not differ

significantly between the groups (Figure 1B). However, phosphorylated ERK (Thr980) levels showed an elevated trend in the CYP substrate + CYP inducer group compared to the NON-CYP + CYP substrate group ($p = 0.08$). Compared to the NON-CYP + CYP substrate and NON-CYP + CYP inducer groups, epileptic brain tissues from the CYP substrate + CYP inducer group showed an increasing trend in levels of BAD ($p = 0.59$ and 0.085, respectively), although not significant (Figure 1B). The cytochrome c and caspase-3 levels within the patients groups did not show a significant difference. However, BAD levels were significantly increased ($^*p = 0.024$) in the CYP substrate + CYP substrate group compared to the NON-CYP + CYP inducer group. In contrast, compared to the NON-CYP + CYP substrate and NON-CYP + CYP inducer groups, a significant decrease in SIRT3 protein levels, depicting mitochondrial dysfunction in the epileptic brain tissues, is noticed across individuals that received a combination of ASMs as CYP substrate + CYP substrate ($^*p = 0.0022$ and 0.034, respectively) or CYP substrate + CYP inducer ($^*p < 0.001$ or $^*p = 0.021$, respectively).

3.3 Oxidative stress related to CYP combination of antiseizure medications

Evidence that the cytotoxic effects were mediated by production of free radicals is provided by measuring reduced glutathione and malondialdehyde (MDA) levels in these epileptic brain tissues. There was no significant difference in reduced glutathione levels between the NON-CYP + CYP substrate, NON-CYP + CYP inducer, CYP substrate + CYP substrate and CYP substrate + CYP inducer groups (Figure 2A). Although, there was a significant increase in MDA levels (Figure 2B), a measure of lipid peroxidation (marker of oxidative stress), in the CYP substrate + CYP substrate group compared to patients taking ASMs as NON-CYP + CYP substrate ($^*p = 0.017$) or NON-CYP + CYP inducer ($^*p = 0.025$). In contrary, the patients that received ASMs as NON-CYP + CYP substrate or inducer, in combination showed relatively increased levels of reduced glutathione and lower MDA levels, indicating negligible oxidative stress.

3.4 Cytotoxicity and mitochondrial membrane potential influenced by antiseizure medications at blood-brain barrier epileptic endothelial cells and neuronal cells

A functional blood-brain barrier protects the brain from circulating neurotoxins. In these experiments, the EPI-ECs derived from the epileptic brain tissues ($n = 3$ each) were exposed to ASM combinations as LCM + OXC (CYP substrate + CYP inducer), LCM + LEV (CYP substrate + NON-CYP) or ASM alone, LCM (CYP substrate) or LEV (NON-CYP) to determine if ASM combination based on CYP-mediated pathway together or alone can exert toxicity at epileptic brain endothelial cells. Further, the blood-brain barrier penetrants from the brain-side of the *in vitro* blood-brain barrier were used for neurotoxicity evaluation on normal primary human dopaminergic neuronal cells. As shown in Figure 3A, the LCM + OXC-induced cytotoxic response on EPI-ECs was significantly elevated compared to LCM + LEV ($^{***}p < 0.001$) in combination, LCM ($^{***}p < 0.001$) or LEV ($^{***}p < 0.001$) alone determined by adenylate kinase levels. Whether the cytotoxicity in EPI-EC observed was due to drug interactions mediated by CYP enzymes was further validated by pre-treatment with CYP inhibitor, ketoconazole, and followed by drug treatment. A significant reduction in cytotoxicity and decreased adenylate kinase levels (Figure 3A) of LCM + OXC ($^{**}p < 0.01$) in EPI-ECs were observed with ketoconazole, compared to EPI-ECs without CYP inhibition. Similarly, exposure of drug penetrant across the epileptic *in vitro* BBB showed increased adenylate kinase levels on neuronal cells (Figure 3B) post-LCM + OXC treatment, compared to non-CYP ASMs ($^{***}p < 0.001$) in combination or ASM alone, i.e., LCM ($^{***}p < 0.001$) or LEV ($^{***}p < 0.001$). Further, the LCM + OXC in combination also showed decreased mitochondrial membrane potential in the neuronal cells (Figure 3C) compared to LCM + LEV ($^{***}p < 0.001$) or LEV alone ($^{**}p < 0.01$) at 24 h.

3.5 Decreased mitochondrial SIRT3 activity in EPI-ECs in LCM + OXC or LCM improved with CYP inhibition

Mitochondrial SIRT3 activity in EPI-ECs was assessed after treatment with ASMs in combinations (LCM + OXC; LCM + LEV) and ASM alone (LCM; LEV) were evaluated to determine CYP-dependent drug interactions. EPI-ECs exposed to LCM + OXC in combination showed relatively low SIRT3 activity (Figure 4A) compared to LCM + LEV in combination ($^*p < 0.05$) or LCM alone ($^{***}p < 0.001$) or LEV alone ($^*p < 0.05$). A similar trend was observed in vehicle-treated EPI-ECs that showed decreased levels of relative SIRT3 activity when compared to LCM alone. Although, the time-course of SIRT3 activity for 60 min with drug treatment were also plotted to identify the relative pattern with time which shows negligible difference overtime.

To further confirm the alteration in the mitochondrial dynamics is due to CYP involvement in the EPI-ECs, we pretreated the EPI-ECs for 24 h with CYP inhibitor, ketoconazole, then followed with the ASM regimen. EPI-ECs pretreated with ketoconazole showed upregulation of SIRT3 activity after LCM + OXC in combination or LCM alone when compared to LCM + LEV in combination ($^{***}p < 0.001$) or LEV alone ($^{***}p < 0.001$) showing a distinct differential time-course pattern followed for 60 min under each condition (Figure 4B). Ketoconazole seems to be beneficial for EPI-ECs as the vehicle alone ($n = 3$) post ketoconazole treatment

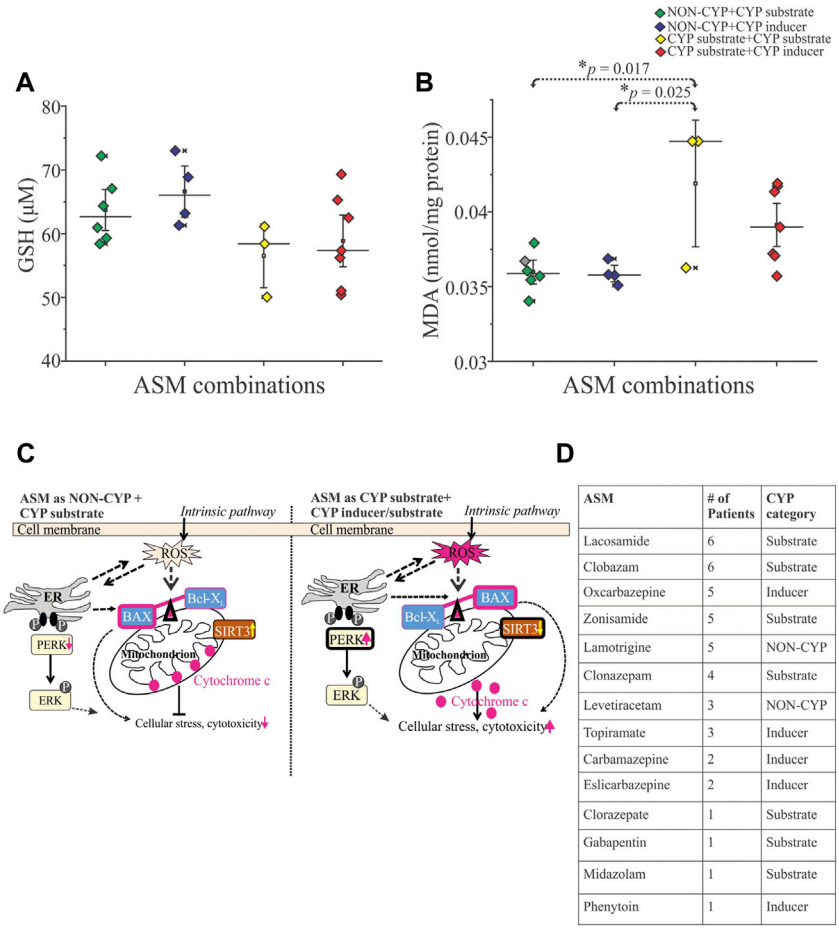

ASM	# of Patients	CYP category
Lacosamide	6	Substrate
Clobazam	6	Substrate
Oxcarbazepine	5	Inducer
Zonisamide	5	Substrate
Lamotrigine	5	NON-CYP
Clonazepam	4	Substrate
Levetiracetam	3	NON-CYP
Topiramate	3	Inducer
Carbamazepine	2	Inducer
Eslicarbazepine	2	Inducer
Clorazepate	1	Substrate
Gabapentin	1	Substrate
Midazolam	1	Substrate
Phenytoin	1	Inducer

FIGURE 2
Reactive oxygen species influenced by ASM combinations based on CYP association in human epileptic brain tissue. **(A,B)** Cytotoxicity associated with oxidative stress (n = 20 subjects total), as shown by decreased trend of reduced glutathione GSH, **(A)** and significantly increased levels of free radical showed by malondialdehyde MDA, **(B)** indicative of increased lipid peroxidation in patients taking multiple CYP substrates compared to the NON-CYP + CYP substrate (*p = 0.017) or inducer groups (*p = 0.025) (n = 20 subjects total). Results are expressed as mean ± SEM by ANOVA. **(C)** Schematic scheme showed two potential scenarios based on the data generated in the human epileptic brain tissues based on ASM combination given before surgery as NON-CYP + CYP substrate vs. CYP substrate + CYP inducer/substrate (in combination) causing cellular distress. Release of reactive oxygen species (ROS), potentially imbalance the BAX (pro-apoptotic)-Bcl-X_L (anti-apoptotic) ratio linking to endoplasmic reticulum (ER) phospho-ERK expression contributing to cellular stress via cytochrome c upregulation and mitochondrial SIRT3 downregulation with majorly CYP-mediated ASMs treatments. **(D)** Table describing the distribution of ASMs taken by this cohort of patients (n = 20) and whether they are a CYP substrate, CYP inducer or NON-CYP-mediated.

(without ASM) also showed a significant increase (*p < 0.05) in SIRT3 activity when compared to LCM + LEV in combination.

3.6 CYP inhibition replenishes the levels of apoptotic and mitochondrial signaling proteins influenced by CYP-dependent antiseizure medication interactions in EPI-ECs and neuronal cells

Consistent with the epileptic brain tissue, an elevated BAX/Bcl-X_L ratio in neuronal cells (n = 3) was noticed post-LCM + OXC (*p < 0.001) and LCM (*p < 0.001) treatment, compared to LCM + LEV and LEV alone (Figure 5B). EPI-ECs (n = 3) also showed upregulated BAX/Bcl-X_L ratio with LCM + OXC (*p < 0.001) and LCM (*p < 0.001) compared to LCM + LEV and LEV alone (Figure 5A and Supplementary Figure S4). Moreover, CYP inhibition with KCZ decreased the BAX (pro-apoptotic)/Bcl-X_L (anti-apoptotic) ratio in spite of follow up-drug treatment, both with LCM + OXC in combination (*p < 0.05) and LCM alone (*p < 0.05) in the same EPI-ECs (n = 3) (Figure 5A). Likewise, a significant decrease in the BAX/Bcl-X_L ratio was also seen with KCZ pre-treatment after LCM + OXC in

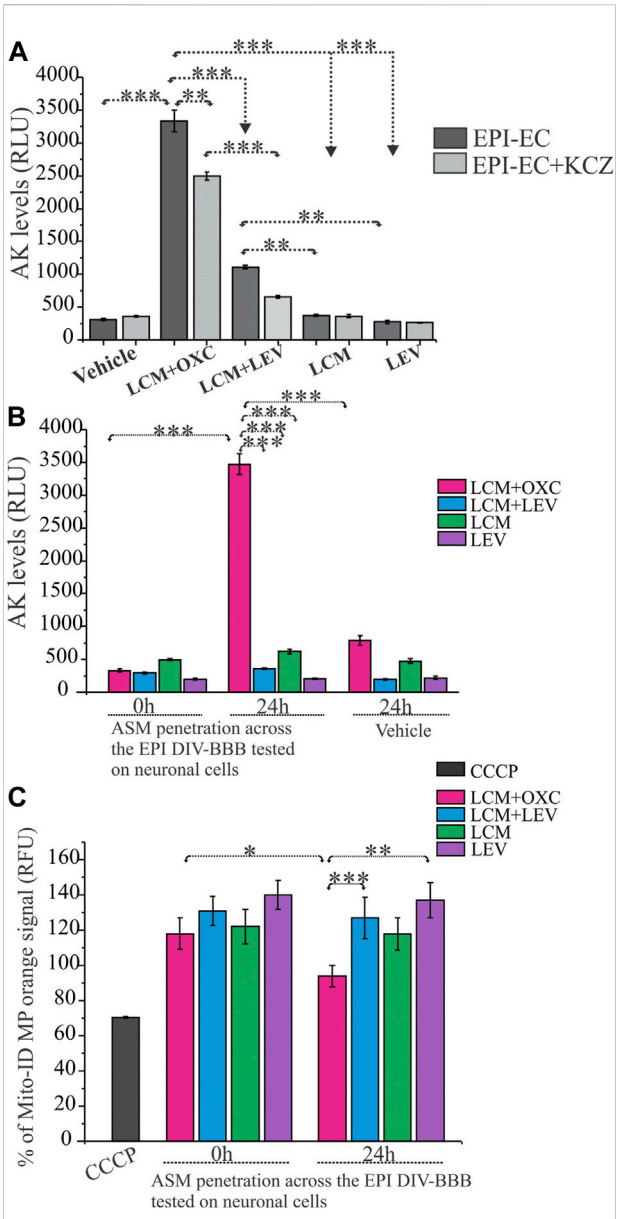

FIGURE 3
CYP-mediated neurotoxicity across the *in vitro* epileptic BBB affects mitochondrial function. **(A,B)** Cytotoxicity after 24-h exposure to LCM + OXC vs. LCM + LEV, LCM or LEV alone on EPI-ECs and neuronal culture after BBB penetration was associated with increased levels of adenylate kinase (AK) released from damaged cells, measured in relative luminescence units (RLU). The elevated LCM + OXC (*$p < 0.001$) induced cytotoxicity **(A)** and neurotoxicity **(B)** compared to LCM + LEV, LCM, LEV or vehicle was measured by adenylate kinase levels and could be prevented in EPI-ECs **(A)** by pre-treatment with CYP inhibitor, ketoconazole (KCZ) for 2 h before ASM co-treatment (*$p < 0.01$). **(C)** LCM + OXC co-exposure at the BBB significantly decreased Mito-ID levels in the neuronal cells (measured by orange RFU levels) at 24 h compared LCM + LEV (*$p < 0.001$) together or LEV (**$p < 0.01$) alone. Also, the Mito-ID alterations was significant (*$p < 0.05$) in 0–24 h, post-LCM + OXC co-treatment. CCCP positive control was used as an indicator for mitochondrial damage tested directly on human neuronal culture. Quantification of adenylate kinase levels **(A–B)** and % Mito-ID membrane potential (MP) are depicted as mean ± SEM by two-way ANOVA, ***$p < 0.001$, **$p < 0.01$, *$p < 0.05$.

combination (***$p < 0.001$) and LCM alone (***$p < 0.05$) in the same neuronal cells ($n = 3$) compared to drug treatment, without CYP inhibition (Figure 5B). The full blots are shown in Supplementary Figure S4.

The expression of other apoptotic signaling proteins, ERK1/2 in EPI-ECs treated with LCM + OXC compared to LCM + LEV (*$p < 0.001$), or LCM (*$p < 0.001$), or LEV (*$p < 0.001$), or vehicle (*$p < 0.001$) was found to be upregulated (Figure 5A). Similarly, phospho-ERK levels were consistently elevated within LCM + OXC co-treatment compared to LCM + LEV (*$p < 0.001$) or LCM (*$p < 0.001$) or LEV (*$p < 0.001$). The levels of other cellular stressors, such as cytochrome c, were also high after LCM + OXC co-treatment compared to LCM + LEV co-treatment (*$p < 0.001$), or LCM (*$p < 0.001$), or LEV (*$p < 0.001$), or vehicle (*$p < 0.001$) in EPI-ECs, and so was the increased caspase-3 levels in EPI-ECs when exposed to LCM + OXC and compared to LCM + LEV (*$p < 0.001$) in combinations, or LCM (*$p < 0.001$). Although, the condition reversed with CYP inhibitor, ketoconazole pretreatment (Figure 5A) as levels of ERK1/2 (*$p < 0.001$), phospho-ERK (*$p < 0.001$), cytochrome c (*$p < 0.001$), caspase-3 (*$p < 0.001$) decreased significantly after co-treatment of LCM + OXC thereafter in EPI-ECs. Also, within these EPI-ECs LCM + OXC or LCM + LEV co-treatment or LCM or LEV also, showed significant reduction in caspase-3 (*$p < 0.001$) and cytochrome c (*$p < 0.001$) levels with CYP inhibition (Figure 5A).

Similarly in neuronal cells, the phospho-ERK levels (Figure 5B) were subsequently elevated with LCM + OXC co-treatment compared to LCM + LEV in combination (*$p < 0.001$) or LCM (*$p < 0.001$) or LEV (*$p < 0.001$) alone. Other cellular stressor, such as cytochrome c levels were also increased in the same cells, after LCM + OXC co-treatment compared to LCM + LEV (*$p < 0.001$), or LCM (*$p < 0.001$), or LEV (*$p < 0.001$), or vehicle (*$p < 0.001$) treatment. Consistent to EPI-ECs, the condition were reversed with CYP inhibitor, ketoconazole in neuronal cells (Figure 5B), as levels of ERK1/2 (*$p < 0.001$), phospho-ERK (*$p < 0.001$), cytochrome c (*$p < 0.001$) were subsequently decreased after LCM + OXC co-treatment. In addition, CYP inhibitor, ketoconazole (Figure 5B) also decreased the levels of ERK1/2 (*$p < 0.05$), phospho-ERK (*$p < 0.05$) and cytochrome c (*$p < 0.001$) after LCM treatment in the neuronal cells.

It is also noteworthy that CYP inhibition with ketoconazole improved mitochondrial SIRT3 levels after LCM + OXC (***$p < 0.001$), LCM + LEV (***$p < 0.001$), LCM (***$p < 0.001$) and LEV (***$p < 0.001$) treatment compared to ASM(s) without (Figure 5A). Similarly, elevated SIRT3 levels in neuronal cells with ketoconazole pre-treatment was also identified after co-treatment with LCM + OXC (***$p < 0.001$), LCM + LEV (***$p < 0.001$), LCM (***$p < 0.001$) and LEV (***$p < 0.001$) treatment, when

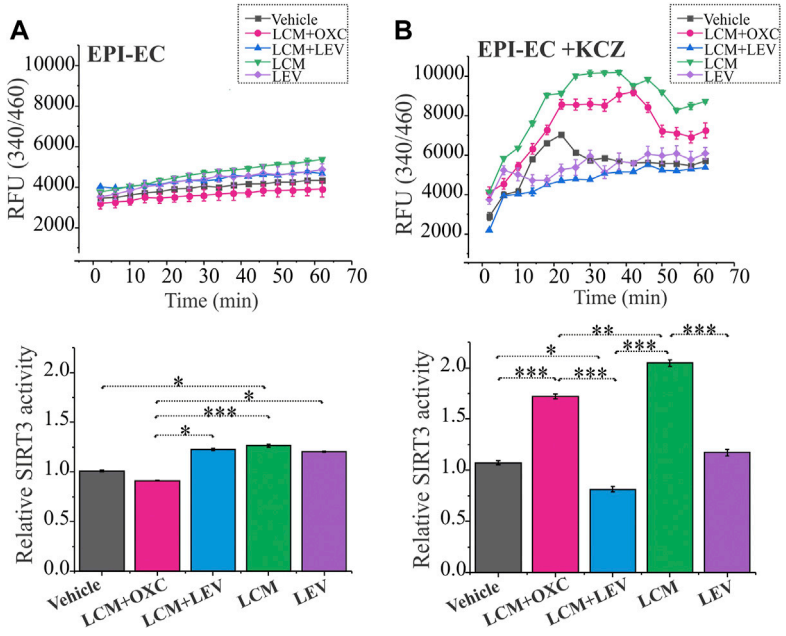

FIGURE 4
Improved SIRT3 activity with CYP-inhibition in human EPI-ECs post-LCM + OXC treatment. **(A)** SIRT3 activity showed a decreased level (depicted by relative fluorescent units, RFU) over time post-LCM + OXC co-treatment compared LCM + LEV, LCM or LEV, with the relative levels at 60 min quantified below. **(B)** CYP inhibition with ketoconazole showed significant elevation in the SIRT3 activity in LCM + OXC and LCM alone compared to LCM + LEV or LEV alone suggesting an association of CYP-mediated drugs (in combination or alone) and mitochondrial activity change in EPI-ECs. Results are expressed as mean ± SEM by one-way ANOVA was performed with a Tukey *post hoc* test, $*p < 0.05$, $**p < 0.01$, $***p < 0.001$.

compared to ASM(s) without (Figure 5B) showing CYP-mediatory effect on ASM response.

4 Discussion

Polytherapy is common in patients with epilepsy, particularly among those with drug-resistant seizures (Patsalos et al., 2002; Perucca and Meador, 2005; Gidal et al., 2009), potentially leading to clinically-relevant drug interactions (Patsalos and Perucca, 2003). This study pinpoints for the *first time* that LCM in combination with certain other ASMs, like OXC as a CYP inducer, affect the pro- and anti-apoptotic protein levels in the epileptic brain, modulated via a CYP-mediated mechanism that controls free radicals, cytotoxicity and mitochondrial activity. The main goal of this study was therefore to identify the functional consequence of CYP-mediated ASM interactions on apoptotic signaling proteins and assessing mitochondrial function in human epileptic brain tissues, focusing at the neurovascular interface. Additionally, the two-ASM approach could aid in delineating the regulatory mechanisms of LCM with and without other CYP-dependent ASMs using alternative metabolic and regulatory pathways, facilitating improved drug efficacy via mitigating drug-induced cellular stress.

4.1 Increased BAX/Bcl-X_L ratio, BAD, phosphorylated ERK, mitochondrial dysfunction and cellular stress in human epileptic brain tissues linked to CYP-mediated drug interactions

We identified that patients taking a combination of multiple ASMs with varying CYP involvement–NON-CYP + CYP substrate, NON-CYP + CYP inducer, CYP substrate + CYP substrate and CYP substrate + CYP inducer–showed differential effects on the ratio of pro-apoptotic (e.g., BAX) and anti-apoptotic (e.g., Bcl-X_L) proteins in the epileptic brain tissues. Evidence supports that both BAX and Bcl-X_L genes/proteins are expressed in the neocortical region of temporal lobe epilepsy (Henshall et al., 2000). Beside, an aberrant expression pattern of BAX and Bcl-X_L has been reported to participate in several other neurological disorders including epilepsy with focal cortical dysplasia and hippocampal sclerosis (McMasters et al., 2000; Chamberlain and Prayson, 2008; Toscano et al., 2019). In focal cortical dysplasia type IIb, balloon cells a histopathological characteristic, have shown apoptotic protein expression in the epileptic tissue regions, with 61% of cases in this study showing >50% of balloon cells expressing BAX (Chamberlain and Prayson, 2008). BAD (Bcl-2-associated death protein) is also

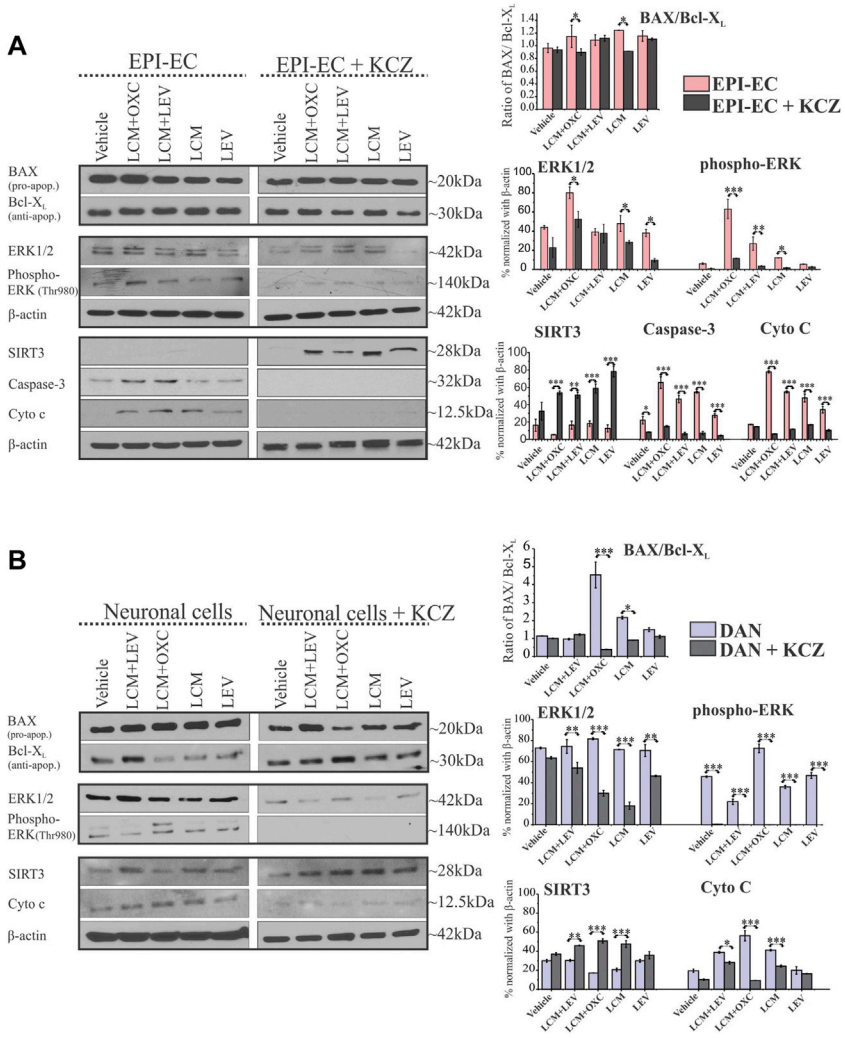

FIGURE 5
CYP inhibition causes a selective decrease in apoptotic proteins and elevated SIRT3 levels in human EPI-ECs and neuronal cells. **(A,B)** Western blot showed a significant decrease in the BAX (pro-apoptotic)/Bcl-X_L (anti-apoptotic) ratio in LCM + OXC (*$p < 0.05$) and LCM (*$p < 0.05$) expression in EPI-ECs **(A)** and in LCM + OXC (***$p < 0.001$) and LCM (*$p < 0.05$) expression in neuronal cells **(B)**, post-CYP inhibition with ketoconazole (KCZ) within the same cell types. Similarly, the levels of ERK1/2 (*$p < 0.05$), phospho-ERK (***$p < 0.001$, LCM + OXC and *$p < 0.05$, LCM), caspase-3 (*$p < 0.001$) and cytochrome c (***$p < 0.001$) showed a significant decrease post-CYP inhibition, markedly in LCM + OXC co-treated and LCM alone group in EPI-ECs along with improved SIRT3 (***$p < 0.001$) levels. Likewise in neuronal cells **(B)**, a similar pattern was seen with significantly decreased levels of ERK1/2 (**$p < 0.01$), phospho-ERK (*$p < 0.001$) and cytochrome c (*$p < 0.001$) post-CYP inhibition in the LCM + OXC co-treated group and increased SIRT3 (*$p < 0.001$) levels. Western blot quantitative data (in right) are normalized with β-actin, and values are plotted as mean ± SEM by two-way ANOVA with a Tukey *post hoc* test for each target, *$p < 0.05$, **$p < 0.01$, ***$p < 0.001$.

another pro-apoptotic factor that associates with BAX and contributes to the regulation of cytochrome c release (Niquet and Wasterlain, 2004). A study found that in a rat model of epilepsy, seizures induced the dimerization of BAD with BcL-X_L in the affected areas of the hippocampus (Henshall et al., 2002). In the current study, we found that CYP association in ASM combination is critical and linked to an elevation in the BAX/Bcl-X_L ratio and increased BAD protein levels, suggestive of more pro-apoptotic and less anti-apoptotic proteins in epileptic brain tissues exposed mostly to ASMs that are CYP-mediated (CYP substrate + CYP substrate or CYP substrate + CYP inducer) compared to NON-CYP + CYP mediated ASMs (Figure 1) within the same patient cohort. A previous report in rats showed that dexamethasone (CYP inducer) treatment increased the cytotoxic effects of an herbal supplement due to elevated reactive metabolite levels (Haouzi et al., 2000). In this current study, the combinations of CYP substrate ASMs with other CYP substrates or inducers could lead to the production of reactive metabolites, as previously touched on by our group (Ghosh et al., 2015). To uncover the consequence, the

findings also indicate relatively low levels of reduced glutathione and elevated lipid peroxidation in the brain tissues, implying oxidative stress influenced by specific ASM interactions (Figure 2). Such drug interaction was reported with haloperidol and valerian, where an increase in lipid peroxidation levels and dichlorofluorescein reactive species production was observed in rat hepatic tissue (Dalla Corte et al., 2008). Further, ASM with non-ASM could also factor into these interactions in epilepsy patients with other comorbidities (Gidal et al., 2009; Bosak et al., 2019). A similar differential modulation of the BAX and Bcl-X_L ratio by two-drug combinations was demonstrated in studies using human colon tumor cells (McMasters et al., 2000) in the past, which was implicated in the development of cancer and related to the mechanism of cell death induced by pro-apoptotic agents. However, other forms of cell death mechanisms could also be at play, which needs to be investigated further.

Interestingly in the epileptic tissues, we evaluated the ERK1/2 as MAP kinases which are necessary for G1-to S-phase progression and are associated with the induction of positive regulators of the cell cycle and inactivation of anti-proliferative genes (Bozzi et al., 2011). ERK1/2 expression was comparable regardless of the ASM combination in both patient groups; however, the endoplasmic reticulum-related stress signified by up-trending levels of the phosphorylated form of ERK was predominant across individuals that received ASMs that are mostly CYP-mediated (either CYP substrates or with an inducer) (Figure 1). Studies show that downstream events lead to activation of caspase-3, an important contributing factor for cellular stress augmented by increased release of cytochrome c from the mitochondria (Kirkland and Franklin, 2001, 2015; Mao et al., 2019). Caspase-3 mRNA levels have been previously found to increase in a rat model of epilepsy (Sun et al., 2012), which could be even further increased in the presence of neurotoxic chemicals (Folch et al., 2010). Further, patient-to-patient variability could play a role in the caspase-3 expression spectrum observed among the patient groups. Moreover SIRT3, a vital indicator of mitochondrial respiration, was decreased in these epileptic brain tissues in individuals taking ASMs as CYP substrate + CYP substrate or CYP substrate + CYP inducer in combinations vs. NON-CYP + CYP substrate or inducer. This suggests that a medication regimen with ASMs eliminated via different drug metabolizing pathways is safer in retaining cellular and mitochondrial integrity (results summarized in Figure 2C). SIRT3 alteration is a critical indicator of reactive oxygen species generation (Figures 2A,B) and underlying cellular stress under the exogenous influence of the interactions of ASMs that are primarily dependent on CYP as a metabolizer, like LCM, in combination with other CYP substrate or CYP inducing medications. Multiple alternative apoptotic signaling pathways also may participate (Henshall and Simon, 2005), beyond pro-apoptotic and anti-apoptotic ratio in epilepsy due to ASM interactions. Another report showed that despite an increase in the Bcl-2/BAX ratio, the granular neurons and glia exhibited active caspase-3 expression in temporal lobe epilepsy hippocampi compared to controls (Toscano et al., 2019), where glial and neuronal death were found to be increased in sclerotic hippocampi, independently of hippocampal type pathology and co-localization found with gliosis. Furthermore, in the current study among the patient cohort, the patients that received ASMs as NON-CYP + CYP substrates or inducers in combination showed relatively balanced redox homeostasis with increased level of reduced glutathione and lower lipid peroxidation levels, together indicating an altered dynamic in apoptotic and mitochondrial proteins levels (schematic representation in Figure 2C). These results may stem from CYP-mediated ASM interactions linked to metabolic pathways and oxidative stress implicating a unique feature based on ASM combination, not solely a disease pathogenesis *per se*. LCM was the most commonly taken CYP-substrate ASM in this cohort of 20 patients retrospectively studied, while OXC was the most commonly taken CYP inducer (Figure 2D).

4.2 Drug-induced cytotoxicity and compromised mitochondrial membrane potential affecting the neurovascular interface

To gain better insight into the mechanism of how this cellular stress could specifically influence the neurovascular interface, we evaluated the impact of LCM, a CYP-associated ASM, in combination with a CYP inducer or a NON-CYP-mediated ASM at the epileptic human *in vitro* blood-brain barrier and applied the penetrants obtained directly from the abluminal or brain-side of the blood-brain barrier onto human neuronal cultures (Supplementary Figure S1). Consistent with our previous studies (Ghosh et al., 2015), we noted CYP-mediated drug interaction in this case with LCM + OXC (CYP substrate + inducer) causing significant cytotoxicity shown by increased adenylate kinase levels in EPI-ECs compared to LCM + LEV or ASM alone (Figure 3A). Earlier studies also indicated changes in epileptic and non-epileptic CYP3A4 expression in the brain, which increased in patients taking ASMs that were CYP-mediated, and was downregulated when CYP- and NON-CYP-mediated ASMs were given together. Brain CYP3A4 levels also correlated with seizure frequency within the same individuals (Williams et al., 2019). However, in the current study, CYP inhibition with ketoconazole decreased the cellular stress observed after LCM + OXC co-treatment in EPI-ECs. Similarly, the ASM interaction at the epileptic blood-brain barrier and penetrants further showed similar cellular stress on the neuronal cells, which was demonstrated by elevated adenylate kinase levels with LCM + OXC treatment (Figure 3B), consistent with previous studies with drug-induced toxicity by two

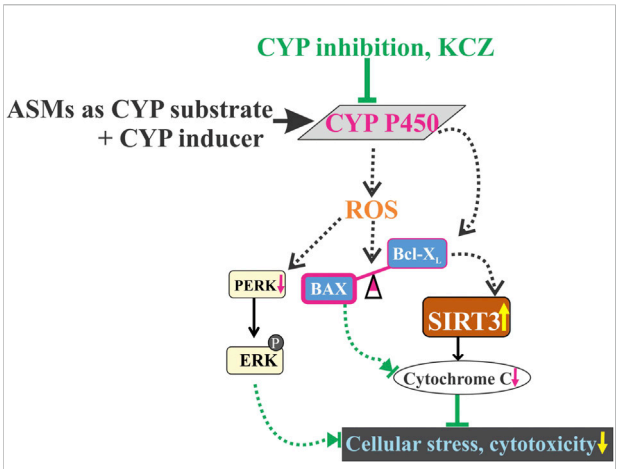

FIGURE 6
Drug-induced cellular stress by CYP-mediated drug combinations of ASMs, CYP substrate + CYP inducer co-treatment which may have contributed towards oxidative stress by reactive oxygen species (ROS) generation and aberrantly expresses an imbalance of increased BAX (pro-apoptotic) and decreased Bcl-X_L (anti-apoptotic) levels, possibly leading to a decrease in SIRT3 activity and expression. ROS release and increased phospho-ERK levels influence cytotoxicity at cellular levels. However, CYP inhibition completely abolished the altered cascade of apoptotic signaling pathway, thereby restoring cell integrity and mitochondrial function.

CYP-mediated ASMs (Ghosh et al., 2015). Furthermore, in neuronal cells, a decrease of mitochondrial membrane potential was also noted after LCM + OXC penetration across the epileptic human *in vitro* BBB compared to LCM + LEV or LEV alone. Overall, the study suggested that the CYP-mediated cellular stress at the epileptic-blood-brain barrier is translated across the barrier into the neuronal cells, altering mitochondrial integrity post-co-treatment with ASMs that broadly undergo CYP-mediated drug metabolism.

SIRT3 dysfunction is related to several neurological conditions such as cancer, aging, metabolic disorder and neurodegenerative diseases (Weir et al., 2013; Yi et al., 2019). In our study, a decrease in SIRT3 activity was noticed in EPI-ECs post LCM + OXC co-treatment and EPI-ECs by itself (Figure 4A); however, co-treatment of LCM + LEV or LCM or LEV alone showed upregulated SIRT3 activity suggesting that CYP-mediated ASM co-treatment does not improve mitochondrial activity as supported by SIRT3 function. Nonetheless, CYP inhibition abolished the breakdown and instead improved the mitochondrial function via upregulated SIRT3 activity post-LCM + OXC co-treatment, compared to EPI-ECs untreated or treated with LCM + LEV or LEV alone (Figure 4B). This is further supported by another study which demonstrated elevation in SIRT3 prevents apoptosis by lowering reactive oxygen species and inhibiting components of the mitochondrial permeability characteristics such as the transition pore and mitochondrial deficits associated with aging and neurodegeneration could be slowed or even prevented by SIRT3 activation (Kincaid and Bossy-Wetzel, 2013). SIRT3 dysfunction is identified in a chronic epilepsy model which is linked to mitochondrial acetylation process (Gano et al., 2018). Drug combination might contribute to this process according to the current findings. ASMs could modify mitochondrial oxidative phosphorylation based on the ASM used as noted in a pilot study (Berger et al., 2010) by evaluating mitochondrial ATP production and enzymatic activities of respiratory chain complexes in children who suffer from epilepsy, treated by a single ASM (phenobarbital, carbamazepine or lamotrigine) in peripheral white blood cells and when compared with healthy non-treated individuals as control.

4.3 Role of CYP inhibition on BAX/Bcl-X_L ratio, apoptotic signaling protein and mitochondrial SIRT3 at the human epileptic brain endothelial cells and neuronal cells

Several chemotherapeutic-induced adverse side-effects are mediated by mitochondrial dysfunction. For example, trastuzumab and sunitinib toxicity is mainly associated with mitochondrial impairment and was mostly reversible (Gorini et al., 2018). However, doxorubicin-induced toxicity not only includes mitochondrial damage but can also lead to more robust and extensive cell injury which is often irreversible and lethal (Gorini et al., 2018). While evaluating the BAX/Bcl-X_L in the EPI-ECs and neuronal cells (Figure 5), we identified a similar alteration pattern as in the human epileptic brain tissues, with elevated BAX/Bcl-X_L post-treatments with LCM + OXC compared to vehicle or untreated cells. However, CYP inhibition prevented this imbalance in both cell types, analyzed as fundamental components of the neurovascular unit, with a significant decrease in the BAX/Bcl-X_L ratio after LCM + OXC with ketoconazole pre-treatment. Similarly, the ERK1/2 levels were found to be elevated in EPI-ECs and neuronal cells as observed in epileptic tissues regardless of drug exposure or not but showed a significant reduction in levels post-CYP inhibition with ketoconazole. Furthermore, the phospho-ERK levels were upregulated with LCM + OXC compared to other ASMs in both EPI-ECs and neurons, as previously seen in epileptic brain tissues exposed to CYP substrates in combination with other CYP substrates or inducers before surgery. The phospho-ERK expression in these cells decreased significantly to almost negligible levels post-CYP inhibition, suggesting the beneficial role of CYP inhibitors when multiple CYP-mediated ASMs are administered, perhaps by balancing out the CYP induction with inhibition, subsequently preventing the CYP substrate from being quickly metabolized.

Downstream, caspase-3 in EPI-ECs and cytochrome c in EPI-ECs and neuronal cells post-drug treatment were similarly rescued by CYP inhibition, and a significant decrease in the protein levels was noted thereafter in these cells pre-treated with ketoconazole followed by ASM alone or ASMs together. SIRT3 consistent with epileptic brain tissues was dismantled in EPI-ECs post-ASM interaction and was reversed back post-CYP inhibition with ketoconazole. The same pattern was identified in neuronal cells. Together, the findings emphasize the relevance of cytochrome P450 enzymes via CYP overactivity that could be detrimental to cell efficacy causing cellular stress due to potential drug interactions.

5 Conclusion

ASMs that are either CYP substrates or inducers used in combination could adversely affect tissue and cell function due to overactivity of CYP enzymes triggered by drug interactions. These interactions result in the release of reactive oxygen species and ER stress, with elevated phospho-ERK compromising cellular integrity. Blood-brain barrier EPI-ECs play an important role in CYP-mediated drug interactions controlling subsequent neuronal stress. The imbalanced BAX/Bcl-X_L ratio could influence the cascade of apoptotic events and consequent mitochondrial dysfunction via decreased SIRT3 activity can be rescued and reversed by CYP inhibition (Figure 6), indicating that this phenomenon involves CYP activity. Better understanding of these effects and development of new drugs that could act against novel targets could allow more rational polytherapy selection in the future.

Data availability statement

The original contributions presented in the study are included in the article/Supplementary Material, further inquiries can be directed to the corresponding author.

Ethics statement

The studies involving human participants were reviewed and approved by Cleveland Clinic Institutional Review Board (IRB 07-322). Written informed consent to participate in this study was provided by the participants' legal guardian/next of kin.

Author contributions

CG contributed to the conceptualization, funding acquisition, investigation, methodology, analysis, interpretation and writing original draft of the manuscript; RW performed investigation, analysis and interpretation; EP contributed in methodology, interpretation and analysis; MH performed investigation and analysis, WB provided resources; IN contributed in providing resources and interpretation; All authors contributed in reviewing and editing.

Funding

This work is supported in part by the National Institute of Neurological Disorders and Stroke/National Institutes of Health grants R01NS095825 (to CG).

Acknowledgments

We would like to thank Lisa Ferguson for her coordination in tissue procurement process.

Conflict of interest

EP received speaker and/or consultancy fees from Angelini, Arvelle, Biogen, Biopas, Eisai, GW Pharma, PMI Life Sciences, Sanofi group of companies, SKL Life Science, Takeda, UCB Pharma, Xenon Pharma and Zogenix, and royalties from Wiley, Elsevier, and Wolters Kluwers. IN serves on the Speaker' bureau for Eisai, Inc., and as a member of ad hoc advisory board for Eisai, Inc. and Liva Nova.

The remaining authors declare that the research was conducted in the absence of any commercial or financial relationships that could be construed as a potential conflict of interest.

Publisher's note

Supplementary material

The Supplementary Material for this article can be found online at: https://www.frontiersin.org/articles/10.3389/fphar.2022.983233/full#supplementary-material

References

Andreasen, A. H., Brosen, K., and Damkier, P. (2007). A comparative pharmacokinetic study in healthy volunteers of the effect of carbamazepine and oxcarbazepine on cyp3a4. *Epilepsia* 48 (3), 490–496. doi:10.1111/j.1528-1167.2007.00924.x

Anna Haduch, A., Bromek, E., and Daniel, W. A. (2013). Role of brain cytochrome P450 (CYP2D) in the metabolism of monoaminergic neurotransmitters. *Pharmacol. Rep.* 65 (6), 1519–1528. doi:10.1016/s1734-1140(13)71513-5

Baird, P. (2002). Beware CYP450 inducers: Prescribing tips to prevent drug-drug interactions. *Curr. Psychiatry* 1 (11), 11–16.

Bauer, S., Willems, L. M., Paule, E., Petschow, C., Zollner, J. P., Rosenow, F., et al. (2017). The efficacy of lacosamide as monotherapy and adjunctive therapy in focal epilepsy and its use in status epilepticus: clinical trial evidence and experience. *Ther. Adv. Neurol. Disord.* 10 (2), 103–126. doi:10.1177/1756285616675777

Berger, I., Segal, I., Shmueli, D., and Saada, A. (2010). The effect of antiepileptic drugs on mitochondrial activity: a pilot study. *J. Child. Neurol.* 25 (5), 541–545. doi:10.1177/0883073809352888

Bittigau, P., Sifringer, M., Genz, K., Reith, E., Pospischil, D., Govindarajalu, S., et al. (2002). Antiepileptic drugs and apoptotic neurodegeneration in the developing brain. *Proc. Natl. Acad. Sci. U. S. A.* 99 (23), 15089–15094. doi:10.1073/pnas.222550499

Bosak, M., Slowik, A., Iwanska, A., Lipinska, M., and Turaj, W. (2019). Co-medication and potential drug interactions among patients with epilepsy. *Seizure* 66, 47–52. doi:10.1016/j.seizure.2019.01.014

Bozzi, Y., Dunleavy, M., and Henshall, D. C. (2011). Cell signaling underlying epileptic behavior. *Front. Behav. Neurosci.* 5, 45. doi:10.3389/fnbeh.2011.00045

Cawello, W., Boekens, H., and Bonn, R. (2012). Absorption, disposition, metabolic fate and elimination of the anti-epileptic drug lacosamide in humans: mass balance following intravenous and oral administration. *Eur. J. Drug Metab. Pharmacokinet.* 37 (4), 241–248. doi:10.1007/s13318-012-0093-x

Chamberlain, W. A., and Prayson, R. A. (2008). Focal cortical dysplasia type II (malformations of cortical development) aberrantly expresses apoptotic proteins. *Appl. Immunohistochem. Mol. Morphol.* 16 (5), 471–476. doi:10.1097/PAI.0b013e31815d9ac7

Contin, M., Albani, F., Riva, R., and Baruzzi, A. (2004). Levetiracetam therapeutic monitoring in patients with epilepsy: effect of concomitant antiepileptic drugs. *Ther. Drug Monit.* 26 (4), 375–379. doi:10.1097/00007691-200408000-00006

Dalla Corte, C. L., Fachinetto, R., Colle, D., Pereira, R. P., Avila, D. S., Villarinho, J. G., et al. (2008). Potentially adverse interactions between haloperidol and valerian. *Food Chem. Toxicol.* 46 (7), 2369–2375. doi:10.1016/j.fct.2008.03.019

Ferguson, C. S., and Tyndale, R. F. (2011). Cytochrome P450 enzymes in the brain: emerging evidence of biological significance. *Trends Pharmacol. Sci.* 32 (12), 708–714. doi:10.1016/j.tips.2011.08.005

Finsterer, J., and Scorza, F. A. (2017). Effects of antiepileptic drugs on mitochondrial functions, morphology, kinetics, biogenesis, and survival. *Epilepsy Res.* 136, 5–11. doi:10.1016/j.eplepsyres.2017.07.003

Folch, J., Alvira, D., Lopez-Querol, M., Tajes, M., Sureda, F. X., Forsby, A., et al. (2010). Evaluation of transcriptional activity of caspase-3 gene as a marker of acute neurotoxicity in rat cerebellar granular cells. *Toxicol. Vitro.* 24 (2), 465–471. doi:10.1016/j.tiv.2009.09.023

Gano, L. B., Liang, L. P., Ryan, K., Michel, C. R., Gomez, J., Vassilopoulos, A., et al. (2018). Altered mitochondrial acetylation profiles in a kainic acid model of temporal lobe epilepsy. *Free Radic. Biol. Med.* 123, 116–124. doi:10.1016/j.freeradbiomed.2018.05.063

Gervasini, G., Carrillo, J. A., and Benitez, J. (2004). Potential role of cerebral cytochrome P450 in clinical pharmacokinetics: modulation by endogenous compounds. *Clin. Pharmacokinet.* 43 (11), 693–706. doi:10.2165/00003088-200443110-00001

Ghosh, C., Hossain, M., Spriggs, A., Ghosh, A., Grant, G. A., Marchi, N., et al. (2015). Sertraline-induced potentiation of the CYP3A4-dependent neurotoxicity of carbamazepine: an *in vitro* study. *Epilepsia* 56 (3), 439–449. doi:10.1111/epi.12923

Ghosh, C., Hossain, M., Solanki, J., Dadas, A., Marchi, N., and Janigro, D. (2016). Pathophysiological implications of neurovascular P450 in brain disorders. *Drug Discov. Today* 21, 1609–1619. doi:10.1016/j.drudis.2016.06.004

Ghosh, C., Hossain, M., Mishra, S., Khan, S., Gonzalez-Martinez, J., Marchi, N., et al. (2018). Modulation of glucocorticoid receptor in human epileptic endothelial cells impacts drug biotransformation in an *in vitro* blood-brain barrier model. *Epilepsia* 59 (11), 2049–2060. doi:10.1111/epi.14567

Ghosh, C., Myers, R., O'Connor, C., Williams, S., Liu, X., Hossain, M., et al. (2022). Cortical dysplasia in rats provokes neurovascular alterations, GLUT1 dysfunction, and metabolic disturbances that are sustained post-seizure induction. *Mol. Neurobiol.* 59, 2389–2406. doi:10.1007/s12035-021-02624-2

Gidal, B. E., French, J. A., Grossman, P., and Le Teuff, G. (2009). Assessment of potential drug interactions in patients with epilepsy: impact of age and sex. *Neurology* 72 (5), 419–425. doi:10.1212/01.wnl.0000341789.77291.8d

Gorini, S., De Angelis, A., Berrino, L., Malara, N., Rosano, G., and Ferraro, E. (2018). Chemotherapeutic drugs and mitochondrial dysfunction: Focus on doxorubicin, trastuzumab, and sunitinib. *Oxid. Med. Cell. Longev.* 2018, 7582730. doi:10.1155/2018/7582730

Haouzi, D., Lekehal, M., Moreau, A., Moulis, C., Feldmann, G., Robin, M. A., et al. (2000). Cytochrome P450-generated reactive metabolites cause mitochondrial permeability transition, caspase activation, and apoptosis in rat hepatocytes. *Hepatology* 32 (2), 303–311. doi:10.1053/jhep.2000.9034

Henshall, D. C., and Simon, R. P. (2005). Epilepsy and apoptosis pathways. *J. Cereb. Blood Flow. Metab.* 25 (12), 1557–1572. doi:10.1038/sj.jcbfm.9600149

Henshall, D. C., Clark, R. S., Adelson, P. D., Chen, M., Watkins, S. C., and Simon, R. P. (2000). Alterations in bcl-2 and caspase gene family protein expression in human temporal lobe epilepsy. *Neurology* 55 (2), 250–257. doi:10.1212/wnl.55.2.250

Henshall, D. C., Araki, T., Schindler, C. K., Lan, J. Q., Tiekoter, K. L., Taki, W., et al. (2002). Activation of Bcl-2-associated death protein and counter-response of Akt within cell populations during seizure-induced neuronal death. *J. Neurosci.* 22 (19), 8458–8465. doi:10.1523/jneurosci.22-19-08458.2002

Hossain, M., Williams, S., Ferguson, L., Bingaman, W., Ghosh, A., Najm, I. M., et al. (2020). Heat shock proteins accelerate the maturation of brain endothelial cell glucocorticoid receptor in focal human drug-resistant epilepsy. *Mol. Neurobiol.* 57, 4511–4529. doi:10.1007/s12035-020-02043-9

Kincaid, B., and Bossy-Wetzel, E. (2013). Forever young: SIRT3 a shield against mitochondrial meltdown, aging, and neurodegeneration. *Front. Aging Neurosci.* 5, 48. doi:10.3389/fnagi.2013.00048

Kirkland, R. A., and Franklin, J. L. (2001). Evidence for redox regulation of cytochrome C release during programmed neuronal death: antioxidant effects of protein synthesis and caspase inhibition. *J. Neurosci.* 21 (6), 1949–1963. doi:10.1523/jneurosci.21-06-01949.2001

Kirkland, R. A., and Franklin, J. L. (2015). Bax and caspases regulate increased production of mitochondria-derived reactive species in neuronal apoptosis: LACK of A role for depletion of cytochrome c from the mitochondrial electron transport chain. *Biochem. Biophys. Rep.* 4, 158–168. doi:10.1016/j.bbrep.2015.09.004

Kwan, P., Schachter, S. C., and Brodie, M. J. (2011). Drug-resistant epilepsy. *N. Engl. J. Med.* 365 (10), 919–926. doi:10.1056/NEJMra1004418

Lin, H., Chen, X., Zhang, C., Yang, T., Deng, Z., Song, Y., et al. (2021). EF24 induces ferroptosis in osteosarcoma cells through HMOX1. *Biomed. Pharmacother.* 136, 111202. doi:10.1016/j.biopha.2020.111202

Lindenmaier, H., Becker, M., Haefeli, W. E., and Weiss, J. (2005). Interaction of progestins with the human multidrug resistance-associated protein 2 (MRP2). *Drug Metab. Dispos.* 33 (11), 1576–1579. doi:10.1124/dmd.105.005314

Mao, X. Y., Zhou, H. H., and Jin, W. L. (2019). Redox-related neuronal death and crosstalk as drug targets: Focus on epilepsy. *Front. Neurosci.* 13, 512. doi:10.3389/fnins.2019.00512

Markoula, S., Teotonio, R., Ratnaraj, N., Duncan, J. S., Sander, J. W., and Patsalos, P. N. (2014). Lacosamide serum concentrations in adult patients with epilepsy: the influence of gender, age, dose, and concomitant antiepileptic drugs. *Ther. Drug Monit.* 36 (4), 494–498. doi:10.1097/FTD.0000000000000051

McGrane, I. R., Loveland, J. G., and de Leon, J. (2018). Possible oxcarbazepine inductive effects on aripiprazole metabolism: A case report. *J. Pharm. Pract.* 31 (3), 361–363. doi:10.1177/0897190017710523

McMasters, R. A., Wilbert, T. N., Jones, K. E., Pitlyk, K., Saylors, R. L., Moyer, M. P., et al. (2000). Two-drug combinations that increase apoptosis and modulate bak and bcl-X(L) expression in human colon tumor cell lines transduced with herpes simplex virus thymidine kinase. *Cancer Gene Ther.* 7 (4), 563–573. doi:10.1038/sj.cgt.7700164

Michalak, S., Florczak-Wyspianska, J., Rybacka-Mossakowska, J., Ambrosius, W., Osztynowicz, K., Baszczuk, A., et al. (2017). Mitochondrial respiration in intact peripheral blood mononuclear cells and sirtuin 3 activity in patients with movement disorders. *Oxid. Med. Cell. Longev.* 2017, 9703574. doi:10.1155/2017/9703574

Miksys, S. L., and Tyndale, R. F. (2002). Drug-metabolizing cytochrome P450s in the brain. *J. Psychiatry Neurosci.* 27 (6), 406–415.

Niquet, J., and Wasterlain, C. G. (2004). Bim, bad, and bax: a deadly combination in epileptic seizures. *J. Clin. Invest.* 113 (7), 960–962. doi:10.1172/JCI21478

Patsalos, P. N., Froscher, W., Pisani, F., and van Rijn, C. M. (2002). The importance of drug interactions in epilepsy therapy. *Epilepsia* 43 (4), 365–385. doi:10.1046/j.1528-1157.2002.13001.x

Patsalos, P. N., and Perucca, E. (2003). Clinically important drug interaction in epilepsy: Interactions between antiepileptic drugs and other drugs. *Lacet Neurol.* 2 (8), 473–481. doi:10.1016/s1474-4422(03)00483-6

Perucca, E., and Meador, K. J. (2005). Adverse effects of antiepileptic drugs. *Acta Neurol. Scand. Suppl.* 181, 30–35. doi:10.1111/j.1600-0404.2005.00506.x

Perucca, E. (2005a). An introduction to antiepileptic drugs. *Epilepsia* 46, 31–37. doi:10.1111/j.1528-1167.2005.463007.x

Perucca, E. (2005b). Pharmacotherapy of epilepsy in women. *Zh. Nevrol. Psikhiatr. Im. S. S. Korsakova* 105 (11), 60–62.

Savran, M., Ozmen, O., Erzurumlu, Y., Savas, H. B., Asci, S., and Kaynak, M. (2019). The impact of prophylactic lacosamide on LPS-induced neuroinflammation in aged rats. *Inflammation* 42 (5), 1913–1924. doi:10.1007/s10753-019-01053-7

Shandra, A., Shandra, P., Kaschenko, O., Matagne, A., and Stohr, T. (2013). Synergism of lacosamide with established antiepileptic drugs in the 6-Hz seizure model in mice. *Epilepsia* 54 (7), 1167–1175. doi:10.1111/epi.12237

Sun, J., Xie, C., Liu, W., Lu, D., Qiao, W., Huang, Q., et al. (2012). The effects of simvastatin on hippocampal caspase-3 and Bcl-2 expression following kainate-induced seizures in rats. *Int. J. Mol. Med.* 30 (4), 739–746. doi:10.3892/ijmm.2012.1076

Sun, H., Sivasubramanian, R., Vaidya, S., Barve, A., and Jarugula, V. (2020). Drug-drug interaction studies with oral contraceptives: Pharmacokinetic/pharmacodynamic and study design considerations. *J. Clin. Pharmacol.* 60, S49–S62. doi:10.1002/jcph.1765

Toscano, E. C. B., Vieira, E. L. M., Portela, A., Reis, J. L. J., Caliari, M. V., Giannetti, A. V., et al. (2019). Bcl-2/Bax ratio increase does not prevent apoptosis of glia and granular neurons in patients with temporal lobe epilepsy. *Neuropathology* 39 (5), 348–357. doi:10.1111/neup.12592

Weir, H. J., Lane, J. D., and Balthasar, N. (2013). SIRT3: A central regulator of mitochondrial adaptation in Health and disease. *Genes Cancer* 4 (3-4), 118–124. doi:10.1177/1947601913476949

Williams, S., Hossain, M., Ferguson, L., Busch, R. M., Marchi, N., Gonzalez-Martinez, J., et al. (2019). Neurovascular drug biotransformation machinery in focal human epilepsies: brain CYP3A4 correlates with seizure frequency and antiepileptic drug therapy. *Mol. Neurobiol.* 56 (12), 8392–8407. doi:10.1007/s12035-019-01673-y

Yi, X., Guo, W., Shi, Q., Yang, Y., Zhang, W., Chen, X., et al. (2019). SIRT3-Dependent mitochondrial dynamics remodeling contributes to oxidative stress-induced melanocyte degeneration in vitiligo. *Theranostics* 9 (6), 1614–1633. doi:10.7150/thno.30398

Zaccara, G., and Perucca, E. (2014). Interactions between antiepileptic drugs, and between antiepileptic drugs and other drugs. *Epileptic Disord.* 16 (4), 409–431. doi:10.1684/epd.2014.0714

Zorova, L. D., Popkov, V. A., Plotnikov, E. Y., Silachev, D. N., Pevzner, I. B., Jankauskas, S. S., et al. (2018). Mitochondrial membrane potential. *Anal. Biochem.* 552, 50–59. doi:10.1016/j.ab.2017.07.009

frontiers | Frontiers in Pharmacology

TYPE Original Research
PUBLISHED 02 September 2022
DOI 10.3389/fphar.2022.985159

OPEN ACCESS

EDITED BY
Simona Pichini,
National Institute of Health (ISS), Italy

REVIEWED BY
Niyaz Ahmad,
Imam Abdulrahman Bin Faisal University, Saudi Arabia
Qilong Chen,
Tongji University, China

*CORRESPONDENCE
Guoxin Hu,
hgx@wmu.edu.cn
Jianping Cai,
caijp61@vip.sina.com
Bin Wu,
drwzyywb@163.com

†These authors have contributed equally to this work

SPECIALTY SECTION
This article was submitted to Drug Metabolism and Transport, a section of the journal Frontiers in Pharmacology

RECEIVED 03 July 2022
ACCEPTED 11 August 2022
PUBLISHED 02 September 2022

CITATION
Ye Z, Chen B, Gao N, Kong Q, Hu X, Lu Z, Qian J, Hu G, Cai J and Wu B (2022), CYP2D6 gene polymorphism and apatinib affect the metabolic profile of fluvoxamine.
Front. Pharmacol. 13:985159.
doi: 10.3389/fphar.2022.985159

CYP2D6 gene polymorphism and apatinib affect the metabolic profile of fluvoxamine

Zhize Ye[1†], Bingbing Chen[1†], Nanyong Gao[1], Qihui Kong[1], Xiaoqin Hu[1], Zhongqiu Lu[2], Jianchang Qian[1], Guoxin Hu[1*], Jianping Cai[1*] and Bin Wu[2*]

[1]Institute of Molecular Toxicology and Pharmacology, School of Pharmaceutical Sciences, Wenzhou Medical University, Wenzhou, China, [2]Emergency Center, The First Affiliated Hospital of Wenzhou Medical University, Wenzhou, China

This study aimed 1) to investigate the influence of CYP2D6 variants on the catalyzing of fluvoxamine, and 2) to study the interaction between fluvoxamine and apatinib. An enzymatic reaction system was setup and the kinetic profile of CYP2D6 in metabolizing fluvoxamine was determined. *In vivo*, drug-drug interaction was investigated using Sprague–Dawley (SD) rats. Fluvoxamine was given gavage with or without apatinib. Ultra-performance liquid chromatography-tandem mass spectrometry (UPLC-MS/MS) was used to determine the concentrations of fluvoxamine and desmethyl-fluvoxamine. The results demonstrated that the relative clearance rates of CYP2D6.A5V, V104A, D337G, F164L, V342M, R440C and R497C increased significantly compared with CYP2D6.1, ranging from 153.626% ± 6.718% to 394.310% ± 33.268%. The activities of other variants reduced to different extent, or even lost function, but there was no statistical difference. The IC_{50} of apatinib against fluvoxamine disposition was determined, which is 0.190 μM in RLM and 6.419 μM in HLM, respectively. *In vivo*, apatinib can enhance the plasma exposure of fluvoxamine remarkably characterized by increased AUC, Tmax and Cmax. Meanwhile, the produce of desmethyl fluvoxamine was dramatically inhibited, both AUC and C_{max} decreased significantly. Mechanistically, apatinib inhibit the generation of fluvoxamine metabolite with a mixed manner both in RLM and HLM. Furthermore, there were differences in the potency of apatinib in suppressing fluvoxamine metabolism among CYP2D6.1, 2 and 10. In conclusion, CYP2D6 gene polymorphisms and drug-drug interaction can remarkably affect the plasma exposure of fluvoxamine. The present study provides basis data for guiding individual application of fluvoxamine.

KEYWORDS

CYP2D6, fluvoxamine, apatinib, interaction, metabolism

Introduction

Fluvoxamine is commonly prescribed to treat depression and anxiety disorders with mechanism of selective inhibit serotonin reuptake (Yuan et al., 2020). Central nervous system symptoms, rash, gastrointestinal symptoms, and suicidal tendencies are common adverse reactions during medicine of fluvoxamine (Lenze et al., 2020). Its clinical efficacy is highly variable among individuals. Drug efficacy stratification may be the result of individual differences in blood concentrations which caused by genetic polymorphisms of metabolic enzymes and drug interactions. Cytochrome P450 family member 2D6 (CYP2D6) is a major enzyme involved in catalyzing metabolism of fluvoxamine, which produced desmethyl fluvoxamine (Hicks et al., 2015; Zastrozhin et al., 2021). However, there are genetic polymorphism of CYP2D6 resulting in large inter-individual variability in enzyme activity, further leading to subtherapeutic phenomena or severe adverse effects (Zastrozhin et al., 2021). Moreover, interactions between fluvoxamine and other drugs are frequently being reported. A study found one fatality in a woman who was taking clotiapine, 7-aminoclonazepam, propranolol, gabapentin and haloperidol alongside fluvoxamine developing antipsychotic malignant syndrome (Vignali et al., 2021). Interactions of fluvoxamine with antiepileptic or antidepressant drugs have also been issued (Mula and Trimble, 2003; Spina et al., 2016). Therefore, defining the correlation between CYP2D6 genotype and fluvoxamine metabolic phenotype, identifying drugs that could potential interact with fluvoxamine are helpful for personalized medicine.

Apatinib is a small molecule drug that targeting inhibition of angiogenesis (Wang N. et al., 2020). It's approved to be safe and effective after failure of standard chemotherapy in advanced gastric cancer (Geng et al., 2018). Interestingly, it is worth noting that apatinib is a pan CYP inhibitor (Zhou et al., 2014). Therefore, the research on the interaction between apatinib and other CYP substrate drugs has gradually attracted people's attention. Statistics data display that cancer patients usually complicated with various psychological symptoms, especially depression and anxiety (Wang YH. et al., 2020). This will diminish benefits of medicine and affects the quality life of patients. Therefore, the combined application of apatinib and fluvoxamine is a feasible clinical treatment option. However, the interaction between them has not been unveiled.

Herein, we evaluated the catalytic activity of CYP2D6.1 and other 23 variants on the disposition of fluvoxamine. In addition, we used microsomes and Spragge-Dawley (SD) rats to clarify the interaction between fluvoxamine and apatinib *in vitro* and *in vivo*. The results will provide fundamental data to facilitate the precision medicine application of fluvoxamine.

Materials and methods

Chemicals and reagents

Fluvoxamine maleate was bought from Shanghai Canspec Scientific & Technology Co., Ltd. Desmethyl fluvoxamine was obtained from TRC Ltd. (Toronto, Canada). Diazepam was purchased from Shanghai Xudong Haipu Pharmaceutical Co., Ltd. and used as internal standard. Apatinib was obtained from Beijing Sunflower Technology Development Co., Ltd. Sodium carboxymethyl cellulose (CMC-Na), methanol, acetonitrile (ACN) and formic acid were purchased from Merck (Darmstadt, Germany). Microsomes were purchased from Corning Life Sciences Co., Ltd. CYP2D6 and cytochrome B5 were prepared as previously issued (Cai et al., 2016).

UPLC-MS/MS and condition

A newly developed and validated UPLC-MS/MS method was used to detect fluvoxamine and desmethyl fluvoxamine. The analytes were separated on a BEH C18 column (2.1 × 100 mm, 1.7 μm; Waters Corp., Millipore, Bedford, MA, United States), which incubated at 40°C. The mobile phase was consisted of 0.1% formic acid and ACN, and elution at 0.40 ml/min for 3.0 min with a gradient condition. The program was set as 10%–90% ACN (0–1.0 min), 90%–10% ACN (1.0–2.0 min), and 10% ACN (2.1–3.0 min).

Determine enzymatic kinetic parameters of recombinant human CYP2D6 using fluvoxamine

Incubation system was dissolved in phosphate buffered saline which contained 1 pmol CYP2D6.1 or variants, 50 μg/ml cytochrome B5, 0.5–50 μM fluvoxamine. Before the reaction, the mixture was pre-incubated at 37°C for 5 min. Subsequently, add 1 mM nicotinamide adenine dinucleotide phosphate oxidase to initiate the reaction. 20 min' later, the reaction was terminated. Add acetonitrile twice volume as much as reaction system and 20 μl internal standard to the mixture. After vortexing and centrifugation, the supernatant was taken and subjected to UPLC-MS/MS.

Animal experiments

Animal ethics was reviewed and approved by Wenzhou Medical University. Male rats weighed 180–220 g were supplied by Vital River Laboratories (Beijing, China), and adaptive feeding for a week. SD rats were divided into two groups. Group A served as control, dosing of vehicle (0.5%

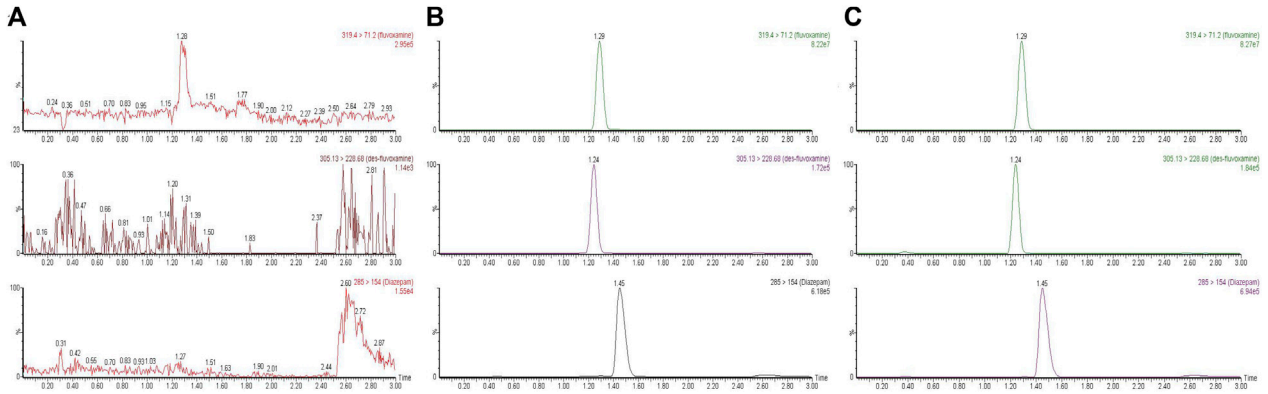

FIGURE 1
Representative chromatograms of fluvoxamine, desmethyl fluvoxamine and IS. **(A)** a blank plasma sample. **(B)** A blank plasma sample spiked with fluvoxamine, desmethyl Fluvoxamine and IS. **(C)** Rat's plasma sample after dosing.

CMC-Na). Group B was administrated 40 mg/kg apatinib. 30 min' later, fluvoxamine (10 mg/kg) was given orally to the rats. Then, the vein blood was collected at 0, 0.25, 0.5, 1, 2, 3, 4, 5, 6, 8, 10, 12, and 24 h after administration. The sample was prepared and subjected to UPLC-MS/MS examination.

Microsomes incubation assay

The microsomes reaction system was set up as indicated in above. In briefly, the reaction was carried out in PBS. The buffer was consisted of 0.2 mg/ml RLM or HLM, 0.5–50 μM fluvoxamine. NADPH was used to initiate the reaction. To determine the half maximal inhibitory concentration (IC_{50}), the concentration of apatinib was set at 0.01, 0.1, 1, 10, 25, 50, and 100 μM. To determine the mechanism underlied the inhibition, the concentration of fluvoxamine was set according to the K_m value, while the concentration of apatinib was set at 0, 0.25, 0.5, 1 μM according to the IC_{50} as well. After incubation, the samples were prepared and determined by UPLC-MS/MS.

Statistical analysis

Lineweaver-Burk double reciprocal plot was performed on GraphPad Prism 5.0 software. The kinetic parameters were obtained using non-compartmental model fitting by Drug and statistics (DAS) software 3.0. The corresponding drug-time curves were drawn by Origin 8.0. All data are expressed as Mean ± SD. Statistical analysis was performed by independent samples *t*-test using GraphPad Prism 5.0 software. $p < 0.05$ indicates a significant difference.

Results

Development of UPLC-MS/MS assay to determine fluvoxamine and desmethyl fluvoxamine

To detect the analytes, a UPLC-MS/MS method was developed and validated. The linear range, precision, accuracy, recovery, matrix effect and stability were evaluated. The detail data was presented in the Supplementary Information. In briefly, the monitoring transitions of diazepam, fluvoxamine and desmethyl fluvoxamine were m/z 285→ 154, m/z 319.4→ 71.2 and m/z 305.13→ 228.68, respectively. As Figure 1 showed, there was no obvious endogenous interference. The retention time of diazepam, fluvoxamine and desmethyl fluvoxamine were 1.45, 1.29 and 1.24 min, accordingly.

Kinetic characterization of recombinant human CYP2D6 in catalyzing of fluvoxamine

Michaelis curves and kinetic parameters of CYP2D6.1 and other variants in metabolizing fluvoxamine were shown in Figure 2 and Table 1, respectively. Based on maximum reaction velocity (V_{max}), they can be divided into four groups. No significant differences were observed between CYP2D6.1 and CYP2D.2, V104, 90, C161S, D337G, E215K, R497C. Among them, CYP2D6.92 and 96 almost lost enzymatic function. Moreover, the V_{max} of CYP2D6.A5V, 89 and 95 increased remarkably, ranging from 270.31% to 441.17%. In opposite, the remaining variants decreased significantly, ranging from 9.93% to 39.25%. From the michaelis constant (K_m), a lot of

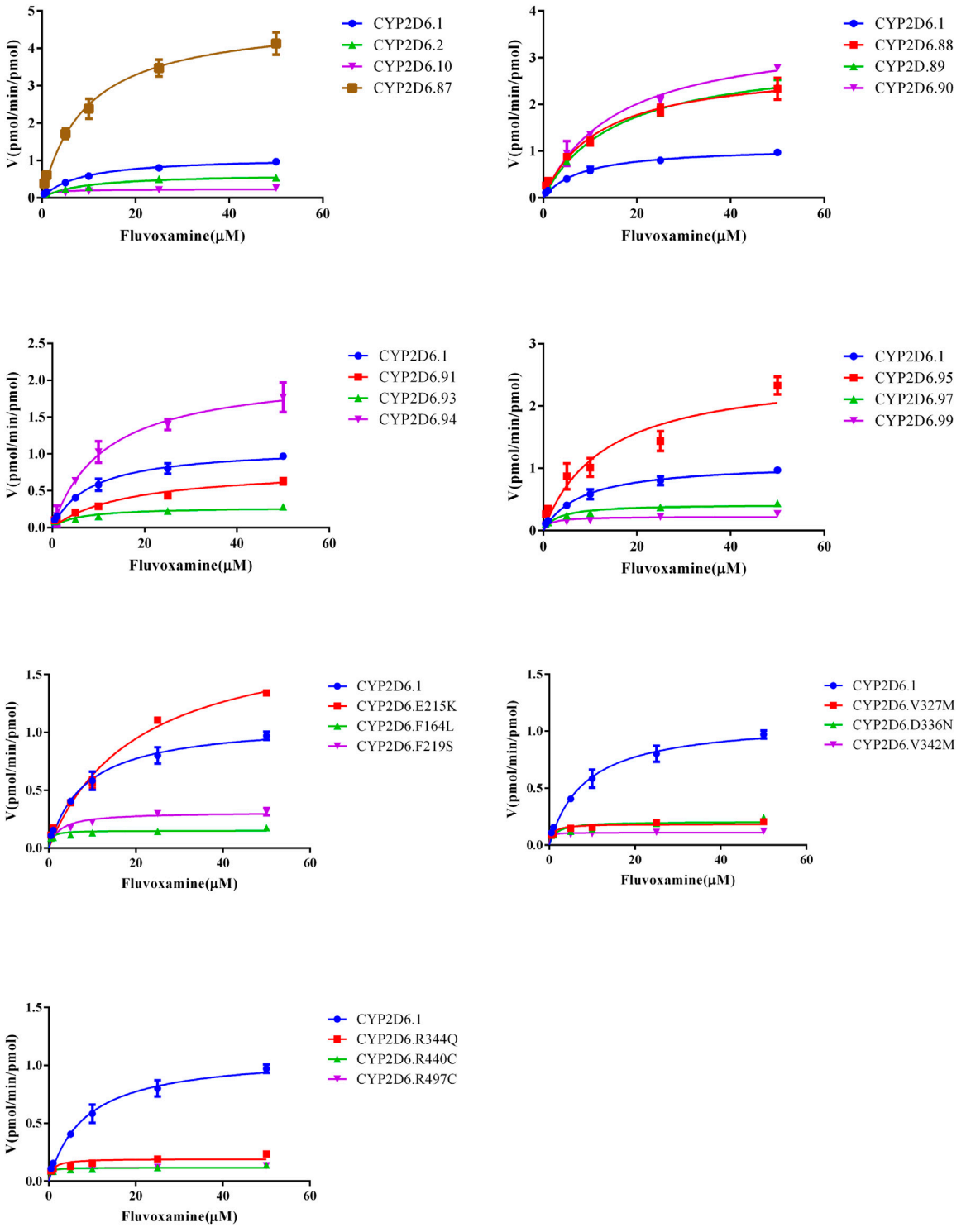

FIGURE 2
Michaelis–Menten curves of CYP2D6 in disposition of fluvoxamine. The reaction was performed as indicated in the section of method, $n = 3$.

them decreased obviously compared with CYP2D6.1, including CYP2D6.10, 97, R88P, F164L, F219S, V327M, D336N, V342M, R344Q, R440C, R497C. Besides, the other variants had no significant difference. Finally, the intrinsic clearance (Clint) and relative clearance were determined. In all, activities of seven variants, involving CYP2D6.A5V, V104A, D337G,

TABLE 1 Kinetic parameters of fluvoxamine catalyzing in CYP2D6.

CYP	V_{max} (pmol/min/pmol)	K_m (pmol)	CL (μL/min/pmol)	%
2D6.1	1.098 ± 0.015	8.415 ± 0.797	0.131 ± 0.012	100.00 ± 9.27
2D6.2	0.652 ± 0.093	9.636 ± 4.023	0.073 ± 0.018	55.254 ± 13.364
2D6.10	0.233 ± 0.001*	1.751 ± 0.169*	0.134 ± 0.013	101.865 ± 9.613
2D6.A5V	4.844 ± 0.434*	9.438 ± 1.358	0.516 ± 0.034*	393.295 ± 25.911*
2D6.V104A	2.879 ± 0.237	12.523 ± 1.792	0.231 ± 0.015*	176.140 ± 11.160*
2D6.89	3.096 ± 0.223*	15.627 ± 1.793	0.199 ± 0.011	151.434 ± 8.154
2D6.90	3.627 ± 0.433	16.373 ± 5.954	0.236 ± 0.059	179.493 ± 45.215
2D6.C161S	0.816 ± 0.110	16.233 ± 2.404	0.050 ± 0.001	38.336 ± 0.864
2D6.92	N.D.	N.D.	N.D.	N.D.
2D6.93	0.259 ± 0.002*	4.058 ± 0.369	0.064 ± 0.006	48.790 ± 4.378
2D6.D337G	2.142 ± 0.187	10.645 ± 1.196	0.202 ± 0.009*	153.626 ± 6.718*
2D6.R388H	2.968 ± 0.109*	18.053 ± 2.090	0.166 ± 0.015	126.083 ± 11.685
2D6.96	N.D.	N.D.	N.D.	N.D.
2D6.97	0.431 ± 0.007*	3.483 ± 0.652*	0.127 ± 0.024	96.463 ± 18.420
2D6. R88P	0.234 ± 0.001*	1.791 ± 0.230*	0.132 ± 0.018	100.802 ± 13.791
2D6.F164L	0.147 ± 0.008*	0.514 ± 0.053*	0.287 ± 0.016*	218.589 ± 12.179*
2D6.E215K	1.723 ± 0.219	17.960 ± 3.975	0.098 ± 0.012	74.351 ± 9.147
2D6.F219S	0.349 ± 0.008*	3.749 ± 0.245*	0.093 ± 0.008	71.168 ± 5.992
2D6.V327M	0.199 ± 0.020*	0.981 ± 0.222*	0.207 ± 0.028	157.504 ± 21.434
2D6.D336N	0.202 ± 0.006*	1.532 ± 0.215*	0.134 ± 0.017	101.831 ± 12.972
2D6.V342M	0.109 ± 0.002*	0.212 ± 0.022*	0.518 ± 0.044*	394.310 ± 33.268*
2D6.R344Q	0.203 ± 0.002*	1.270 ± 0.194*	0.162 ± 0.024	123.621 ± 18.515
2D6.R440C	0.117 ± 0.001*	0.282 ± 0.013*	0.416 ± 0.018*	317.234 ± 14.091*
2D6.R497C	0.116 ± 0.0018	0.266 ± 0.014*	0.436 ± 0.021*	331.993 ± 15.802*

N = 3, variants vs. CYP2D6.1.
*$p < 0.05$.

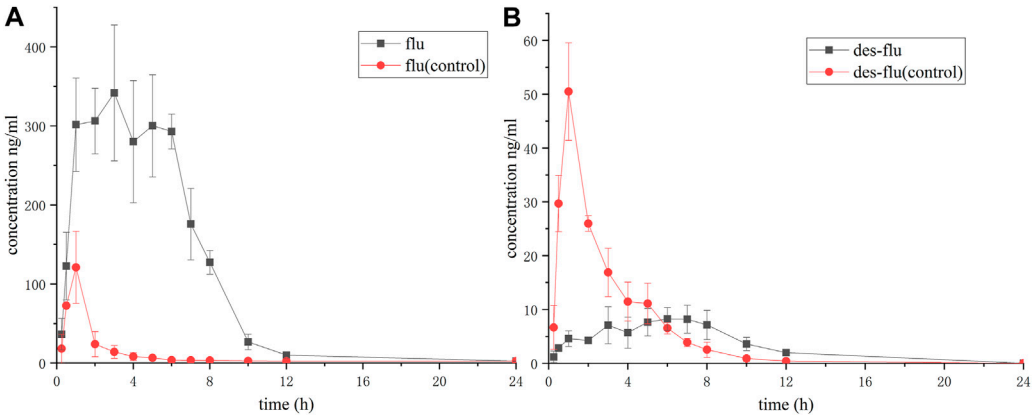

FIGURE 3
Concentration-time curve of fluvoxamine and its metabolite. The rats were administrated with fluvoxamine via gavage. As follows, the tail vein blood was collected, and was subjected to UPLC-MS/MS assay. **(A)** Desmethyl fluvoxamine, **(B)** Fluvoxamine. The curve was plotted using Prism 5, n = 6.

TABLE 2 Pharmacokinetic parameters of desmethyl fluvoxamine.

Pharmacokinetic parameters	Unit	Group B	Group A
AUC(0-t)	μg/L*h	80.103 ± 18.294	113.125 ± 37.015
AUC(0-∞)	μg/L*h	80.178 ± 18.307	113.246 ± 37.062
MRT (0-t)	h	6.781 ± 1.005*	3.446 ± 0.578
MRT (0-∞)	h	6.8 ± 1.01*	3.473 ± 0.578
t1/2z	h	1.9 ± 0.224	2.525 ± 0.793
T_{max}	h	5.333 ± 2.251*	1.803 ± 0.492
CLz/F	L/h/kg	131.088 ± 34.451	99.297 ± 41.451
Vz/F	L/kg	356.789 ± 85.786	358.178 ± 217.799
C_{max}	μg/L	10.665 ± 3.71*	34.263 ± 19.449

AUC, area under curve; MRT, mean retention time; $t_{1/2z}$, elimination half time; T_{max}, peak time; Vz/F, apparent volume of distribution; CLz/F, blood clearance; C_{max}, maximum blood concentration. Group B vs. Group A.
*$p < 0.05$, $n = 6$.

TABLE 3 Pharmacokinetic parameters of fluvoxamine.

Pharmacokinetic parameters	Unit	Group B	Group A
$AUC_{(0-t)}$	μg/L*h	1,723.097 ± 602.157*	180.900 ± 100.454
$AUC_{(0-\infty)}$	μg/L*h	1,724.820 ± 600.410*	456.181 ± 163.803
$MRT_{(0-t)}$	h	5.191 ± 0.673	6.095 ± 2.380
$MRT_{(0-\infty)}$	h	5.225 ± 0.659*	92.049 ± 44.632
$t_{1/2\ z}$	h	1.637 ± 0.961*	2.145 ± 37.094
T_{max}	h	4.000 ± 1.549*	0.833 ± 0.258
CLz/F	L/h/kg	6.396 ± 2.110*	24.166 ± 7.713
Vz/F	L/kg	16.228 ± 13.475*	2,618.204 ± 879.13
C_{max}	μg/L	274.989 ± 100.275*	70.595 ± 62.901

Group B vs. Group A.
*$p < 0.05$, $n = 6$.

F164L, V342M, R440C, R497C, increased compared with CYP2D6.1, ranging from 153.63% to 394.31%. The others' The remaining variants showed no statistical difference in intrinsic clearance. In addition, CYP2D6.92 and 96 had no significant activity. The rest of the variants had different effect of reduced metabolic activity.

Effects of apatinib on fluvoxamine metabolism in rats

As Figure 3A showed, when co-administration of fluvoxamine with apatinib, the production of desmethyl fluvoxamine was inhibited dramatically. The peak of the Y-axis of the time-concentration curve decreased, and the curve shifted to the right with significantly enhanced in T_{max}. The AUC, $t_{1/2}$, and C_{max} reduced, but no significant difference was found, Table 2. Accordingly, the concentration of fluvoxamine increased remarkably after combination, Figure 3B. The $AUC_{(0-t)}$, $AUC_{(0-\infty)}$ and C_{max} values of fluvoxamine increased by 8.52-, 2.78-, 2.90-time, respectively. In addition, T_{max} is prolonged by 3.80 times, CLz/F is reduced by about one time, and $t_{1/2z}$ is reduced by nearly one time, Table 3.

The effect of apatinib on fluvoxamine metabolism *in vitro*

To study the mechanism underlied drug-drug interaction, the enzymatic reaction was performed using RLM, HLM. As shown in Figure 4, the K_m of fluvoxamine metabolizing was 4.738 μM in RLM and 13.54 μM in HLM. To evaluate the inhibitory potency, the IC_{50} was determined. Fluvoxamine was dose-dependently inhibited by apatinib in RLM with IC_{50} of 0.19 μM, Figure 5A. In HLM, it's 6.419 μM, Figure 5A. Mechanistically, apatinib inhibited fluvoxamine metabolism with a mixed manner in the RLM. The Ki is 0.05 μM, Figure 5B. Meanwhile, it is the same in HLM with Ki of 2.23 μM, Figure 5C. To further investigate differences in inhibitory activity among different CYP2D6 variants, IC_{50} was

determined using CYP2D6.1, CYP2D6.2 and CYP2D6.10. It's 17.58, 14.46 and 3.673 μM accordingly, Figure 6A. The relative metabolic rates of fluvoxamine were 44.32%, 54.03%, and 57.69%, respectively.

Discussion

CYP2D6 accounts for about 2% of total CYP abundance in liver, and catalyzing metabolism of 20%–30% therapeutic drugs (Zhou et al., 2016; Taylor et al., 2020). To date, 149 CYP2D6 alleles have been reported (LLerena et al., 2014). However, the activities of a vast majority of variants are still unclear. Therefore, elucidating the effect of mutation on enzyme activity will help to understand the metabolic characteristics of CYP2D6 substrate drugs. Moreover, it will provide the basic data for precise medicine.

Fluvoxamine is almost completely absorbed through the gastrointestinal tract, and is mainly metabolized into desmethyl fluvoxamine in the liver through CYP2D6 and CYP1A2 pathway (van Harten, 1995). Interestingly, CYP2D6 is rarely being induced, but has abundance gene polymorphism. Therefore, genetic polymorphisms of CYP2D6 are likely to cause differences in plasma exposure of fluvoxamine. This study demonstrated that CYP2D6.A5V, V104A, D337G, F164L, V342M, R440C, R497C showed higher catalytic activity compared with CYP2D6.1. The patients carry these mutations would probably be sub-therapied. In contrast, *CYP2D6*92* and **96* almost lost function in catalyzing fluvoxamine. *CYP2D6*10* is predominantly distributed in East-Asia (Lin et al., 2016). It has been reported that its activity is significantly reduced. In the present study, we found that the V_{max} of CYP2D6 decreased, the K_m was also decreased accordingly. Therefore, the relative clearance is nearly the equal to CYP2D6.1. We think CYP2D6 has a certain selectivity for substrate drugs (Ingelman-Sundberg, 2005). The structure of the compound and the affinity of compound to the enzyme determine the characteristics of reaction (Zhou et al., 2009). However, these speculations require further study. Taken together, our data suggest that CYP2D6 gene polymorphisms indeed have varying degrees of impact on fluvoxamine metabolism.

Due to the existence of various complications, cancer patients usually take multiple drugs in combination, which can easily lead to drug-drug interaction (Flepisi et al., 2014; Moghaddas et al., 2021). Identifying potential drug interactions will help guide rational drug use and improve patients' quality of life. Anxiety is a common complication in cancer patients (Kapfhammer, 2015). Therefore, combining apatinib with fluvoxamine is an effective dosing strategy. Many studies had shown that apatinib interacts with antipsychotics like buspirone and venlafaxine (Bao et al., 2018; Zhang et al., 2020). In this study, the data demonstrated that it can also inhibit the metabolizing of fluvoxamine via suppression the activities of microsomes system, especially CYP2D6. This inhibitory effect was similar even with different CYP2D6 alleles. Although this study preliminarily demonstrated differences in the rates of mutants metabolizing fluvoxamine through *in vitro* experiments, the affinity of the substrate to the enzyme was not determined, as well as *in vivo* experiments. Therefore, further data cannot be used to explain the *in vivo* situation, which has certain limitations in guiding clinical drug treatment. Since fluvoxamine and apatinib may be used clinically in combination, in this study we combined *in vivo* and *in vitro* experiments to demonstrate the interaction between fluvoxamine and apatinib. At the same time, the relevant experiments of HLM *in vitro* confirmed that apatinib may have a certain inhibitory effect on fluvoxamine in humans. In all, the present study provides basic data for the clinical application of fluvoxamine, especially in cancer

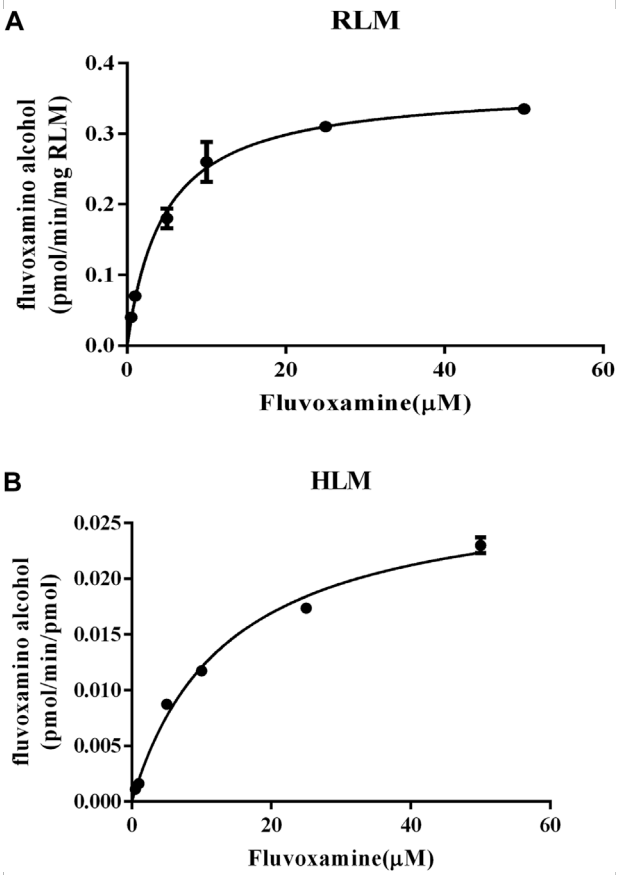

FIGURE 4
Michaelis–Menten curves of fluvoxamine metabolism in microsomes. **(A)** RLM. **(B)** HLM. *n* = 3.

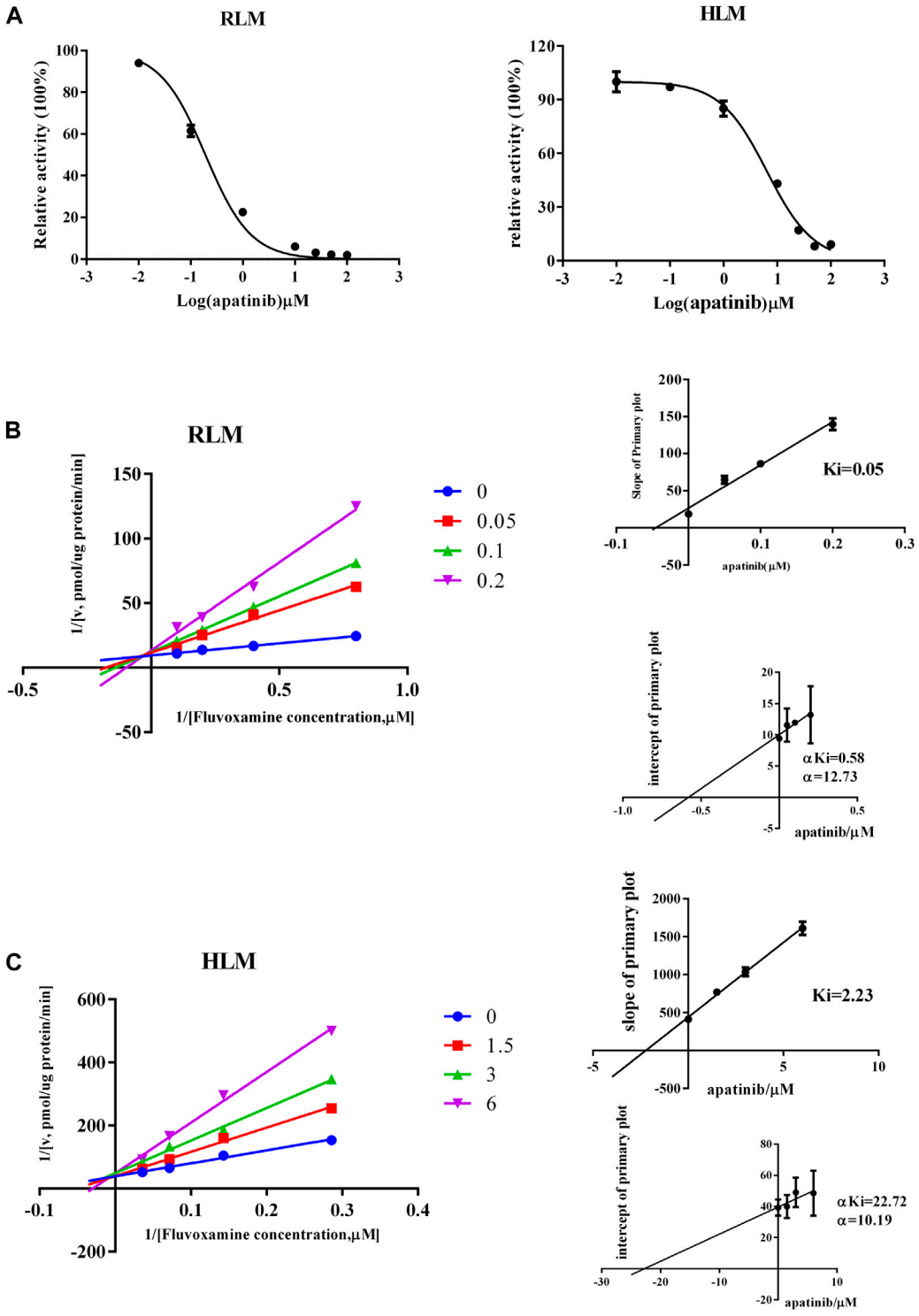

FIGURE 5
Apatinib inhibited the metabolism of fluvoxamine with a mixed mechanism both in RLM and HLM. **(A)** The effect of apatinib on inhibiting fluvoxamine metabolism. **(B,C)** Lineweaver-Burk plot and the secondary plot for Ki in the inhibition of fluvoxamine catalyzing, n = 3.

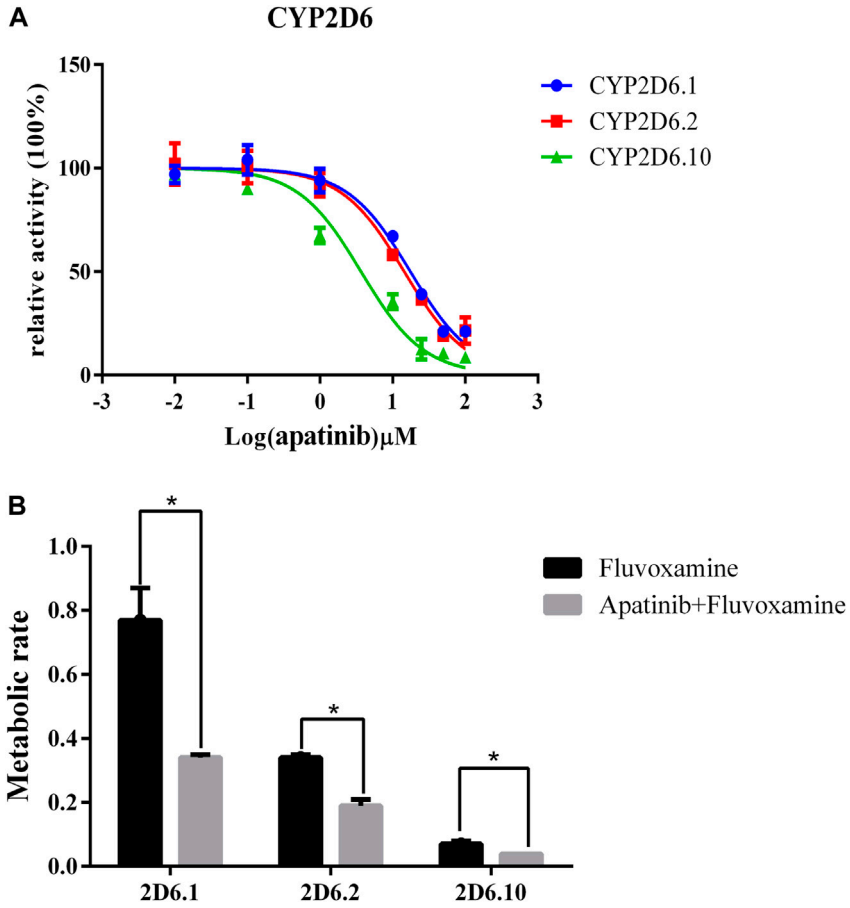

FIGURE 6
The different effect of apatinib on fluvoxamine metabolism in three CYP2D6 variants. **(A)** The catalytic profile of fluvoxamine in CYP2D6.1, 2 and 10. **(B)** The effect of apatinib on the metabolic rate of fluvoxamine in CYP2D6.1, 2, and 10, $n = 3$, $^*p < 0.05$.

patients. This prescription needs to be vigilant and prevent the occurrence of adverse reactions. Although prolonging lifespan is the primary goal for cancer patients, maximizing the quality of life is an urgent clinical problem, and this study provides limited data support for this goal.

Data availability statement

The original contributions presented in the study are included in the article/Supplementary Material, further inquiries can be directed to the corresponding authors.

Ethics statement

The animal study was reviewed and approved by Ethics Committee of Wenzhou Medical University.

Author contributions

GH, JC, ZL, and BW contributed to the literature search and study design. BC, JQ, and ZY participated in drafting of the article. ZY, QK, XH, and NG carried out the experiments and analysis. GH and JQ revised the manuscript. All authors contributed to data analysis, drafting, or revising the article; agreed on the journal to which the article will be submitted; and have agreed to be accountable for all aspects of the work.

Funding

This work was supported by the Natural Science Foundation of Zhejiang Province (LGF20H310001), the National Key Research and Development Program of China (2020YFC2008301), and the National Natural Science Foundation of China (81973397).

Conflict of interest

The authors declare that the research was conducted in the absence of any commercial or financial relationships that could be construed as a potential conflict of interest.

Publisher's note

All claims expressed in this article are solely those of the authors and do not necessarily represent those of their affiliated organizations, or those of the publisher, the editors and the reviewers. Any product that may be evaluated in this article, or claim that may be made by its manufacturer, is not guaranteed or endorsed by the publisher.

Supplementary material

The Supplementary Material for this article can be found online at: https://www.frontiersin.org/articles/10.3389/fphar.2022.985159/full#supplementary-material

References

Bao, S. S., Wen, J., Lin, Q. M., Li, Y. H., Huang, Y. G., Zhou, H. Y., et al. (2018). Evaluation of the effects of apatinib on the pharmacokinetics of venlafaxine and O-desmethylvenlafaxine in SD male rats by UPLC-MS/MS. *Basic Clin. Pharmacol. Toxicol.* 123, 721–726. doi:10.1111/bcpt.13081

Cai, J., Dai, D. P., Geng, P. W., Wang, S. H., Wang, H., Zhan, Y. Y., et al. (2016). Effects of 22 novel CYP2D6 variants found in the Chinese population on the bufuralol and dextromethorphan metabolisms *in vitro*. *Basic Clin. Pharmacol. Toxicol.* 118, 190–199. doi:10.1111/bcpt.12478

Flepisi, B. T., Bouic, P., Sissolak, G., and Rosenkranz, B. (2014). Drug-drug interactions in HIV positive cancer patients. *Biomed. Pharmacother. = Biomedecine Pharmacother.* 68, 665–677. doi:10.1016/j.biopha.2014.04.010

Geng, R., Song, L., Li, J., and Zhao, L. (2018). The safety of apatinib for the treatment of gastric cancer. *Expert Opin. Drug Saf.* 17, 1145–1150. doi:10.1080/14740338.2018.1535592

Hicks, J. K., Bishop, J. R., Sangkuhl, K., Müller, D. J., Ji, Y., Leckband, S. G., et al. (2015). Clinical pharmacogenetics implementation consortium (CPIC) guideline for CYP2D6 and CYP2C19 genotypes and dosing of selective serotonin reuptake inhibitors. *Clin. Pharmacol. Ther.* 98, 127–134. doi:10.1002/cpt.147

Ingelman-Sundberg, M. (2005). Genetic polymorphisms of cytochrome P450 2D6 (CYP2D6): Clinical consequences, evolutionary aspects and functional diversity. *Pharmacogenomics J.* 5, 6–13. doi:10.1038/sj.tpj.6500285

Kapfhammer, H. P. (2015). Comorbid depressive and anxiety disorders in patients with cancer. *Nervenarzt* 86 (294-298), 291300–292291. doi:10.1007/s00115-014-4156-x

Lenze, E. J., Mattar, C., Zorumski, C. F., Stevens, A., Schweiger, J., Nicol, G. E., et al. (2020). Fluvoxamine vs placebo and clinical deterioration in outpatients with symptomatic COVID-19: A randomized clinical trial. *Jama* 324, 2292–2300. doi:10.1001/jama.2020.22760

Lin, G., Zhang, K., Yi, L., Han, Y., Xie, J., and Li, J. (2016). National prociency testing result of CYP2D6*10 genotyping for adjuvant tamoxifen therapy in China. *PloS one* 11, e0162361. doi:10.1371/journal.pone.0162361

LLerena, A., Naranjo, M. E., Rodrigues-Soares, F., Penas, L. E. M., Fariñas, H., and Tarazona-Santos, E. (2014). Interethnic variability of CYP2D6 alleles and of predicted and measured metabolic phenotypes across world populations. *Expert Opin. Drug Metab. Toxicol.* 10, 1569–1583. doi:10.1517/17425255.2014.964204

Moghaddas, A., Adib-Majlesi, M., Sabzghabaee, A. M., Hajigholami, A., and Riechelmann, R. (2021). Potential drug-drug interactions in hospitalized cancer patients: A report from the middle-east. *J. Oncol. Pharm. Pract.* 27, 46–53. doi:10.1177/1078155220910209

Mula, M., and Trimble, M. R. (2003). Pharmacokinetic interactions between antiepileptic and antidepressant drugs. *World J. Biol. Psychiatry* 4, 21–24. doi:10.3109/15622970309167906

Spina, E., Pisani, F., and de Leon, J. (2016). Clinically significant pharmacokinetic drug interactions of antiepileptic drugs with new antidepressants and new antipsychotics. *Pharmacol. Res.* 106, 72–86. doi:10.1016/j.phrs.2016.02.014

Taylor, C., Crosby, I., Yip, V., Maguire, P., Pirmohamed, M., and Turner, R. M. (2020). A review of the important role of CYP2D6 in pharmacogenomics. *Genes (Basel)* 11, E1295. doi:10.3390/genes11111295

van Harten, J. (1995). Overview of the pharmacokinetics of fluvoxamine. *Clin. Pharmacokinet.* 29 (1), 1–9. doi:10.2165/00003088-199500291-00003

Vignali, C., Moretti, M., Quaiotti, J., Freni, F., Tajana, L., Osculati, A. M. M., et al. (2021). Distribution of fluvoxamine and identification of the main metabolite in a fatal intoxication. *J. Anal. Toxicol.* 45, e1–e5. doi:10.1093/jat/bkaa084

Wang, N., Chen, S., Liu, D., Guo, J., Sun, Y., Zhang, J., et al. (2020a). Therapeutic effect of small molecule targeting drug apatinib on gastric cancer and its role in prognosis and anti-infection mechanism. *Saudi J. Biol. Sci.* 27, 606–610. doi:10.1016/j.sjbs.2019.11.036

Wang, Y. H., Li, J. Q., Shi, J. F., Que, J. Y., Liu, J. J., Lappin, J. M., et al. (2020b). Depression and anxiety in relation to cancer incidence and mortality: A systematic review and meta-analysis of cohort studies. *Mol. Psychiatry* 25, 1487–1499. doi:10.1038/s41380-019-0595-x

Yuan, Z., Chen, Z., Xue, M., Zhang, J., and Leng, L. (2020). Application of antidepressants in depression: A systematic review and meta-analysis. *J. Clin. Neurosci.* 80, 169–181. doi:10.1016/j.jocn.2020.08.013

Zastrozhin, M., Skryabin, V., Smirnov, V., Zastrozhina, A., Grishina, E., Ryzhikova, K., et al. (2021). Effect of genetic polymorphism of the CYP2D6 gene on the efficacy and safety of fluvoxamine in major depressive disorder. *Am. J. Ther.* 29, e26–e33. doi:10.1097/MJT.0000000000001388

Zhang, X. D., Li, Y. H., Chen, D. X., You, W. W., Hu, X. X., Chen, B. B., et al. (2020). The effect of apatinib on pharmacokinetic profile of buspirone both *in vivo* and *in vitro*. *J. Pharm. Pharmacol.* 72, 1405–1411. doi:10.1111/jphp.13320

Zhou, H. Y., Gu, E. M., Chen, Q. L., Zhan, Y. Y., Wang, S. H., Liang, B. Q., et al. (2016). Effects of 22 CYP2D6 genetic variations newly identified in Chinese population on olanzapine metabolism *in vitro*. *Pharmacology* 98, 124–133. doi:10.1159/000446807

Zhou, S. F., Liu, J. P., and Chowbay, B. (2009). Polymorphism of human cytochrome P450 enzymes and its clinical impact. *Drug Metab. Rev.* 41, 89–295. doi:10.1080/03602530902843483

Zhou, Y., Wang, S., Ding, T., Chen, M., Wang, L., Wu, M., et al. (2014). Evaluation of the effect of apatinib (YN968D1) on cytochrome P450 enzymes with cocktail probe drugs in rats by UPLC-MS/MS. *J. Chromatogr. B Anal. Technol. Biomed. Life Sci.* 973c, 68–75. doi:10.1016/j.jchromb.2014.10.013

frontiers | Frontiers in Pharmacology

TYPE Original Research
PUBLISHED 07 September 2022
DOI 10.3389/fphar.2022.962731

OPEN ACCESS

EDITED BY
Simona Pichini,
National Institute of Health (ISS), Italy

REVIEWED BY
Ignacio Segarra,
Catholic University San Antonio of Murcia, Spain
Juzaili Azizi,
Universiti Sains Malaysia (USM), Malaysia
Li Zhiling,
Shanghai Jiao Tong University, China

*CORRESPONDENCE
Huadong Deng,
402571598@qq.com
Yongquan Zheng,
5515058@zju.edu.cn

†These authors have contributed equally to this work

SPECIALTY SECTION
This article was submitted to Drug Metabolism and Transport, a section of the journal Frontiers in Pharmacology

RECEIVED 06 June 2022
ACCEPTED 25 July 2022
PUBLISHED 07 September 2022

CITATION
Wang L, Wu F, Xu J, Wang Y, Fei W, Jiang H, Geng P, Zhou Q, Wang S, Zheng Y and Deng H (2022), Differential effects of ketoconazole, fluconazole, and itraconazole on the pharmacokinetics of pyrotinib in vitro and in vivo.
Front. Pharmacol. 13:962731.
doi: 10.3389/fphar.2022.962731

Differential effects of ketoconazole, fluconazole, and itraconazole on the pharmacokinetics of pyrotinib *in vitro* and *in vivo*

Li Wang[1†], Fan Wu[2†], Jia Xu[3†], Yu Wang[3], Weidong Fei[1], Hui Jiang[3], Peiwu Geng[3], Quan Zhou[3], Shuanghu Wang[3], Yongquan Zheng[1*] and Huadong Deng[4*]

[1]Department of Pharmacy, Women's Hospital, Zhejiang University School of Medicine, Hangzhou, China, [2]Department of Pharmacy, The First Affiliated Hospital of Zhejiang Chinese Medical University, Hangzhou, China, [3]The Laboratory of Clinical Pharmacy, The Sixth Affiliated Hospital of Wenzhou Medical University, Lishui People's Hospital, Lishui, China, [4]Department of Ultrasonography, The Sixth Affiliated Hospital of Wenzhou Medical University, Lishui People's Hospital, Lishui, China

It has been reported that drug-drug interactions (DDIs) can affect the pharmacokinetics and pharmacodynamics of various oral drugs. To better understand the effects of azole antifungal drugs (ketoconazole, fluconazole, and itraconazole) on pyrotinib's pharmacokinetics, DDIs between pyrotinib and three azoles were studied with Sprague-Dawley (SD) rat liver microsomes *in vitro*. Additionally, *in vivo* pyrotinib metabolic experiment was also performed. Twenty-four male SD rats were randomly divided into four groups: the ketoconazole (40 mg/kg), fluconazole (40 mg/kg), itraconazole (40 mg/kg), and the control group. UPLC-MS/MS was used for the determination of Pyrotinib's plasma concentration in rats. *In vitro* experiments showed that IC_{50} values of ketoconazole, fluconazole and itraconazole were 0.06, 11.55, and 0.27 μM, respectively, indicating that these drugs might reduce the clearance rate of pyrotinib at different degrees. In rat studies, coadministration of pyrotinib with ketoconazole or fluconazole could dramatically increase the C_{max} and $AUC_{(0-t)}$ values and decrease the clearance rate of pyrotinib, especially for ketoconazole. However, coadministration with itraconazole had no impact on the pharmacokinetic characters of pyrotinib. These data indicated that ketoconazole and fluconazole could significantly decrease the metabolism of pyrotinib both *in vitro* and *in vivo*. More attentions should be paid when pyrotinib is combined with azole antifungal drugs in clinic although further investigation is still required in future.

KEYWORDS

pyrotinib, drug-drug interaction, metabolism, pharmacokinetics, CYP3A4, azole antifungal

1 Introduction

Pyrotinib is a potent epidermal growth factor receptor/human epidermal growth factor receptor 2 (EGFR/HER2) inhibitor and can be used to treat HER2-positive breast cancer (Li et al., 2017; Blair, 2018; Huang et al., 2020). Pyrotinib gained its first global conditional authorization in August 2018 in China because of the promising outcome of a phase II trial for use with capecitabine in patients who had previously received anthracycline or taxane chemotherapy for HER2-positive or metastatic breast cancer (MBC) (Blair, 2018). It has been reported that combination of pyrotinib with palbociclib, a CDK4/6 inhibitor, could inhibit the reproductive capacity of several HER2-positive BC human cell lines (Zhang et al., 2019; Iancu et al., 2022). In one human study, pyrotinib was well-tolerated and showed promising efficacy in HER2-positive patients with metastatic breast cancer (Ma et al., 2017).

Pyrotinib's pharmacokinetic (PK) characters have been previously investigated in many studies (Zhu et al., 2016; Meng et al., 2019). It was reported that the time required to attain maximum plasma concentration (T_{max}) following the initial dose of 80–400 mg pyrotinib was 3–5 h, and the mean terminal half-life ($t_{1/2}$) was 11.4–15.9 h. The maximum concentration (C_{max}) and area under the concentration-time curve in steady state (AUCss) of pyrotinib were shown to have a linear PK profile (Ma et al., 2017). It has been reported that pyrotinib is largely metabolized by cytochrome P450 3A4 (CYP3A4) and is primarily eliminated in the feces. SHR150980 (O-depicolyl pyrotinib, M1), SHR151468 (O-depicolyl and pyrrolidine lactam pyrotinib, M2), and SHR151136 (pyrrolidine lactam pyrotinib, M5) were the primary metabolites for pyrotinib and M1 was the major metabolite in human body (Wen et al., 2021). CYP3A4 belongs to the CYP isoform family, one major monooxygenase superfamily, that is, responsible for the drug metabolism. CYP3A4 mediates the metabolism of 45%–60% of currently prescribed medicines, and many inhibitors and activators can alter the drug metabolic activity of CYP3A4 toward specific substrates (Lv et al., 2018). Therefore, the coadministration of pyrotinib with drugs that can modulate CYP3A4 enzyme activity may alter pyrotinib's exposure time in human body.

Azoles are substrates of cytochrome P450 (CYP) isoenzyme and are also regarded as the typical inhibitors for CYPs that play an important role in various drug-drug interactions (DDIs) (Bellmann and Smuszkiewicz, 2017). Previous PK studies also suggested that phase 1 and 2 biotransformation enzymes, including transporter proteins, play an important role in azole-related drug interactions (Nivoix et al., 2009). Ketoconazole, fluconazole, and itraconazole are the most commonly used azole medications to treat fungal infections in cancer patients (Parasrampuria et al., 2016). These drugs are also reported to be the powerful CYP3A4 and P-gp inhibitors that could inhibit several substrates of other tyrosine kinase inhibitors, including apatinib and sunitinib (Lou et al., 2019; Wang et al., 2021). It was reported that itraconazole could increase pyrotinib's plasma concentration in healthy Chinese individuals (Liu et al., 2021). However, no data have been reported on the effects of ketoconazole and fluconazole on pyrotinib's PK parameters, and additional experimental studies should be performed to evaluate the potential DDIs between azole drugs and pyrotinib. The aim of this study was to investigate the interactions between the three azoles and pyrotinib both *in vitro* and *in vivo*. We forecast that the results may be helpful for the clinical safety evaluation of interactions between pyrotinib and three azole antifungal drugs.

2 Materials and methods

2.1 Chemicals and reagents

Ketoconazole, fluconazole, and itraconazole were obtained from Melone Biotechnology Co. Ltd. (Beijing, China). Pyrotinib and its metabolite, pyrotinib M1 (purity >98%), were obtained from Guangzhou Zero One Biological Technology Co., Ltd. (Guangzhou, China). Midazolam [used as an internal standard (IS)] was obtained from Jiangsu Nhwa Pharmaceutical Co., Ltd. (Jiangsu, China). Formic acid (gradient grade for liquid chromatography) was obtained from Sigma-Aldrich. Methanol (MeOH) and acetonitrile (ACN) (gradient grade for liquid chromatography) were obtained from Merck (Billerica, MA, United States). Purified water was produced by the Milli-Q Plus filtration system (Millipore, Billerica, MA, United States). The coenzyme NADPH was obtained from Roche Diagnostics GmbH (Mannheim, Germany).

2.2 Preparation of rat liver microsomes

The rats were anesthetized with 10% chloral hydrate after 12 h of starvation. The rats' abdominal cavity was opened to expose the liver after disinfection, and 0.15 mol/L KCl buffer (pH = 7.4) was injected through the superior vena cava until the blood was flushed clean. The rat liver tissue was then accurately removed and transferred to Petri dishes at 0–4°C. The tissues were homogenized in 0.15 mol/L KCl-PBS buffer and stored at 4°C. The homogenate (CR30NX, Eppendorf, Germany) was centrifuged at 9000 rpm at 4°C for 30 min. The supernatant was transferred to another tube and was centrifuged at 105000 rpm at 4°C for 60 min. The precipitate containing liver microsomes was removed and suspended in 0.15 mol/L KCl-PBS buffer (containing 0.25 mol/L sucrose) and stored at −80°C for later use. The liver microsomal concentration was 8.838 mg/ml after the determination with the BCA protein quantification kit (Thermo Scientific, Waltham, MA, United States).

2.3 Instruments and UPLC-MS/MS conditions

Waters Acquity UPLC I-Class (Waters, USA) was used to separate pyrotinib and midazolam. A binary solvent manager (BSM) and sample manager with a flow-through needle (SM-FTN) were used in the UPLC system. The metabolites' effective separation was achieved using Acquity UPLC HSS T3 (100 × 2.1 mm, 1.8 μm particle size) (Waters Corporation, Milford, MA, USA) with a mobile phase of acetonitrile (solvent A) and 0.1% formic acid water containing 20 mmol ammonium acetate (solvent B). The gradient program was set as following: 0–0.3 min 10–30% A; 0.3–1 min 30–95% A; 1–2 min 95% A; 2–2.3 min 95–10% A. The mobile phase's flow rate was 0.4 mL/min, the column temperature was set as 40 °C, and the injection volume was 2 μL. The XEVO TQD triple quadrupole mass spectrometer was equipped with an electrospray ionization (ESI) source, and the multiple reaction monitoring (MRM) mode was selected for quantification. The data were collected using the Mass lynx 4.1 software (Waters Corp.). Mass spectral data were obtained in positive electrospray mode (ESI+) in MRM mode. Nitrogen was used as desolvation (1000 L/h) and cone gases (50 L/h). The ion monitoring voltage conditions were as follows: capillary voltage, 2.5 kV; source temperature, 150°C; desolvation temperature, 500°C. Various reaction monitoring methods were used for quantitative analysis. The pyrotinib, pyrotinib M1, and midazolam transitions are shown in Table 1.

2.4 *In vitro* drug-drug interaction studies in RLMs

200 μl of the incubation mixture was set up as following: 0.3 mg/ml RLMs, 100 mM potassium phosphate buffer (pH 7.4), 1 mM NADPH, and three azole antifungal drugs. A series concentrations of ketoconazole (0.01, 0.05, 0.1, 0.5, 1, 5, and 10 μM) were used to determine its IC_{50} (half maximum inhibitory concentration). For fluconazole and itraconazole, the concentrations of them were all adjusted to 0.01, 0.1, 1, 5, 10, 50, and 100 μM. For the inhibition type determination experiment, a range of pyrotinib (1, 2, 4, and 8 μM) and a series concentrations of ketoconazole (0, 0.03, 0.06, and 0.12 μM), fluconazole (0, 6, 12, and 24 μM), itraconazole (0, 0.15, 0.3, and 0.6 μM) were used for the Lineweaver-Burk Plot analysis and inhibition constants (Ki and αKi) calculation. The ingredients were combined and pre-warmed for 5 min at 37°C. The reaction was initiated with NADPH and incubated at 37°C for 30 min. Then, 200 μl of acetonitrile-midazolam solution (containing midazolam 200 ng/ml) was added and the mixture was vortexed for 2 min to stop the reaction. After been centrifuged at 13000 rpm for 5 min, 2 μl aliquot of the supernatant was then used for the UPLC-MS/MS analysis.

2.5 Method validation

The test method was extensively verified regarding precision, accuracy, and stability, according to the EMA (European Medicines Agency) 2011 and FDA (Food and Drug Administration) 2018 criteria. In six replicates, quality control (QC) samples were generated at low, medium, and high concentrations and were utilized to validate the procedure.

2.6 Animal experiments

Male Sprague-Dawley rats (180–220 g) were supplied by the Experimental Animal Center of Wenzhou Medical University. The animals were placed in a controlled environment of 20–26°C and 55 ± 15% relative humidity under a 12 h light-dark cycle. Except for the 12-h fasting period before the PK study, all rats were fed a standard rodent diet and freely consumed tap water. All experimental procedures and protocols were reviewed and approved by the Animal Care and Use Committee of the Wenzhou Medical University (No. wydw 2019-650), following the Guidelines for The Care and Use of Laboratory Animals.

2.7 *In vivo* pharmacokinetic experiments

The rats were randomly divided into groups A (control group), B (the multiple dose of 40 mg/kg ketoconazole for consecutive 7 days), C (the multiple dose of 40 mg/kg fluconazole for consecutive 7 days), and D (the multiple dose of 40 mg/kg itraconazole for consecutive 7 days). After the last administration of the three azoles or 0.5% CMC-Na (control group), a single dose of 8 mg/kg pyrotinib was administered orally to all rats in each group. Each group consisted of 6 rats. The azole antifungal medication was dissolved in 0.5% carboxymethylcellulose sodium solution (CMC-Na). The experimental timeline showed in Figure 1. All groups were administered pyrotinib in 0.5% CMC-Na, and blood samples were obtained from the caudal vein and deposited in Eppendorf tubes containing heparin sodium at different times (0.083, 0.25, 0.5, 1, 2, 3, 4, 6, 12, and 24 h). The plasma was obtained by centrifuging the blood samples at 4000 rpm for 10 min at 4°C and stored at −80°C until analysis.

2.8 Preparation of plasma samples

The frozen plasma samples were thawed at room temperature and uniformly mixed; 50 μL of plasma sample was removed and mixed with 150 μL acetonitrile-midazolam solution (containing midazolam 200 ng/ml) to precipitate the proteins, followed by vortexing for 30 s and centrifuging at 13,000 rpm for 5 min. Then 150 μL of the supernatant was collected and placed into UPLC vials with 2 μL of sample was subjected to UPLC-MS/MS analysis.

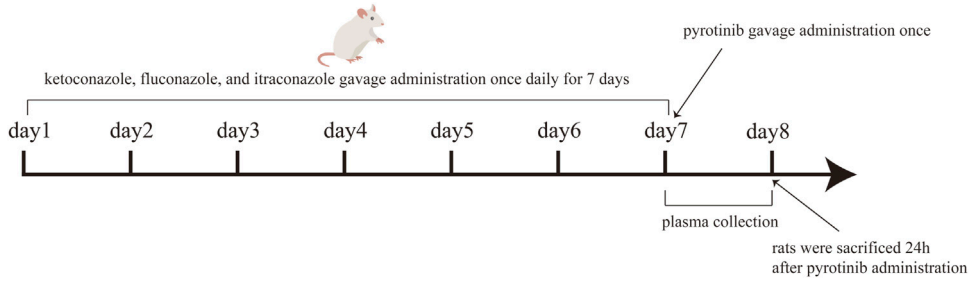

FIGURE 1
The experimental timeline.

TABLE 1 The transition parameters of pyrotinib, pyrotinib M1, and midazolam.

Compound name	Parent (m/z)	Daughter (m/z)	Dwell (s)	Cone (V)	Collision (V)
Pyrotinib	583.16	138.10	0.08	55	30
Pyrotinib M1	492.15	138.10	0.08	55	30
Midazolam	325.98	291.07	0.08	50	26

TABLE 2 Evaluation of the intra- and inter-day precision by the proposed UPLC-MS/MS method for determination of pyrotinib and pyrotinib M1 in rat plasma (n = 6).

Analytes	Preparation Concentration (μM)	Inter-day		Intra-day	
		Precision RSD (%)	Accuracy RE (%)	Precision RSD (%)	Accuracy RE (%)
Pyrotinib	15	8.34	105.51	8.42	107.87
	150	5.99	107.78	2.27	108.51
	4500	2.55	103.17	1.94	103.02
Pyrotinib M1	0.015	11.64	106.67	9.90	104.07
	0.15	7.81	108.67	5.78	106.07
	0.75	5.00	106.93	3.22	105.77

TABLE 3 Stability evaluation results of pyrotinib and pyrotinib M1 in rat plasma under different conditions (n = 6).

Analytes	Preparation Concentration (μM) h	Room temperature, 6 h		4°C, 24 h		−80°C, 7 days	
		RSD (%)	RE (%)	RSD (%)	RE (%)	RSD (%)	RE (%)
Pyrotinib	15	10.06	105.41	11.85	102.40	9.11	98.95
	150	3.47	106.18	9.66	107.05	7.58	108.01
	4500	2.63	103.56	5.91	101.04	4.69	100.79
Pyrotinib M1	0.015	9.82	102.22	7.73	104.44	10.20	109.33
	0.15	5.79	102.44	4.23	108.67	4.36	107.56
	0.75	7.61	108.42	1.94	103.58	2.87	104.47

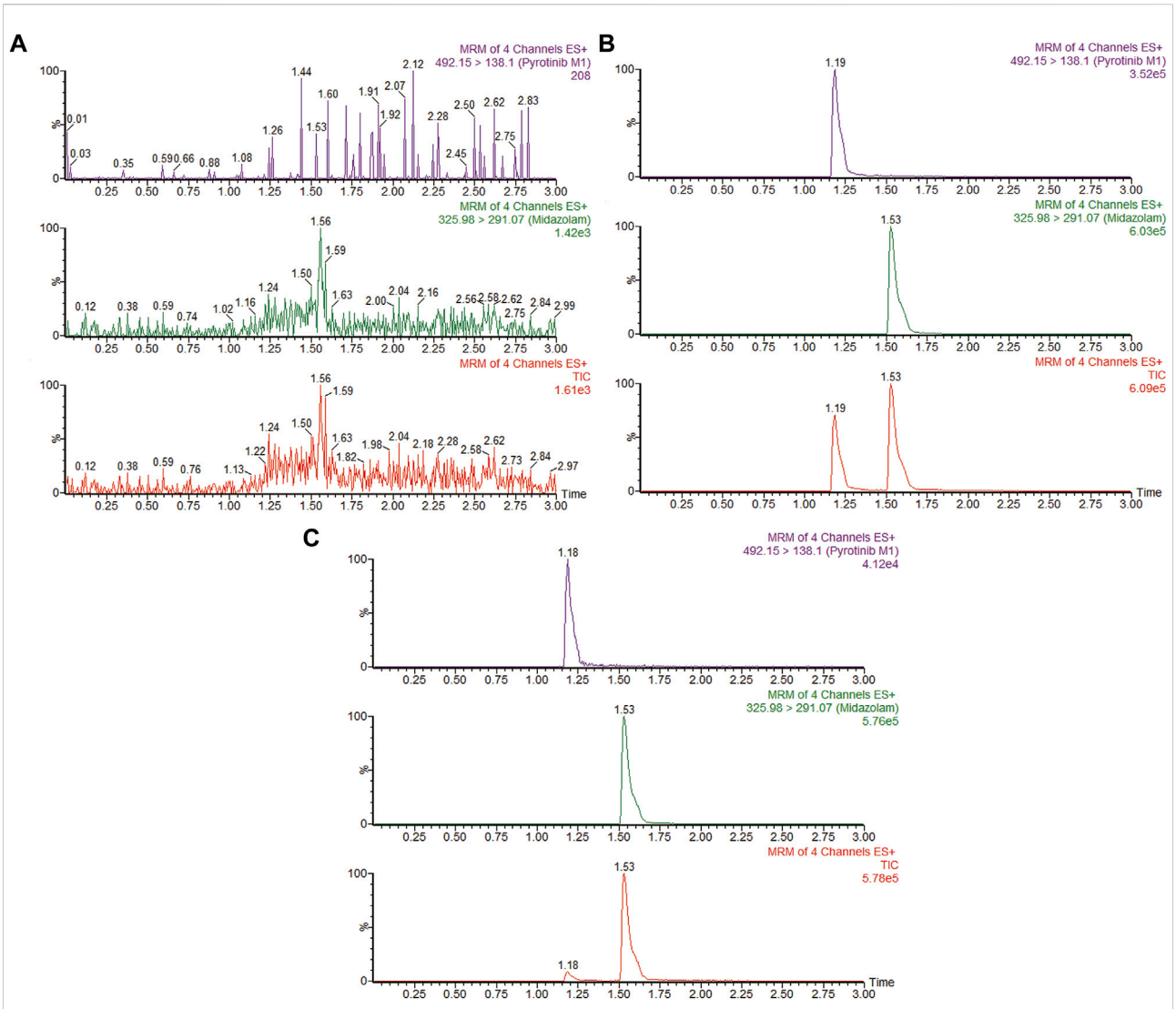

FIGURE 2
MRM chromatograms of pyrotinib M1 and IS in RLMs. **(A)** Blank RLMs **(B)** Denatured RLMs with pyrotinib M1 and IS, and **(C)** Incubation sample.

2.9 Data analyses

GraphPad Prism 7.0 software (GraphPad Software Inc.) was used to calculate the enzyme kinetic parameters of substrates which include V_{max}, K_m, IC_{50}, Ki, and αKi values. The enzyme inhibition mode was obtained using the Linear Lineweaver-Burk plots. The PK characteristics, maximal plasma concentration (C_{max}), time to peak plasma concentration (T_{max}), apparent volume of distribution (Vz/F), area under the plasma concentration-time curve (AUC), elimination half-life ($t_{1/2}$), plasma clearance (Cl/F), and mean residence time (MRT), were calculated using DAS (Drug and Statistics) software (Version 3.2.8, The People's Hospital of Lishui, China). The one-way ANOVA and a Dunnet's multiple range test were used for the statistical comparisons within groups with SPSS software (Version 25.0; SPSS Inc.). Statistical significance was set at $p < 0.05$.

3 Results

3.1 Method validation

This method was designed to conform to EMA and FDA regulatory requirements for bioanalytical methods. The details of the method validation results were presented in Tables 2, 3.

3.2 Effects of ketoconazole, fluconazole, and itraconazole on the metabolism of pyrotinib *in vitro*

A quantification method for the detection of pyrotinib M1 and IS in RLMs was successfully established with no other interfering

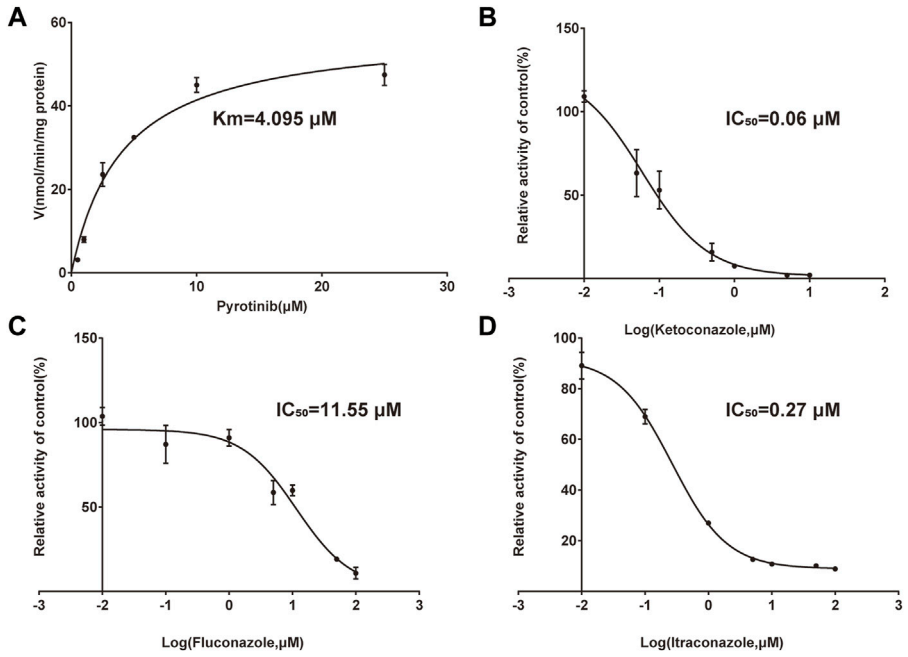

FIGURE 3
Michaelis-Menten curve of pyrotinib (0.5–25 μM) metabolism in RLMs **(A)**. The half-maximal inhibitory concentration (IC_{50}) curve of ketoconazole **(B)**, fluconazole **(C)**, and itraconazole **(D)** (values are means ± standard deviations, *n* = 3).

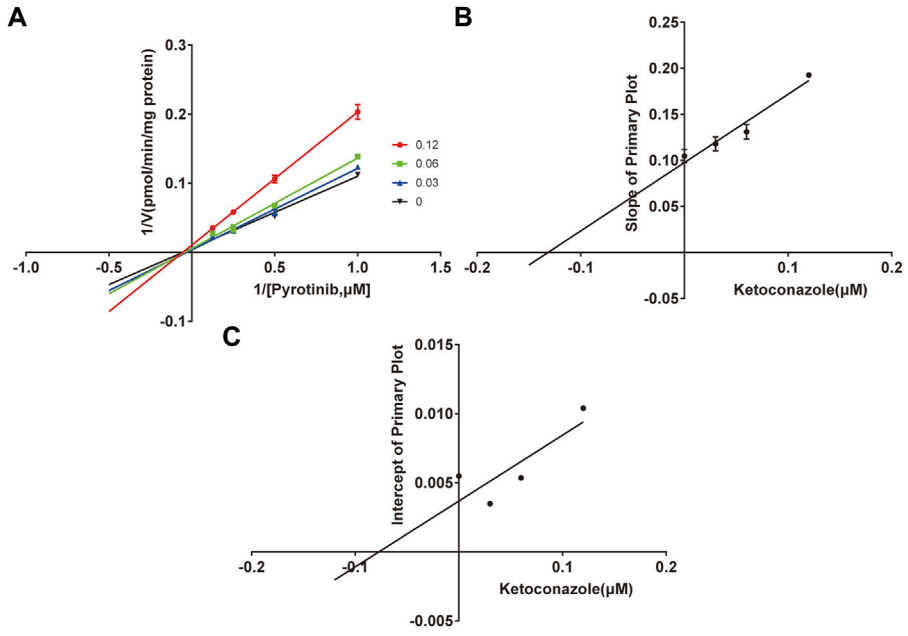

FIGURE 4
The Primary Lineweaver-Burk plots of ketoconazole inhibition on pyrotinib **(A)**; Slope of the primary plot of ketoconazole **(B)**; Intercept of the primary plot of ketoconazole **(C)** (values are means ± standard deviations, *n*=3).

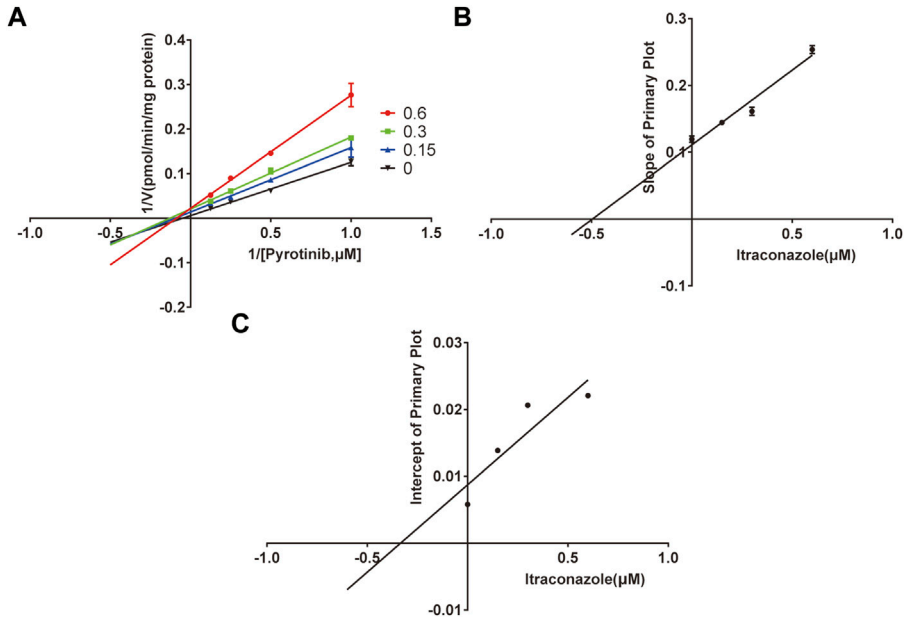

FIGURE 5
The Primary Lineweaver-Burk plots of itraconazole inhibition on pyrotinib **(A)**; Slope of the primary plot of itraconazole **(B)**; Intercept of the primary plot of itraconazole **(C)** (values are means ± standard deviations, *n*=3).

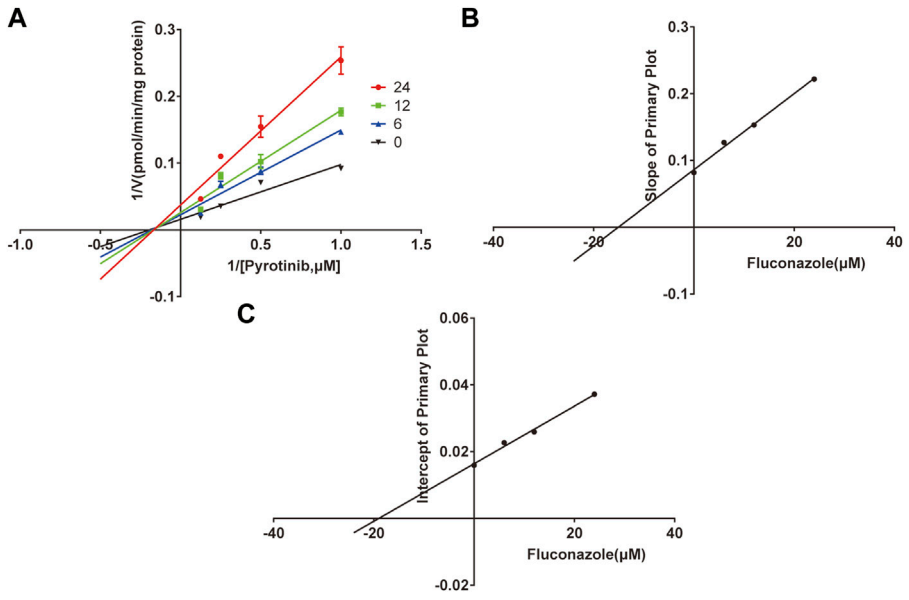

FIGURE 6
The Primary Lineweaver-Burk plots of fluconazole inhibition on pyrotinib **(A)**; Slope of the primary plot of fluconazole **(B)**; Intercept of the primary plot of fluconazole **(C)** (values are means ± standard deviations, *n*=3).

peaks, as shown in Figure 2. Pyrotinib's K_m and V_{max} values were determined by nonlinear regression of the reaction velocity versus substrate concentration. As shown in Figure 3, V_{max} and K_m values of pyrotinib were 58.33 pmol/min/mg protein and 4.095 μM, respectively. Ketoconazole and itraconazole could strongly inhibit the metabolism of pyrotinib with IC_{50} value 0.06 and 0.27 μM,

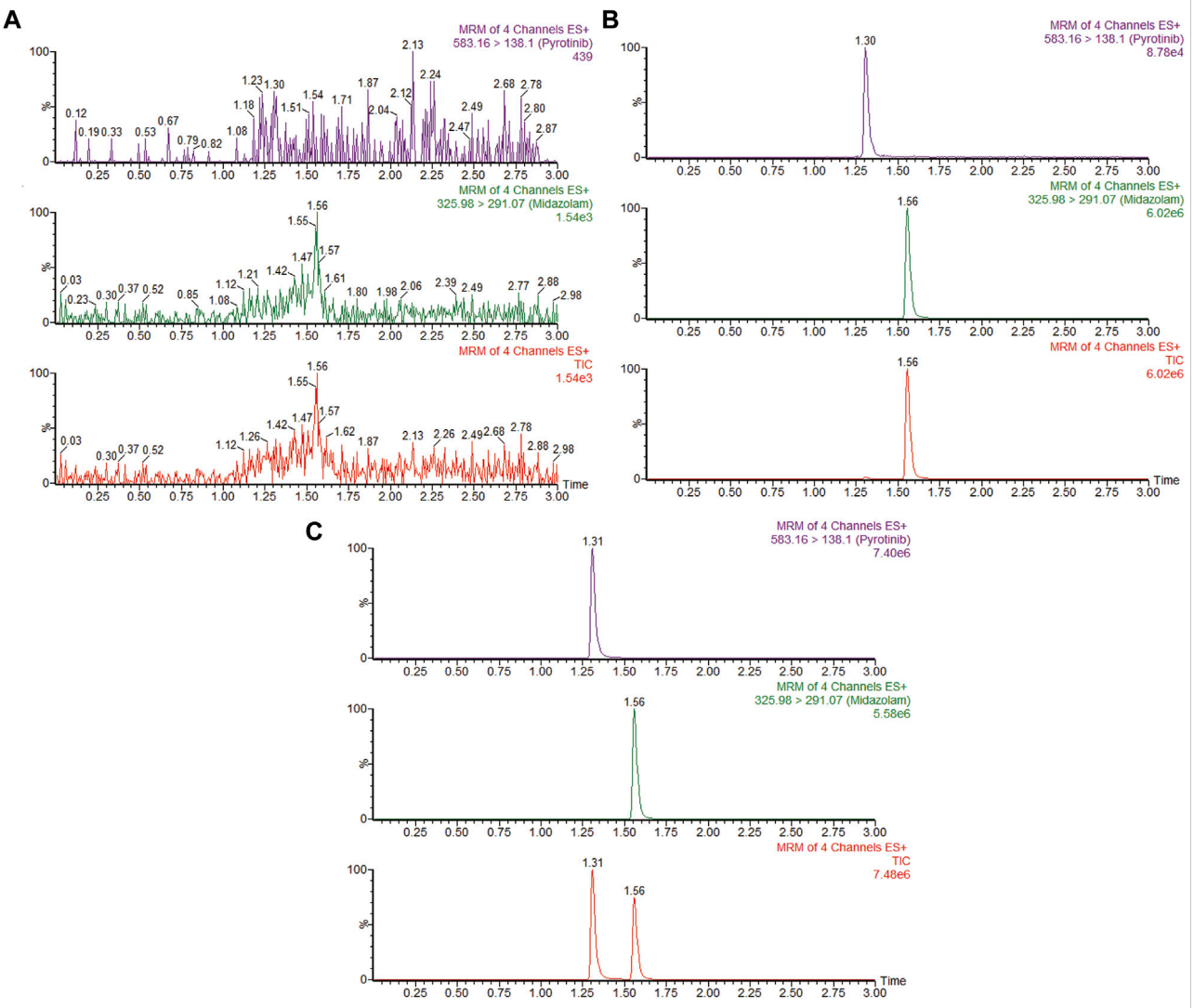

FIGURE 7
MRM chromatograms of pyrotinib and IS *in vivo*. **(A)** Blank rat plasma sample. **(B)** Denatured blank rat plasma sample with pyrotinib and IS. **(C)** Rat plasma sample after dosing pyrotinib with oral administration.

respectively. However, fluconazole only exhibited a relatively weak inhibition effect on pyrotinib (IC_{50} = 11.55 μM). As shown in Figures 4A, 5A, the Lineweaver-Burk plot showed that the family of straight lines intersected in the fourth quadrant, which indicated ketoconazole and itraconazole expressed mixed-type inhibition of noncompetitive/competitive. In detail, Ki and αKi (α = 0.583) values for ketoconazole were 0.132 and 0.077 μM, respectively. The Ki and αKi (α = 0.673) values for itraconazole were 0.496 and 0.334 μM, respectively. Fluconazole weakly inhibited pyrotinib with Ki and αKi (α = 1.259) values of 15.10 and 19.01 μM, respectively. The Lineweaver-Burk plot displayed that the family of straight lines intersected in the secondary quadrant in Figure 6A, indicating that fluconazole expressed mixed-type inhibition of noncompetitive/uncompetitive.

3.3 Effects of ketoconazole, fluconazole, and itraconazole on the metabolism of pyrotinib *in vivo*

The UPLC-MS/MS chromatogram results of pyrotinib and internal standard midazolam in blank rat plasma sample, denatured blank plasma samples pre-incorporated with pyrotinib and IS, and rat plasma samples after oral pyrotinib administration are shown in Figure 7. Blank plasma samples had a negligible effect on the peak shift during the elution time window, demonstrating no endogenous perturbation in the experimental samples. The pharmacokinetic parameter results revealed a significant difference between control group and ketoconazole or

TABLE 4 Main pharmacokinetic parameters of pyrotinib in the control group, ketoconazole group, fluconazole group and itraconazole group (n = 6, mean ± SD).

Parameter	Unit	Control	Ketoconazole	Fluconazole	Itraconazole
$AUC_{(0-t)}$	ug/L*h	17,833.05 ± 2,953.65	36,304.55 ± 8,441.54*	29,069.82 ± 5,995.20*	18,002.86 ± 2,988.37
$AUC_{(0-\infty)}$	ug/L*h	17,840.03 ± 2,964.84	36,452.10 ± 8,474.10*	29,195.61 ± 6,033.37*	18,010.69 ± 2,979.02
$MRT_{(0-t)}$	H	4.32 ± 0.40	5.38 ± 0.38*	5.28 ± 0.24*	4.55 ± 0.36
$MRT_{(0-\infty)}$	H	4.32 ± 0.42	5.47 ± 0.38*	5.37 ± 0.27*	4.56 ± 0.37
t1/2	H	1.26 ± 0.54	2.66 ± 0.20*	2.66 ± 0.15*	1.47 ± 0.63
T_{max}	H	3.50 ± 1.23	4.00 ± 1.10	3.83 ± 0.41	4.00 ± 1.10
Vz/F	L/kg	0.81 ± 0.25	0.89 ± 0.24	1.09 ± 0.21	1.00 ± 0.58
Cl/F	L/h/kg	0.46 ± 0.08	0.23 ± 0.06*	0.29 ± 0.07*	0.45 ± 0.07
C_{max}	ug/L	3,055.07 ± 358.30	4,680.18 ± 1,123.59*	4,291.18 ± 1,071.07*	3,004.65 ± 414.77

*$p < 0.05$, a significant difference compared to the control group (ANOVA).

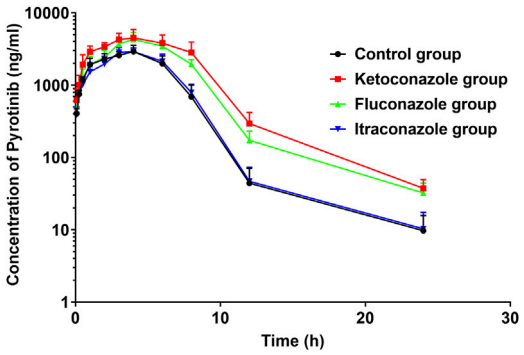

FIGURE 8
Average arterial plasma concentration-time curves of pyrotinib in rats in the Control group, ketoconazole group, fluconazole group and itraconazole group (n = 6).

fluconazole treated groups ($p < 0.05$), especially for the values of $AUC_{(0-t)}$, $AUC_{(0-\infty)}$, $MRT_{(0-t)}$, $MRT_{(0-\infty)}$, $t_{1/2}$, Cl/F, and C_{max} (Table 4). Mean plasma concentration-time curves of pyrotinib in rats of control group and experimental groups were shown in Figure 8. Compared with those of control group, the Cl/F value of pyrotinib in ketoconazole group decreased by 0.50-fold, but the $AUC_{(0-t)}$ and C_{max} values were increased by 1.04-fold and 0.53-fold, respectively. Similarly, the Cl/F value of pyrotinib in fluconazole group decreased by 0.37-fold, but the $AUC_{(0-t)}$ and C_{max} values were increased by 0.63-fold and 0.40-fold, respectively. These data suggest that ketoconazole and fluconazole could truly inhibit the metabolism of pyrotinib in rats. However, no significant difference could be found in pharmacokinetic parameters between the itraconazole and control groups, indicating that itraconazole had no inhibitory effect on pyrotinib *in vivo*.

4 Discussion

In this study, an UPLC-MS/MS based method was developed and validated to measure the concentration of pyrotinib and its metabolite, pyrotinib M1, simultaneously. Previous studies revealed that pyrotinib may get higher value of therapeutic efficacy when combined with other drugs. For example, pyrotinib combined with vinorelbine exhibited encouraging results in HER2-positive metastatic breast cancer, with little toxicity. Furthermore, this combination also showed promising antitumor activity in individuals with brain metastases (Li et al., 2021).

CYP3A4 is reported to be the main metabolic enzyme for pyrotinib; therefore, any CYP3A4 inducer or inhibitor may affect the metabolism of pyrotinib. Rifampicin, a strong index CYP3A4 inducer, has been shown to induce pyrotinib metabolism and decrease its exposure time in healthy adults (Cai et al., 2022). DDIs are very common among CYP3A4-mediated drugs but little attentions have been paid on the interactions between pyrotinib and azoles to date. In this study, effects of three azoles ketoconazole, fluconazole, and itraconazole on pyrotinib's PK parameters were investigated both *in vitro* and *in vivo*.

Previous studies revealed that ketoconazole could increase the plasma exposure of ruxolitinib by 91% compared with ruxolitinib alone (Shi et al., 2011). Furthermore, ketoconazole could also interfere with the metabolism of one CYP3A4 probe drug midazolam (Lam et al., 2003). Similarly, our data indicated that ketoconazole could significantly inhibit pyrotinib metabolism both *in vitro* and *in vivo*. PK data in RLMs indicated that the inhibition effect of ketoconazole on pyrotinib belonged to the mixed inhibition type of noncompetitive/competitive, with an IC_{50} value of 0.06 μM IC_{50} < 1 mM indicates strong inhibitory efficiency based on the judgment. Similar to these data, ketoconazole have been reported to exhibit the stronger inhibition effect on CYP3A4 substrates than fluconazole or itraconazole, (Lou

et al., 2019; Chen et al., 2020). Our *in vivo* experiment result also support this conclusion because when pyrotinib was coadministrated with ketoconazole in rat, its $AUC_{(0-t)}$, $AUC_{(0-\infty)}$, and C_{max} values were significantly increased, while Cl/F value was decreased by approximately 50%, as compared to that of the control group. Therefore, ketoconazole's negative effect on pyrotinib's PK can be attributed to its inhibitory effect on CYP3A4 activity.

Fluconazole was reported to be a moderate CYP3A4/CYP2C9 inhibitor (Debruyne, 1997; Bellmann and Smuszkiewicz, 2017). In a previous study, coadministration of fluconazole with ruxolitinib could considerably increase systemic exposure to ruxolitinib and slowed down ruxolitinib's elimination rate as compared with administrating ruxolitinib alone in healthy subjects (Aslanis et al., 2019). This study was similar to the results of our study, which the $AUC_{(0-t)}$, $AUC_{(0-\infty)}$, and C_{max} values were significantly increased when coadministration of fluconazole with pyrotinib. Our *in vitro* data revealed that fluconazole could weakly inhibit the metabolism of pyrotinib with IC_{50} value of 11.55 μM, and the Ki and αKi (α = 1.259) values were 15.10 and 19.01 μM, respectively. This inhibition resulted from a mixed mechanism, incorporating uncompetitive and non-competitive inhibition. For the *in vitro* parameters, the apparent Ki values exhibited the dissociation constant for the interaction between the inhibitor and the enzyme, The parameter *α* was indicative of the inhibition type (Kim et al., 2019; Kim et al., 2021). When Ki = αKi, namely α = 1, it demonstrated noncompetitive inhibition. When α→0, it represented uncompetitive inhibition. When α→∞, it presented competitive inhibition. The mixed inhibition includes competitive, uncompetitive, and noncompetitive inhibition. When Ki > αKi, it showed the mixed inhibition of competitive and noncompetitive. When Ki < αKi, it represented mixed inhibition of uncompetitive and noncompetitive (Jin et al., 2015). The *α* value also represented the extent to which the binding affinity between enzyme and substrate is altered by the inhibitor. In our study, all three azole antifungals showed mixed inhibition. Ketoconazole and itraconazole revealed the mixed the inhibition of competitive and noncompetitive, with the value of *α* 0.583 and 0.673, respectively, while itraconazole represented the mixed inhibition of uncompetitive and noncompetitive.

Previous studies revealed that itraconazole was a potent CYP3A4 inhibitor (Prieto Garcia et al., 2018; Vishwanathan et al., 2018). In this study, itraconazole strongly inhibited pyrotinib *in vitro* with an IC_{50} value of 0.27 μM; however, it exhibited no effect *in vivo*. These results were similar to the previous study, where itraconazole had no effect or weak effect on the pharmacokinetic parameters of sunitinib and imatinib also mainly metabolized by CYP3A4 enzyme (Lin et al., 2014; Wang et al., 2021). Why the results of itraconazole *in vivo* were inconsistent with the results *in vitro*? It was reported that four isomers of itraconazole with different pharmacokinetic and pharmacological effects had been found, and different isomers of itraconazole have a significant distinction in the ability to inhibit the activities of CYP3A enzymes (Krasulova et al., 2019; Luo et al., 2020). This partly explains that although the itraconazole exerts strong CYP3A4 enzyme inhibitory activity *in vitro*, weaker inhibitory effect *in vivo* studies, which need further researches in the future.

5 Limitations

Current experiments are all based on animal models, and it could not fully simulate the actual state of DDIs in humans. Therefore, more work is still needed to further study the possible interaction mechanism between azole antifungal agents and pyrotinib in humans.

6 Conclusion

Ketoconazole showed more stronger inhibitory effects on pyrotinib metabolism than fluconazole, both *in vivo* and *in vitro*. Itraconazole had no effect on pyrotinib *in vivo* although it exhibited strong inhibitory effects *in vitro*. These data indicated that ketoconazole and fluconazole might be cautiously coadministered with pyrotinib in clinic, and a close therapeutic drug monitoring of pyrotinib concentration is suggested to avoid its potential adverse drug reactions.

Data availability statement

The original contributions presented in the study are included in the article/supplementary material, further inquiries can be directed to the corresponding authors.

Ethics statement

The animal study was reviewed and approved by the Animal Care and Use Committee of the Wenzhou Medical University (No. wydw 2019-650).

Author contributions

LW: Conceptualization, writing-original draft preparation; FW: Methodology, writing-review and editing, visualization, supervision; JX: Formal analysis; YW: Methodology; WF: Visualization, formal analysis; HJ: Methodology, data curation; PG: Software; QZ: Validation, investigation; SW: Resources, funding acquisition; YZ:

Writing-review and editing; HD: Conceptualization, validation, investigation. All the authors have read and agreed to the published version of the manuscript.

Funding

This work was supported by the Public Welfare Technology Research Funding Project of Zhejiang (LGD20H060001 and LGF21H310002), the Public Welfare Technology Research Funding Project of Lishui (2020GYX18 and 2020GYX23), the Key Research and Development Project of Lishui (2020ZDYF12, 2021ZDYF13 and 2021ZDYF15), and the Municipal public welfare self-financing technology application research project of Lishui (2021SJZC023).

Conflict of interest

The authors declare that the research was conducted in the absence of any commercial or financial relationships that could be construed as a potential conflict of interest.

Publisher's note

All claims expressed in this article are solely those of the authors and do not necessarily represent those of their affiliated organizations, or those of the publisher, the editors and the reviewers. Any product that may be evaluated in this article, or claim that may be made by its manufacturer, is not guaranteed or endorsed by the publisher.

References

Aslanis, V., Umehara, K., Huth, F., Ouatas, T., Bharathy, S., Butler, A. A., et al. (2019). Multiple administrations of fluconazole increase plasma exposure to Ruxolitinib in healthy adult subjects. *Cancer Chemother. Pharmacol.* 84, 749–757. doi:10.1007/s00280-019-03907-1

Bellmann, R., and Smuszkiewicz, P. (2017). Pharmacokinetics of antifungal drugs: Practical implications for optimized treatment of patients. *Infection* 45, 737–779. doi:10.1007/s15010-017-1042-z

Blair, H. A. (2018). Pyrotinib: First global approval. *Drugs* 78, 1751–1755. doi:10.1007/s40265-018-0997-0

Cai, M. M., Dou, T., Tang, L., Sun, Q. Y., Zhai, Z. H., Wang, H. P., et al. (2022). Effects of rifampicin on antineoplastic drug pyrotinib maleate pharmacokinetics in healthy subjects. *Invest. New Drugs* 40 (4), 756–761. doi:10.1007/s10637-022-01241-7

Chen, M., Zhang, X., Chen, Y., Sun, W., Wang, Z., Huang, C., et al. (2020). Comparison of the inhibitory effect of ketoconazole, voriconazole, fluconazole, and itraconazole on the pharmacokinetics of bosentan and its corresponding active metabolite hydroxy bosentan in rats. *Xenobiotica.* 50, 280–287. doi:10.1080/00498254.2019.1628321

Debruyne, D. (1997). Clinical pharmacokinetics of fluconazole in superficial and systemic mycoses. *Clin. Pharmacokinet.* 33, 52–77. doi:10.2165/00003088-199733010-00005

Huang, T., Luo, X., Wu, B., Peng, P., Dai, Y., Hu, G., et al. (2020). Pyrotinib enhances the radiosensitivity of HER2-overexpressing gastric and breast cancer cells. *Oncol. Rep.* 44, 2634–2644. doi:10.3892/or.2020.7820

Iancu, G., Serban, D., Badiu, C. D., Tanasescu, C., Tudosie, M. S., Tudor, C., et al. (2022). Tyrosine kinase inhibitors in breast cancer (Review). *Exp. Ther. Med.* 23, 114. doi:10.3892/etm.2021.11037

Jin, C. H., He, X., Zhang, F. L., He, L. N., Chen, J. X., Wang, L. L., et al. (2015). Inhibitory mechanisms of celastrol on human liver cytochrome P450 1A2, 2C19, 2D6, 2E1 and 3A4. *Xenobiotica*. 45, 571–577. doi:10.3109/00498254.2014.1003113

Kim, J. M., Seo, S. W., Han, D. G., Yun, H., and Yoon, I. S. (2021). Assessment of metabolic interaction between repaglinide and quercetin via mixed inhibition in the liver: *In vitro* and *in vivo*. *Pharmaceutics* 13, 782. doi:10.3390/pharmaceutics13060782

Kim, S. B., Kim, K. S., Kim, D. D., and Yoon, I. S. (2019). Metabolic interactions of rosmarinic acid with human cytochrome P450 monooxygenases and uridine diphosphate glucuronosyltransferases. *Biomed. Pharmacother.* 110, 111–117. doi:10.1016/j.biopha.2018.11.040

Krasulova, K., Dvorak, Z., and Anzenbacher, P. (2019). *In vitro* analysis of itraconazole cis-diastereoisomers inhibition of nine cytochrome P450 enzymes: stereoselective inhibition of CYP3A. *Xenobiotica.* 49, 36–42. doi:10.1080/00498254.2018.1425510

Lam, Y. W., Alfaro, C. L., Ereshefsky, L., and Miller, M. (2003). Pharmacokinetic and pharmacodynamic interactions of oral midazolam with ketoconazole, fluoxetine, fluvoxamine, and nefazodone. *J. Clin. Pharmacol.* 43, 1274–1282. doi:10.1177/0091270003259216

Li, X., Yang, C., Wan, H., Zhang, G., Feng, J., Zhang, L., et al. (2017). Discovery and development of pyrotinib: A novel irreversible EGFR/HER2 dual tyrosine kinase inhibitor with favorable safety profiles for the treatment of breast cancer. *Eur. J. Pharm. Sci.* 110, 51–61. doi:10.1016/j.ejps.2017.01.021

Li, Y., Qiu, Y., Li, H., Luo, T., Li, W., Wang, H., et al. (2021). Pyrotinib combined with vinorelbine in HER2-positive metastatic breast cancer: A multicenter retrospective study. *Front. Oncol.* 11, 664429. doi:10.3389/fonc.2021.664429

Lin, G. T., Wang, C. M., Qiu, X. J., Wang, Z., Han, A. Y., Xu, T., et al. (2014). Differential effects of ketoconazole, itraconazole and voriconazole on the pharmacokinetics of imatinib and its main metabolite GCP74588 in rat. *Drug Dev. Ind. Pharm.* 40, 1616–1622. doi:10.3109/03639045.2013.838582

Liu, Y., Zhang, Q., Lu, C., and Hu, W. (2021). Multiple administrations of itraconazole increase plasma exposure to Pyrotinib in Chinese healthy adults. *Drug Des. devel. Ther.* 15, 2485–2493. doi:10.2147/DDDT.S312310

Lou, D., Cui, X., Bao, S. S., Sun, W., Pan, W. H., Chen, M. C., et al. (2019). Effects of ketoconazole, voriconazole, and itraconazole on the pharmacokinetics of apatinib in rats. *Drug Dev. Ind. Pharm.* 45, 689–693. doi:10.1080/03639045.2019.1569042

Luo, X. X., Xue, X. C., Li, T. F., Zhang, Y., Huang, L., and Cheng, G. (2020). Differential impacts of azole antifungal drugs on the pharmacokinetic profiles of dasatinib in rats by LC-MS-MS. *Curr. Drug Metab.* 21, 1022–1030. doi:10.2174/1389200221666201022140656

Lv, J., Liu, F., Feng, N., Sun, X., Tang, J., Xie, L., et al. (2018). CYP3A4 gene polymorphism is correlated with individual consumption of sufentanil. *Acta Anaesthesiol. Scand.* 62, 1367–1373. doi:10.1111/aas.13178

Ma, F., Li, Q., Chen, S., Zhu, W., Fan, Y., Wang, J., et al. (2017). Phase I study and biomarker analysis of Pyrotinib, a novel irreversible Pan-ErbB receptor tyrosine kinase inhibitor, in patients with human epidermal growth factor receptor 2-positive metastatic breast cancer. *J. Clin. Oncol.* 35, 3105–3112. doi:10.1200/JCO.2016.69.6179

Meng, J., Liu, X. Y., Ma, S., Zhang, H., Yu, S. D., Zhang, Y. F., et al. (2019). Metabolism and disposition of pyrotinib in healthy male volunteers: Covalent binding with human plasma protein. *Acta Pharmacol. Sin.* 40, 980–988. doi:10.1038/s41401-018-0176-6

Nivoix, Y., Ubeaud-Sequier, G., Engel, P., Levêque, D., and Herbrecht, R. (2009). Drug-drug interactions of triazole antifungal agents in multimorbid patients and implications for patient care. *Curr. Drug Metab.* 10, 395–409. doi:10.2174/138920009788499012

Parasrampuria, D. A., Mendell, J., Shi, M., Matsushima, N., Zahir, H., and Truitt, K. (2016). Edoxaban drug-drug interactions with ketoconazole, erythromycin, and cyclosporine. *Br. J. Clin. Pharmacol.* 82, 1591–1600. doi:10.1111/bcp.13092

Prieto Garcia, L., Janzén, D., Kanebratt, K. P., Ericsson, H., Lennernäs, H., and Lundahl, A. (2018). Physiologically based pharmacokinetic model of itraconazole and two of its metabolites to improve the predictions and the mechanistic understanding of CYP3A4 drug-drug interactions. *Drug Metab. Dispos.* 46, 1420–1433. doi:10.1124/dmd.118.081364

Shi, J. G., Chen, X., McGee, R. F., Landman, R. R., Emm, T., Lo, Y., et al. (2011). The pharmacokinetics, pharmacodynamics, and safety of orally dosed INCB018424 phosphate in healthy volunteers. *J. Clin. Pharmacol.* 51, 1644–1654. doi:10.1177/0091270010389469

Vishwanathan, K., Dickinson, P. A., So, K., Thomas, K., Chen, Y. M., De Castro Carpeño, J., et al. (2018). The effect of itraconazole and rifampicin on the pharmacokinetics of osimertinib. *Br. J. Clin. Pharmacol.* 84, 1156–1169. doi:10.1111/bcp.13534

Wang, J., Cui, X., Cheng, C., Wang, Y., Sun, W., Huang, C. K., et al. (2021). Effects of CYP3A inhibitors ketoconazole, voriconazole, and itraconazole on the pharmacokinetics of sunitinib and its main metabolite in rats. *Chem. Biol. Interact.* 338, 109426. doi:10.1016/j.cbi.2021.109426

Wen, H. N., Liu, Y. X., Xu, D., Zhao, K. J., and Jiao, Z. (2021). Population pharmacokinetic modeling of pyrotinib in patients with HER2-positive advanced or metastatic breast cancer. *Eur. J. Pharm. Sci.* 159, 105729. doi:10.1016/j.ejps.2021.105729

Zhang, K., Hong, R., Kaping, L., Xu, F., Xia, W., Qin, G., et al. (2019). CDK4/6 inhibitor palbociclib enhances the effect of pyrotinib in HER2-positive breast cancer. *Cancer Lett.* 447, 130–140. doi:10.1016/j.canlet.2019.01.005

Zhu, Y., Li, L., Zhang, G., Wan, H., Yang, C., Diao, X., et al. (2016). Metabolic characterization of pyrotinib in humans by ultra-performance liquid chromatography/quadrupole time-of-flight mass spectrometry. *J. Chromatogr. B Anal. Technol. Biomed. Life Sci.* 1034, 117–127. doi:10.1016/j.jchromb.2016.08.009

frontiers | Frontiers in Pharmacology

TYPE Original Research
PUBLISHED 16 September 2022
DOI 10.3389/fphar.2022.1008207

OPEN ACCESS

EDITED BY
Simona Pichini,
National Institute of Health (ISS), Italy

REVIEWED BY
Angelo Montana,
University of Catania, Italy
Su Chen,
Capital Medical University, China

*CORRESPONDENCE
Shugeng Wu,
2011105134@nbu.edu.cn

SPECIALTY SECTION
This article was submitted to Drug Metabolism and Transport, a section of the journal Frontiers in Pharmacology

RECEIVED 31 July 2022
ACCEPTED 26 August 2022
PUBLISHED 16 September 2022

CITATION
Zhou B, Yu J, Cai X and Wu S (2022), Constructing a molecular subtype model of colon cancer using machine learning .
Front. Pharmacol. 13:1008207.
doi: 10.3389/fphar.2022.1008207

Constructing a molecular subtype model of colon cancer using machine learning

Bo Zhou[1], Jiazi Yu[1], Xingchen Cai[2] and Shugeng Wu[2]*

[1]Department of General Surgery, Ningbo Medical Center Lihuili Hospital, Ningbo University, Ningbo, China, [2]Medical School, Ningbo University, Ningbo, China

Background: Colon cancer (CRC) is one of the malignant tumors with a high incidence in the world. Many previous studies on CRC have focused on clinical research. With the in-depth study of CRC, the role of molecular mechanisms in CRC has become increasingly important. Currently, machine learning is widely used in medicine. By combining machine learning with molecular mechanisms, we can better understand CRC's pathogenesis and develop new treatments for it.

Methods and materials: We used the R language to construct molecular subtypes of colon cancer and subsequently explored prognostic genes with GEPIA2. Enrichment analysis is used by WebGestalt to obtain differential genes. Protein–protein interaction networks of differential genes were constructed using the STRING database and the Cytoscape tool. TIMER2.0 and TISIDB databases were used to investigate the correlation of these genes with immune-infiltrating cells and immune targets. The cBioportal database was used to explore genomic alterations.

Results: In our study, the molecular prognostic model of CRC was constructed to study the prognostic factors of CRC, and finally, it was found that Charcot–Leyden crystal galectin (CLC), zymogen granule protein 16 (ZG16), leucine-rich repeat-containing protein 26 (LRRC26), intelectin 1 (ITLN1), UDP-GlcNAc: betaGal beta-1,3-N-acetylglucosaminyltransferase 6 (B3GNT6), chloride channel accessory 1 (CLCA1), growth factor independent 1 transcriptional repressor (GFI1), aquaporin 8 (AQP8), HEPACAM family member 2 (HEPACAM2), and UDP glucuronosyltransferase family 2 member B15 (UGT2B15) were correlated with the subtype model of CRC prognosis. Enrichment analysis shows that differential genes were mainly associated with immune-inflammatory pathways. GFI1 and CLC were associated with immune cells, immunoinhibitors, and immunostimulator. Genomic analysis shows that there were no significant changes in differential genes.

Conclusion: By constructing molecular subtypes of colon cancer, we discovered new colon cancer prognostic markers, which can provide direction for new treatments in the future.

KEYWORDS

colon cancer, machine learning, molecular subtype model, pathogenesis, prognosis

Introduction

CRC is the most common digestive system tumors in the world. In the USA, the incidence of colon adenocarcinoma is roughly equal between men and women, and is expected to increase by 100,000 new cases and 50,000 deaths in 2022 (Siegel et al., 2022). In China, where the incidence is slightly higher in men than in women, an estimated 590,000 new cases and 300,000 new deaths are expected (Xia et al., 2022). With the development of detection technology, the early screening of CRC plays an increasingly important role. For example, colonoscopy is the most commonly used detection method. In addition, due to the development of treatment, including surgical treatment and neoadjuvant therapy, the 5-year survival rate of CRC is close to 64% (Miller et al., 2019). Although the development of new technologies has brought treatment progress in the CRC, the carcinogenesis is still unclear. Tumor development is influenced by the tumor microenvironment (TME), which contains a variety of cell types, including immune-infiltrating cells and cancer-associated fibroblasts. These cells can detach from the original normal growth and play an important role in tumor cell proliferation, differentiation, invasion, and metastasis (Schmitt and Greten, 2021). Except that the pathogenic mechanism for CRC is not clear, the classification of CRC is still mainly based on TNM staging, and this classification has insufficient understanding of CRC. Therefore, it contributes to the diagnosis and treatment of CRC by elucidating the molecular mechanism of colon carcinogenesis. In recent years, machine learning (ML)-based methods for understanding tumors have received increasing attention (Liu et al., 2020; Collins et al., 2021; Masud et al., 2021), and many algorithms for predicting and classifying tumors have emerged (Aziz et al., 2021; Karhade et al., 2021; Tohka and van Gils, 2021). Existing machine learning algorithms include linear regression, logistic regression, decision trees, support vector machines (SVM), naive Bayes, K-mean clustering method, random forest, dimensionality reduction algorithms, gradient boosts, and AdaBoost. Jiang et al. used convolution neural networks to predict the prognosis of stage III CRC (Jiang et al., 2020). Previous cases of applying machine learning have achieved good results and demonstrated strong practicality. In the present study, we construct a CRC prognostic model based on machine learning and public databases to find new prognostic markers and their relationship with CRC.

Materials and methods

Data source

RNA-seq data and clinical data are from the TCGA database, and these data are downloaded from the University of California Santa Cruz (UCSC) Xena database.

Cluster analysis

We used consensus clustering analysis to randomly select 5,000 genes in the CRC samples from the TCGA database to construct molecular subtypes of CRC. The key parameters include 80% resampling, k-estimated maximum value of 6,500 repetitions, and PAC measure (PAC measure (proportion of ambiguous clustering) explained; optimal k is the k with the lowest PAC value) to filter the best k value. Prognosis between different clusters is compared using Kaplan–Meier analysis. All these analyses are performed using R package "ConsensusClusterPlus" (Wilkerson and Hayes, 2010). The clustering results will be presented in the heatmaps, and the survival analysis results will be presented by GraphPad prism7.

Differential expression genes analysis

We performed the clusters of prognostic value for RNA-seq differential gene analysis using the R package "limma". We performed RNA-seq data differential analysis on cluster1, which consisted of 144 samples, and cluster3 which consisted of 150 samples. To exclude the influence of extreme values or outliers, we deleted genes with no expression significance (including $p > 0.05$ or FDR>0.05). Finally, we screened the genes with $|\log FC| \geq 1$ as the differential genes of cluster1 and cluster3 of the CRC subgroup.

Survival analysis

In order to explore whether the expression levels of differential genes between the two clusters have an impact on prognosis, we used an external database to analyze the differentially expressed genes. Gene expression profiling interactive analysis (Tang et al., 2019) (GEPIA2, http://gepia2.cancer-pku.cn, version 2) is an online tool that searches the TCGA database, which collected RNA sequencing data of 9,736 tumors and 8,587 normal samples in total. The GEPIA2 database was used to analyze the effect of two clusters of differentially expressed genes on survival.

Enrichment analysis

A web-based gene set analysis toolkit (Liao et al., 2019) (WebGestalt, http://www.webgestalt.org/option.php) can enrich genes of interest to understand their functions and pathways involved. GO analysis is a common annotation method for genes and gene products, including molecular functions, biological pathways, and cellular components.

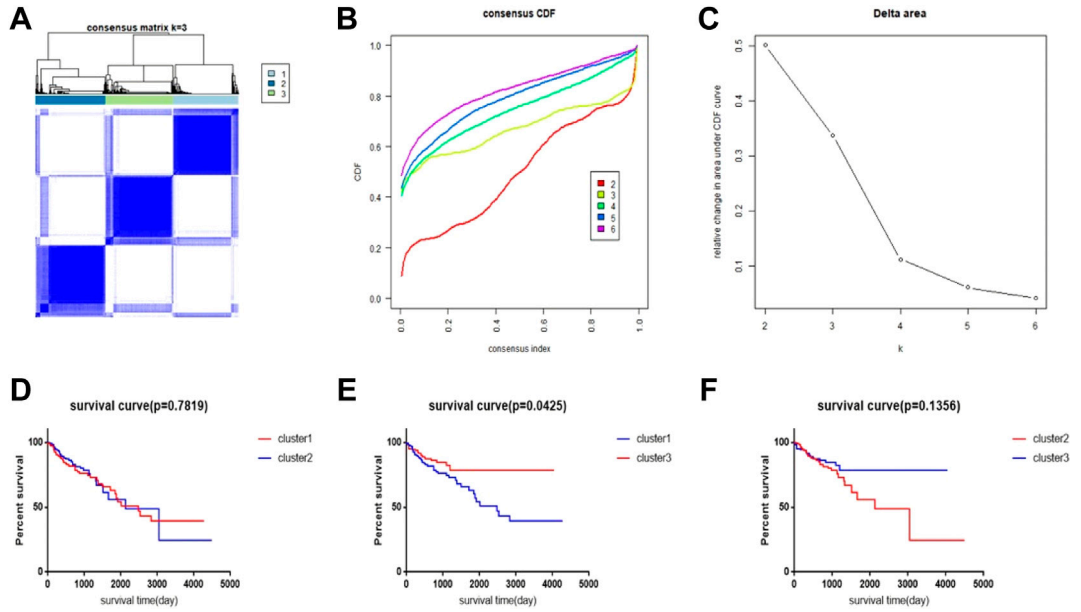

FIGURE 1
CRC subtype characteristics and difference in overall survival (OS). **(A)** Consensus clustering analysis yields three matrices, each representing one CRC subtype. **(B)** Consensus clustering cumulative distribution function (CDF) for k = 2–9. **(C)** Relative change in area under the CDF curve for k = 2–6. **(D–F)** Survival time curve between 3 clusters.

KEGG analysis is a resource for analyzing gene functions and information. In order to study the differentially expressed genes' enrichment information of cluster1 and cluster3, we used the WebGestalt website to conduct GO and KEGG online enrichment analyses; parameters considered analytically meaningful for enrichment analysis included $p < 0.05$ and FDR<0.05.

Protein–protein interaction analysis

We used the STRING database (https://string-db.org/) (Szklarczyk et al., 2021; Siegel et al., 2022) to explore the interaction between the proteins expressed by these genes. Through the PPI network, we could study whether these genes played a role in the prognosis of subtype models of CRC, independently or together. Then, we used the MCODE plugin of the Cytoscape software to find the core network of PPI.

Immune infiltration analysis

In order to study the impact of these differential genes on immune function between the two clusters, we used the TIMER2.0 (Li et al., 2020) database for analysis. TIMER2.0 (http://timer.comp-genomics.org/) is a database that comprehensively analyzes the correlation between tumors and immune infiltrating cells. In addition to the TIMER2.0 database, we also used the TISIDB database to analyze the relationship of these DEGs with immunoinhibitors and immunostimulators. TISIDB (Ru et al., 2019) (http://cis.hku.hk/TISIDB/) is an online database for immune infiltration analysis based on the TCGA database.

Genomic alteration analysis

The cBio Cancer Genomics Portal (Wu et al., 2019) (cBioportal, http://cbioportal.org) is a database that collects multiple tumor genomics. We used this tool to analyze genomic alterations in 10 genes with prognostic significance in subtypes of CRC to explore their impact.

Results

Machine learning divides CRC into different subtypes

We performed a consensus clustering method of CRC samples in the TCGA database using the PAC measure to select the best value of k = 2 (Figures 1A–C). In the TCGA database, 448 samples with complete follow-up information were included in the study. The 448 samples were divided into

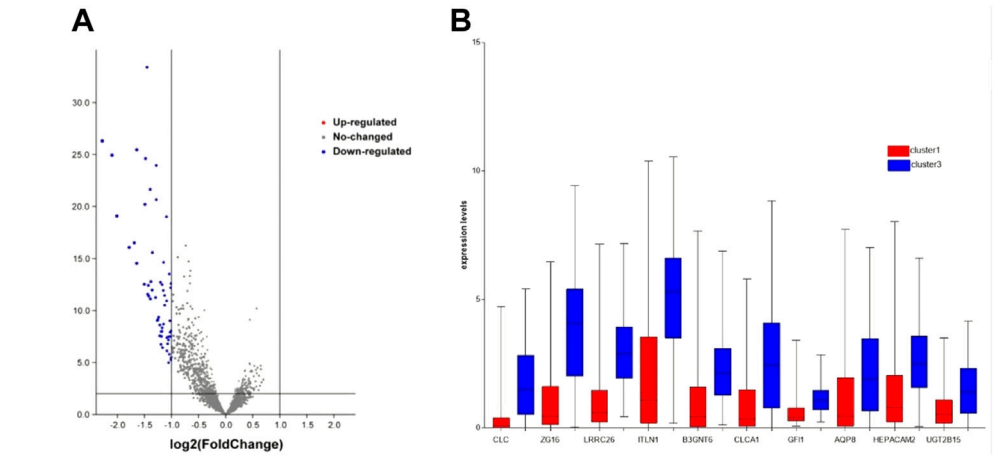

FIGURE 2
DEG's expression between cluster1 and cluster3. **(A)** DEGs of two clusters *via* volcano. **(B)** DEGs with prognostic significance *via* boxplot.

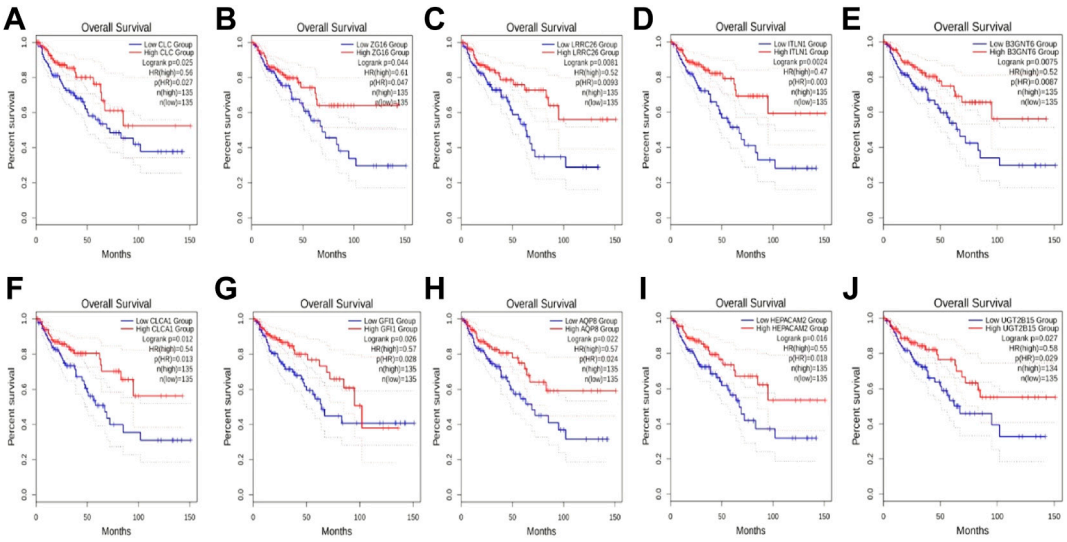

FIGURE 3
The effect of DEGs on survival time. **(A)** CLC, **(B)** ZG16, **(C)** LRRC26, **(D)** ITLN1, **(E)** B3GNT6, **(F)** CLCA1, **(G)** GFI1, **(H)** AQP8, **(I)** HEPACAM2, and **(J)** UGT2B15.

three subtypes; cluster1 included 144 samples, cluster2 included 154 samples, and cluster3 included 150 samples. The rest of the clustering results are shown in Supplementary Figure S1. By comparing the survival times of the three clusters, we found a significant survival difference between clusters 1 and 3. The survival time of cluster3 was better than that of cluster1, while there was no significant difference in survival time between clusters 1 and 2 and between clusters 2 and 3 (Figures 1D–F).

Screening of DEGs

To explore which genes are responsible for the difference in survival times between cluster1 and cluster3, we performed a differential analysis of 5,000 genes in clusters 1 and 3 using package "limma". A total of 58 genes were differentially expressed between the two clusters (Figure 2A). All DEGs were described in Supplementary Table S1. The expression levels of these genes in cluster3 were significantly higher than

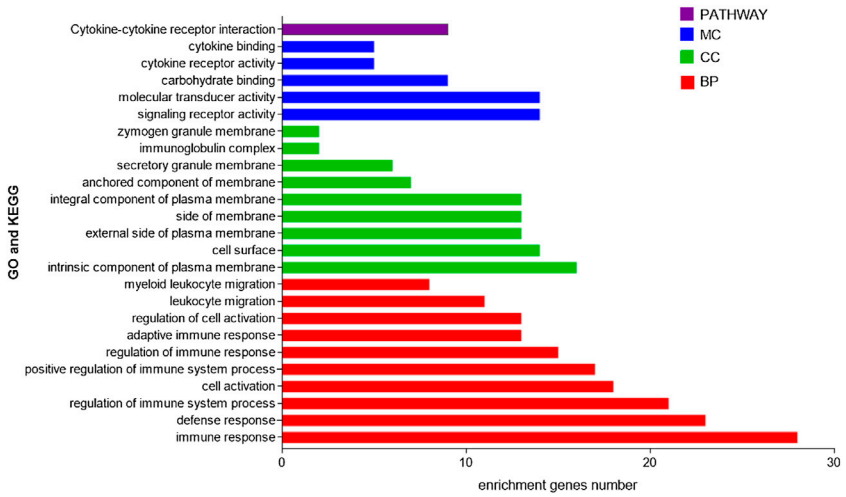

FIGURE 4
GO and KEGG enrichment analyses of DEGs in two subtypes.

those in cluster1 (Figure 2B). Through external database validation with GEPIA2, we found a total of 10 genes whose differential expression played a significant role in prognosis, including CLC, ZG16, LRRC26, ITLN1, B3GNT6, CLCA1, GFI1, AQP8, HEPACAM2, and UGT2B15 (Figures 3A–J). The increased expression of these genes will have a better prognosis; when combined with the above model, we speculated that these genes will have a greater impact in CRC.

Enrichment analysis

We then used the WebGestalt online tool to perform enrichment analysis for all 58 DEGs between the two subtypes. Both GO and KEGG enrichment analysis results are shown in Figure 4, and the results showed that these genes were mainly enriched in immune-related pathways. GO includes immune response, defense response, and regulation of immune system processes. In addition, pathways related to cell morphology and cell membrane were also enriched, including cell activation, intrinsic component of the plasma membrane, and cell surface. The KEGG pathway showed that it is mainly enriched in the cytokine–cytokine receptor interaction pathway. These results suggest that immune factors play an important role in the prognosis of both subtypes.

Genome alteration analysis

By studying changes in the genome, we found no significant changes (less than 5%) in each of these 10 genes (Figure 5). Therefore, we speculate that these changes do not have a significant impact on gene function.

Protein–protein interaction network analysis

We performed protein interaction analysis on DEGs using the STRING database (Figure 6A), and the results suggested that among the 10 genes with significant effects on CRC prognosis, CLC, ITLN1, ZG16, AQP8, CLCA1, and GFI1 interacted with other DEGs. This indicates that some genes play a role in the prognosis of CRC independently, and some of them may be regulated by other genes, thus having a complex impact on the prognosis of CRC. We used the MCODE plugin to select the core regulation network, setting the parameters as the degree cutoff of 2, node score cutoff of 0.2, and k-core of 2, and the module with an MCODE score >4 was presented. The results are shown in Figure 6B. These results suggest that AQP8 and ZG16 have an impact on the prognosis of CRC subtypes, but they are still regulated by other DEGs. The remaining DEGs have no direct impact on the prognosis of CRC subtypes, but they indirectly affect prognosis by regulating AQP8 and ZG16.

Immune-infiltration analysis

In order to explore the relationship between these 10 DEGs and immune genes and immune infiltrating cells, we used the TIMER2.0 database. As shown in Figure 7, GFI1 is significantly correlated with $CD8^+$ T cells (cor = 0.388, p = 2.49e-11), neutrophils (cor = 0.489, p = 6.41e-18), and DC (cor = 0.462,

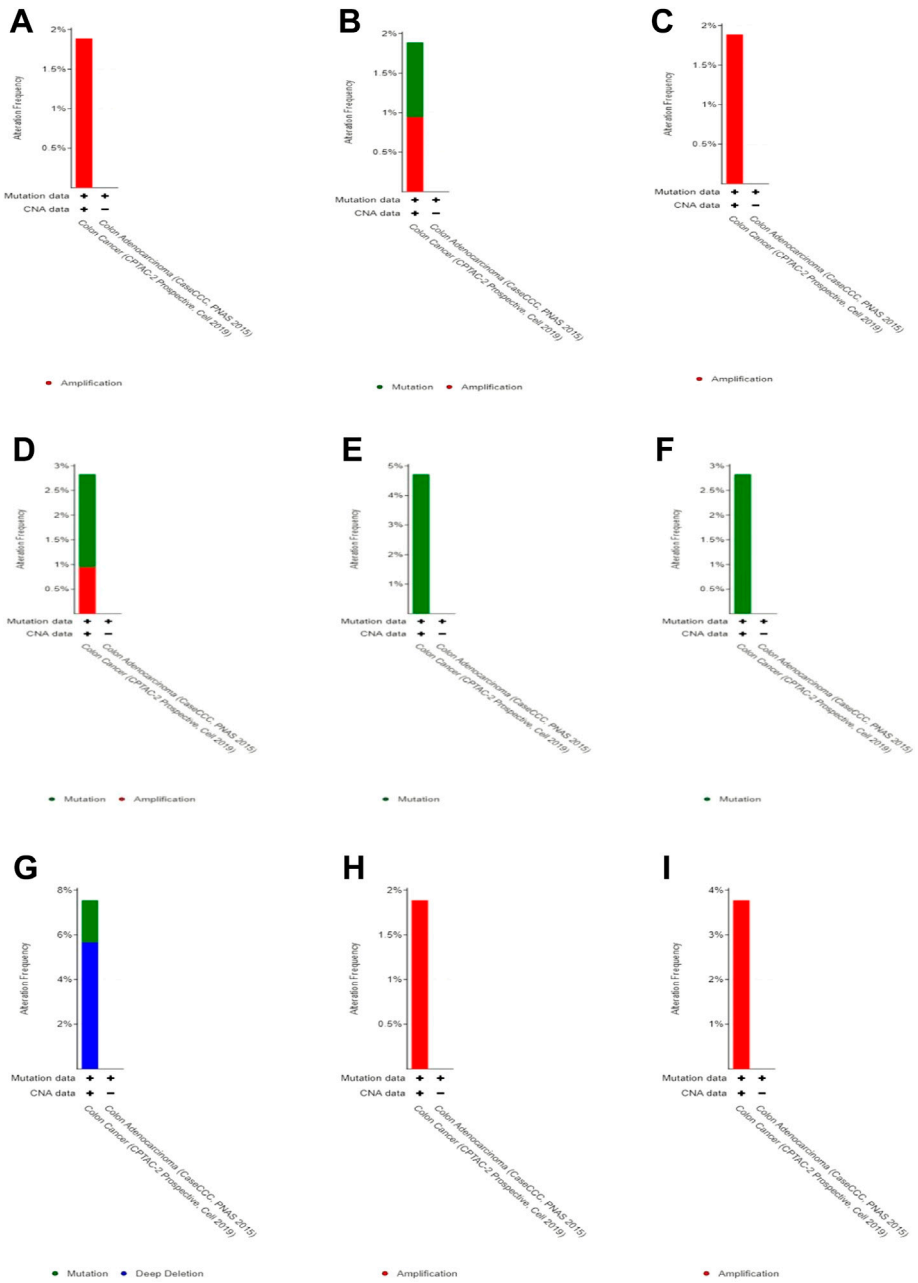

FIGURE 5
Genomic alteration in DEGs. **(A)** CLC, **(B)** ZG16, **(C)** LRRC26, **(D)** ITLN1, **(E)** B3GNT6,**(F)** CLCA1, **(G)** GFI1, **(H)** HEPACAM2, and **(I)** UGT2B15.

p = 5.64e-16), and CLC is significantly correlated with DC (cor = 0.488, p = 7.24e-18), macrophage (cor = 0.329, p = 2.38e-8), and neutrophils (cor = 0.447, p = 6.55e-15). These results suggest that not only genes but also immune-infiltrating cells were involved in two subtypes of CRC. Then, we used the TISIDB database to explore the relationship between these 10 genes and immunoinhibitors and immunostimulators. CLC was significantly correlated with ADORA2A (cor = 0.444, p < 2.2e-16), CD244 (cor = 0.507, p < 2.2e-16), CSF1R (cor = 0.532, p < 2.2e-16), HAVCR2 (cor = 0.462, p < 2.2e-16), IL10 (cor = 0.544, p < 2.2e-16), PDCD1LG2 (cor = 0.492, p < 2.2e-16), and TGFB1 (cor = 0.41, p < 2.2e-16) of immunoinhibitor, and GFI1 was significantly correlated with ADORA2A (cor = 0.404, p < 2.2e-16), CD244 (cor = 0.623, p < 2.2e-16), CD274 (cor =

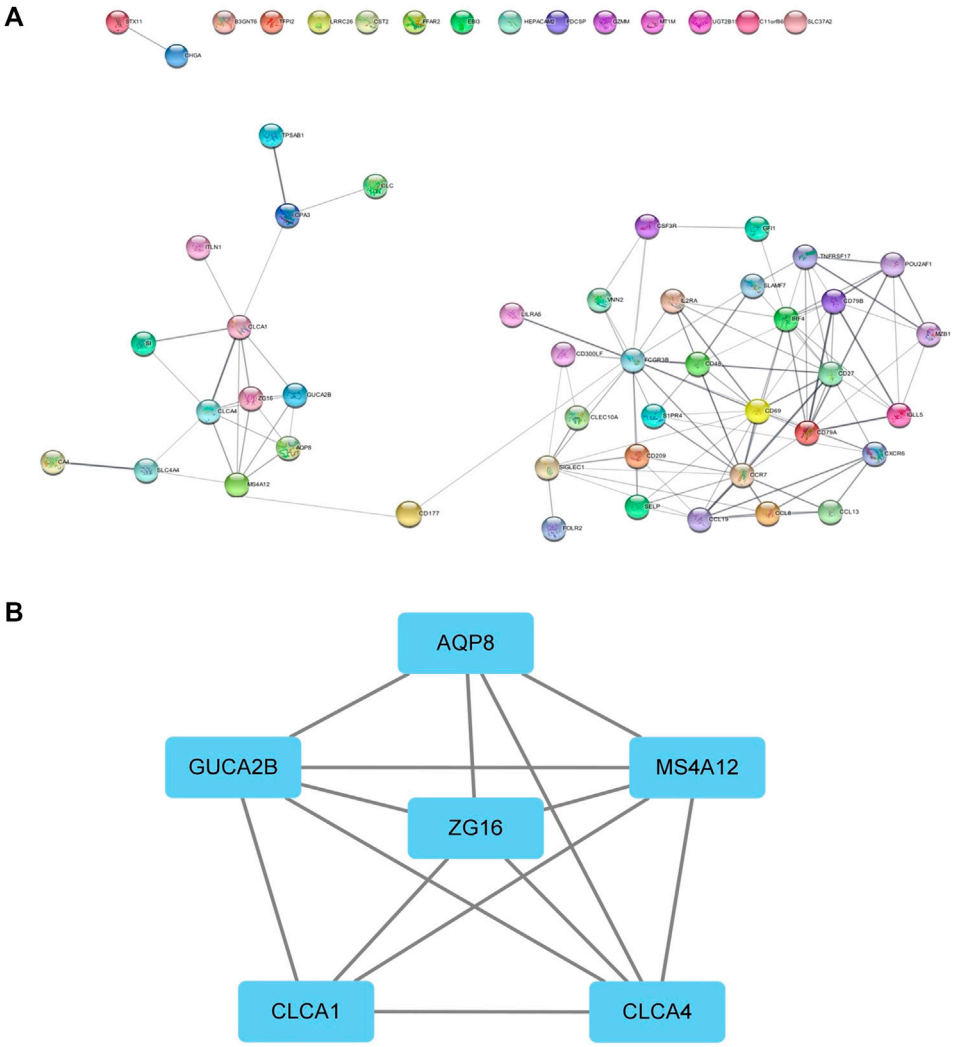

FIGURE 6
PPI network. **(A)** PPI of the STRING database. **(B)** Core regulatory networks selected by the MCODE plugin for Cytoscape.

0.507, p < 2.2e-16), CD96 (cor = 0.581, p < 2.2e-16), CSF1R (cor = 0.407, p < 2.2e-16), CTLA4 (cor = 0.523, p < 2.2e-16), HAVCR2 (cor = 0.431, p < 2.2e-16), IDO1 (cor = 0.435, p < 2.2e-16), LAG3 (cor = 0.587, p < 2.2e-16), PDCD1 (cor = 0.529, p < 2.2e-16), PDCD1LG2 (cor = 0.436, p < 2.2e-16), and TIGIT (cor = 0.561, p < 2.2e-16) (Figure 8A). CLC was significantly correlated with CD27 (cor = 0.441, p < 2.2e-16), CD28 (cor = 0.457, p < 2.2e-16), CD48 (cor = 0.583, p < 2.2e-16), CD80 (cor = 0.458, p < 2.2e-16), CD86 (cor = 0.494, p < 2.2e-16), ICOS (cor = 0.441, p < 2.2e-16), IL2RA (cor = 0.534, p < 2.2e-16), TNFRSF17 (cor = 0.48, p < 2.2e-16), TNFRSF4 (cor = 0.423, p < 2.2e-16), TNFRSF9 (cor = 0.436, p < 2.2e-16), and TNFSF13B (cor = 0.457, p < 2.2e-16), and GFI1 was significantly correlated with C10orf54 (cor = 0.452, p < 2.2e-16), CD27 (cor = 0.506, p < 2.2e-16), CD28 (cor = 0.427, p < 2.2e-16), CD48 (cor = 0.483, p < 2.2e-16), CD80 (cor = 0.438, p < 2.2e-16), CD86 (cor = 0.444, p < 2.2e-16), CXCR4 (cor = 0.534, p < 2.2e-16), ICOS (cor = 0.444, p < 2.2e-16), IL2RA (cor = 0.514, p < 2.2e-16), KLRC1 (cor = 0.515, p < 2.2e-16), KLRK1 (cor = 0.572, p < 2.2e-16), LTA (cor = 0.44, p < 2.2e-16), TNFRSF13C (cor = 0.517, p < 2.2e-16), TNFRSF17 (cor = 0.417, p < 2.2e-16), TNFRSF18 (cor = 0.525, p < 2.2e-16), TNFRSF8 (cor = 0.403, p < 2.2e-16), TNFRSF9 (cor = 0.438, p < 2.2e-16), TNFSF13B (cor = 0.4, p < 2.2e-16), and TNFSF14 (cor = 0.465, p < 2.2e-16) of immunostimulator (Figure 8B). In the correlation of tumor-infiltrating lymphocytes (TILs) with DEGs, we found that CLC and GFI1 were significantly associated with immune cells. CLC was associated with T-follicular helper cells (Tfh, cor = 0.506, p < 2.2e-16), gamma delta T cells (Tgd, cor = 0.486, p < 2.2e-16), type 1 T-helper cells (Th1, cor = 0.544, p < 2.2e-16), regulatory T cells (Treg, cor = 0.555, p < 2.2e-16),

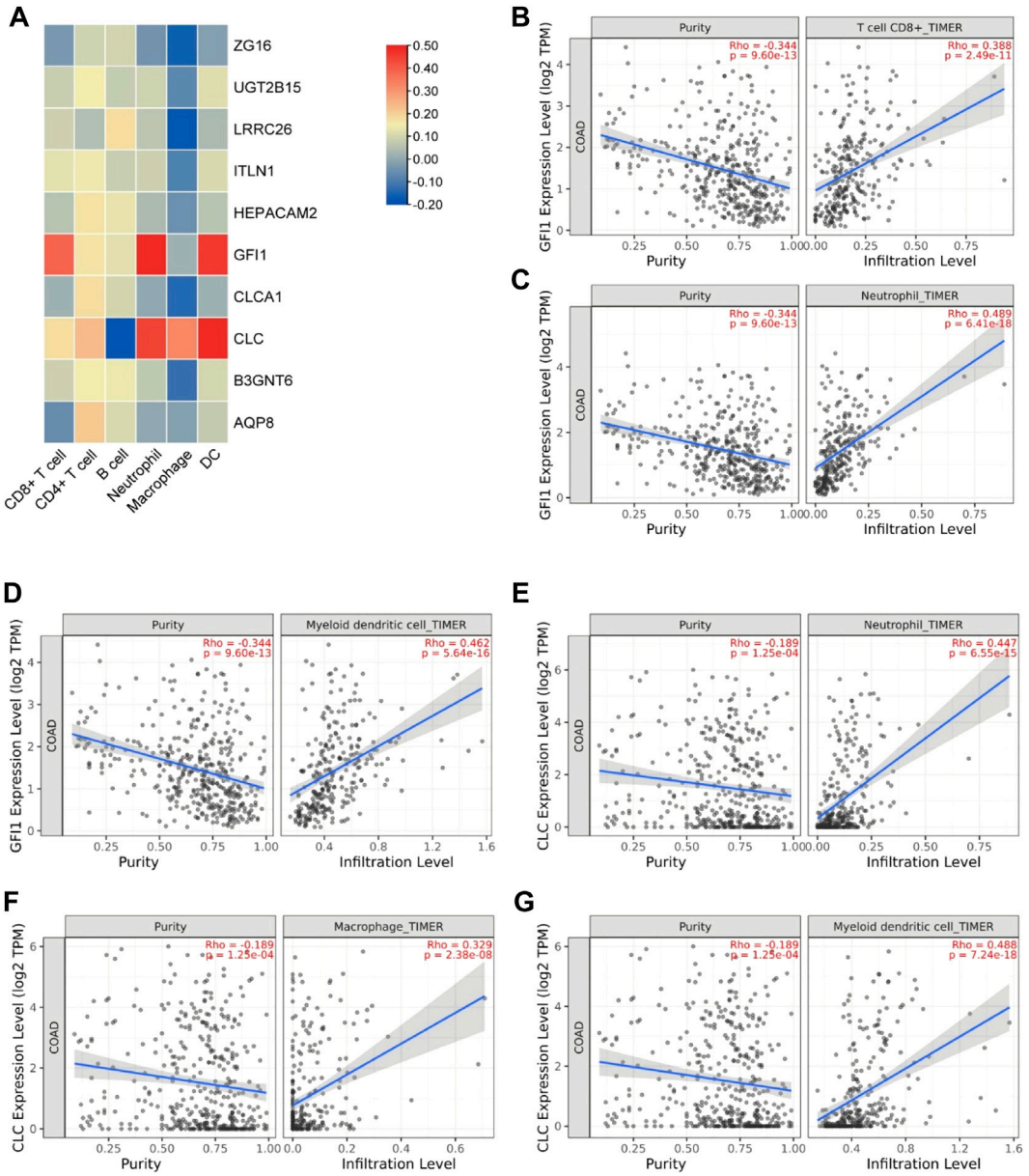

FIGURE 7
The relationship between DEGs and immune infiltrating cells. **(A)** Heatmap of the correlation between DEGs and immune cells. **(B)** Relationship between GFI1 and $CD8^+$ T cells. **(C)** Relationship between GFI1 and neutrophils. **(D)** Relationship between GFI1 and DC. **(E)** Relationship between CLC and neutrophils. **(F)** Relationship between CLC and macrophages. **(G)** Relationship between CLC and DC.

activated B cells (Act_B, cor = 0.452, $p < 2.2e\text{-}16$), immature B cells (Imm_B, cor = 0.495, $p < 2.2e\text{-}16$), myeloid-derived suppressor cells (MDSC, cor = 0.509, $p < 2.2e\text{-}16$), activated dendritic cells (Act_DC, cor = 0.454, $p < 2.2e\text{-}16$), macrophages (cor = 0.545, $p < 2.2e\text{-}16$), mast cells (Mast, cor = 0.624, $p < 2.2e\text{-}16$), and neutrophils (cor = 0.548, $p < 2.2e\text{-}16$), and GFI1 was associated with activated CD8 T cells (Act_CD8, cor = 0.466, $p < 2.2e\text{-}16$), effector memory CD8 T cells (Tem_CD8, cor = 0.622, $p < 2.2e\text{-}16$), activated CD4 T cells (Act_CD4, cor = 0.448, $p < 2.2e\text{-}16$), Tfh (cor = 0.403, $p < 2.2e\text{-}16$), Th1 (cor = 0.441, $p < 2.2e\text{-}16$), type 2 T-helper cells (Th2, cor = 0.559, $p < 2.2e\text{-}16$), Act_B (cor = 0.463, $p < 2.2e\text{-}16$), Imm_B (cor = 0.501, $p < 2.2e\text{-}16$), MDSC (cor = 0.554, $p < 2.2e\text{-}16$), Act_DC (cor = 0.426, $p < 2.2e\text{-}16$), and macrophages (cor = 0.411, $p < 2.2e\text{-}16$) (Figure 8C). The results showed that GFI1 and CLC were significantly related to immune and inflammation factors, further suggesting that GFI1 and CLC may be involved in immune and inflammation factors in the process of regulating the prognosis of CRC subtypes.

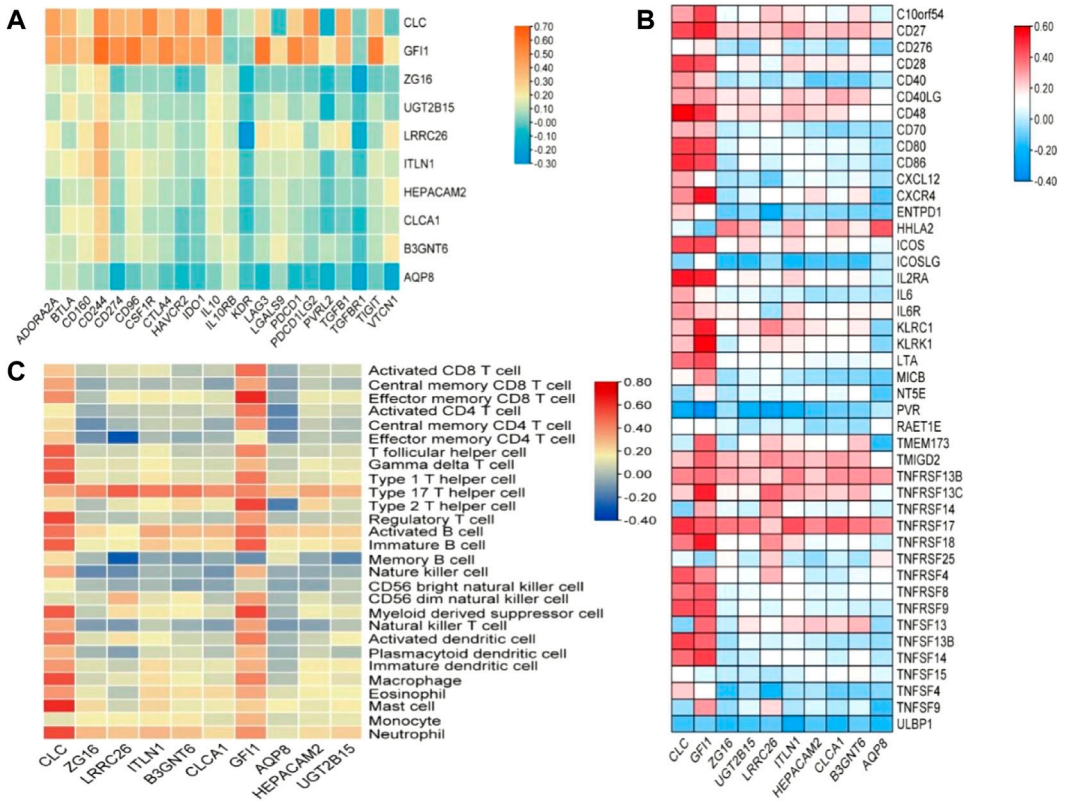

FIGURE 8
The relationship between DEGs and immunomodulator. **(A)** The relationship between DEGs and immunoinhibitor, **(B)** the relationship between DEGs and immunostimulator, and **(C)** relations between abundance of tumor-infiltrating lymphocytes (TILs) and expression of DEGs.

Discussion

With the development of technology, the scope of artificial intelligence in the medical field is also expanding. Unsupervised clustering is a technique that has been applied to the tumor level in recent years, and consensus clustering (CC) is used to estimate the number of unsupervised classes in a dataset, providing both quantitative and visual stability evidence (Wilkerson and Hayes, 2010; Greener et al., 2022). Using this technology to construct molecular subtypes of CRC can help us better understand the disease and develop new drugs and treatments. In this study, we constructed subtypes of CRC based on selected genes with significant prognostic differences. To investigate what caused this difference, we explored which of these genes is at work. The model we constructed found that cluster3 had a better prognosis than cluster1. When comparing the DEGs of two clusters, we found that there were 58 DEGs between the two clusters, and all of them were highly expressed in cluster3. Then, we used external databases to explore 10 genes (including CLC, ZG16, LRRC26, ITLN1, B3GNT6, CLCA1, GFI1, AQP8, HEPACAM2, and UGT2B15) that play a crucial role in the prognosis between the two clusters. The high expression of these 10 genes is associated with a better prognosis for CRC. Combined with the high expression of these genes in cluster3, the results also fit the conclusions from the model. Genomic analysis showed that the DEGs did not change significantly. Gene enrichment analysis provided a way for us to understand the functions of these genes. Through GO and KEGG enrichment analysis, we found that DEGs are closely related to immune function and inflammation. This suggests that the immune inflammation response system may play an important role in the prognosis of two clusters. Since these genes are highly expressed in cluster3, we hypothesized that the immune system has a positive effect on CRC in cluster3 and these DEGs interact with the immune system to improve prognosis. To test our hypothesis, we analyzed 10 DEGs associated with the immune system. Results show that CLC and GFI1 have the highest correlation with immunity. The immunosuppressive pathway can regulate the immune environment of the body and prevent the over-activation of the immune mechanism from causing damage to itself, and immunoinhibitors are the key factors in this regulation. Immune stimulation is to activate the immune system, enhance our immunity, and play an important role in responding to foreign pathogens, removing self-damaging cells and monitoring and inhibiting the occurrence and development of tumors. Our study

suggests that CLC and GFI1 have dual roles in regulating immune mechanisms and resulting in a better prognosis for CRC. The protein encoded by CLC is a lysophospholipase that is expressed on eosinophils and basophils, implying its function in relation to inflammation (Su, 2018).

Next, it was found through enrichment analysis that the DEGs of the two CRC subtypes were related to the inflammatory pathway, and the PPI network revealed that these genes interacted with CLC, indicating that the inflammatory response has an important role in CRC subtypes in prognosis. Previous research found that CLC can activate macrophages to secrete IL-1β, thereby aggravating inflammation (Rodriguez-Alcazar et al., 2019). Our study also came to the same conclusion. CLC has a significant correlation with macrophages and mast cells, so inflammatory mediators under the regulation of CLC in CRC play a role in the prognosis of both subtypes. Future studies are expected to explore the role and mechanism of the inflammatory response. GFI1 encodes a nuclear zinc finger protein, which functions as a transcriptional repressor. It has also been shown to be associated with neutrophils (the TIMER database also shows a correlation). When GFI1 is mutated, it can lead to neutropenia (Moroy et al., 2015). The relationship between GFI1 and immunoinhibitors and immunostimulators, as well as the way of regulating TILs, provides a direction for the development of new targeted drugs in the future. In addition to the impact of immune-inflammatory factors on the prognosis of both subtypes, ZG16, ITLN1, CLCA1, AQP8 and other genes encoding the transport channels on the cell membrane and involved in the transport of intracellular substances are also among the prognostic factors. Although the remaining DEGs did not directly affect the prognosis of the two subtypes of CRC, we found that by constructing the protein interaction network of all DEGs, they could interact with CLC, GFI1, ZG16, ITLN1, CLCA1, and AQP8 and indirectly participate in the regulation of prognosis of the subtypes of CRC. According to the model, we found that the factors that cause the difference in the prognosis of CRC are very complex, which is the result of multiple factors.

In summary, our study revealed the prognostic factors affecting CRC based on immunity, inflammation, transporters, and ion channels. Despite the positive results, this study has a number of limitations. For one thing, due to the differences in the original data and algorithms of the database, the results of this study may be biased. The small sample size of the database may also lead to discrepancies in the data, and real-time updates to the database can also change results. For another, our data need to be confirmed by *in vivo*/*in vitro* experiments, such as gene expression or proteomic analyses based on clinical samples. In the future, research should further explore the mechanism of action and pathogenesis of these genes in order to validate the proposed model's effectiveness and provide a new way for the treatment of CRC.

Data availability statement

The datasets presented in this study can be found in online repositories. The names of the repository/repositories and accession number(s) can be found in the article/ Supplementary Material.

Author contributions

BZ and SW designed the study and performed the experiments, JY collected the data, XC analyzed the data, and BZ and SW prepared the manuscript. All authors read and approved the final manuscript.

Funding

This study was supported by the Medical and Health Science and Technology Program of Zhejiang Province (2021KY1036); funded by Ningbo medical and health brand discipline (2022-F01).

Acknowledgments

We sincerely thank the AIM Workshop for technical support.

Conflict of interest

The authors declare that the research was conducted in the absence of any commercial or financial relationships that could be construed as a potential conflict of interest.

Publisher's note

Supplementary material

The Supplementary Material for this article can be found online at: https://www.frontiersin.org/articles/10.3389/fphar.2022.1008207/full#supplementary-material

References

Aziz, S., Ahmed, S., and Alouini, M. S. (2021). ECG-based machine-learning algorithms for heartbeat classification. *Sci. Rep.* 11 (1), 18738. doi:10.1038/s41598-021-97118-5

Collins, T., Maktabi, M., Barberio, M., Bencteux, V., Jansen-Winkeln, B., Chalopin, C., et al. (2021). Automatic recognition of colon and esophagogastric cancer with machine learning and hyperspectral imaging. *Diagn. (Basel)* 1810 (10). doi:10.3390/diagnostics11101810

Greener, J. G., Kandathil, S. M., Moffat, L., and Jones, D. T. (2022). A guide to machine learning for biologists. *Nat. Rev. Mol. Cell Biol.* 23 (1), 40–55. doi:10.1038/s41580-021-00407-0

Jiang, D., Liao, J., Duan, H., Wu, Q., Owen, G., Shu, C., et al. (2020). A machine learning-based prognostic predictor for stage III colon cancer. *Sci. Rep.* 10 (1), 10333. doi:10.1038/s41598-020-67178-0

Karhade, A. V., Bongers, M., Groot, O. Q., Cha, T. D., Doorly, T. P., Fogel, H. A., et al. (2021). Development of machine learning and natural language processing algorithms for preoperative prediction and automated identification of intraoperative vascular injury in anterior lumbar spine surgery. *Spine J.* 21 (10), 1635–1642. doi:10.1016/j.spinee.2020.04.001

Li, T., Fu, J., Zeng, Z., Cohen, D., Li, J., Chen, Q., et al. (2020). TIMER2.0 for analysis of tumor-infiltrating immune cells. *Nucleic Acids Res.* 48 (W1), W509–W514. doi:10.1093/nar/gkaa407

Liao, Y., Wang, J., Jaehnig, E. J., Shi, Z., and Zhang, B. (2019). WebGestalt 2019: Gene set analysis toolkit with revamped UIs and APIs. *Nucleic Acids Res.* 47 (W1), W199–W205. doi:10.1093/nar/gkz401

Liu, J., Dong, C., Jiang, G., Lu, X., Liu, Y., and Wu, H. (2020). Transcription factor expression as a predictor of colon cancer prognosis: A machine learning practice. *BMC Med. Genomics* 13 (9), 135. doi:10.1186/s12920-020-00775-0

Masud, M., Sikder, N., Nahid, A. A., Bairagi, A. K., and AlZain, M. A. (2021). A machine learning approach to diagnosing lung and colon cancer using a deep learning-based classification framework. *Sensors (Basel)* 748 (3). doi:10.3390/s21030748

Miller, K. D., Nogueira, L., Mariotto, A. B., Rowland, J. H., Yabroff, K. R., Alfano, C. M., et al. (2019). Cancer treatment and survivorship statistics, 2019. *Ca. Cancer J. Clin.* 69 (5), 363–385. doi:10.3322/caac.21565

Moroy, T., Vassen, L., Wilkes, B., and Khandanpour, C. (2015). From cytopenia to leukemia: The role of Gfi1 and Gfi1b in blood formation. *Blood* 126 (24), 2561–2569. doi:10.1182/blood-2015-06-655043

Rodriguez-Alcazar, J. F., Ataide, M. A., Engels, G., Schmitt-Mabmunyo, C., Garbi, N., Kastenmuller, W., et al. (2019). Charcot-leyden crystals activate the NLRP3 inflammasome and cause IL-1β inflammation in human macrophages. *J. Immunol.* 202 (2), 550–558. doi:10.4049/jimmunol.1800107

Ru, B., Wong, C. N., Tong, Y., Zhong, J. Y., Zhong, S., Wu, W. C., et al. (2019). TISIDB: An integrated repository portal for tumor-immune system interactions. *Bioinformatics* 35 (20), 4200–4202. doi:10.1093/bioinformatics/btz210

Schmitt, M., and Greten, F. R. (2021). The inflammatory pathogenesis of colorectal cancer. *Nat. Rev. Immunol.* 21 (10), 653–667. doi:10.1038/s41577-021-00534-x

Siegel, R. L., Miller, K. D., Fuchs, H. E., and Jemal, A. (2022). Cancer statistics, 2022. *Ca. Cancer J. Clin.* 72 (1), 7–33. doi:10.3322/caac.21708

Su, J. (2018). A brief history of charcot-leyden crystal protein/galectin-10 research. *Molecules* 23 (11), E2931. doi:10.3390/molecules23112931

Szklarczyk, D., Gable, A. L., Nastou, K. C., Lyon, D., Kirsch, R., Pyysalo, S., et al. (2021). The STRING database in 2021: Customizable protein-protein networks, and functional characterization of user-uploaded gene/measurement sets. *Nucleic Acids Res.* 49 (D1), D605–D612. doi:10.1093/nar/gkaa1074

Tang, Z., Kang, B., Li, C., Chen, T., and Zhang, Z. (2019). GEPIA2: An enhanced web server for large-scale expression profiling and interactive analysis. *Nucleic Acids Res.* 47 (W1), W556–W560. doi:10.1093/nar/gkz430

Tohka, J., and van Gils, M. (2021). Evaluation of machine learning algorithms for health and wellness applications: A tutorial. *Comput. Biol. Med.* 132, 104324. doi:10.1016/j.compbiomed.2021.104324

Wilkerson, M. D., and Hayes, D. N. (2010). ConsensusClusterPlus: A class discovery tool with confidence assessments and item tracking. *Bioinformatics* 26 (12), 1572–1573. doi:10.1093/bioinformatics/btq170

Wu, P., Heins, Z. J., Muller, J. T., Katsnelson, L., de Bruijn, I., Abeshouse, A. A., et al. (2019). Integration and analysis of CPTAC proteomics data in the context of cancer genomics in the cBioPortal. *Mol. Cell. Proteomics* 18 (9), 1893–1898. doi:10.1074/mcp.TIR119.001673

Xia, C., Dong, X., Li, H., Cao, M., Sun, D., He, S., et al. (2022). Cancer statistics in China and United States, 2022: Profiles, trends, and determinants. *Chin. Med. J.* 135 (5), 584–590. doi:10.1097/CM9.0000000000002108

frontiers | Frontiers in Pharmacology

TYPE Original Research
PUBLISHED 23 September 2022
DOI 10.3389/fphar.2022.972411

OPEN ACCESS

EDITED BY
Francesco Paolo Busardò,
Marche Polytechnic University, Italy

REVIEWED BY
Jing Yang,
First Affiliated Hospital of Zhengzhou University, China
Yurong Lai,
Gilead, United States

*CORRESPONDENCE
Dongyang Liu,
liudongyang@vip.sina.com

SPECIALTY SECTION
This article was submitted to Drug Metabolism and Transport, a section of the journal Frontiers in Pharmacology

RECEIVED 18 June 2022
ACCEPTED 12 September 2022
PUBLISHED 23 September 2022

CITATION
Zhang M, Yu Z, Yao X, Lei Z, Zhao K, Wang W, Zhang X, Chen X and Liu D (2022), Prediction of pyrotinib exposure based on physiologically-based pharmacokinetic model and endogenous biomarker. *Front. Pharmacol.* 13:972411. doi: 10.3389/fphar.2022.972411

Prediction of pyrotinib exposure based on physiologically-based pharmacokinetic model and endogenous biomarker

Miao Zhang[1,2,3], Zhiheng Yu[1,2,4], Xueting Yao[1,2], Zihan Lei[1,2,3], Kaijing Zhao[5], Wenqian Wang[5], Xue Zhang[5], Xijing Chen[3] and Dongyang Liu[1,2]*

[1]Drug Clinical Trial Center, Peking University Third Hospital, Beijing, China, [2]Institute of Medical Innovation, Peking University Third Hospital, Beijing, China, [3]School of Basic Medicine and Clinical Pharmacy, China Pharmaceutical University, Nanjing, China, [4]Department of Obstetrics and Gynecology, Peking University Third Hospital, Beijing, China, [5]Jiangsu Hengrui Pharmaceuticals Co, Ltd, Shanghai, China

Pyrotinib, a novel irreversible epidermal growth factor receptor dual tyrosine kinase inhibitor, is mainly (about 90%) eliminated through cytochrome P450 (CYP) 3A mediated metabolism *in vivo*. Meanwhile, genotype is a key factor affecting pyrotinib clearance and 4β-hydroxycholesterol is an endogenous biomarker of CYP3A activity that can indirectly reflect the possible pyrotinib exposure. Thus, it is necessary to evaluate the clinical drug-drug interactions (DDI) between CYP3A perpetrators and pyrotinib, understand potential exposure in specific populations including liver impairment and geriatric populations, and explore the possible relationships among pyrotinib exposure, genotypes and endogenous biomarker. Physiologically-based pharmacokinetic (PBPK) model can be used to replace prospective DDI studies and evaluate external and internal factors that may influence system exposure. Herein, a basic PBPK model was firstly developed to evaluate the potential risk of pyrotinib coadministration with strong inhibitor and guide the clinical trial design. Subsequently, the mechanistic PBPK model was established and used to quantitatively estimate the potential DDI risk for other CYP3A modulators, understand the potential exposure of specific populations, including liver impairment and geriatric populations. Meanwhile, the possible relationships among pyrotinib exposure, genotypes and endogenous biomarker were explored. With the help of PBPK model, the DDI clinical trial of pyrotinib coadministration with strong inhibitor has been successfully completed, some DDI clinical trials may be waived based on the predicted results and clinical trials in specific populations can be reasonably designed. Moreover, the mutant genotypes of CYP3A4*18A and CYP3A5*3 were likely to have a limited influence on pyrotinib clearance, and the genotype-independent linear correlation coefficient between endogenous biomarker and system exposure was larger than 0.6. Therefore, based on the reliable predicted results and the linear correlations between pyrotinib exposure and endogenous biomarker, dosage adjustment of pyrotinib can be designed for clinical practice.

KEYWORDS

pyrotinib, PBPK model, clinical trial design, drug-drug interaction, 4βhydroxycholesterol, genotype

Introduction

Pyrotinib is a novel irreversible epidermal growth factor receptor/human epidermal growth factor receptor 2 (EGFR/HER2) dual tyrosine kinase inhibitor, which can covalently bind to adenosine triphosphate binding sites of intracellular EGFR/HER2 to prevent self-phosphorylation or down-regulation of signal transduction, thereby inhibiting the growth of tumor. Currently, multiple clinical trials are evaluating the anticancer efficiency of pyrotinib in various solid tumors. Successfully, pyrotinib has obtained promising antitumor activity and acceptable tolerance in the treatment of patients with HER2-positive metastatic breast cancer and non-small-cell lung cancer harboring HER2 mutations (Ma et al., 2019; Zhou et al., 2020). With its unique advantages, pyrotinib has obtained the first global conditional approval for the treatment of HER2-positive, advanced or metastatic breast cancer in China (Blair, 2018; Ma et al., 2019).

Pyrotinib is a clinical oral dosage form with a therapeutic dose of 400 mg, and its bioavailability will be increased when taken with meals. The absorption of pyrotinib is slow with a median time to maximum plasma concentration (T_{max}) of 3–5 h under different dosage regimens. Binding of pyrotinib to plasma proteins is strong (~95%), leading to its wide distribution (Apparent volume of distribution, V_d/F, ~4000 L) *in vivo*. Mass balance study (CTR20170528) has shown that about 92.6% (Meng et al., 2019) of the radioactivity is recovered from excretions, including limited parent drug in feces (~12.0% in fasted state and ~3.27% in fed state) and urine (~0.13%). Based on the biliary intubation experiment in rats, biliary excretion is likely to have minimal effects (~0.16%) on pyrotinib clearance in human. Last but not least, metabolism plays the major role for pyrotinib clearance and cytochrome P450 3A (CYP3A), responsible for approximately 90% of pyrotinib metabolism, is the predominant isoform (Zhu et al., 2016).

Hence, pyrotinib may be a sensitive CYP3A substrate and drug-drug interaction (DDI) studies should be conducted in clinic according to the guidance of cytochrome P450 enzyme and transporter mediated drug interactions (Food and Drug Administration, 2020). Considering that physiologically based pharmacokinetic (PBPK) model can be used to narrow the knowledge gap between *in vitro* and *in vivo* (Grimstein et al., 2019), the pyrotinib PBPK model is proposed to develop firstly according to the preclinical data and limited clinical PK data, including single-ascending dose (SAD) and multiple-ascending dose (MAD) so as to support the clinical trial design of pyrotinib coadministration with perpetrators. Moreover, PBPK models can be used in lieu of some prospective DDI studies after the mechanistic model validated by pharmacokinetic (PK) data and information from DDI studies that used strong index perpetrators (Food and Drug Administration, 2020). Therefore, the DDI studies of pyrotinib *in vivo* are planned to conduct with strong inhibitor/inducer as the prospective clinical trials, and then use the PBPK model to estimate the effects of other CYP3A modulators on the exposure of pyrotinib *in vivo*. Likewise, patients with hepatic dysfunction or senile patients who have the weaken hepatic metabolic rate may have higher levels of pyrotinib exposure (Hunt et al., 1992; Elbekai et al., 2004), and evaluating the potential exposure of pyrotinib in these populations by the mechanistic PBPK model can provide scientific and reasonable suggestions for the designs of corresponding clinical trials.

Moreover, individual difference of CYP3A expression levels can also influence the exposure of substrate, which may be caused by changes in protein abundance under different genotypes (Tracy et al., 2016). CYP3A has several genetic variations and CYP3A4*1G, CYP3A4*18A and CYP3A5*3 have shown a high mutation frequency in the Chinese (Hu et al., 2005, 2006; Du et al., 2007), which can significantly impact the activity of isozymes (Kuehl et al., 2001; Fukushima-Uesaka et al., 2004). Cholesterol is catalyzed by CYP3A to form 4β-hydroxylcholesterol (4β-OHC) and the molar ratio (4β-OHC/CHO) of 4β-OHC to total cholesterol (CHO) is an endogenous biomarker of hepatic CYP3A activity (Bodin et al., 2001; Gravel et al., 2019). Thus, the relationships among pyrotinib exposure, genotypes and the biomarker are worthy of exploration to know the possible exposure in advance.

Herein, we are aimed to: 1) develop a basic pyrotinib PBPK model based on the limited clinical data to support clinical trial design of pyrotinib coadministration with strong perpetrator; 2) establish a mechanistic PBPK model to evaluate the potential exposure of pyrotinib under different DDI scenarios and in specific populations; 3) explore possible relationships among clearance of pyrotinib, gene polymorphism and biomarker, and 4) simulate pyrotinib exposure under various genotypes with corresponding protein abundance information *in vivo* to comprehensively integrate limitation and knowledge gaps and support reasonable dosage adjustment in clinical practice.

Materials and methods

Study strategy

Firstly, the basic pyrotinib PBPK model was developed with the parameters both collected from preclinical and limited clinical data (SAD and MAD, NCT01937689) to describe the intracorporal process of the compound and then to support the

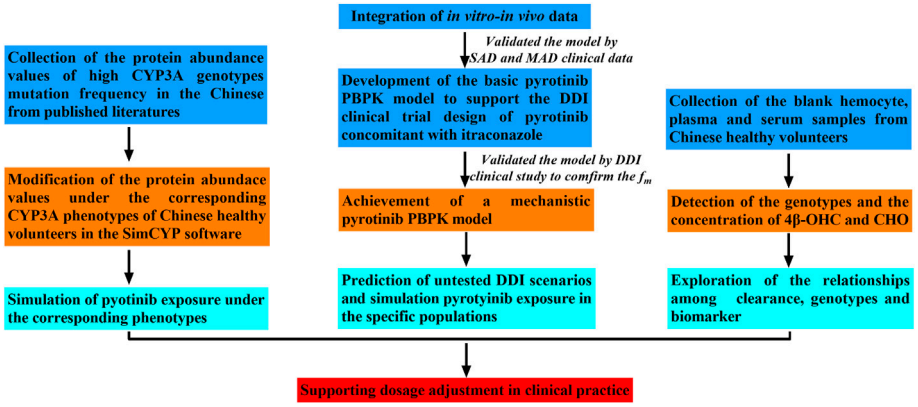

FIGURE 1
Strategy map for this study.

TABLE 1 Summary of the simulation scenarios in this study.

(A) Simulation scenarios of potential DDI			
Perpetrators	Dosage regimens	Treatment (days)	Pyrotinib dosage regimens
Itraconazole (Strong inhibitor)	200 mg (D1-D10, QD[a])	10	400 mg on D4
Ketoconazole (Strong inhibitor)	200 mg (D1-D11, BID[b])	11	400 mg on D5
Clarithromycin (Strong inhibitor)	250 mg (D1-D11, BID)	11	400 mg on D5
Erythromycin (Moderate inhibitor)	500 mg (D1-D11, QID[c])	11	400 mg on D5
Diltiazem (Moderate inhibitor)	60 mg (D1-D11, TID[d])	11	400 mg on D5
Fluconazole (Moderate inhibitor)	200 mg (D1-D14, QD)	14	400 mg on D8
Ciprofloxacin (Moderate inhibitor)	500 mg (D1-D11, BID)	11	400 mg on D5
Fluvoxamine (Mild inhibitor)	150 mg (D1-D11, BID)	11	400 mg on D5
Fluoxetine (Mild inhibitor)	40 mg (D1-D16, BID)	16	400 mg on D10
Efavirenz (Moderate inducer)	600 mg (D1-D15, QD)	15	400 mg on D9
(B) Simulation scenarios for specific populations with pyrotinib 400 mg			
Healthy Volunteers (20–50 years)			
Cirrhosis CP-A populations (20–50 years)			
Cirrhosis CP-B populations (20–50 years)			
Cirrhosis CP-C populations (20–50 years)			
Geriatrics populations (65–75, 75–85, and 85–95 years)			

[a]QD: quaque die.
[b]BID: bis in die.
[c]QID: qualer in die.
[d]TID: ter in die.

DDI clinical trial design. Secondly, in order to improve the prediction performance of the model, and confirm the contribution of CYP3A to the metabolism of pyrotinib, the basic model was optimized and the mechanistic PBPK model was formed. Multi-dimensional validation was carried out on the mechanistic PBPK model, including not only SAD and MAD (NCT01937689) data, which were the same as the validation data of the basic model, but also the data of pyrotinib coadministration with capecitabine (NCT02361112) and pyrotinib coadministration with itraconazole (NCT04479891). Thirdly, untested scenarios including pyrotinib coadministration with CYP3A modulators, pyrotinib administration in hepatic dysfunction and elderly populations were simulated with the mechanistic pyrotinib PBPK model. Moreover, genotypes of CYP3A4*1G, CYP3A4*18A and CYP3A5*3, and the concentrations of 4β-OHC and CHO were also detected based on the blank hemocyte/plasma/serum samples from eighteen Chinese (NCT04479891). Meanwhile, based on the published

protein abundance information of corresponding genotypes, the correlation between pyrotinib clearance and CYP3A5*3 allele was explored with the mechanistic model. Figure 1 displays the strategy diagram and Table 1 shows the simulation scenarios with the mechanistic PBPK model.

Development of mechanistic pyrotinib PBPK model

Since the basic pyrotinib PBPK model was originally developed to support clinical trial design, and the mechanistic PBPK model has been validated with multiple clinical data, only the final model parameters are presented here. The mechanistic pyrotinib PBPK model was developed using advanced dissolution, absorption and metabolism (ADAM) model in the SimCYP Population-Based Simulator (Version 19, SimCYP Limited, Sheffield, United Kingdom, Certara Company). The permeability of compound in Caco-2 Transwell model and dissolution profile in aqueous buffer were used to develop the absorption model. Full-PBPK model was used to describe the distribution characteristics of pyrotinib. The volume of distribution at steady state (V_{ss}) and partition coefficient of tissue to plasma (K_p) were predicted. Meanwhile, K_p scalar of 1.80 was used to match the observed concentration-time profiles. Elimination of pyrotinib in PBPK model was jointly depicted by intrinsic clearance of human recombinant CYP isoforms (CL_{int}), renal clearance (CL_R), additional systemic clearance ($CL_{additional\ systemic}$) and biliary clearance (CL_{int_Bile}) in SimCYP. The contribution of each CYP isoform to the overall hepatic metabolism was calculated according to the protein abundance of the specific CYP450 isoforms in human liver and its corresponding CL_{int}. Moreover, the contributions of kidney, unknown pathway and bile to the clearance of pyrotinib were obtained from the results of mass balance study in human (CTR20170528) and biliary intubation experiment in rats. Except for the CL_R (0.17 L/h) that were collected from clinical data, CL_{int_Bile} (0.4 μL/min/10^6) and $CL_{additional\ systemic}$ (4.5 L/h) were fitted according to the contribution percentage of pyrotinib clearance mentioned above and the PK profiles of pyrotinib in SAD clinical study. Physicochemical parameters, such as protein binding, B/P ratio and molecular weight (MW) were obtained from experimental results *in vitro*. Log*P* and pK_a were predicted based on the structure of pyrotinib. The detailed model parameters are summarized in Supplementary Table S1 of supplemental file.

Model validation

The basic PBPK model was validated with limited clinical data, and the mechanistic PBPK model was fully validated with the clinical data that were obtained from the clinical studies of pyrotinib in healthy volunteers (SAD clinical study), the clinical studies of pyrotinib in breast cancer patients (MAD clinical study, NCT01937689), the efficacy study of pyrotinib coadministration with capecitabine (NCT02361112) and the DDI study of pyrotinib concomitant used with itraconazole (NCT04479891). The trial design in SimCYP Simulator was set to match population demographics (ethnicity, age and sex), dosage regimens and blood collection time points of each clinical study. The prediction performance of the mechanistic pyrotinib PBPK model was evaluated based on two criteria: 1) the observed values were within the 90% confidence interval (CI) of the predicted concentration-time profile; 2) the ratios of simulated area under the curve (*AUC*) and maximum concentration (C_{max}) values to those observed values were within a predefined boundary of 0.5 to 2.0-fold. All simulations were performed based on 10 trials with 10 subjects (n = 100).

Clinical trial design of pyrotinib coadministration with itraconazole

Considering the selectivity, safety, quantitative predictability and maximum inhibition of inhibitor (Ke et al., 2014), itraconazole was selected as the strong inhibitor in pyrotinib clinical DDI study. To identify the optimal design of itraconazole concomitant with pyrotinib in clinical DDI study, a series of dosage regimens of itraconazole and pyrotinib, including dose, interval and duration, were simulated with the basic PBPK model. Combined with the safety of pyrotinib and itraconazole, the predicted AUC ratio (AUCR) and C_{max} ratio (C_{max} R) of pyrotinib coadministration with itraconazole versus pyrotinib given alone were used as the reference for the design of dosage regimens. All simulations were performed based on representative population (SimCYP, Version 18). The simulated scenarios of itraconazole combined with pyrotinib are shown in Supplementary Table S2 of supplemental file.

Pharmacokinetic DDI simulations

The mechanistic pyrotinib PBPK model was used to simulate the untested clinical DDI scenarios and estimate the effect of strong CYP3A inhibitors (clarithromycin, ketoconazole and itraconazole), moderate CY3A inhibitors (fluconazole, erythromycin, ciprofloxacin and diltiazem), mild CY3A inhibitors (fluvoxamine, fluoxetine and cyclosporine) and moderate CYP3A inducer (efavirenz) on the exposure of pyrotinib. “Chinese Healthy Volunteer” (20–50 years old, male:female = 1:1) and the default model of perpetrators within SimCYP were directly used for DDI simulations. To maximize the effect of perpetrators on pyrotinib, perpetrators were taken according to the clinical maximum dosage regimen,

and a single dose of pyrotinib (400 mg, recommended dose in clinical treatment) was taken after the predicted plasma concentration of perpetrators reached the steady state. The detailed dosage regimens of untested DDI scenarios are shown in Table 1A.

Simulation of pyrotinib administration in specific populations

The PK characteristics of pyrotinib in specific populations, including Chinese healthy volunteers, healthy volunteers (Caucasians), geriatrics and cirrhotic patients with Child-Pugh scores (CP) A, B and C (corresponding to mild, moderate and severe hepatic impairment) were simulated as well. As only 0.13% parent drug was excreted by kidney, the PK characteristic of renal impairment population was not estimated in this study. Except for Chinese healthy volunteers, other populations in SimCYP population library were Caucasians, so healthy volunteer (20–50 years old) was used as the baseline population. Geriatric population was divided into three subsets including 65–75, 75–85 and 85–95 age groups. For other specific populations, the simulated age range was set to 20–50 years old. Unless otherwise specified, physiological models within SimCYP database were directly used and all the simulations in this part included 10 trials with 10 subjects (n = 100) with the same proportion of male to female. Ultimately, the comparison of 400 mg pyrotinib system exposure in a specific population to that of baseline population (Healthy Volunteers of 20–50 years old, male: female = 1:1) was calculated in order to quantify the potential influence of internal factors on pyrotinib exposure. The detailed dosage regimens of simulations in specific populations are shown in Table 1B.

Sample collection and detection of genotyping and endogenous biomarker

After overnight fasting, whole blood samples (before administration pyrotinib) were collected from 18 healthy volunteers participating in the DDI clinical study. The blood samples were immediately centrifuged at 2000×g, 4°C for 10 min. The hemocytes were collected for the detection of genotyping and the well-known single nucleotide polymorphisms (SNP) including CYP3A4*1G (rs2241480), CYP3A4*18A (rs28371759) and CYP3A5*3 (rs776746) were analyzed by polymerase chain reaction (PCR) and Sanger Sequencing. The content of serum CHO, one of the blood biochemical items, was detected during pre-enrollment screening (Day -2). The plasma samples were collected for the detection of 4β-OHC concentration by the method of LC-MS/MS. The detailed detection method of 4β-OHC concentration was as follows:

The ACQUITY UPLC® I Class HPLC system (Waters, United States) connected to the API5500 Triple Quad mass spectrometer equipped with the Analyst 1.63 software (AB Sciex, Darmstadt, Germany) was used for the quantitative analysis. Chromatographic separation was performed on a XBridgeTM BEH C18 XP Column (4.6 × 75 mm, 2.5 μm, Waters). The mobile phases were (A) aqueous solution containing 0.1% formic acid (LC/MS grade, Fisher Scientific, United States) and (B) methanol (HPLC grade, Fisher Chemical, United States). Gradient elution was used as follows: 95% B at 0–4.9 min with a flow rate of 0.8 ml/min, 95%–60% B at 4.9–5.0 min with a flow rate of 0.8 ml/min, 60%–98% B at 5.0–5.3 min with a flow rate of 0.8 ml/min, 98% B at 5.3–5.9 min with a flow rate of 1.0 ml/min, 98%–95% B at 5.9–6.0min with a flow rate of 1.0 ml/min, 95% B at 6.0–8.0min with a flow rate of 0.8 ml/min. The injection volume was 5 μL. Mass spectrometric analysis was performed using positive ESI in multiple reaction-monitoring (MRM) mode. Ion transitions were m/z 385.3→109.1 and m/z 392.5→109.1 for 4β-OHC (Sigma-Aldrich/Avanti, Germany) and 4β-hydroxycholesterol-d7 (Internal standard, Sigma-Aldrich/Avanti, Germany), respectively. The analyte 4β-OHC displayed a good linearity at the range of 5–500 ng/ml. The developed method was validated according to the latest FDA guidelines for bioanalytical method validation.

Prediction of pyrotinib exposure under various genotypes

Protein abundances of corresponding CYP3A4*1G, CYP3A4*18A and CYP3A5*3 genotypes in Chinese liver were retrieved from PubMed database with the keywords of "CYP3A4*1G/CYP3A4*18A/CYP3A5*3", "protein abundance" and "Chinese volunteers". Considering the inter-individual variation, protein abundance of individuals was obtained from literature (Xiao et al., 2019) by Plot Digitizer (Version 2.26, GetData, China). Variable coefficients were also calculated based on the observed values. The trial design in SimCYP Simulator was set to match the clinical study and the simulations were conducted based on 10 trials with 10 subjects (n = 100). In addition to changing the abundance of corresponding isoenzyme in the liver of Chinese physiological model, other parameters were directly used.

Statistical analyses

The statistical analyses about significance levels and correlation analyses were assessed with the GraphPad Prism Version 8.0 (GraphPad Software, San Diego, CA, United States), and p-value < 0.05 was used to estimate the significance.

Results

The dosage regimen of pyrotinib coadministration with itraconazole

Various dosage regimens (See Supplementary Table S2) of pyrotinib concomitant with strong inhibitor, itraconazole, were simulated with the basic PBPK model to explore the "worst-case" DDI scenario. The predicted DDI magnitude increased with the duration of itraconazole treatment, and the loading dose of itraconazole on the first day could also increase the inhibition of CYP3A4. Meanwhile, the increase of pyrotinib dose could not alter the value of *AUC*R. Since the predicted C_{max}R was lower than two and the clinical dose of pyrotinib was 400 mg per day, the low-dose pyrotinib (80 mg, single dose) and itraconazole (200 mg, QD for 17 days), dosage regimen G in Supplementary Table S2 of supplemental file, were used in the DDI clinical trial to obtain the potential maximum DDI effect while ensuring the safety and tolerability of subjects (Liu et al., 2021).

PBPK model development and validation

The mechanistic pyrotinib PBPK model was developed and validated based on preclinical and clinical data. The final pyrotinib PBPK model parameters were presented in Supplementary Table S1. The observed and simulated geomean plasma concentration-time profiles for single or multiple dose(s) of pyrotinib were shown in Supplementary Figures S1–S3. Ratios (predicted value vs. observed value) of main pharmacokinetic parameters were approximate to 0.80–1.25 folds (See Supplementary Figure S4). All of them indicated that the model could well capture the absorption, distribution and elimination characteristics of pyrotinib *in vivo*. In addition, the mechanistic PBPK model was also validated by the data from clinical DDI study. The predicted and observed pyrotinib concentration-time profiles in the presence and absence of itraconazole were well matched and presented in Supplementary Figure S5, and the ratios of PK parameter between predicted values and observed values were within 0.80–1.25 folds. Meanwhile, the predicted metabolism fraction (f_m) of CYP3A4 to the total clearance of pyrotinib was consistent with the experimental results (Zhu et al., 2016), which illustrated that pyrotinib PBPK model was a mechanistic model and could be used to simulate preset scenarios without further modification. The predicted contribution percentage of each organ/CYP isoform was shown in Supplementary Figure S6.

Evaluating the effects of perpetrators on pyrotinib exposure

The mechanistic PBPK model was used to evaluate the effects of perpetrators (CYP3A inhibitors and inducers) on pyrotinib exposure in "Chinese healthy volunteer" aged 20–50 years with the same proportion of male and female. In the presence of strong CYP3A inhibitors itraconazole, ketoconazole and clarithromycin, the $AUC_{0-168\ h}$ of pyrotinib (400 mg, clinical dosage) was increased by 7.4-fold, 7.5-fold and 3.4-fold, respectively, compared with that of 400 mg pyrotinib alone. Although clinical DDI study indicated that itraconazole could increase the systemic exposure of pyrotinib (80 mg) by 11.8-fold, this was obtained by comparing the $AUC_{0-168\ h}$ of pyrotinib in the DDI clinical study with the $AUC_{0-24\ h}$ of pyrotinib (80 mg) administrated alone. Actually, under the same comparison criteria ($AUC_{0-24\ h}$), pyrotinib exposure could be increased by 6.36-fold in the presence of itraconazole. Therefore, there was no contradiction between the predicted and observed values of pyrotinib exposure in the presence of itraconazole. The pyrotinib exposure increased by 7.1-fold, 2.5-fold, 2.6-fold and 2.1-fold when combined with erythromycin, diltiazem, fluconazole and ciprofloxacin, respectively. However, erythromycin was an exception as its effect on pyrotinib exposure was similar to itraconazole. In fact, erythromycin was a time-dependent CYP 3A inhibitor, which had a potent impact on CYP3A isoenzyme (Yadav et al., 2018). The mild CYP3A inhibitors might also produce significant effects on the pyrotinib disposition due to that the predicted systemic exposure increased by 1.58-fold and 2.07-fold when pyrotinib combined with fluvoxamine and fluoxetine, respectively. CYP3A moderate inducer, efavirenz, appeared to significantly reduce the pyrotinib exposure (76%). Detailed results were shown in Figure 2.

Simulation results of pyrotinib exposure in specific populations

Since pyrotinib was mainly metabolized by the liver, the exposure of pyrotinib in the liver impairment and geriatrics was estimated. Compared with the baseline population, the liver impairment patients with CP score A, B and C had the increasing exposure along with the progression of disease, and the ratios of the main PK parameters ($AUC_{0\text{-}96\ h}$ and C_{max}) ranged from 1.62 to 5.42 and 1.24 to 3.09, respectively. The exposure of pyrotinib in geriatric population (aged 65–95 years) increased with age, and the detailed $AUC_{0\text{-}96\ h}$ increments were 79, 105 and 131% corresponding to geriatric with 65–75, 75–85 and 85–95 years old, respectively. Results were exhibited in Figure 3.

Relationships amont exposure, genotypes and endogenous biomarker

In the limited samples, CYP3A4*18A (rs28371759) and CYP3A5*3 (rs776746) exhibited high mutation frequency, while CYP3A4*1G (rs2241480) showed a monomorphic genotype. The clearance of pyrotinib in individuals with different genotypes was statistically significant (Figure 4A), and only the CYP3A5*3 gene mutation had the notable influence on 4β-OHC concentration or the molar ratio of 4β-OHC to CHO (Figures 4B,C). Moreover, a genotype-independent linear correlation was found between

10.3389/fphar.2022.972411

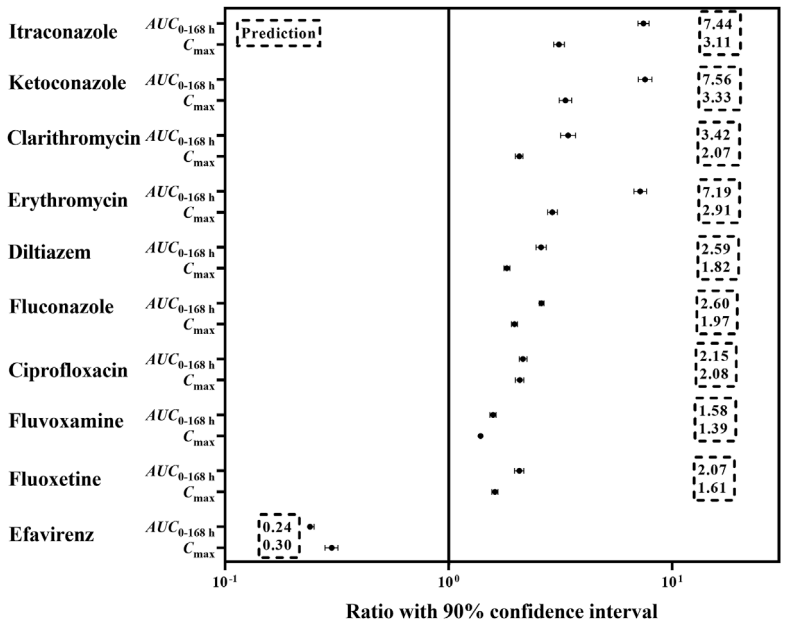

FIGURE 2
The predicted change in exposure after pyrotinib coadministration with potential CYP 3A perpetrators.

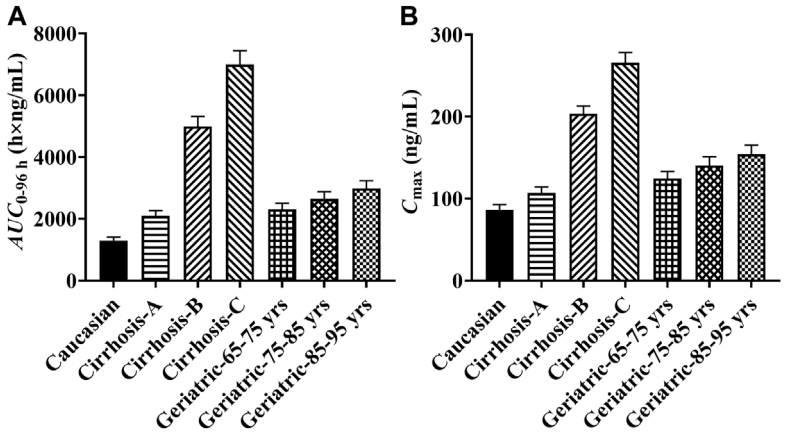

FIGURE 3
The predicted pyrotinib exposure in specific populations. (Note: yrs: years old; **(A)** comparison of pyrotinib $AUC_{0\text{-}96h}$ in specific populations; **(B)** comparison of pyrotinib C_{max} in specific populations).

exposure/clearance of pyrotinib and 4β-OHC concentration, and the correlation coefficient (r) was about 0.535, $p < 0.05$ (Figure 5A). Actually, there was a better genotype-independent linear correlation between the exposure/clearance of pyrotinib and 4β-OHC/CHO ($r > 0.6$, $p < 0.05$; Figure 5B). Therefore, the CYP3A basal expression level indeed had an impact on system exposure and plasma 4β-OHC concentration, and the ratio of 4β-OHC to CHO could be used as an indicator for pyrotinib exposure.

Exploring the effect of genotypes on the clearance of pyrotinib with the PBPK model

There were few published data about the protein abundance of CYP3A4*18A in the Chinese, and the median protein abundance values of corresponding CYP3A5*1/*1, CYP3A5*1/*3 and CYP3A5*3/*3 in Chinese population were obtained from reference

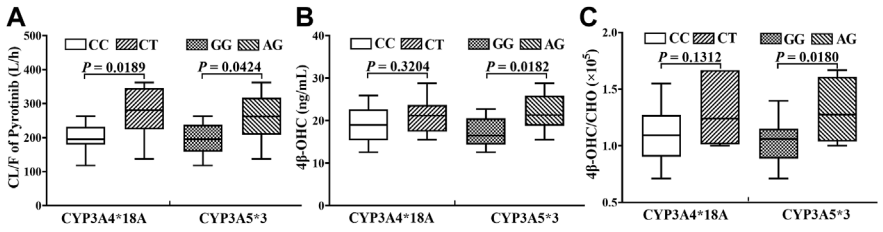

FIGURE 4
The statistical analyses results about the influence of genotypes on pyrotinib clearance **(A)** and endogenous biomarker **(B, C)**.

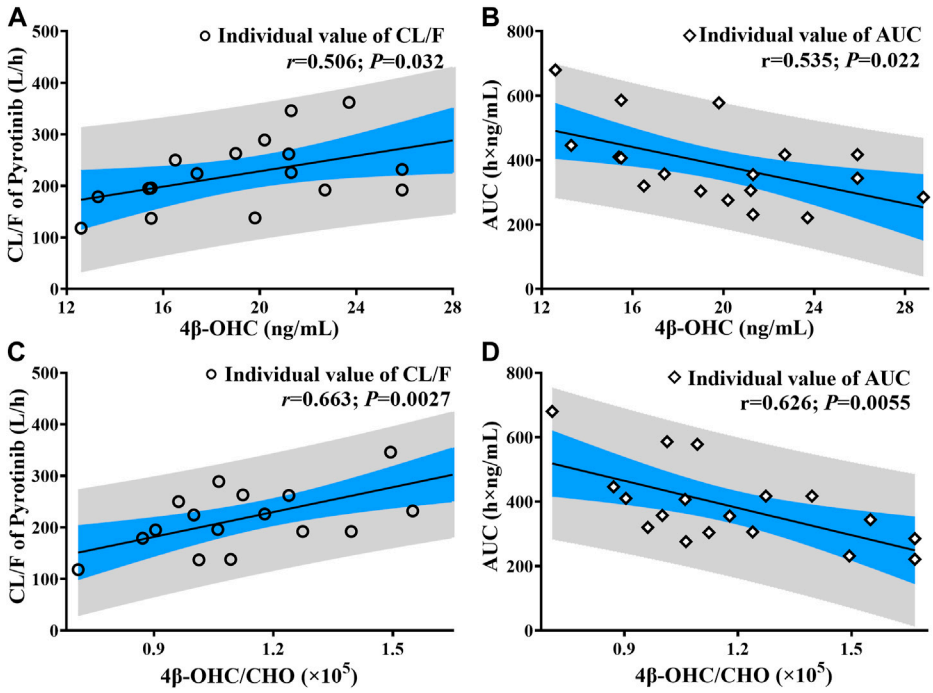

FIGURE 5
The correlation analysis results between pyrotinib clearance/exposure and endogenous biomarker (4β-OHC and 4β-OHC/CHO) (The black line: Linear fitting for individual value; r: correlation coefficient; P: statistical analysis results; **(A, C)** correlation analysis results between pyrotinib clearance and endogenous biomarker; **(B, D)**: correlation analysis results between pyrotinib AUC and endogenous biomarker).

(Xiao et al., 2019). The collected data were separately put into the liver module of Chinese population database to predict the *CL*/F of pyrotinib at different genotypes. Due to the small sample size (n = 18), only CYP3A5*1/*3 and CYP3A5*3/*3 genotypes were detected among those hemocyte samples. Thus, the predicted concentration-time profiles were validated according to the limited data. All of the observations were within the 90% confidence interval of the predicted values, which exhibited good prediction performance under corresponding protein abundance values. However, there was no significant difference in *CL*/F among different genotypes, and the *p*-value was 0.85. Validation results were shown in Figure 6.

Discussion

Although the basic PBPK model was not validated by PK data from the DDI study, the results of mass balance study and the renal excretion fraction in human are known (Meng et al., 2019), which provide the clues for speculating the fraction of metabolism. Moreover, combined with the contribution of CY3A to the metabolism (90%) (Zhu et al., 2016) and the intrinsic clearance of CYP3A to pyrotinib metabolism *in vitro*, the metabolism and elimination characteristics of pyrotinib were primary understood. To simplify the basic PBPK model and

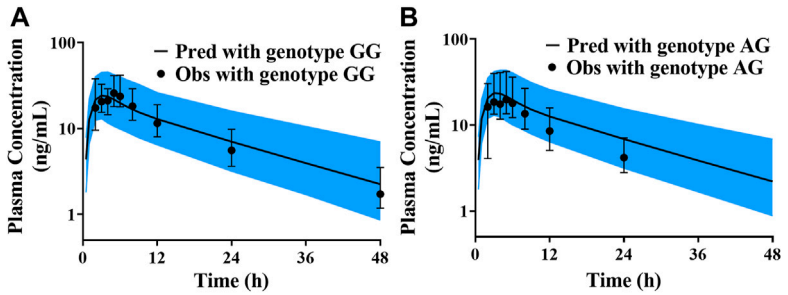

FIGURE 6
The validated results for pyrotinib exposure under different CYP3A5*3 genotypes **(A)** simulation and validated with the genotype of CYP3A5*3/*3; **(B)** simulation and validated with the genotype of CYP3A5*1/*3).

ensure the accuracy of metabolism and elimination evaluation, the first-order absorption model was used to describe the absorption characteristics by fitting the absorption parameters. After the basic PBPK model could capture the PK profiles of pyrotinib in SAD and MAD clinical trials with the predicted f_m of approximately 96.5%, the model was used to simulate various DDI dosage regimens. Actually, the predicted AUCR (population representative) was slightly overestimated observed value, and then the mechanistic PBPK model was established based on multiple *in vitro* and *in vivo* data.

With the "bottom-up" method, the mechanistic pyrotinib PBPK model was developed, which was able to capture the absorption and disposition characteristics of pyrotinib in healthy subjects and HER2 positive breast cancer patients at single dose, multiple-dose and DDI scenarios. Thus, the PBPK model can be used to quantitatively evaluate the influences of CYP3A perpetrators on pyrotinib exposure. As pyrotinib is mainly metabolized by CYP3A isoenzymes (f_m, ~90%) *in vitro* (Zhu et al., 2016), the potential inhibition may be exhibited after pyrotinib coadministration with erythromycin (CYP3A moderate inhibitor). Coincidentally, after coadministration with erythromycin (500 mg, three times a day) (Olkkola et al., 1993), the exposure of CYP3A substrate midazolam (f_m, ~96%) increased by 4.42-fold, which was similar to the 3.40-fold increase of pyrotinib exposure at the same dosing interval. Although clarithromycin is a strong CYP3A inhibitor, the 3.42-fold increment of pyrotinib exposure is less than that of itraconazole. Actually, clarithromycin (250 mg, twice daily) could enhance midazolam exposure by 3.57-fold (Yeates et al., 1996), and the megadose clarithromycin (2,500 mg, twice daily) could improve midazolam exposure by a factor of 7 (Gorski et al., 1998). Therefore, the DDI predicted results in this study are reliable for guiding dose adjustment. Though, the pyrotinib PBPK model was not validated by the clinical data of CYP3A inducer, the predicted low exposure of pyrotinib after coadministration with efavirenz also suggested that the potential impact of moderate CYP3A inducer on the pyrotinib efficacy should not be ignored, and the predicted result has been used as a reference for the design of corresponding clinical trial (NCT04680091).

In fact, the effect of rifampin, a strong CYP3A inducer, on the exposure of pyrotinib was also estimated *in vivo,* and the *AUC* and C_{max} of pyrotinib were reduced by 96 and 89%, respectively. However, pyrotinib PBPK model is inadequate to predict the effect of rifampin on pyrotinib exposure with the default rifampin model in SimCYP. Considering that the lower exposure may lead to inefficacious concentration and the f_m of pyrotinib PBPK model has been verified by the clinical data of itraconazole concomitant used with pyrotinib, the rifampin model is no longer optimized. Actually, the rifampin model in the SimCYP software cannot accurately capture the observed concentration-time profiles in some case (Wagner et al., 2016) because of the complex drug interaction mechanisms associated with rifampin, such as the induction of CYP3A isoform and intestinal P-gp in human by rifampin (Greiner et al., 1999; Westphal et al., 2000).

The mass balance (400 mg, single dose) study in human subjects showed that after administration pyrotinib under fed state, about 0.13 and 3.27% parent drug were secreted and excreted through urine and feces, respectively. In addition, about 0.16% of the parent drug was excreted by bile in rats. Therefore, P-gp has little effect on the elimination of pyrotinib in the kidney and liver. Although pyrotinib is a compound with weak permeability, food can significantly reduce the excretion of pyrotinib compared with taking pyrotinib under fasted state (~12%). Hence, intestinal P-gp has the finite role in the absorption of pyrotinib under fed state. As rifampin was concomitant administrated with pyrotinib under fed state, the low exposure of pyrotinib might be caused by the overexpression of CYP3A. Although itraconazole can also inhibit the efflux of P-gp (Mathis and Friedman, 2001), the limited inhibition may be caused by itraconazole according to the above discussion.

Sensitive analyses of the unmeasured parameters, such as log *P*, $CL_{additional\ systemic}$ and CL_{int_Bile} were performed to estimate their rationality. Meanwhile, the importance of P-gp transporter was also assessed. Noteworthily, all of these parameters had no significant effects on the

prediction performance of pyrotinib exposure. Considering the robustness of pyrotinib PBPK model and the pyrotinib disposition characteristic, the pyrotinib PK in liver impairment and geriatric populations were simulated. Because the specific populations in SimCYP population library were developed based on Caucasians, pyrotinib exposure under 400 mg (recommended dosage in clinical practice) in healthy subjects (20–50 years old) was served as a reference for safety. Since genotype-independent linear correlation exists between dose and exposure, dosage adjustment can be designed according to the predicted results for future clinical trials in liver impairment and geriatric populations.

Genotypes of CY3A4*18A (rs28371759) and CYP3A5*3 (rs776746) have shown high-frequency in the Chinese (Hu et al., 2005), and can impact the clearance of pyrotinib according to the results of a clinical trial in eighteen Chinese healthy volunteers after taking 80 mg of pyrotinib. The gene mutation of CY3A4*18A has the subtle influence on 4β-OHC content, and whether the molar ratio (4β-OHC/CHO) can be used as the biomarker of CYP3A4*18 metabolic activity may depend on the type of substrate (Kang et al., 2009). Although the samples used for the detection of 4β-OHC and CHO contents were not collected at the same time, both samples were taken from the same person who fasted overnight. Moreover, 4β-OHC has a long half-life (about 60 h) (Bodin et al., 2002) leading to a stable content of 4β-OHC *in vivo*. Therefore, with the genotype-independent linear correlation between endogenous biomarker and pyrotinib exposure/clearance, the possible system exposure can be obtained in advance to provide a reference for precision medication.

Based on the limited protein abundance values of CYP3A5*3 mutant and wild types in Chinese population, the pyrotinib exposure was simulated (10 trials with 10 subjects) under the corresponding CYP3A5 protein abundance values. However, the predicted results were almost the same among the genotypes of CYP3A5*1/*1, CYP3A5*1/*3 and CYP3A5*3/*3. The phenotype of CYP3A5 isoenzyme is related to the expression of CYP3A5*3 allele, which can encode an abnormal splicing mRNA with a premature termination codon, resulting in the loss of CYP3A5 expression (Kuehl et al., 2001) and then reduce the clearance of substrate compound. However, there exists a correlation between the abundance of CYP3A4 and CYP3A5 (Lin et al., 2002), and the pyrotinib is rarely metabolized by CYP3A5 isoform, which may lead to the approximate simulation results. Moreover, both CYP3A4*18A and CYP3A5*3 genotypes are mutants, and the heterozygotes of CYP3A4*18 A (7/18) and CYP3A5*3 (9/18) are found in the same individual, which may result in the high clearance with the large abundance value of CYP3A4 and CYP3A5 *in vivo*. Nevertheless, the observed geomean *AUC* ratio of homozygote to heterozygote is 1.31, indicating that the mutant genotypes cannot produce powerful effects on the safety. Hence, there is no need to pay too much attention to the genotypes of CYP3A.

Throughout the approved new drugs by FDA between 2015 and 2019, mechanistic PBPK model has become an effective means to help applicant to waive some DDI clinical trials. Actually, in the early stages of DDI clinical trial design, the pyrotinib PBPK model, validated only by SAD and MAD clinical data, was used to simulate potential DDI scenarios to help researchers develop a reliable dosage regimen. Hence, PBPK model is a useful tool in the whole process of new drug development. Likewise, in this study, the mechanistic pyrotinib PBPK model would allow a conservative evaluation for the effects of CYP3A inhibitors on pyrotinib exposure. Meanwhile, the predicted pyrotinib exposure in the specific populations including liver impairment and geriatric can also be used as a reference for clinical trial in the future. Furthermore, the genotype-independent linear correlation between endogenous biomarker and pyrotinib exposure can provide a simple and convenient method to predict the system exposure in advance. Due to the underestimation, the model is inadequate to predict the effects of CYP3A inducer on the pyrotinib exposure. Actually, rifampin, a strong CYP3A inducer, has the unlimited potential to induce the expression of CYP isoforms and transporters, which exceed the predictive power of rifampin model built-in SimCYP, such as abemaciclib (Posada et al., 2020), palbociclib (Yu et al., 2017), ixazomib (Gupta et al., 2018), upadacitinib (Food and Drug Administration, 2019) and so on. Therefore, it is crucial and urgent to develop a verifiable rifampin model with multiple inductive mechanisms. In addition, PBPK model is sufficient to simulate the effects of gene mutations on the exposure of one compound (Food and Drug Administration, 2018). However, limited protein abundance values and small sample sizes genetic testing may result in insignificant differences in the predicted results. Thus, it is necessary and meaningful to study the correlation between CYP3A4*18A genotype and protein abundance in the future.

Conclusion

Pyrotinib PBPK model is used to support clinical trial design and new drug marketing application, providing a successful case for the application of PBPK model in new drug development. Although, the basic pyrotinib PBPK model was developed without the validation of DDI clinical data, the mass balance study *in vivo* and metabolic study *in vitro* were the fundamental data to ensure the accuracy of the disposition. Subsequently, the mechanistic PBPK model was established, and validated by the clinical DDI PK data. Therefore, the mechanistic model can be used to explore untested scenarios such as DDI and taken in specific populations to assist in dosage regimen design, inform

regulatory decisions and support drug labeling. Moreover, the genotype-independent linear correlation coefficients between biomarker and the system exposure of pyrotinib were obtained, which provided another approach for scientific exploration of pyrotinib exposure. Therefore, dosage adjustment of pyrotinib can be designed by the mechanistic PBPK model and endogenous biomarker in clinical practice.

Data availability statement

The original contributions presented in the study are included in the article/Supplementary Material, further inquiries can be directed to the corresponding author.

Ethics statement

The studies involving human participants were reviewed and approved by the Second Hospital of Anhui Medical University, Ethics Committee. The patients/participants provided their written informed consent to participate in this study.

Author contributions

DL designed the research; MZ performed the research and wrote the manuscript; ZY and ZL conducted quality control on the research results; XY and XC provided some suggestions; KZ, WW, and XZ reviewed the manuscript and provided the clinical data.

Funding

This work was supported by Key Clinical Projects of Peking University Third Hospital (No. BYSY2018063).

Conflict of interest

KZ, WW, and XZ were employed by the company Jiangsu Hengrui Pharmaceuticals Co., Ltd.

The remaining authors declare that the research was conducted in the absence of any commercial or financial relationships that could be construed as a potential conflict of interest.

Publisher's note

Supplementary material

The Supplementary Material for this article can be found online at: https://www.frontiersin.org/articles/10.3389/fphar.2022.972411/full#supplementary-material

References

Blair, H. A. (2018). Pyrotinib: First global approval. *Drugs* 78, 1751–1755. doi:10.1007/s40265-018-0997-0

Bodin, K., Bretillon, L., Aden, Y., Bertilsson, L., Broomé, U., Einarsson, C., et al. (2001). Antiepileptic drugs increase plasma levels of 4beta-hydroxycholesterol in humans: evidence for involvement of cytochrome p450 3A4. *J. Biol. Chem.* 276, 38685–38689. doi:10.1074/jbc.M105127200

Bodin, K., Andersson, U., Rystedt, E., Ellis, E., Norlin, M., Pikuleva, I., et al. (2002). Metabolism of 4 beta -hydroxycholesterol in humans. *J. Biol. Chem.* 277, 31534–31540. doi:10.1074/jbc.M201712200

Du, J., Yu, L., Wang, L., Zhang, A., Shu, A., Xu, L., et al. (2007). Differences in CYP3A41G genotype distribution and haplotypes of CYP3A4, CYP3A5 and CYP3A7 in 3 Chinese populations. *Clin. Chim. Acta.* 383, 172–174. doi:10.1016/j.cca.2007.04.027

Elbekai, R. H., Korashy, H. M., and El-Kadi, A. O. (2004). The effect of liver cirrhosis on the regulation and expression of drug metabolizing enzymes. *Curr. Drug Metab.* 5, 157–167. doi:10.2174/1389200043489054

Food and Drug Administration (2018). Multi-discipline review for doptelet. . Available at: https://www.accessdata.fda.gov/drugsatfda_docs/nda/2018/210238Orig1s000MultidisciplineR.pdf (Accessed May 21, 2018).

Food and Drug Administration (2019). Clinical Pharmacology and biopharmaceutics review(s) for upadacitinib. Available at: https://www.accessdata.fda.gov/drugsatfda_docs/nda/2019/211675Orig1s000ClinPharmR.pdf (Accessed August 16, 2019).

Food and Drug Administration (2020). Clinical drug interaction studies-cytochrome P450 enzyme-and transporter-mediated drug interactions. Guidance for industry. Available at: https://www.fda.gov/media/134581/download (Access January 23, 2020).

Fukushima-Uesaka, H., Saito, Y., Watanabe, H., Shiseki, K., Saeki, M., Nakamura, T., et al. (2004). Haplotypes of CYP3A4 and their close linkage with CYP3A5 haplotypes in a Japanese population. *Hum. Mutat.* 23, 100. doi:10.1002/humu.9210

Gorski, J. C., Jones, D. R., Haehner-Daniels, B. D., Hamman, M. A., O'Mara, E. M., Jr, and Hall, S. D. (1998). The contribution of intestinal and hepatic CYP3A to the interaction between midazolam and clarithromycin. *Clin. Pharmacol. Ther.* 64, 133–143. doi:10.1016/S0009-9236(98)90146-1

Gravel, S., Chiasson, J. L., Gaudette, F., Turgeon, J., and Michaud, V. (2019). Use of 4β-hydroxycholesterol plasma concentrations as an endogenous biomarker of CYP3A activity: Clinical validation in individuals with type 2 diabetes. *Clin. Pharmacol. Ther.* 106, 831–840. doi:10.1002/cpt.1472

Greiner, B., Eichelbaum, M., Fritz, P., Kreichgauer, H. P., von Richter, O., Zundler, J., et al. (1999). The role of intestinal P-glycoprotein in the interaction of digoxin and rifampin. *J. Clin. Invest.* 104, 147–153. doi:10.1172/JCI6663

Grimstein, M., Yang, Y., Zhang, X., Grillo, J., Huang, S. M., Zineh, I., et al. (2019). Physiologically based pharmacokinetic modeling in regulatory science: An update from the U.S. Food and drug administration's office of clinical Pharmacology. *J. Pharm. Sci.* 108, 21–25. doi:10.1016/j.xphs.2018.10.033

Gupta, N., Hanley, M. J., Venkatakrishnan, K., Bessudo, A., Rasco, D. W., Sharma, S., et al. (2018). Effects of strong CYP3A inhibition and induction on the pharmacokinetics of ixazomib, an oral proteasome inhibitor: Results of drug-drug interaction studies in patients with advanced solid tumors or lymphoma and a physiologically based pharmacokinetic analysis. *J. Clin. Pharmacol.* 58, 180–192. doi:10.1002/jcph.988

Hu, Y. F., He, J., Chen, G. L., Wang, D., Liu, Z. Q., Zhang, C., et al. (2005). CYP3A5*3 and CYP3A4*18 single nucleotide polymorphisms in a Chinese population. *Clin. Chim. Acta.* 353, 187–192. doi:10.1016/j.cccn.2004.11.005

Hu, Y. F., Qiu, W., Liu, Z. Q., Zhu, L. J., Liu, Z. Q., Tu, J. H., et al. (2006). Effects of genetic polymorphisms of CYP3A4, CYP3A5 and MDR1 on cyclosporine pharmacokinetics after renal transplantation. *Clin. Exp. Pharmacol. Physiol.* 33, 1093–1098. doi:10.1111/j.1440-1681.2006.04492.x

Hunt, C. M., Westerkam, W. R., Stave, G. M., and Wilson, J. A. (1992). Hepatic cytochrome P-4503A (CYP3A) activity in the elderly. *Mech. Ageing Dev.* 64, 189–199. doi:10.1016/0047-6374(92)90106-n

Kang, Y. S., Park, S. Y., Yim, C. H., Kwak, H. S., Gajendrarao, P., Krishnamoorthy, N., et al. (2009). The CYP3A4*18 genotype in the cytochrome P450 3A4 gene, a rapid metabolizer of sex steroids, is associated with low bone mineral density. *Clin. Pharmacol. Ther.* 85, 312–318. doi:10.1038/clpt.2008.215

Ke, A. B., Zamek-Gliszczynski, M. J., Higgins, J. W., and Hall, S. D. (2014). Itraconazole and clarithromycin as ketoconazole alternatives for clinical CYP3A inhibition studies. *Clin. Pharmacol. Ther.* 95, 473–476. doi:10.1038/clpt.2014.41

Kuehl, P., Zhang, J., Lin, Y., Lamba, J., Assem, M., Schuetz, J., et al. (2001). Sequence diversity in CYP3A promoters and characterization of the genetic basis of polymorphic CYP3A5 expression. *Nat. Genet.* 27, 383–391. doi:10.1038/86882

Lin, Y. S., Dowling, A. L., Quigley, S. D., Farin, F. M., Zhang, J., Lamba, J., et al. (2002). Co-regulation of CYP3A4 and CYP3A5 and contribution to hepatic and intestinal midazolam metabolism. *Mol. Pharmacol.* 62, 162–172. doi:10.1124/mol.62.1.162

Liu, Y., Zhang, Q., Lu, C., and Hu, W. (2021). Multiple administrations of itraconazole increase plasma exposure to pyrotinib in Chinese healthy adults. *Drug Des. Devel. Ther.* 15, 2485–2493. doi:10.2147/DDDT.S312310

Ma, F., Ouyang, Q., Li, W., Jiang, Z., Tong, Z., Liu, Y., et al. (2019). Pyrotinib or lapatinib combined with capecitabine in HER2-positive metastatic breast cancer with prior taxanes, anthracyclines, and/or trastuzumab: A randomized, phase II study. *J. Clin. Oncol.* 37, 2610–2619. doi:10.1200/JCO.19.00108

Mathis, A. S., and Friedman, G. S. (2001). Coadministration of digoxin with itraconazole in renal transplant recipients. *Am. J. Kidney Dis.* 37, E18. doi:10.1053/ajkd.2001.21363

Meng, J., Liu, X. Y., Ma, S., Zhang, H., Yu, S. D., Zhang, Y. F., et al. (2019). Metabolism and disposition of pyrotinib in healthy male volunteers: covalent binding with human plasma protein. *Acta Pharmacol. Sin.* 40, 980–988. doi:10.1038/s41401-018-0176-6

Olkkola, K. T., Aranko, K., Luurila, H., Hiller, A., Saarnivaara, L., Himberg, J. J., et al. (1993). A potentially hazardous interaction between erythromycin and midazolam. *Clin. Pharmacol. Ther.* 53, 298–305. doi:10.1038/clpt.1993.25

Posada, M. M., Morse, B. L., Turner, P. K., Kulanthaivel, P., Hall, S. D., and Dickinson, G. L. (2020). Predicting clinical effects of CYP3A4 modulators on abemaciclib and active metabolites exposure using physiologically based pharmacokinetic modeling. *J. Clin. Pharmacol.* 60, 915–930. doi:10.1002/jcph.1584

Tracy, T. S., Chaudhry, A. S., Prasad, B., Thummel, K. E., Schuetz, E. G., Zhong, X. B., et al. (2016). Interindividual variability in cytochrome P450-mediated drug metabolism. *Drug Metab. Dispos.* 44, 343–351. doi:10.1124/dmd.115.067900

Wagner, C., Pan, Y., Hsu, V., Sinha, V., and Zhao, P. (2016). Predicting the effect of CYP3A inducers on the pharmacokinetics of substrate drugs using physiologically based pharmacokinetic (PBPK) modeling: An analysis of PBPK submissions to the US FDA. *Clin. Pharmacokinet.* 55, 475–483. doi:10.1007/s40262-015-0330-y

Westphal, K., Weinbrenner, A., Zschiesche, M., Franke, G., Knoke, M., Oertel, R., et al. (2000). Induction of P-glycoprotein by rifampin increases intestinal secretion of talinolol in human beings: a new type of drug/drug interaction. *Clin. Pharmacol. Ther.* 68, 345–355. doi:10.1067/mcp.2000.109797

Xiao, K., Gao, J., Weng, S. J., Fang, Y., Gao, N., Wen, Q., et al. (2019). CYP3A4/5 activity probed with testosterone and midazolam: Correlation between two substrates at the microsomal and enzyme levels. *Mol. Pharm.* 16, 382–392. doi:10.1021/acs.molpharmaceut.8b01043

Yadav, J., Korzekwa, K., and Nagar, S. (2018). Improved predictions of drug-drug interactions mediated by time-dependent inhibition of CYP3A. *Mol. Pharm.* 15, 1979–1995. doi:10.1021/acs.molpharmaceut.8b00129

Yeates, R. A., Laufen, H., and Zimmermann, T. (1996). Interaction between midazolam and clarithromycin: comparison with azithromycin. *Int. J. Clin. Pharmacol. Ther.* 34, 400–405.

Yu, Y., Loi, C. M., Hoffman, J., and Wang, D. (2017). Physiologically based pharmacokinetic modeling of palbociclib. *J. Clin. Pharmacol.* 57, 173–184. doi:10.1002/jcph.792

Zhou, C., Li, X., Wang, Q., Gao, G., Zhang, Y., Chen, J., et al. (2020). Pyrotinib in HER2-mutant advanced lung adenocarcinoma after platinum-based chemotherapy: A multicenter, open-label, single-arm, phase II study. *J. Clin. Oncol.* 38, 2753–2761. doi:10.1200/JCO.20.00297

Zhu, Y., Li, L., Zhang, G., Wan, H., Yang, C., Diao, X., et al. (2016). Metabolic characterization of pyrotinib in humans by ultra-performance liquid chromatography/quadrupole time-of-flight mass spectrometry. *J. Chromatogr. B Anal. Technol. Biomed. Life Sci.* 1033-1034, 117–127. doi:10.1016/j.jchromb.2016.08.009

frontiers | Frontiers in Pharmacology

TYPE Original Research
PUBLISHED 10 October 2022
DOI 10.3389/fphar.2022.960186

OPEN ACCESS

EDITED BY
Oscar Garcia-Algar,
Hospital Clinic of Barcelona, Spain

REVIEWED BY
Ronette Gehring,
Utrecht University, Netherlands
Ning Ji,
Tianjin Medical University Cancer Institute and Hospital, China

*CORRESPONDENCE
Wanyi Chen,
32003371@qq.com

†These authors have contributed equally to this work

SPECIALTY SECTION
This article was submitted to Drug Metabolism and Transport, a section of the journal Frontiers in Pharmacology

RECEIVED 02 June 2022
ACCEPTED 26 September 2022
PUBLISHED 10 October 2022

CITATION
Chen L, Li C, Bai H, Li L and Chen W (2022), Use of modeling and simulation to predict the influence of triazole antifungal agents on the pharmacokinetics of zanubrutinib and acalabrutinib.
Front. Pharmacol. 13:960186.
doi: 10.3389/fphar.2022.960186

Use of modeling and simulation to predict the influence of triazole antifungal agents on the pharmacokinetics of zanubrutinib and acalabrutinib

Lu Chen[1†], Chao Li[1†], Hao Bai[1], Lixian Li[1] and Wanyi Chen[1,2*]

[1]Department of Pharmacy, Chongqing University Cancer Hospital, Chongqing, China, [2]Chongqing University, Chongqing, China

Background: Bruton's tyrosine kinase (BTK) inhibitors are commonly used in the targeted therapy of B-cell malignancies. It is reported that myelosuppression and fungal infections might occur during antitumor therapy of BTK inhibitors, therefore a combination therapy with triazole antifungals is usually required.

Objective: To evaluate the influence of different triazoles (voriconazole, fluconazole, itraconazole) on the pharmacokinetics of BTK inhibitors (zanubrutinib, acalabrutinib) and to quantify the drug-drug interactions (DDIs) between them.

Methods: The physiologically-based pharmacokinetic (PBPK) models were developed based on pharmacokinetic parameters and physicochemical data using Simcyp® software. These models were validated using clinically observed plasma concentrations data which based on existing published studies. The successfully validated PBPK models were used to evaluate and predict potential DDIs between BTK inhibitors and different triazoles. BTK inhibitors and triazole antifungal agents were simulated by oral administration.

Results: Simulated plasma concentration-time profiles of the zanubrutinib, acalabrutinib, voriconazole, fluconazole, and itraconazole are consistent with the clinically observed profiles which based on existing published studies, respectively. The exposures of BTK inhibitors increase by varying degrees when co-administered with different triazole antifungals. At multiple doses regimen, voriconazole, fluconazole and itraconazole may increase the area under plasma concentration-time curve (AUC) of zanubrutinib by 127%, 81%, and 48%, respectively, and may increase the AUC of acalabrutinib by 326%, 119%, and 264%, respectively.

Conclusion: The PBPK models sufficiently characterized the pharmacokinetics of BTK inhibitors and triazole antifungals, and were used to predict untested clinical scenarios. Voriconazole exhibited the greatest influence on the exposures of BTK inhibitors. The dosage of zanubrutinib or acalabrutinib need to be reduced when co-administered with moderate CYP3A inhibitors.

KEYWORDS

BTK inhibitors, voriconazole, fluconazole, itraconazole, drug-drug interactions, physiologically-based pharmacokinetic

Introduction

Hematologic malignancies are severe hematopoietic diseases which often accompanied by invasive fungal infections (IFIs) (Neofytos et al., 2013; Zeng et al., 2021). This not only due to the malignancies, but also due to the antitumor treatment, such as cytotoxic chemotherapy (Hamalainen et al., 2008), targeted immunotherapies (Lanini et al., 2011), long-term intravenous catheters (Heidenreich et al., 2022), and chemo-radiotherapy (Martino et al., 1997). Hematological malignancies accompanied by IFIs may increase the tumor recurrence and mortality of the patients (Lewis et al., 2013), so it is necessary to start the antifungal treatment as soon as possible.

According to the clinical practice guidelines of Infectious Diseases Society of America (IDSA), triazole antifungal agents are recommended for the prevention and treatment of IFIs, such as voriconazole, fluconazole and itraconazole (Perfect et al., 2010; Pappas et al., 2016; Patterson et al., 2016). Triazole antifungals are mainly metabolized by cytochrome P450 enzymes (CYP450), including CYP2C19, CYP2C9, and CYP3A4 (Bellmann and Smuszkiewicz, 2017), meanwhile they strongly inhibit CYP3A enzymes (Bellmann and Smuszkiewicz, 2017; Han et al., 2021; Ou et al., 2021). In fact, it is difficult to avoid the long-term consolidation therapy for antitumor and antifungal. In this process, the drug-drug interactions (DDIs) may increase the risk of drug toxicities, sub-optimal therapy, and drug resistance.

Over the past decade, with the rapid development of targeted therapy, many tyrosine kinase inhibitors (TKIs) have been approved for the treatment of hematological malignancies. Bruton's tyrosine kinase (BTK) inhibitors such as zanubrutinib and acalabrutinib are increasingly replacing chemotherapy-based regimens, especially for patients with mantle cell lymphoma (MCL), chronic lymphocytic leukemia (CLL) (Burger, 2019) and small lymphocytic lymphoma (SLL) (Abbas and Wierda, 2021; Tam et al., 2021). According to the pharmacokinetic studies, zanubrutinib and acalabrutinib are mainly metabolized by CYP3A in the liver. When BTK inhibitors are co-administered with triazoles, the exposures of BTK inhibitors tend to increase, which may result in serious adverse effects, such as hematological toxicity, dermatological toxicities and diarrhea (Lipsky and Lamanna, 2020). To the best of our knowledge, at present, only a few reports have suggested the empirical reduction of BTK inhibitors in combination with CYP inhibitors (Hardy-Abeloos et al., 2020; Bruggemann et al., 2022). Therefore, it is essential to evaluate the DDIs between triazoles and BTK inhibitors.

Physiologically-based pharmacokinetic (PBPK) model is a mathematical model that integrated knowledge of physiology, biochemistry and anatomy, in order to simulate the absorption, distribution, metabolism and excretion (ADME) characteristics of drugs in humans (Ellison, 2018). Recently PBPK model has been increasingly accepted by regulatory agencies as a method to inform clinical research strategies. And it has become a useful tool in the simulation of multiple inducers or inhibitors, relevant metabolites, and multiple mechanisms of interaction. Therefore, it has been allowed to predict the complex DDIs involving transporters, enzymes, and multiple interaction mechanisms (Sinha et al., 2014; Sager et al., 2015). The U.S. Food and Drug Administration (FDA) Office of Clinical Pharmacology has been tracking the use of PBPK models in regulatory submissions since 2008. According to 2013 submissions, the models included in regulatory files were most commonly used for DDI (60%), pediatric (21%), and absorption (6%) predictions (Sager et al., 2015). Simcyp (version 20, Certara, Sheffield, United Kingdom), a platform and database for "bottom-up" mechanistic modeling and simulation of the processes of oral absorption, tissue distribution, metabolism and excretion of drugs and drug candidates in healthy and disease populations, is often used to develop PBPK models and to predict the pharmacokinetics and DDIs (Jamei et al., 2009).

In this study, a PBPK model was used to investigate the influence of different triazoles on the pharmacokinetics of BTK inhibitors (zanubrutinib, acalabrutinib) by Simcyp, and the DDIs were quantified to provide a general guidance for the dosage adjustment of BTK inhibitors when co-administered with triazole antifungals.

Materials and methods

Physiologically-based pharmacokinetic model development and verification of bruton's tyrosine kinase inhibitors

A basic framework of PBPK model development and verification is presented in Figure 1. The developments of zanubrutinib and acalabrutinib PBPK models were based on clinical pharmacokinetic parameters, physicochemical properties data, and *in vitro* experiments parameters. The essential physicochemical properties parameters for the development of PBPK models including molecular weight, the acid dissociation constant (pKa), solubility, octanol/water partition coefficient (logP), fraction unbound in plasma (f_{up}), fraction unbound in gut ($f_{u,gut}$), blood-to-plasma concentration ratio (R_{bp}), and effective permeability (P_{eff}). These physicochemical properties parameters and the corresponding references (Zane and Thakker, 2014; Qi et al., 2017; Li et al., 2018; Zhou et al., 2019; Cai et al., 2020; Li et al., 2020; Wang et al., 2021) are

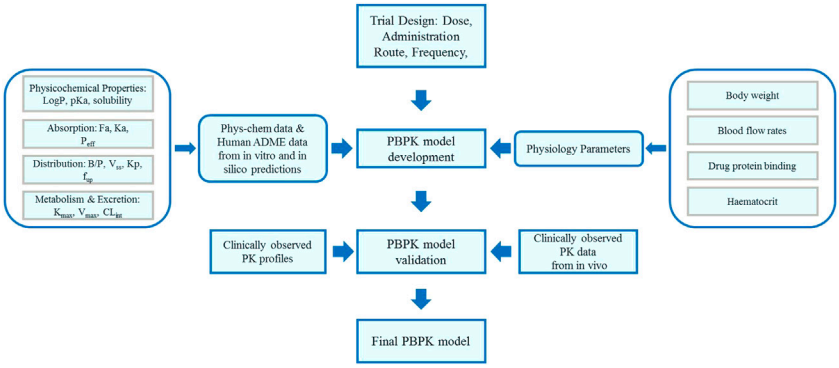

FIGURE 1
A basic framework of PBPK model development and DDI simulation.

TABLE 1 Physicochemical property values used for PBPK modeling of zanubrutinib, acalabrutinib, voriconazole, fluconazole and itraconazole.

Parameter	Zanubrutinib Wang et al. (2021)	Acalabrutinib Zhou et al. (2019)	Voriconazole Zane and Thakker. (2014); Qi et al. (2017); Li et al. (2018); Li et al. (2020)	Fluconazole Cai et al. (2020)	Itraconazole Cai et al. (2020)
Base pKa	3.3	3.54, 5.77	1.6	1.76[a]	4.28[a]
Molecular weight (g/mol)	471.55	465.5	349.3	306.3[a]	705.6
Solubility (mg/ml)			3.2	1.39	0.00964
R_{bp}	0.804	0.787	1	1[a]	0.58[a]
P_{eff} ($\times10^{-4}$cm/s)	0.9	4	3.8	-	0.28
logP	4.2	2.03	1.8	0.2[a]	4.47[a]
$P_{app,caco-2}$ ($\times10^{-6}$cm/s)	-	-	-	29.8[a]	-
$f_{u,gut}$ (%)	-	2.6		89[a]	1.6[a]
f_{up} (%)	5.82	2.6	42	89[a]	1.6[a]
CYP3A4 K_m (μM)	-	-	-	-	0.004
CYP3A4 V_{max} [pmol/(min·pmol)]	-	-	-	-	0.065
CL_{int} [μL/(min·mg)]	120	9.63μL/min/pmol		-	-
Hepatic CLint [μL/(min·mg)]	-	-	4.3	-	-
Additional clearance HLM [μL/(min·mg)]	60	289.5		-	-
CL_R (L/h)	0.5	1.33	0.096	0.86[a]	-
CYP3A4 K_i	-	-	0.66 μM	10.7 μM[a]	0.001 μM[a]

[a]From Simcyp Data Management system.
pKa, acid dissociation constant; R_{bp}, blood-to-plasma concentration ratio; P_{eff}, effective permeability; logP, octanol/water partition coefficient; $P_{app,caco-2}$, apparent permeability of Caco-2 cell line; $f_{u,gut}$, fraction unbound in gut; f_{up}, fraction unbound in plasma; K_m, MichaelisMenten constant; V_{max}, maximum rate of metabolism formation; CL_{int}, intrinsic clearance; CL_R, renal clearance.

listed in Table 1. The first order absorption model and advanced dissolution, absorption, and metabolism (ADAM) model were used to describe the absorption processes of acalabrutinib and zanubrutinib, respectively. The minimal PBPK model and full PBPK model were used to simulate the distribution processes of acalabrutinib and zanubrutinib, respectively. The selected

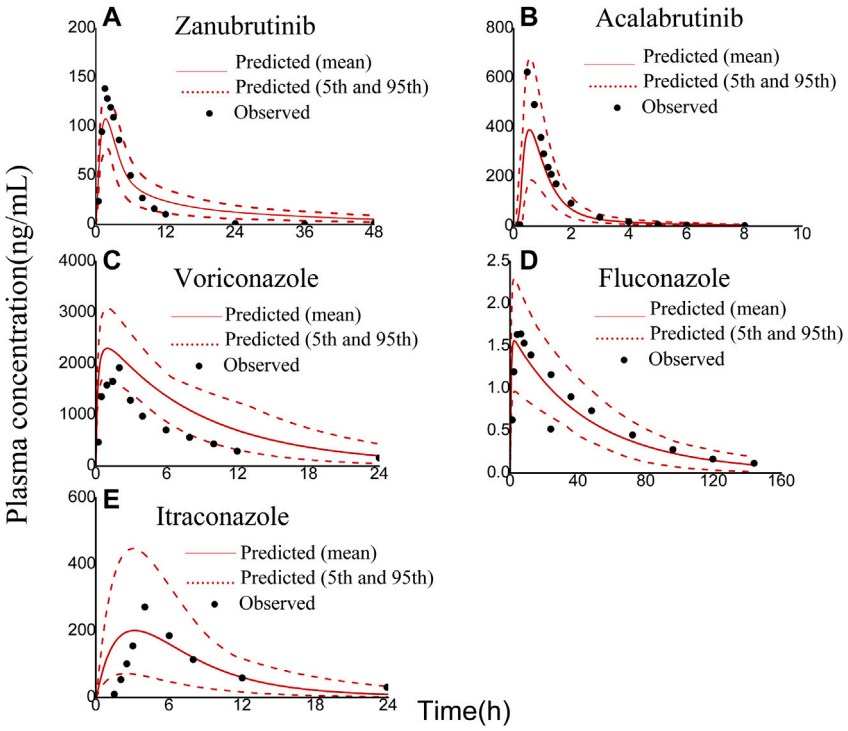

FIGURE 2
Observed (symbols) and physiologically based pharmacokinetic (PBPK) model simulated (solid lines) plasma concentration-time profiles of zanubrutinib, acalabrutinib, voriconazole, fluconazole, and itraconazole: **(A)** 80 mg zanubrutinib oral; **(B)** 100 mg acalabrutinib oral; **(C)** 200 mg voriconazole oral; **(D)** 100 mg fluconazole oral; **(E)** 200 mg itraconazole oral. The red dashed lines represent the 95th and 5th percentiles of the simulated concentrations.

TABLE 2 Observed and predicted PK parameters of zanubrutinib, acalabrutinib, voriconazole, fluconazole and itraconazole.

		C_{max} (ng/ml)	T_{max} (h)	AUC (ng·h/mL)*
Zanubrutinib 80 mg	Observed	162.8	1.5	663
	Predicted	108	1.68	1030
	Fold-error	1.51	1.12	1.55
Acalabrutinib 100 mg	Observed	639	0.5	643
	Predicted	390	0.56	491
	Fold-error	1.64	1.12	1.31
Voriconazole 300 mg	Observed	2360	1.41	12650
	Predicted	2300	0.99	21800
	Fold-error	1.03	1.42	1.72
Fluconazole 100 mg	Observed	1700	4.29	93000
	Predicted	1560	2.49	75200
	Fold-error	1.09	1.72	1.24
Itraconazole 200 mg	Observed	280	4.36	1970
	Predicted	201	3.24	1930
	Fold-error	1.39	1.35	1.02

*AUC_{last} for zanubrutinb, acalabrutinib and voriconazole; AUC_{inf} for fluconazole; AUC_{24} for itraconazole (single dose).
PK, pharmacokinetics; AUC, area under the plasma concentration-time curve; C_{max}, maximum plasma concentration; T_{max}, time-to-maximum plasma concentration.

TABLE 3 Model-predicted PK parameters and ratios of zanubrutinib given alone and with triazoles.

Compound		Parameters		
		C_{max} (ng/ml)	T_{max} (h)	AUC (ng·h/mL)
Zanubrutinib	Alone (single dose)	161	1.44	1290
	DDI with voriconazole (single dose)	238	1.44	2200
	Ratio with voriconazole (single dose)	1.48	1.00	1.71
	Alone (multiple doses)	216	1.92	1580
	DDI with voriconazole (multiple doses)	419	1.92	3580
	Ratio with voriconazole (multiple doses)	1.94	1.00	2.27
	Alone (single dose)	161	1.44	1290
	DDI with fluconazole (single dose)	197	1.44	1760
	Ratio with fluconazole (single dose)	1.22	1.00	1.36
	Alone (multiple doses)	216	1.92	1580
	DDI with fluconazole (multiple doses)	345	1.92	2860
	Ratio with fluconazole (multiple doses)	1.60	1.00	1.81
	Alone (single dose)	164	1.44	1350
	DDI with itraconazole (single dose)	243	1.44	2250
	Ratio with itraconazole (single dose)	1.48	1.00	1.67
	Alone (multiple doses)	222	1.92	1640
	DDI with itraconazole (multiple doses)	299	1.92	2430
	Ratio with itraconazole (multiple doses)	1.34	1.00	1.48

PK, pharmacokinetics; DDI, drug-drug interaction.

distribution models are based on published literatures (Zhou et al., 2019; Wang et al., 2021), and the results of model validation showed that the models are reliable and robust. For zanubrutinib, according to the human liver microsome study, the intrinsic clearance value for CYP3A is 120 μL/(minmg); an additional clearance value of 60 μL/(minmg) was inputted to account for non-CYP3A mediated clearance. The renal clearance value is 0.5 L/h (Wang et al., 2021).

After the PBPK models were developed, simulations were performed at doses of 80 mg zanubrutinib capsule and 100 mg acalabrutinib capsule which were based on the conventional clinical administration regimens. The time-concentration curves were simulated by PBPK models and the maximum plasma concentration (C_{max}) is calculated as the peak concentration in the curve and area under the plasma concentration-time curve (AUC) integrated from 0.00 to t is calculated using log-linear trapezoidal rule in Simcyp. Specifically, Simcyp calculates AUC from 0.00 to t as $AUC_0^t = \sum_{i=1}^{n} AUC_{t_i}^{t_{i+1}}$ where n is the number of time points in which $t_1 = 0$ and $t_{n+1} = t$. The rule for $AUC_{t_i}^{t_{i+1}}$ is as follows. If $C_i > C_{i+1}$, the log-down formula is used to calculate $AUC_{t_i}^{t_{i+1}} = \frac{C_i - C_{i+1}}{\ln(\frac{C_i}{C_{i+1}})} \times t$. Otherwise, the linear-up formula is applied as $AUC_{t_i}^{t_{i+1}} = \frac{C_i + C_{i+1}}{2} \times t$. The developed PBPK models were verified by comparing the simulated plasma concentration curves and pharmacokinetic parameters with corresponding clinically observed plasma concentration curves and pharmacokinetic data in healthy adults which based on existing published studies (Podoll et al., 2019; Ou et al., 2020). The observed data was extracted by applying GetData Graph Digitizer (http://getdata-graph-digitizer.com/). GetData Graph Digitizer is software used to digitize and extract sufficient data (Giang et al., 2019; Shen et al., 2021). The fold-error was used to assess the credibility of the developed PBPK models. The developed PBPK models were considered credible only when the fold-error was less than 2 (Cai et al., 2020). If the observed value is greater than the predicted value, fold-error = observed/predicted; if the observed value is smaller than the predicted value, fold-error = predicted/observed (Fan et al., 2019).

Physiologically-based pharmacokinetic model development and verification of triazole antifungal agents

The PBPK models developed for triazole antifungal agents were similar to the BTK inhibitors. Voriconazole, fluconazole and itraconazole are all described as inhibitors of CYP3A4 (Bellmann and Smuszkiewicz, 2017). The physicochemical properties parameters used in PBPK models and the corresponding references (Zane and Thakker, 2014; Qi et al., 2017; Li et al., 2018; Zhou et al., 2019; Cai et al., 2020; Li et al., 2020; Wang

TABLE 4 Model-predicted PK parameters and ratios of acalabrutinib given alone and with triazoles.

Compound		Parameters		
		C_{max} (ng/ml)	T_{max} (h)	AUC (ng·h/mL)
Acalabrutinib	Alone (single dose)	385	0.6	513
	DDI with voriconazole (single dose)	1170	0.6	1930
	Ratio with voriconazole (single dose)	3.04	1.00	3.76
	Alone (multiple doses)	402	1.08	513
	DDI with voriconazole (multiple doses)	1286	1.08	2184
	Ratio with voriconazole (multiple doses)	3.20	1.00	4.26
	Alone (single dose)	385	0.6	513
	DDI with fluconazole (single dose)	658	0.6	937
	Ratio with fluconazole (single dose)	1.71	1.00	1.83
	Alone (multiple doses)	402	1.08	513
	DDI with fluconazole (multiple doses)	776	1.08	1124
	Ratio with fluconazole (multiple doses)	1.93	1.00	2.19
	Alone (single dose)	387	0.6	512
	DDI with itraconazole (single dose)	1160	0.6	1790
	Ratio with itraconazole (single dose)	3.00	1.00	3.50
	Alone (multiple doses)	404	1.08	513
	DDI with itraconazole (multiple doses)	1213	1.08	1865
	Ratio with itraconazole (multiple doses)	3.00	1.00	3.64

PK, pharmacokinetics; DDI, drug-drug interaction.

et al., 2021) are listed in Table 1. The absorption processes of voriconazole, fluconazole and itraconazole were dscribed using the first order absorption models. The distribution processes of voriconazole, fluconazole and itraconazole were dscribed using full PBPK model, minimal PBPK model and minimal PBPK model, respectively. The recombinant enzyme and kinetic parameters [Michaelis-Menten constant (K_m) and maximum reaction velocity (V_{max})] were used to describe the metabolic process of drugs. The apparent K_m and V_{max} values of itraconazole were 0.004 μM and 0.065 pmol/(minpmol) for CYP3A4, respectively. The essential parameters of voriconazole, fluconazole and itraconazole were listed in Table 1. The accuracy of developed PBPK models were verified by comparing the simulated plasma concentration curves and pharmacokinetic parameters with corresponding clinically observed data (Thorpe et al., 1990; Jaruratanasirikul and Sriwiriyajan, 1998; Purkins et al., 2002).

Drug-drug interactions simulations of bruton's tyrosine kinase inhibitors and triazole antifungal agents

After the verification, the PBPK model was used to simulate clinical DDI scenarios to quantitatively evaluate the pharmacokinetic changes of zanubrutinib or acalabrutinib when co-administered with triazoles. For the simulation of single dose, all virtual volunteers were given zanubrutinib capsule 160 mg or acalabrutinib capsule 100 mg, combined with 200 mg voriconazole or 200 mg fluconazole or 200 mg itraconazole orally. For the simulation of multiple doses zanubrutinib, the virtual volunteers were given 160 mg zanubrutinib capsule twice daily concomitantly with 200 mg fluconazole once daily for 14 days or 200 mg itraconazole once-daily for 14 days or voriconazole at a loading dose of 400 mg twice-daily (day 1) and a subsequent dose of 200 mg twice-daily (days 2–14). For acalabrutinib group, the virtual volunteers were given 100 mg acalabrutinib capsule twice daily concomitantly with 200 mg fluconazole once daily for 7 days or 200 mg itraconazole once-daily for 7 days or voriconazole at a loading dose of 400 mg twice-daily (day 1) and a subsequent dose of 200 mg twice-daily (days 2–7). The inhibitory potency of triazole antifungals can be measured by the inhibition constant (K_i) value. The K_i values of triazole antifungals were entered into PBPK models to predict the potential DDIs. The K_i values of voriconazole, fluconazole and itraconazole were laid in Table 1.

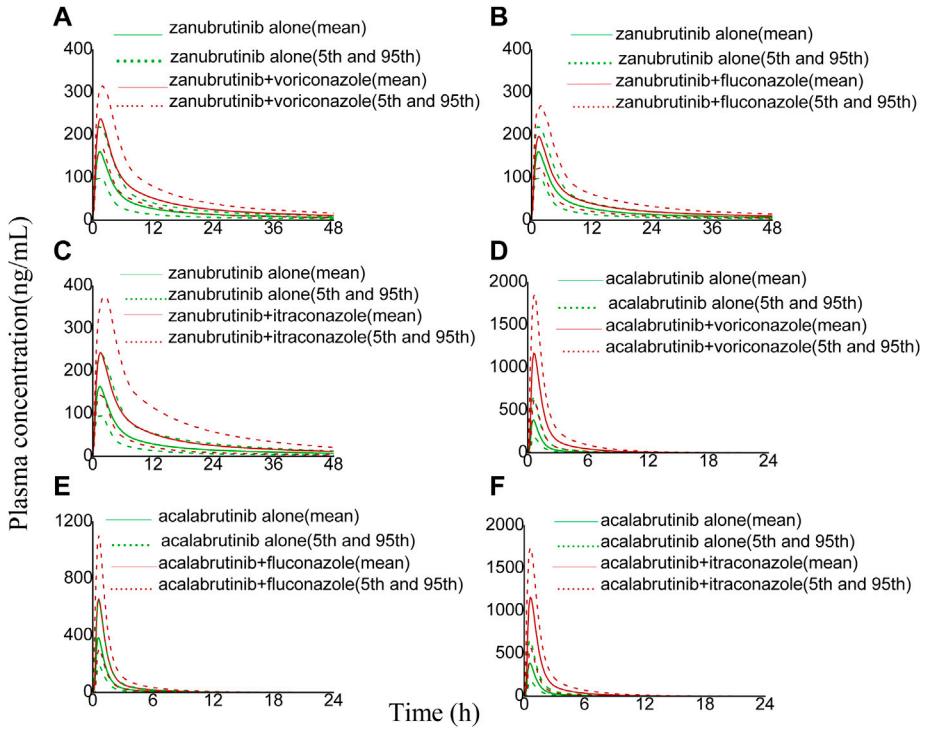

FIGURE 3
Simulated plasma concentrations of a single-dose zanubrutinib (160 mg) dosed alone or concomitant with **(A)** voriconazole (200 mg), **(B)** fluconazole (200 mg), **(C)** itraconazole (200 mg), and a single-dose acalabrutinib (100 mg) dosed alone or concomitant with **(D)** voriconazole (200 mg), **(E)** fluconazole (200 mg), **(F)** itraconazole (200 mg).

Results

Physiologically-based pharmacokinetic model development and verification of bruton's tyrosine kinase inhibitors and triazole antifungal agents

The robustness of the PBPK models were assessed by comparing predicted with corresponding clinically observed plasma concentration-time profiles and pharmacokinetic parameters (Thorpe et al., 1990; Jaruratanasirikul and Sriwiriyajan, 1998; Purkins et al., 2002; Podoll et al., 2019; Ou et al., 2020). As presented in Figure 2, the predicted plasma concentration curves of zanubrutinib, acalabrutinib, voricoanzole, fluconazole and itraconazole were consistent with the observed curves. Besides, the C_{max} and AUC values were successfully predicted with fold-errors ≤ 2. The C_{max} and AUC values of zanubrutinib, acalabrutinib, voricoanzole, fluconazole and itraconazole and the fold-error values are presented in Table 2. It is obvious that the developed PBPK models are credible.

Drug-drug interactions simulations of bruton's tyrosine kinase inhibitors and triazole antifungal agents

The developed PBPK model was applied to predict clinical DDI scenarios for zanubrutinib or acalabrutinib when co-administered with triazole antifungal agents. The simulated DDI results are presented in Table 3, Table 4, Figure 3, Figure 4, Figure 5 and Figure 6. The results indicate that exposures of zanubrutinib and acalabrutinib may increase when co-administered with triazole antifungals. The C_{max} of zanubrutinib increased by 94%, 60%, and 34% and the AUC increased by 127%, 81%, and 48% when co-administered with voriconazole, fluconazole or itraconazole at multiple doses, respectively. The C_{max} of acalabrutinib increased by 220%, 93%, and 200% and the AUC increased by 326%, 119% and 264% when co-administered with voriconazole, fluconazole or itraconazole at multiple doses, respectively. Compared with fluconazole and itraconazole, voriconazole exhibited the greatest influence on exposures of zanubrutinib and acalabrutinib.

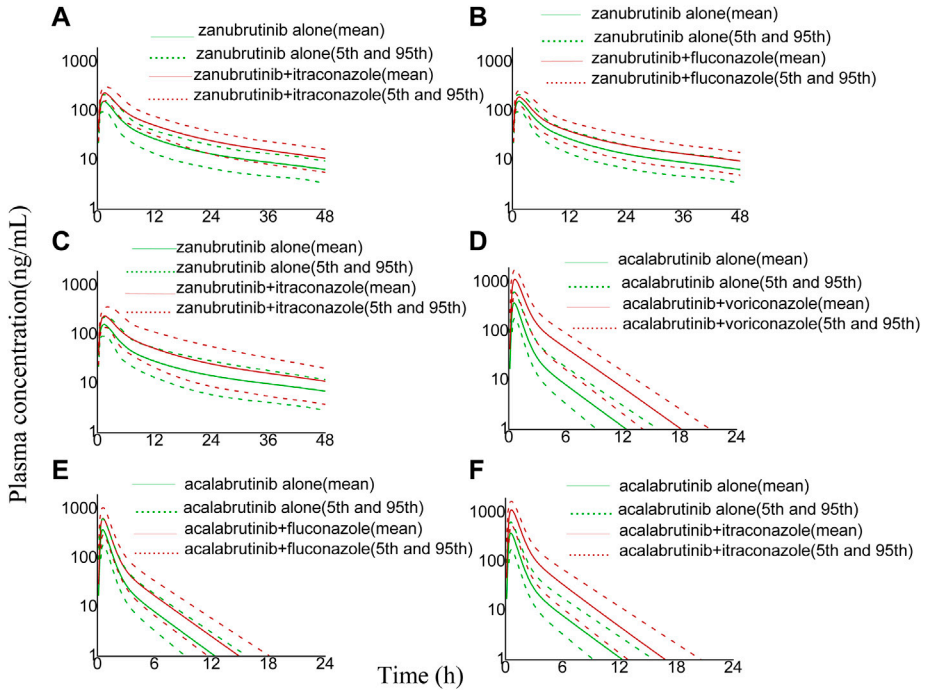

FIGURE 4
Simulated plasma concentrations (logarithmic concentration axis) of a single-dose zanubrutinib (160 mg) dosed alone or concomitant with **(A)** voriconazole (200 mg), **(B)** fluconazole (200 mg), **(C)** itraconazole (200 mg), and a single-dose acalabrutinib (100 mg) dosed alone or concomitant with **(D)** voriconazole (200 mg), **(E)** fluconazole (200 mg), **(F)** itraconazole (200 mg).

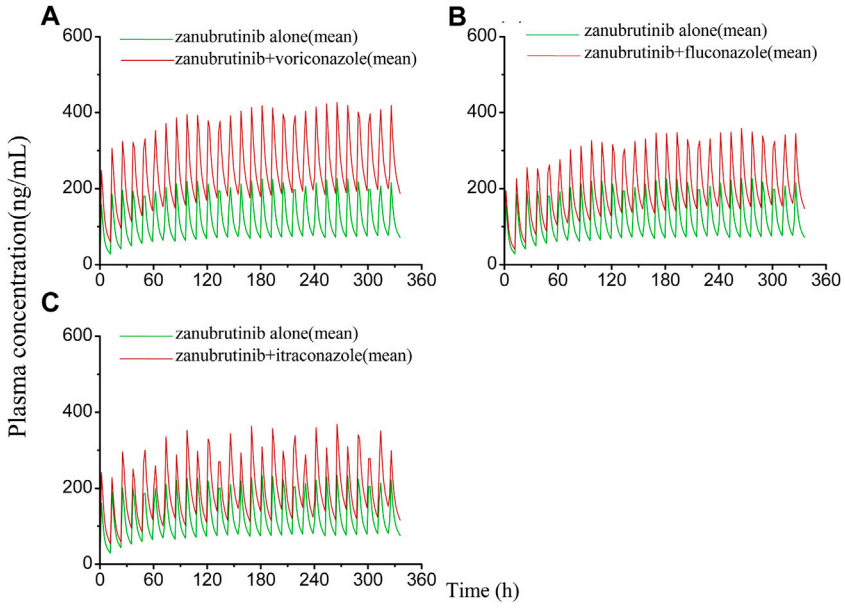

FIGURE 5
Simulated plasma concentrations of multiple doses (14 days doses) of zanubrutinib (160 mg twice daily) dosed alone or concomitant with **(A)** voriconazole (400 mg twice-daily (day 1) and a subsequent dose of 200 mg twice-daily); **(B)** fluconazole (200 mg once daily); **(C)** itraconazole (200 mg once daily).

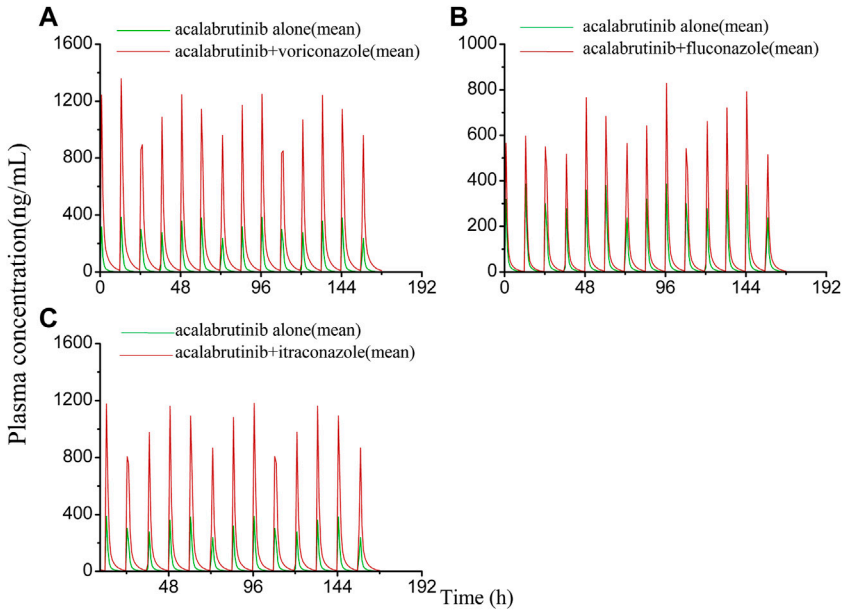

FIGURE 6
Simulated plasma concentrations of multiple doses (7 days doses) of acalabrutinib (100 mg twice daily) dosed alone or concomitant with **(A)** voriconazole (400 mg twice-daily (day 1) and a subsequent dose of 200 mg twice-daily); **(B)** fluconazole (200 mg once daily); **(C)** itraconazole (200 mg once daily).

Discussion

The results of the DDI simulations showed that the pharmacokinetic exposures of zanubrutinib and acalabruitnib increased to varying degrees when combined with voriconazole, fluconazole, or itraconazole, respectively. In brief, compared with taking zanubrutinib alone, the AUC of zanubrutinib increased by 127%, 81%, and 48% when combined with voriconazole, fluconazole or itraconazole at multiple doses, respectively. Furthermore, compared with taking acalabrutinib alone, the AUC of acalabrutinib increased by 326%, 119%, and 264% when combined with voriconazole, fluconazole or itraconazole at multiple doses, respectively.

According to the results above, co-administered of BTK inhibitors and triazoles will increase the pharmacokinetic exposures of BTK inhibitors, and among the three triazoles, voriconazole exhibited the most significant effect on the pharmacokinetic exposures of zanubrutinib and acalabruitnib. Nonetheless, the degree of elevation was markedly different between zanubrutinib and acalatinib, especially co-administered with voriconazole and itraconazole. The reason may be related to the fact that zanubrutinib can decrease the systemic exposure of CYP3A and CYP2C19 substrates (Ou et al., 2021). Voriconazole, which happens to be a substrate for CYP2C19, CYP2C9 and CYP3A4, and itraconazole is a substrate for CYP3A4 (Bellmann and Smuszkiewicz, 2017). Therefore, zanubrutinib decreased the systemic exposures of voriconazole and itraconazole, resulting in less inhibitory effects on zanubrutinib caused by voriconazole and itraconazole compared with acalabrutinib. Whereas fluconazole's metabolic pathways are not qualitatively or quantitatively significant, and its main route of elimination is renal excretion (Debruyne and Ryckelynck, 1993), which will not be influenced by zanubrutinib and acalabruitnib, so both of the pharmacokinetic exposures increased in similar degree.

Therapeutic drug monitoring (TDM) is the clinical practice of measuring drugs at specified time intervals to support individualized PK-based dose adjustments, thus maintaining consistent concentrations in patient's blood, reducing regimen-related toxicities and improving treatment efficacy. TDM has been shown its advantage in optimization the dosing of voriconazole (Ashbee et al., 2014), vancomycin (Pai et al., 2014), valproic acid (Johannessen Landmark et al., 2020), cyclosporine (Jorga et al., 2004) and so on. Moreover, the exposure-response and/or exposure-toxicity relationships of several oral targeted antineoplastic drugs have been established, and TDM has been proven to be practical for individualized dosing of imatinib, sunitinib, abiraterone, everolimus, etc., (Verheijen et al., 2017; Mueller-Schoell et al., 2021). Even though there has not any recommendation for TDM of the BTK inhibitors to date, TDM can still be conducted to clarify the DDIs between BTK inhibitors and triazole antifungal

agents, so as to guide individualized dosing, optimize therapy and prevent toxicity. Overall, our study indicated that in order to avoid the increased concentration of BTK inhibitors, we should reduce the dosage of BTK inhibitors when co-administered with triazoles, especially voriconazole.

Although the PBPK model is well-established, reasonably refined and validated, limitations still exist in the present study. Firstly, genetic polymorphisms of CYP3A4 may alter the metabolic enzyme activities of zanubrutinib and acalabrutinib. The inhibitory potency also varies among different variants when co-administered with a CYP inhibitor (Han et al., 2021). Secondly, the DDIs between zanubrutinib, acalabrutinib and triazoles were predicted in healthy subjects in our study. However, the enzyme activity of CYP3A4 may be different in disease state such as CLL, SLL, and MCL (Gao et al., 2022). Therefore, the DDIs between zanubrutinib, acalabrutinib and triazoles in patients with hematologic malignancies need to be studied in further research.

Conclusion

In conclusion, the developed and validated PBPK models were successfully used to predict the DDIs between zanubrutinib, acalabrutinib and different triazoles. Compared with taking zanubrutinib or acalabrutinib alone, the pharmacokinetic exposures of zanubrutinib and acalabruitnib increased to varying degrees when co-administered with voriconazole, fluconazole, or itraconazole, respectively. The dosage of zanubrutinib and acalabrutinib need to be reduced when co-administered with triazole antifungal agents.

Data availability statement

The original contributions presented in the study are included in the article/supplementary material, further inquiries can be directed to the corresponding author.

Author contributions

LC, CL, and WC contributed to conception and design of the study. CL collected the data. LC performed the statistical analysis. LC wrote the first draft of the manuscript. CL, HB, LL, WC and LC wrote sections of the manuscript. All authors contributed to manuscript revision, read, and approved the submitted version.

Funding

The authors appreciate the support of the Fundamental Research Funds for the Central Universities (2021CDJYGRH-014), the Natural Science Foundation of Chongqing, China (cstc2021jcyj-msxmX1154) and the Chongqing Key Specialty Construction Project of Clinical Pharmacy.

Acknowledgments

Certara United Kingdom (Simcyp Division) granted free access to the Simcyp® Simulators through an academic licence.

Conflict of interest

The authors declare that the research was conducted in the absence of any commercial or financial relationships that could be construed as a potential conflict of interest.

Publisher's note

References

Abbas, H. A., and Wierda, W. G. (2021). Acalabrutinib: A selective Bruton tyrosine kinase inhibitor for the treatment of B-cell malignancies. *Front. Oncol.* 11, 668162. doi:10.3389/fonc.2021.668162

Ashbee, H. R., Barnes, R. A., Johnson, E. M., Richardson, M. D., Gorton, R., and Hope, W. W. (2014). Therapeutic drug monitoring (TDM) of antifungal agents: Guidelines from the British society for medical mycology. *J. Antimicrob. Chemother.* 69, 1162–1176. doi:10.1093/jac/dkt508

Bellmann, R., and Smuszkiewicz, P. (2017). Pharmacokinetics of antifungal drugs: Practical implications for optimized treatment of patients. *Infection* 45, 737–779. doi:10.1007/s15010-017-1042-z

Bruggemann, R. J., Verheggen, R., Boerrigter, E., Stanzani, M., Verweij, P. E., Blijlevens, N. M. A., et al. (2022). Management of drug-drug interactions of targeted therapies for haematological malignancies and triazole antifungal drugs. *Lancet. Haematol.* 9, e58–e72. doi:10.1016/S2352-3026(21)00232-5

Burger, J. A. (2019). Bruton tyrosine kinase inhibitors: Present and future. *Cancer J.* 25, 386–393. doi:10.1097/PPO.0000000000000412

Cai, T., Liao, Y., Chen, Z., Zhu, Y., and Qiu, X. (2020). The influence of different triazole antifungal agents on the pharmacokinetics of cyclophosphamide. *Ann. Pharmacother.* 54, 676–683. doi:10.1177/1060028019896894

Debruyne, D., and Ryckelynck, J. P. (1993). Clinical pharmacokinetics of fluconazole. *Clin. Pharmacokinet.* 24, 10–27. doi:10.2165/00003088-199324010-00002

Ellison, C. A. (2018). Structural and functional pharmacokinetic analogs for physiologically based pharmacokinetic (PBPK) model evaluation. *Regul. Toxicol. Pharmacol.* 99, 61–77. doi:10.1016/j.yrtph.2018.09.008

Fan, J., Chen, L., Lu, X., Li, M., and Zhu, L. (2019). The pharmacokinetic prediction of cyclosporin A after coadministration with wuzhi capsule. *Aaps Pharmscitech* 20, 247. doi:10.1208/s12249-019-1444-6

Gao, N., Zhang, X., Hu, X., Kong, Q., Cai, J., Hu, G., et al. (2022). The influence of CYP3A4 genetic polymorphism and proton pump inhibitors on osimertinib metabolism. *Front. Pharmacol.* 13, 794931. doi:10.3389/fphar.2022.794931

Giang, H. T. N., Ahmed, A. M., Fala, R. Y., Khattab, M. M., Othman, M. H. A., Abdelrahman, S. A. M., et al. (2019). Methodological steps used by authors of systematic reviews and meta-analyses of clinical trials: A cross-sectional study. *BMC Med. Res. Methodol.* 19, 164. doi:10.1186/s12874-019-0780-2

Hamalainen, S., Kuittinen, T., Matinlauri, I., Nousiainen, T., Koivula, I., and Jantunen, E. (2008). Neutropenic fever and severe sepsis in adult acute myeloid leukemia (AML) patients receiving intensive chemotherapy: Causes and consequences. *Leuk. Lymphoma* 49, 495–501. doi:10.1080/10428190701809172

Han, M., Qian, J., Ye, Z., Xu, R., Chen, D., Xie, S., et al. (2021). Functional assessment of the effects of CYP3A4 variants on acalabrutinib metabolism *in vitro*. *Chem. Biol. Interact.* 345, 109559. doi:10.1016/j.cbi.2021.109559

Hardy-Abeloos, C., Pinotti, R., and Gabrilove, J. (2020). Ibrutinib dose modifications in the management of CLL. *J. Hematol. Oncol.* 13, 66. doi:10.1186/s13045-020-00870-w

Heidenreich, D., Hansen, E., Kreil, S., Nolte, F., Jawhar, M., Hecht, A., et al. (2022). The insertion site is the main risk factor for central venous catheter-related complications in patients with hematologic malignancies. *Am. J. Hematol.* 97, 303–310. doi:10.1002/ajh.26445

Jamei, M., Marciniak, S., Feng, K., Barnett, A., Tucker, G., and Rostami-Hodjegan, A. (2009). The Simcyp population-based ADME simulator. *Expert Opin. Drug Metab. Toxicol.* 5, 211–223. doi:10.1517/17425250802691074

Jaruratanasirikul, S., and Sriwiriyajan, S. (1998). Effect of omeprazole on the pharmacokinetics of itraconazole. *Eur. J. Clin. Pharmacol.* 54, 159–161. doi:10.1007/s002280050438

Johannessen Landmark, C., Johannessen, S. I., and Patsalos, P. N. (2020). Therapeutic drug monitoring of antiepileptic drugs: Current status and future prospects. *Expert Opin. Drug Metab. Toxicol.* 16, 227–238. doi:10.1080/17425255.2020.1724956

Jorga, A., Holt, D. W., and Johnston, A. (2004). Therapeutic drug monitoring of cyclosporine. *Transpl. Proc.* 36, 396S–403S. doi:10.1016/j.transproceed.2004.01.013

Lanini, S., Molloy, A. C., Fine, P. E., Prentice, A. G., Ippolito, G., and Kibbler, C. C. (2011). Risk of infection in patients with lymphoma receiving rituximab: Systematic review and meta-analysis. *BMC Med.* 9, 36. doi:10.1186/1741-7015-9-36

Lewis, R. E., Cahyame-Zuniga, L., Leventakos, K., Chamilos, G., Ben-Ami, R., Tamboli, P., et al. (2013). Epidemiology and sites of involvement of invasive fungal infections in patients with haematological malignancies: A 20-year autopsy study. *Mycoses* 56, 638–645. doi:10.1111/myc.12081

Li, N., Zhu, L., Qi, F., Li, M., Xu, G., and Ge, T. (2018). Prediction of the effect of voriconazole on the pharmacokinetics of non-steroidal anti-inflammatory drugs. *J. Chemother.* 30, 240–246. doi:10.1080/1120009X.2018.1500197

Li, X., Frechen, S., Moj, D., Lehr, T., Taubert, M., Hsin, C. H., et al. (2020). A physiologically based pharmacokinetic model of voriconazole integrating time-dependent inhibition of CYP3A4, genetic polymorphisms of CYP2C19 and predictions of drug-drug interactions. *Clin. Pharmacokinet.* 59, 781–808. doi:10.1007/s40262-019-00856-z

Lipsky, A., and Lamanna, N. (2020). Managing toxicities of Bruton tyrosine kinase inhibitors. *Hematol. Am. Soc. Hematol. Educ. Program* 2020, 336–345. doi:10.1182/hematology.2020000118

Martino, R., Lopez, R., Sureda, A., Brunet, S., and Domingo-Albos, A. (1997). Risk of reactivation of a recent invasive fungal infection in patients with hematological malignancies undergoing further intensive chemo-radiotherapy. A single-center experience and review of the literature. *Haematologica* 82, 297–304.

Mueller-Schoell, A., Groenland, S. L., Scherf-Clavel, O., van Dyk, M., Huisinga, W., Michelet, R., et al. (2021). Correction to: Therapeutic drug monitoring of oral targeted antineoplastic drugs. *Eur. J. Clin. Pharmacol.* 77, 465. doi:10.1007/s00228-020-03067-9

Neofytos, D., Lu, K., Hatfield-Seung, A., Blackford, A., Marr, K. A., Treadway, S., et al. (2013). Epidemiology, outcomes, and risk factors of invasive fungal infections in adult patients with acute myelogenous leukemia after induction chemotherapy. *Diagn. Microbiol. Infect. Dis.* 75, 144–149. doi:10.1016/j.diagmicrobio.2012.10.001

Ou, Y. C., Preston, R. A., Marbury, T. C., Tang, Z., Novotny, W., Tawashi, M., et al. (2020). A phase 1, open-label, single-dose study of the pharmacokinetics of zanubrutinib in subjects with varying degrees of hepatic impairment. *Leuk. Lymphoma* 61, 1355–1363. doi:10.1080/10428194.2020.1719097

Ou, Y. C., Tang, Z., Novotny, W., Tawashi, M., Li, T. K., Coleman, H. A., et al. (2021). Evaluation of drug interaction potential of zanubrutinib with cocktail probes representative of CYP3A4, CYP2C9, CYP2C19, P-gp and BCRP. *Br. J. Clin. Pharmacol.* 87, 2926–2936. doi:10.1111/bcp.14707

Pai, M. P., Neely, M., Rodvold, K. A., and Lodise, T. P. (2014). Innovative approaches to optimizing the delivery of vancomycin in individual patients. *Adv. Drug Deliv. Rev.* 77, 50–57. doi:10.1016/j.addr.2014.05.016

Pappas, P. G., Kauffman, C. A., Andes, D. R., Clancy, C. J., Marr, K. A., Ostrosky-Zeichner, L., et al. (2016). Executive summary: Clinical practice guideline for the management of candidiasis: 2016 update by the infectious diseases society of America. *Clin. Infect. Dis.* 62, 409–417. doi:10.1093/cid/civ1194

Patterson, T. F., Thompson, G. R., Denning, D. W., Fishman, J. A., Hadley, S., Herbrecht, R., et al. (2016). Practice guidelines for the diagnosis and management of aspergillosis: 2016 update by the infectious diseases society of America. *Clin. Infect. Dis.* 63, e1–e60. doi:10.1093/cid/ciw326

Perfect, J. R., Dismukes, W. E., Dromer, F., Goldman, D. L., Graybill, J. R., Hamill, R. J., et al. (2010). Clinical practice guidelines for the management of cryptococcal disease: 2010 update by the infectious diseases society of America. *Clin. Infect. Dis.* 50, 291–322. doi:10.1086/649858

Podoll, T., Pearson, P. G., Evarts, J., Ingallinera, T., Bibikova, E., Sun, H., et al. (2019). Bioavailability, biotransformation, and excretion of the covalent Bruton tyrosine kinase inhibitor acalabrutinib in rats, dogs, and humans. *Drug Metab. Dispos.* 47, 145–154. doi:10.1124/dmd.118.084459

Purkins, L., Wood, N., Ghahramani, P., Greenhalgh, K., Allen, M. J., and Kleinermans, D. (2002). Pharmacokinetics and safety of voriconazole following intravenous- to oral-dose escalation regimens. *Antimicrob. Agents Chemother.* 46, 2546–2553. doi:10.1128/AAC.46.8.2546-2553.2002

Qi, F., Zhu, L., Li, N., Ge, T., Xu, G., and Liao, S. (2017). Influence of different proton pump inhibitors on the pharmacokinetics of voriconazole. *Int. J. Antimicrob. Agents* 49, 403–409. doi:10.1016/j.ijantimicag.2016.11.025

Sager, J. E., Yu, J., Ragueneau-Majlessi, I., and Isoherranen, N. (2015). Physiologically based pharmacokinetic (PBPK) modeling and simulation approaches: A systematic review of published models, applications, and model verification. *Drug Metab. Dispos.* 43, 1823–1837. doi:10.1124/dmd.115.065920

Shen, T., Yue, Y., He, T., Huang, C., Qu, B., Lv, W., et al. (2021). The association between the gut microbiota and Parkinson's disease, a meta-analysis. *Front. Aging Neurosci.* 13, 636545. doi:10.3389/fnagi.2021.636545

Sinha, V., Zhao, P., Huang, S. M., and Zineh, I. (2014). Physiologically based pharmacokinetic modeling: From regulatory science to regulatory policy. *Clin. Pharmacol. Ther.* 95, 478–480. doi:10.1038/clpt.2014.46

Tam, C. S., Ou, Y. C., Trotman, J., and Opat, S. (2021). Clinical pharmacology and PK/PD translation of the second-generation Bruton's tyrosine kinase inhibitor, zanubrutinib. *Expert Rev. Clin. Pharmacol.* 14, 1329–1344. doi:10.1080/17512433.2021.1978288

Thorpe, J. E., Baker, N., and Bromet-Petit, M. (1990). Effect of oral antacid administration on the pharmacokinetics of oral fluconazole. *Antimicrob. Agents Chemother.* 34, 2032–2033. doi:10.1128/AAC.34.10.2032

Verheijen, R. B., Yu, H., Schellens, J. H. M., Beijnen, J. H., Steeghs, N., and Huitema, A. D. R. (2017). Practical recommendations for therapeutic drug monitoring of kinase inhibitors in oncology. *Clin. Pharmacol. Ther.* 102, 765–776. doi:10.1002/cpt.787

Wang, K., Yao, X., Zhang, M., Liu, D., Gao, Y., Sahasranaman, S., et al. (2021). Comprehensive PBPK model to predict drug interaction potential of Zanubrutinib as a victim or perpetrator. *CPT. Pharmacometrics Syst. Pharmacol.* 10, 441–454. doi:10.1002/psp4.12605

Zane, N. R., and Thakker, D. R. (2014). A physiologically based pharmacokinetic model for voriconazole disposition predicts intestinal first-pass metabolism in children. *Clin. Pharmacokinet.* 53, 1171–1182. doi:10.1007/s40262-014-0181-y

Zeng, H., Wu, Z., Yu, B., Wang, B., Wu, C., Wu, J., et al. (2021). Network meta-analysis of triazole, polyene, and echinocandin antifungal agents in invasive fungal infection prophylaxis in patients with hematological malignancies. *BMC Cancer* 21, 404. doi:10.1186/s12885-021-07973-8

Zhou, D., Podoll, T., Xu, Y., Moorthy, G., Vishwanathan, K., Ware, J., et al. (2019). Evaluation of the drug-drug interaction potential of acalabrutinib and its active metabolite, ACP-5862, using a physiologically-based pharmacokinetic modeling approach. *CPT. Pharmacometrics Syst. Pharmacol.* 8, 489–499. doi:10.1002/psp4.12408

frontiers | Frontiers in Pharmacology

TYPE Original Research
PUBLISHED 25 October 2022
DOI 10.3389/fphar.2022.1033667

OPEN ACCESS

EDITED BY
Simona Pichini,
National Institute of Health (ISS), Italy

REVIEWED BY
Yuichi Uwai,
Aichi Gakuin University, Japan
Shang-Gao Liao,
Guizhou Medical University, China

*CORRESPONDENCE
Yuhong Huang,
hyh101@126.com

SPECIALTY SECTION
This article was submitted to Drug Metabolism and Transport, a section of the journal Frontiers in Pharmacology

RECEIVED 31 August 2022
ACCEPTED 14 October 2022
PUBLISHED 25 October 2022

CITATION
Li Z, Du X, Tian S, Fan S, Zuo X, Li Y, Wang R, Wang B and Huang Y (2022), Pharmacokinetic herb-drug interactions: Altered systemic exposure and tissue distribution of ciprofloxacin, a substrate of multiple transporters, after combined treatment with Polygonum capitatum Buch.-Ham. ex D. Don extracts.
Front. Pharmacol. 13:1033667.
doi: 10.3389/fphar.2022.1033667

Pharmacokinetic herb-drug interactions: Altered systemic exposure and tissue distribution of ciprofloxacin, a substrate of multiple transporters, after combined treatment with *Polygonum capitatum* Buch.-Ham. ex D. Don extracts

Ziqiang Li[1], Xi Du[1], Shuang Tian[1], Shanshan Fan[2], Xurui Zuo[2], Yanfen Li[1], Ruihua Wang[1], Baohe Wang[1] and Yuhong Huang[1]*

[1]Second Affiliated Hospital of Tianjin University of Traditional Chinese Medicine, Tianjin, China, [2]Graduate School, Tianjin University of Traditional Chinese Medicine, Tianjin, China

Background: Combination of *Polygonum capitatum* Buch.-Ham. ex D. Don extract (PCE) and ciprofloxacin (CIP) was commonly prescribed in the treatment of urinary tract infections. Their pharmacokinetic herb-drug interactions (HDIs) were focused in this study to assess potential impact on the safety and effectiveness.

Methods: A randomized, three-period, crossover trial was designed to study the pharmacokinetic HDI between PCE and CIP in healthy humans. Their pharmacokinetic- and tissue distribution-based HDIs were also evaluated in rats. Gallic acid (GA) and protocatechuic acid (PCA) were chosen as PK-markers of PCE in humans and rats. Potential drug interaction mechanisms were revealed by assessing the effects of PCE on the activity and expression of multiple transporters, including OAT1/3, OCT2, MDR1, and BCRP.

Results: Concurrent use of PCE substantially reduced circulating CIP (approximately 40%–50%) in humans and rats, while CIP hardly changed circulating GA and PCA. PCE significantly increased the tissue distribution of CIP in the prostate and testis of rats, but decreased in liver and lungs. Meanwhile, CIP significantly increased the tissue distribution of GA or PCA in the prostate and testis of rats, but decreased in kidney and heart. In the transporter-mediated *in vitro* HDI, GA and PCA presented inhibitory effects on OAT1/3 and inductive effects on MDR1 and BCRP.

Conclusion: Multiple transporter-mediated HDI contributes to effects of PCE on the reduced systemic exposure and altered tissue distribution of CIP. More attention should be paid on the potential for PCE-perpetrated interactions.

KEYWORDS

herb-drug interaction (HDI), *Polygonum capitatum* extract, drug-drug interaction (DDI), ciprofloxacin (CIP), drug transporters, tissue distribution

1 Introduction

Communicable diseases are still leading causes of death and disability globally, according to WHO's Global Health Estimates 2000–2019 (GBD Diseases and Injuries, 2020). Antibiotics present a vital role in universal health insurance and global health protection. However, the clinical pipeline and recently approved antibiotics are insufficient to tackle the challenge of increasing emergence and spread of antimicrobial resistance. In recent years, traditional Chinese medicine (TCM)-based herbal therapies have been widely used to treat infectious diseases and solve the problem of microbial resistance. In particular, since the outbreak of COVID-19, TCM has fully participated in the prevention, control and treatment of the epidemic and made important contributions (Huang et al., 2021). According to the WHO Expert Meeting on Evaluation of TCM in the Treatment of COVID-19, WHO encouraged Member States to consider the integrated traditional Chinese and Western medicine model (WHO, 2022).

Polygonum capitatum Buch.-Ham. ex D. Don (*P. capitatum*), a Chinese herbal plant, is often used alone or in combination with antibacterial agents to treat urinary tract infections, pyelonephritis, and prostatitis in China (Chinese Pharmacopoeia Commission, 2010; Liao et al., 2011). Relinqing® granule, a *P. capitatum*-based Chinese patent medicine, has been approved by the National Medical Products Adminnistration (NMPA) and officially listed in the Chinese Pharmacopoeia since 2010 (Chinese Pharmacopoeia Commission, 2010). A systematic review of randomized controlled trials indicated that the combination of Relinqing® with antibiotics can improve the total effective rate of urinary tract infections in comparison with the antibiotic therapy alone (Pu et al., 2016). Evidence-based herb-drug interactions (HDI) studies are expected to become a necessary evaluation for the rational use of *P. capitatum*-based product with other drugs prescribed for the same indications. Therefore, we focused on pharmacokinetic- and tissue distribution-based HDIs between *P. capitatum* extracts (PCE) and fluoroquinolone antibacterial agents in this study.

Gallic acid (GA) and protocatechuic acid (PCA) were identified as appropriate pharmacokinetic markers (PK-markers) of *P. capitatum* because of their extensive pharmacological activities, high systemic exposures, and acceptable pharmacokinetic properties. Specifically, they are the two most abundant phenolic acids in *P. capitatum* (Liao et al., 2013; Zhang et al., 2013a; Zhang et al., 2013b; Li et al., 2021b), and their anti-microbial, anti-inflammatory, anti-oxidant, and analgesic activities associated with *P. capitatum* efficacy (Liao et al., 2011; Khan et al., 2015; Choubey et al., 2018; Song et al., 2020; Bai et al., 2021). The qualitative and quantitative analysis of PCE systemic exposure showed that GA and PCA possess a relatively high exposure in rats (Ma et al., 2015, 2016; Huang et al., 2019; Guan et al., 2022) and humans (Li et al., 2021b). After oral administration of PCE, GA and PCA underwent a rapid absorption (Ma et al., 2015; Li et al., 2021b), a dose-dependent profile (Ma et al., 2015), and a relatively targeted distribution in kidney tissue (Ma et al., 2016). Consequently, GA and PCA were chosen as PCE tracer components in the pharmacokinetic- and tissue distribution-based HDIs studies.

Ciprofloxacin (CIP) was selected as a representative fluoroquinolone agent in this study because 1) it is a commonly used antibiotic in the treatment of urinary system diseases alone or in combination (Bonkat et al., 2022), and 2) it is cleared by active tubular secretion and intestinal excretion (Höffken et al., 1985; Rohwedder et al., 1990; Vance-Bryan et al., 1990). CIP's absolute bioavailability is approximately 70%, with no substantial loss by first pass metabolism, and its metabolites together account for approximately 10% of an oral dose (Vance-Bryan et al., 1990). Renal clearance of CIP accounts for 2/3 of its total clearance and exceeds the normal glomerular filtration rate, suggesting that active tubular secretion may play a role (Höffken et al., 1985; Mulgaonkar et al., 2012). Approximately 60% of CIP is excreted in unchanged form into the urine (Vance-Bryan et al., 1990). Approximately 20% of an intravenous dose of CIP is eliminated into the intestine (Rohwedder et al., 1990; Haslam et al., 2011). At physiological pH = 7.4, CIP predominantly exists as a zwitterion indicating that both anion and cation transporters may contribute to its excretion (Vanwert et al., 2008; Haslam et al., 2011; Arakawa et al., 2012; Mulgaonkar et al., 2012). CIP is a known substrate of the ATP-binding cassette transporters, which have been implicated in its intestinal secretion, biliary excretion and secretion into breast milk (Vance-Bryan et al., 1990; Merino et al., 2006; Ando et al., 2007; Mulgaonkar et al., 2012). Overall, drug transporter-mediated HDIs were assessed to reveal the altered systemic exposure and tissue distribution of CIP after combined treatment with PCE in this study.

2 Materials and methods

2.1 Chemicals and reagents

Relinqing® granules (4 g, 170207) and *P. capitatum* extract (PCE, 19338D) were kindly provided by Guizhou Warmen Pharmaceutical Co., Ltd. (Guiyang, China). Ciprofloxacin

hydrochloride tablets (0.25 g, 150202) and ciprofloxacin lactate and sodium chloride injection (Ciprobay®, 100 ml:0.2 g ciprofloxacin and 0.9 g sodium chloride, BXHK JX1) were commercially obtained from PKU HealthCare Corp., Ltd. (Chongqing, China) and Bayer Pharma AG (Leverkusen, Germany), respectively. Reference standards of GA (110831–201906), PCA (110809–201906), CIP (130451–201904), chloromycetin (130555–201704), and ofloxacin (130454–202007) were purchased from National Institute for Food and Drug Control (Beijing, China). Dulbecco's modified Eagle's medium (DMEM), nonessential amino acids solution (NEAA), fetal bovine serum (FBS), and penicillin-streptomycin solution were purchased from Invitrogen (Grand Island, NY, United States). BCA Protein Assay Kit (P0011) and complete Freund's adjuvant (CFA, P2036-10 ml) were provided by Beyotime Biotechnology (Shanghai, China). Isoflurane (S10010533) was obtained from Shanghai Yuyan Instrument Co., Ltd. (Shanghai, China). Acetonitrile, methanol and formic acid were purchased from Thermo Fisher Scientific (Waltham, MA). Other reagents were commercially available and of analytical grade.

2.2 Pharmacokinetic herb-drug interactions in healthy volunteers

2.2.1 Healthy subjects

Twelve healthy male volunteers aged 18–35 years who weighed at least 50 kg and had a body mass index of 19–24 kg/m^2 were eligible for recruitment. Additional inclusion criteria included a healthy status confirmed by a review of the medical history, a physical examination, clinical laboratory tests, and a non-smoking status. Subjects were excluded if they had any allergies, hematological abnormalities, or a history of renal, hepatic, or gastrointestinal diseases. Subjects were also excluded if they recently had taken any medications or ingested grapefruit juice, St. John's wort, or agents that interact with either *P. capitatum* or CIP for at least 2 weeks prior to dosing and during the study. Safety was monitored by performing clinical laboratory tests, 12-lead ECGs, recordings of vital signs, and physical examinations at baseline and scheduled times. The protocol was approved by the Ethics Committee of the Second Affiliated Hospital of Tianjin University of Traditional Chinese Medicine (Ethical Approval No: 2015-033-03). All subjects provided written informed consent prior to enrollment.

2.2.2 Study design in healthy volunteers

A randomized, three-period, crossover trial was designed to study the herb-drug interactions in healthy male subjects following the administration of single-dose treatments with PCE (8 g Relinqing®), CIP (0.5 g), or PCE (8 g) + CIP (0.5 g) (Registration No: ChiCTR-OPh-16010029). Each treatment period was separated by a washout period of 7 days. Subjects received multiple doses of PCE from day 22 to day 28 and a single dose of the combination of PCE and CIP treatment on day 29 (Figure 1). Subjects were offered standard meals 4 and 10 h after dosing. Water was not permitted during the hour before and the hour after dosing, with the exception of 240 ml administered with dosing; additional water intake was allowed at all other times. On days 1, 8, 15 and 29, 3 ml blood samples were collected from the antecubital vein catheter prior to drug administration and at 0.08, 0.17, 0.33, 0.5, 0.75, 1, 1.5, 2, 3, 4, 6, 8, 12, and 24 h after dosing. All samples were stored at −80°C until analysis.

2.3 Pharmacokinetic- and tissue distribution-based herb-drug interaction studies in rats

2.3.1 Experimental animals

Male Sprague-Dawley rats weighing 200–220 g were purchased from HFK Bioscience Co., Ltd. (SCXK 2019–0008, Beijing, China). All of the experimental procedures were carried out according to the Guidance for Ethical Treatment of Laboratory Animals. Approval for this study was granted by the Institutional Animal Care and Use Committee of Tianjin University of Traditional Chinese Medicine. All animals were housed at the individually ventilated cages (three rats per cage) in a temperature-controlled room under a 12-h light/dark cycle. Water and food were supplied *ad libitum* and the rats were fasted only with free access to water for 12 h prior to experiment.

2.3.2 Pharmacokinetic-based herb-drug interaction study in rats

In the pharmacokinetic-HDI study, eighteen rats were randomly assigned to three experimental groups (n = 6 per group). Rats in the PCE, CIP, and PCE + CIP groups were orally given a single dose of PCE (0.72 g/kg, comparable to a clinical dose of 8 g Relinqing®), CIP (0.045 g/kg, comparable to a clinical dose of 0.5 g ciprofloxacin hydrochloride tablets), PCE (0.72 g/kg) and CIP (0.045 g/kg), respectively. Blood samples (approx. 200 μl) were collected into heparinized tubes prior to dosing and at 0.17, 0.5, 1, 1.5, 2, 2.5, 3, 4, 6, 8, 12, and 24 h after oral dosing. Rats were euthanized with isoflurane at the end of the experiment. Plasma samples were separated after centrifugation at 3,000 rpm for 10 min and stored at −80°C until analysis.

2.3.3 Tissue distribution-based herb-drug interaction study in rats

In the tissue distribution-HDI study, thirty-six rats were randomly assigned to three experimental groups (n = 12 per group). Rats in the PCE, CIP, and PCE + CIP groups were given a single dose of PCE (0.72 g/kg, comparable to a clinical dose of 8 g

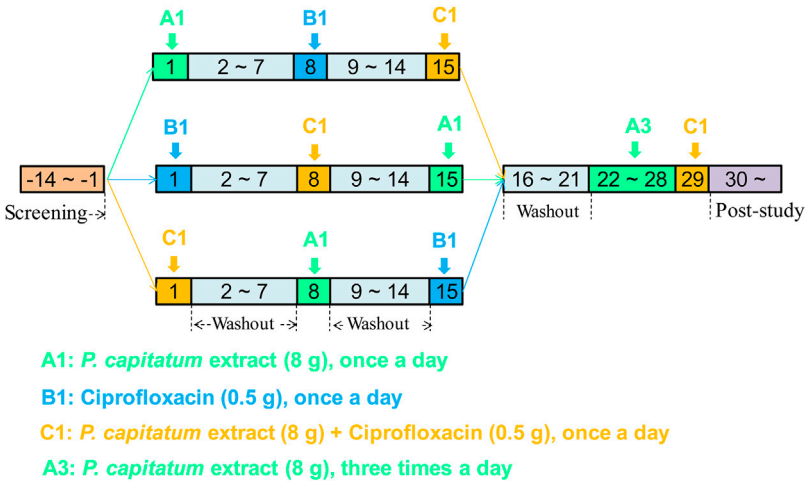

FIGURE 1
Schematic illustration of the study design in healthy subjects.

Relinqing®, *i.g.*), CIP (0.036 g/kg, comparable to a clinical dose of 0.4 g Ciprobay®, *i.v.*), PCE (0.72 g/kg) and CIP (0.036 g/kg), respectively. Three rats in each group were randomly euthanized with isoflurane at 0.5, 1, 3, and 5 h, respectively. The heart was perfused with normal saline to remove blood from the tissues. The heart, liver, lung, kidney, prostate, testis, seminal vesicle gland (SVG), and spleen were collected and then blotted on filter paper. Plasma and tissue samples were stored at −80°C until analysis.

2.4 Effect of PCE on the transport of ciprofloxacin mediated by multiple transporters

2.4.1 Inhibitory effects of gallic acid and protocatechuic acid on the activity of multiple transporters

Considering the relative exposure characteristics, GA and PCA were selected as PK-marker and Q-marker components of PCE in previous studies (Ma et al., 2015; Ma et al., 2016; Li et al., 2021b). In this study, we investigated the concentration-dependent inhibitions of GA and PCA on multiple transporters, including OAT1, OAT3, OCT2, MDR1, and BCRP. Stably expressing cell lines of hOAT1-MDCK, hOAT3-MDCK, hOCT2-S2, hMDR1-MDCK, hBCRP-MDCK, and their mock cells were obtained from Japan Fuji Biomedical Co., Ltd. The cells were maintained in DMEM (Sigma) supplemented with 10% FCS, 1% non-essential amino acids (Sigma), and 2% L-glutamine. The medium for the Transwell® plates (Corning Costar, Cambridge, MA, United States) was supplemented with 0.1% gentamicin. Membrane filters were placed in a 12 mm well with 1.5 and 0.5 ml of culture medium in the basolateral and apical compartments, respectively. Cells were cultured at 37°C in an atmosphere of 5% CO_2. The inhibition experiments were adapted from previous methods with minor modifications (Li et al., 2021a; 2021b).

Briefly, the hOAT1-MDCK, hOAT3-MDCK, and hOCT2-S2 cells were trypsinized and suspended in the culture medium to provide a density of 1.5×10^5 cells/ml. After incubating for 48 h, the cells were washed twice with preheated DPBS and then pre-incubated with DPBS for 10 min at 37°C. 500 µl of DPBS containing probe substrates was added to initiate the uptake in the presence or absence of GA, PCA or positive inhibitors. The hMDR1-MDCK and hBCRP-MDCK cells were suspended at a density of 4.0×10^5 cells/ml. After cultivation for 7 days, cells were washed twice and equilibrated for 30 min at 37°C with the pre-warmed HBSS buffer. 1.5 ml of transport buffer containing probe substrates was added in the basolateral compartment to initiate the efflux in the presence or absence of GA, PCA or positive inhibitors. The designated GA or PCA concentrations were 0.3, 1, 3, 10, 30 µM in the incubation system. ^{14}C-PAH (5 µM), ^{3}H-ES (0.05 µM), ^{14}C-TEA (5 µM), rhodamine 123 (10 µM), and lucifer yellow (10 µM) were chosen as probe substrates of hOAT1, hOAT3, hOCT2, hMDR1, and hBCRP, respectively. Probenecid (100 µM), cimetidine (600 µM), probenecid (100 µM), verapamil (10 µM), and cyclosporine (20 µM) were selected as positive inhibitors of hOAT1, hOAT3, hOCT2, hMDR1, and hBCRP, respectively. The content of DMSO was below 1% and constant in all inhibition experiments. All experiments were performed in triplicate. The cell lysate and 3.0 ml of aquasol-2 scintillation fluid were put into a scintillation flask. The radioactive intensity

of ^{14}C-PAH, ^{3}H-ES, and ^{14}C-TEA was measured using a Tri-Carb 2910TR scintillator (PerkinElmer, United States). Fluorescence was measured at 485 nm (excitation) and 546 nm (emission) for rhodamine 123, and 425 nm (excitation) and 528 nm (emission) for lucifer yellow. IC_{50} values were determined by employing GraphPad Prism 9.

2.4.2 Effects of PCE on the Bi-directional transport of ciprofloxacin in Caco-2 cells

A bidirectional assay in Caco-2 cells is a preferred method to determine whether an investigational drug is a substrate for P-gp/BCRP or whether an investigational drug is an inhibitor of P-gp/BCRP (US FDA, 2020). The Caco-2 cell lines were obtained from the National Collection of Authenticated Cell Cultures (NCACC, Shanghai, China). The bi-directional transport assay was performed on 12-mm Transwell Permeable Supports with 0.4 mm-pore polycarbonate membrane insert and 1.12 cm^2 growth areas. Caco-2 cells were maintained in DMEM complete high-glucose medium with L-glutamine, supplemented with 10% FBS and 1% NEAA. The cells were seeded at a density of 3×10^5 cells/well, incubated at 37°C and 5% CO_2, and cultured for 21 days with replacement of cell culture medium supplemented with 1% penicillin-streptomycin every second day. Membrane filters were placed in a 12 mm well with 1.5 and 0.5 ml of culture medium in the basolateral and apical compartments, respectively. TEER was measured as an indication of an intact monolayer using a Millicell ERS voltohmmeter (Millipore, Merck). After washing the monolayers with prewarmed PBS, the cells were preincubated with DMEM with and without the investigated drugs, including GA (5, 50 μM), PCA (5, 50 μM) and PCE (10, 100 mg/ml). The transport assays were initiated by the addition of CIP (25 μM) with or without the investigated drugs into the apical or basal compartment. Aliquots of 50 μl were collected from the acceptor compartment at 0.5 h. The apparent permeability coefficient (P_{app}) was calculated using the following formula: $P_{app} = (dC/dt) \times V_r/(A \times C_0)$, where dC/dt is the alteration in concentration over time, V_r is the volume of the receiver compartment, A is the area of the cell monolayer, and C_0 is the initial concentration in the donor compartment. The permeation of drug from the apical (A) to the basolateral (B) side of the cells ($P_{app,A\text{-}B}$) is compared with the permeation in the opposite direction ($P_{app,B\text{-}A}$). If the net flux ratio is >2, this suggests a probable P-gp or BCRP substrate. If the net flux ratio decreases with increasing concentrations of the investigational drug, this suggests a probable P-gp or BCRP inhibitor (US FDA, 2020).

2.4.3 Effects of PCE on the MDR1 and BCRP mRNA expressions in Caco-2 cells

Caco-2 cells induced with the positive control or tested drugs were then incubated in a 37°C incubator with 5% CO_2 for 48 h. Bosentan served as a positive control for the induction of MDR1 and BCRP (van Giersbergen et al., 2002). After the incubation period, cells were harvested from the Transwell inserts for RNA extraction. The mRNA expressions of MDR1 and BCRP in cells were detected at 48 h after pretreatments with bosentan (20 μM), GA (50 μM), PCA (50 μM), and PCE (100 mg/ml). Real-time quantitative PCR (qRT-PCR) was performed on an ABI Prism 7900HT Sequence Detection System (Applied Biosystems, Foster City, CA, United States) for the analysis of MDR1 and BCRP genes. Primers of housekeeping gene β-actin was used as internal controls. The primer sequences used for MDR1 amplification were CGCACCTGCATTGTGATTGC (forward) and AGATGC CTTTCTGTGCCAGC (reverse). The primer sequences used for BCRP amplification were AGCAGCAGGTCAGAGTGTGG (forward) and CTGAAGCCATGACAGCCAAG (reverse). The relative gene expression levels were determined using the comparative CT method (ΔΔCT method). The cut-off CT was set at 35 cycles for all analyses. An arbitrary classification system was assigned to the data, designating relative expression levels >2 as high mRNA expression, levels between 2 and 1 as moderate mRNA expression, levels between 1 and 0.1 as low mRNA expression and levels <0.1 as unexpressed.

2.5 LC-MS/MS assay for PCE and ciprofloxacin

2.5.1 Sample preparation

The tissue samples were homogenized using a tissue homogenizer (JXFSTPRP-24, Shanghaijingxin Experimental Technology, Shanghai, China) in physiological saline solution (1:4, *w*/*v*). The analytes and internal standards were extracted from tissue homogenates and plasma samples by a simple protein precipitation method. Briefly, an aliquot of 100 μl biological samples, 5 μl internal standard solutions, and 300 μl acetonitrile were vortex-mixed for 3 min and then centrifuged at 14,000 rpm for 10 min. The supernatant was transferred and dried using a gentle stream of nitrogen at 35°C. The residues were reconstituted with 100 μl of 20% acetonitrile solution, vortex-mixed for 1 min, and centrifugated at 14,000 rpm for 10 min. The supernate was utilized for the quantification of GA, PCA, and CIP.

2.5.2 LC-MS/MS conditions

Samples were analyzed using a Waters ACQUITY™ ultra performance liquid chromatography system (Waters Corp., Milford, MA, United States) equipped with an QTRAP5500 triple-quadrupole mass spectrometer (SCIEX, Framingham, MA, United States) and an electrospray source. Data acquisition was controlled by Analyst 1.7.2 software (SCIEX, Concord, ON, Canada).

Chromatographic separation of GA and PCA was achieved on an ACQUITY UPLC BEH C18 (2.1 mm × 100 mm, 1.7 μm;

Waters Corp., Milford, MA, United States) with a mobile phase of (A) 0.1% formic acid aqueous solution and (B) 0.1% formic acid acetonitrile at a flow rate of 0.3 ml/min. The gradient elution program was as follows: 0–8.5 min, 97% A; 8.7–11 min, 60% A; 11.5–13.5 min, 10% A; 14–15 min, 97% A. The quantitation of GA and PCA was performed using multiple reaction monitoring (MRM) mode with an electron spray ionization (ESI) source in negative-ionization mode. The source operation parameters were optimized as follows: ion spray voltage, −4,500 V; source temperature, 550°C; ion source gas1, 55 psi; ion source gas2, 60 psi; curtain gas, 35 psi. The precursor-product ion transitions of GA, PCA, and chloramphenicol (internal standard) were 169.0→125.1, 153.1→109.0, and 321.1→152.1, respectively.

The separation of CIP was performed on the same column and mobile phase as GA and PCA. The gradient elution program was as follows: 0–2.5 min, 85% A; 3–4 min, 10% A; 4.5–6 min, 85% A; 14–15 min, 97% A. The quantitation of CIP was performed using MRM mode with an ESI source in positive-ionization mode. The source parameters were chosen as follows: ion spray voltage, 5,500 V; source temperature, 450°C; ion source gas1, 50 psi; ion source gas2, 50 psi; curtain gas, 35 psi. The precursor-product ion transitions of CIP and ofloxacin (internal standard) were 332.1→288.1 and 362.2→318.1, respectively.

2.6 Pharmacokinetic analysis

PK parameters were estimated with noncompartmental methods using WinNonlin version 6.4 (Certara, Princeton, NJ). The peak plasma concentration (C_{max}) and time to reach the peak plasma concentration (T_{max}) were calculated from the actual plasma concentration data. The area under the plasma concentration-time curve from zero to the last measurable concentration ($AUC_{0\text{-}t}$) was calculated *via* the linear trapezoidal rule. The $AUC_{0\text{-}\infty}$ was calculated using the following formula: $AUC_{0\text{-}\infty} = AUC_{0\text{-}t} + C_t/k_e$, where C_t is the last plasma concentration measured. The terminal elimination half-life ($t_{1/2}$) was calculated as $0.693/k_e$. The oral clearance (CL/F) and volume of distribution (V_z/F) were defined as $Dose/AUC_{0\text{-}\infty}$ and $Dose/(k_e \cdot AUC_{0\text{-}\infty})$, respectively.

2.7 Data analysis

All data were summarized as mean ± standard deviation (SD). All statistical analyses were performed using SPSS software (Chicago, IL, United States). Comparisons between groups were performed using unpaired Student's *t*-test. A *p*-value of less than 0.05 was considered statistically significant. Pharmacokinetic interactions were reported as 90% confidence intervals (CI) for the geometric mean ratios (GMR) of the observed pharmacokinetic measures in the presence and absence of the interacting drug. If the 90% CI for systemic exposure ratios was entirely encompassed within the equivalence range of 0.80–1.25, we concluded that clinically significant difference was not present.

3 Results

3.1 Pharmacokinetic herb-drug interaction between PCE and ciprofloxacin in healthy volunteers

All recruited subjects were healthy Chinese natives. All enrolled subjects completed the study protocol as planned. Their age, height, weight, and body mass index were summarized in Supplementary Table S1. No major protocol deviations were identified, and no serious adverse reactions were observed throughout the study.

3.1.1 Effect of PCE on the pharmacokinetics of ciprofloxacin in human

The effects of PCE on CIP plasma concentrations were investigated by comparing alterations in PK exposure measures between control and treatment groups. The CIP concentration-time profiles and PK parameters are shown in Figure 2A and Table 1, respectively. The plasma ciprofloxacin $AUC_{0\text{-}t}$ and C_{max} were significantly decreased in the presence of single-dose/multiple-dose PCE (Figures 2B,C). Following combination therapy with a single dose of PCE, the GMRs±90% CI of ciprofloxacin $AUC_{0\text{-}t}$ and C_{max} were 0.61 (0.55, 0.68) and 0.52 (0.45, 0.62), respectively. After pretreatment with multiple doses of PCE, the GMRs ± 90% CI of ciprofloxacin $AUC_{0\text{-}t}$ and C_{max} were 0.64 (0.54, 0.78) and 0.54 (0.42, 0.74), respectively, falling out of the equivalence range of 0.80–1.25 (Figure 2D). The results indicated that the co-administration of PCE significantly reduces the systemic exposure of CIP in human.

3.1.2 Effect of ciprofloxacin on the pharmacokinetics of PCE PK-markers in human

GA and PCA were identified as PK-markers of PCE to present the effects of CIP on PCE systemic exposures. After co-administration of CIP and PCE, the PK changes of GA and PCA are displayed in Figures 3, 4, respectively. Their PK parameters (Table 2) were calculated from the plasma concentration-time curves (Figures 3A, 4A). No significant differences between control and combination treatment groups were observed on the systemic exposure parameters of GA (Figures 3B,C) and PCA (Figures 4B,C). Following co-treatment with CIP and a single dose of PCE, the GMRs ±90% CI of GA $AUC_{0\text{-}t}$ and C_{max} were 1.15 (0.94, 1.49) and 0.95 (0.83, 1.16), respectively (Figure 3D), and the GMRs ± 90% CI of PCA $AUC_{0\text{-}t}$ and C_{max} were 1.26 (1.12, 1.49) and 1.02 (0.85, 1.30), respectively (Figure 4D). Following co-

10.3389/fphar.2022.1033667

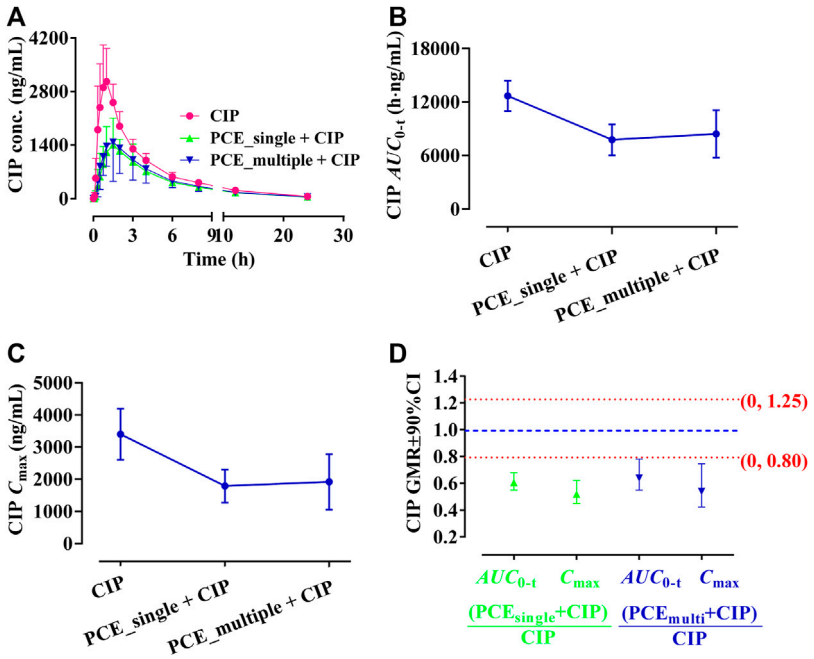

FIGURE 2
Plasma ciprofloxacin (CIP) concentration-time profiles **(A)**, the systemic exposure parameters including $AUC_{0\text{-}t}$ **(B)** and C_{max} **(C)**, and their 90% CIs for the geometric mean ratios [GMR, **(D)**] in the presence and absence of the single-dose/multiple-dose PCE to healthy humans (mean ± SD, n = 12).

TABLE 1 Pharmacokinetic parameters of ciprofloxacin after the oral administration of ciprofloxacin hydrochloride tablets (CIP, 0.5 g) with and without PCE (8 g) to human subjects (mean ± SD, n = 12).

Parameters	CIP	CIP + PCE_{single}[b]	CIP + $PCE_{multiple}$[c]
C_{max} (ng/ml)	3400 ± 796	1920 ± 863*	1790 ± 510*
$AUC_{0\text{-}t}$ (h·ng/mL)	12700 ± 1690	8410 ± 2640*	7770 ± 1730*
$AUC_{0\text{-}\infty}$ (h·ng/mL)	13200 ± 1800	8790 ± 2690*	8110 ± 1770*
t_{max} (h)[a]	1.0 (0.33–1.5)	1.25 (0.5–3)	1.5 (0.5–3)
k_e (h^{-1})	0.12 ± 0.01	0.12 ± 0.01	0.12 ± 0.01
$t_{1/2}$ (h)	5.64 ± 0.49	5.79 ± 0.50	5.66 ± 0.40
V_z/F (L)	313 ± 35.9	524 ± 183*	525 ± 110*
CL/F (L/h)	0.64 ± 0.08	1.03 ± 0.31*	1.07 ± 0.21*

[a]Median (range).
[b]PCE_{single}, a single dose of PCE (8 g).
[c]Multiple doses of PCE (8 g, TID) for seven consecutive days. *p< 0.05, significant differences were observed when compared with the CIP, group.

treatment with ciprofloxacin and multiple doses of PCE, the GMRs ± 90% CI of GA $AUC_{0\text{-}t}$ and C_{max} were 1.08 (0.84, 1.54) and 1.02 (0.88, 128), respectively (Figure 3D), and the GMRs±90% CI of PCA $AUC_{0\text{-}t}$ and C_{max} were 1.06 (0.92, 1.25) and 0.96 (0.84, 1.14), respectively (Figure 4D). The results indicated that the co-treatment with CIP does not significantly alter the PK behaviors of PCE PK-markers in humans.

3.2 Pharmacokinetic herb-drug interaction between PCE and ciprofloxacin in rats

3.2.1 Effect of PCE on the pharmacokinetics of ciprofloxacin in rats

The effects of PCE on circulating CIP concentrations were observed by comparing changes in PK exposure measures

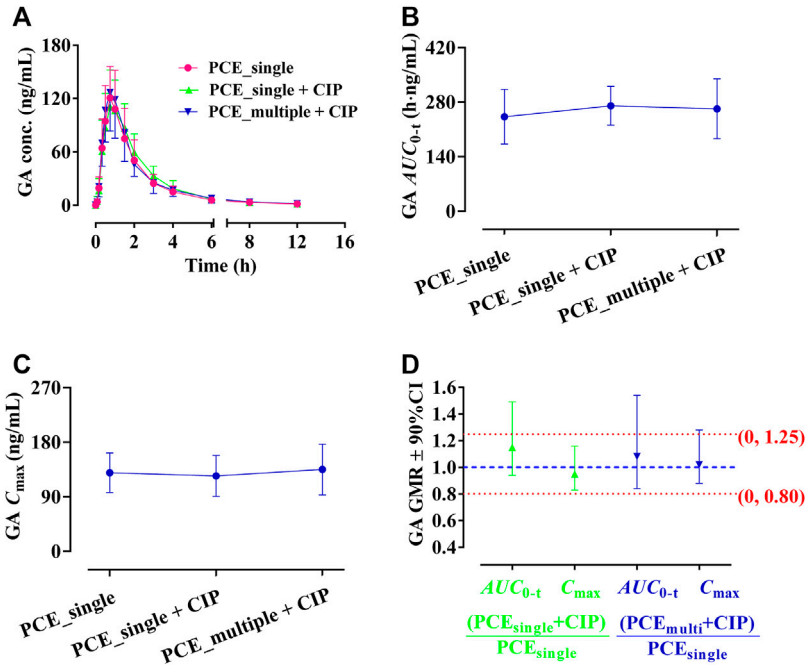

FIGURE 3
Plasma gallic acid (GA) concentration-time profiles **(A)**, the systemic exposure parameters of GA including AUC_{0-t} **(B)** and C_{max} **(C)**, and their 90% CIs for the geometric mean ratios [GMR, **(D)**] in the presence and absence of oral ciprofloxacin hydrochloride tablets (CIP) to healthy humans (mean ± SD, n = 12).

between CIP and CIP + PCE groups. The CIP concentration-time profiles and PK parameters are presented in Figure 5A and Table 3, respectively. The AUC_{0-t}, $AUC_{0-\infty}$ and C_{max} of circulating CIP were significantly decreased in the presence of single-dose PCE, while the V_z/F and CL/F were significantly increased (Table 3). After combination therapy, the GMRs ±90%CI of ciprofloxacin AUC_{0-t} and C_{max} were 0.50 (0.27, 0.74) and 0.36 (0.27, 0.46), respectively, falling out of the equivalence range of 0.80–1.25 (Figure 5B). The results indicated that the co-administration of PCE significantly reduces the circulating exposure of CIP in rats.

3.2.2 Effect of ciprofloxacin on the pharmacokinetics of gallic acid and protocatechuic acid in rats

After combination therapy, the altered circulating exposures of PCE PK-markers (GA and PCA) are shown in Figures 5C–F. The PK parameters of GA and PCA are summarized in Table 4. No significant differences between PCE and PCE + CIP groups were observed on the main PK parameters of GA and PCA. After co-treatment with CIP and PCE, the GMRs ±90% CI of GA AUC_{0-t} and C_{max} were 0.78 (0.54, 1.01) and 1.10 (0.82, 1.36), respectively (Figure 5D), and the GMRs ± 90% CI of PCA AUC_{0-t} and C_{max} were 0.97 (0.81, 1.09) and 1.17 (1.02, 1.62), respectively (Figure 5F). The results indicated that the co-treatment with CIP does not significantly change the PK behaviors of GA and PCA in rats, which was the same conclusion drawn from the study in humans.

3.3 Changed tissue distribution of ciprofloxacin and PCE in rats

3.3.1 Effect of PCE on the Tissue Distribution of ciprofloxacin in Rats

PCE had little effect on plasma CIP after intravenous injection using rats (Supplementary Figure S1; Supplementary Table S2). The tissue distribution profiles of CIP in normal rats after intravenous administration of CIP in the absence and presence of PCE are charted in Figures 6A,B, respectively. PCE significantly increased the tissue to plasma distribution coefficients (K_p) of CIP in the prostate and SVG, but decreased its K_p in the liver ($p < 0.05$, Figure 6C). The AUC_{0-t} of CIP in tissues was arranged as follows: kidney > SVG > liver > spleen > prostate > lung in the CIP group, and kidney > SVG > prostate > spleen > liver > lung in the CIP + PCE group (Figure 6D). The C_{max} of CIP in tissues was arranged as

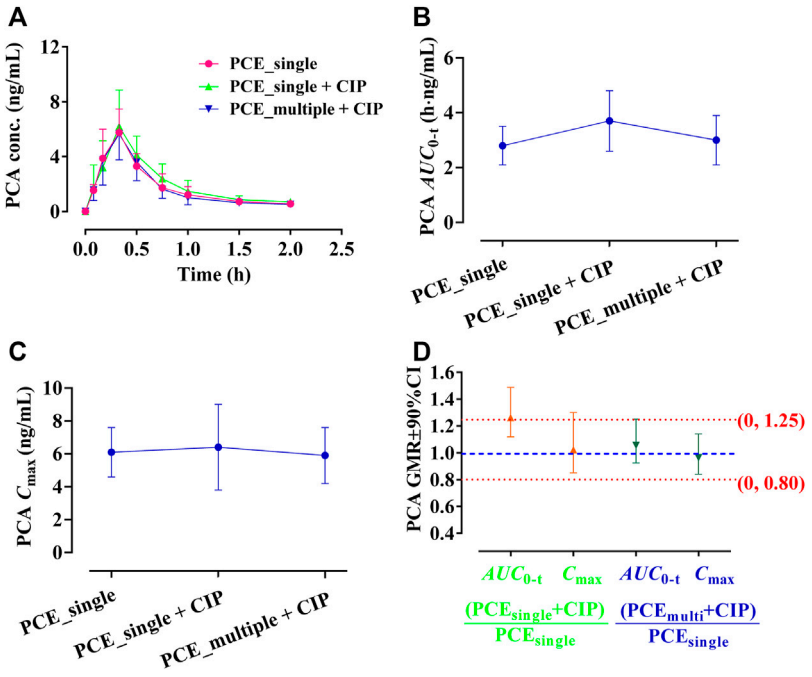

FIGURE 4
Plasma protocatechuic acid (PCA) concentration-time profiles **(A)**, the systemic exposure parameters of PCA including $AUC_{0\text{-}t}$ **(B)** and C_{max} **(C)**, and their 90% CIs for the geometric mean ratios [GMR, **(D)**] in the presence and absence of oral ciprofloxacin hydrochloride tablets (CIP) to healthy humans (mean ± SD, n = 12).

TABLE 2 Pharmacokinetic parameters of gallic acid (GA) and protocatechuic acid (PCA) after the oral administration of PCE (8 g) with and without ciprofloxacin hydrochloride tablets (CIP, 0.5 g) to human subjects (mean ± SD, n = 12).

Parameters	GA			PCA		
	PCE_{single}[b]	PCE_{single} + CIP	$PCE_{multiple}$[c]+ CIP	PCE_{single}	PCE_{single} + CIP	$PCE_{multiple}$+ CIP
C_{max} (ng/ml)	130 ± 32.7	124 ± 33.8	135 ± 41.9	6.07 ± 1.48	6.44 ± 2.57	5.88 ± 1.66
$AUC_{0\text{-}t}$ (h·ng/mL)	242 ± 70.0	271 ± 50.0	263 ± 76.7	2.84 ± 0.72	3.68 ± 1.15	3.03 ± 0.9
$AUC_{0\text{-}\infty}$ (h·ng/mL)	248 ± 67.0	274 ± 50.8	268 ± 77.3	3.39 ± 0.94	4.40 ± 0.93	3.35 ± 0.99
t_{max} (h)[a]	0.88 (0.5, 1)	1 (0.5, 1.5)	0.75 (0.5, 1.5)	0.33 (0.17, 0.75)	0.33 (0.33, 0.5)	0.33 (0.17, 0.75)
k_e (h^{-1})	0.51 ± 0.19	0.47 ± 0.14	0.42 ± 0.11	2.36 ± 0.82	2.05 ± 1.02	2.51 ± 0.85
$t_{1/2}$ (h)	1.64 ± 0.92	1.59 ± 0.50	1.78 ± 0.55	0.32 ± 0.11	0.42 ± 0.19	0.31 ± 0.14
V_z/F (L)	322 ± 295	245 ± 71.8	286 ± 75.2	148 ± 23.9	149 ± 65.6	150 ± 54.4
CL/F (L/h)	2.10 ± 0.64	1.98 ± 0.71	1.82 ± 0.35	5.64 ± 1.45	4.26 ± 0.91	5.78 ± 1.57

[a]Median (range).
[b]PCE_{single}, a single dose of PCE (8 g).
[c]Multiple doses of PCE (8 g, TID) for seven consecutive days. No significant differences were observed when compared with the PCE_{single} group (p> 0.05).

follows: kidney > liver > SVG > spleen > prostate > lung in the CIP group, and prostate > SVG > kidney > liver > spleen > lung in the CIP + PCE group (Figure 6E). The mean ratios of CIP tissue exposure with and without PCE were more than 1.25 times in the prostate, testis and SVG, but less than 0.8 times in the kidney, liver and lung. PCE significantly increased tissue exposure of CIP in the prostate and testis, but decreased its exposure in the liver and lungs ($p < 0.05$).

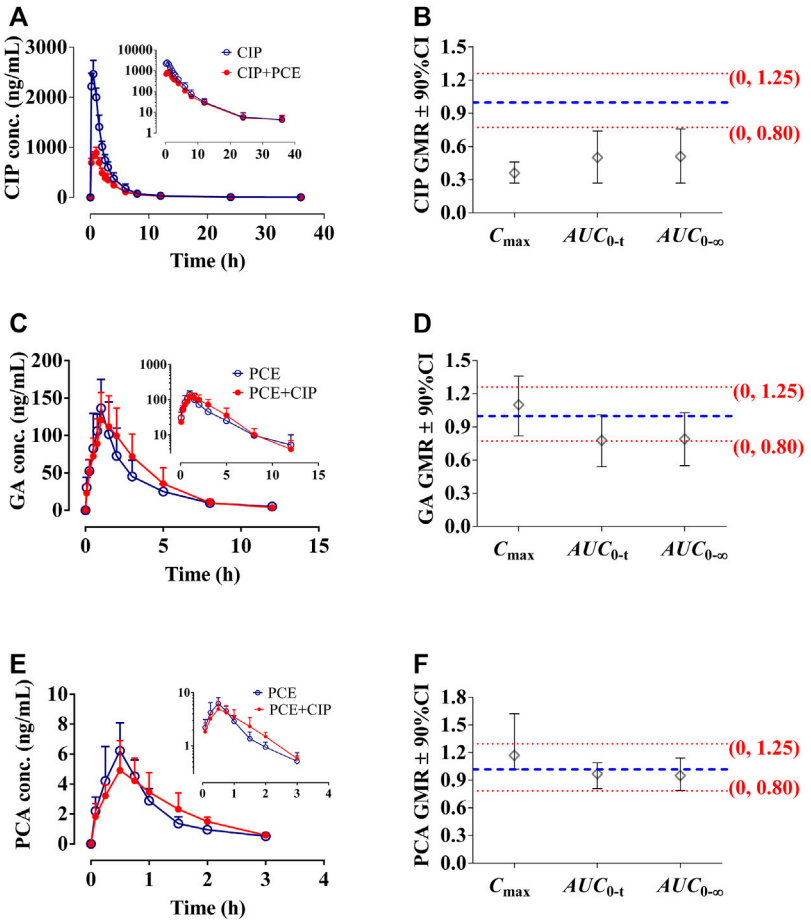

FIGURE 5
Circulating ciprofloxacin (CIP) concentration-time profiles **(A)** and the 90% confidence intervals (CI) for the geometric mean ratios [GMR, **(B)**] of C_{max}, AUC_{0-t} and $AUC_{0-\infty}$ in the presence and absence of PCE to rats, as well as gallic acid [GA, **(C,D)**] and protocatechuic acid [(PCA, **(E,F)**] in the presence and absence of CIP (mean ± SD, n = 6).

TABLE 3 Pharmacokinetic parameters of ciprofloxacin after intragastric administration of ciprofloxacin (CIP, 0.045 g/kg) with and without PCE (0.72 g/kg) to rats (mean ± SD, n = 6).

Parameters	CIP	CIP + PCE
C_{max} (ng/ml)	2470 ± 272	892 ± 108*
AUC_{0-t} (h·ng/mL)	6090 ± 884	3070 ± 633*
$AUC_{0-\infty}$ (h·ng/mL)	6120 ± 889	3110 ± 665*
t_{max} (h)[a]	0.5 (0.5–0.5)	1.0 (0.5–1.0)*
k_e (h^{-1})	0.135 ± 0.04	0.143 ± 0.039
$t_{1/2}$ (h)	5.49 ± 1.66	5.22 ± 1.84
V_z/F (L)	12.16 ± 5.48	21.40 ± 3.31*
CL/F (L/h)	1.50 ± 0.25	2.99 ± 0.60*

[a]Median (range). *p< 0.05, significant differences were observed when compared with the CIP, group.

3.3.2 Effect of ciprofloxacin on the Tissue Distribution of PCE PK-markers in Rats

The tissue distribution curves of GA in normal rats after intragastric administration of PCE in the absence and presence of CIP are displayed in Figures 7A,B, respectively. CIP significantly increased the K_p of GA in the lungs, but did not significantly alter its K_p in other tissues (Figure 7C). The AUC_{0-t} of GA in tissues was ranked as follows: SVG > prostate > kidney > testis > plasma (Figure 7D). The C_{max} of GA in tissues was ranked as follows: SVG > prostate > kidney > plasma > testis in the PCE group, and SVG > prostate > kidney > lung > plasma in the CIP + PCE group (Figure 7E). CIP significantly increased the AUC_{0-t} and/or C_{max} of GA in the prostate and testis, but decreased its C_{max} in the kidney and heart (p < 0.05).

TABLE 4 Pharmacokinetic parameters of gallic acid and protocatechuic acid after intragastric administration of PCE (0.72 g/kg) with and without ciprofloxacin (CIP, 0.045 g/kg) to rats (mean ± SD, n = 6).

Parameters	Gallic acid (GA)		Protocatechuic acid (PCA)	
	PCE	PCE + CIP	PCE	PCE + CIP
C_{max} (ng/ml)	133.84 ± 36.38	146.75 ± 37.94	5.08 ± 1.82	6.69 ± 1.87
$AUC_{0\text{-}t}$ (h·ng/mL)	465.36 ± 171.00	363.91 ± 137.00	6.72 ± 2.39	6.37 ± 1.18
$AUC_{0\text{-}\infty}$ (h·ng/mL)	482.79 ± 169.05	384.51 ± 1.49	7.32 ± 2.39	7.04 ± 1.55
t_{max} (h)[a]	1.5 (1–1.5)	1 (0.5–1)	0.5 (0.5–0.75)	0.5 (0.25–0.75)
k_e (h^{-1})	0.35 ± 0.16	0.44 ± 0.26	1.11 ± 0.38	1.10 ± 0.45
$t_{1/2}$ (h)	2.62 ± 1.78	1.92 ± 0.74	0.68 ± 0.21	0.76 ± 0.43
V_z/F (L)	8.93 ± 9.83	6.41 ± 1.80	6.50 ± 3.16	6.87 ± 2.54
CL/F (L/h)	2.06 ± 0.85	2.58 ± 0.95	6.72 ± 2.19	6.67 ± 1.54

[a]Median (range). No significant differences were observed when compared with the PCE, group (p > 0.05).

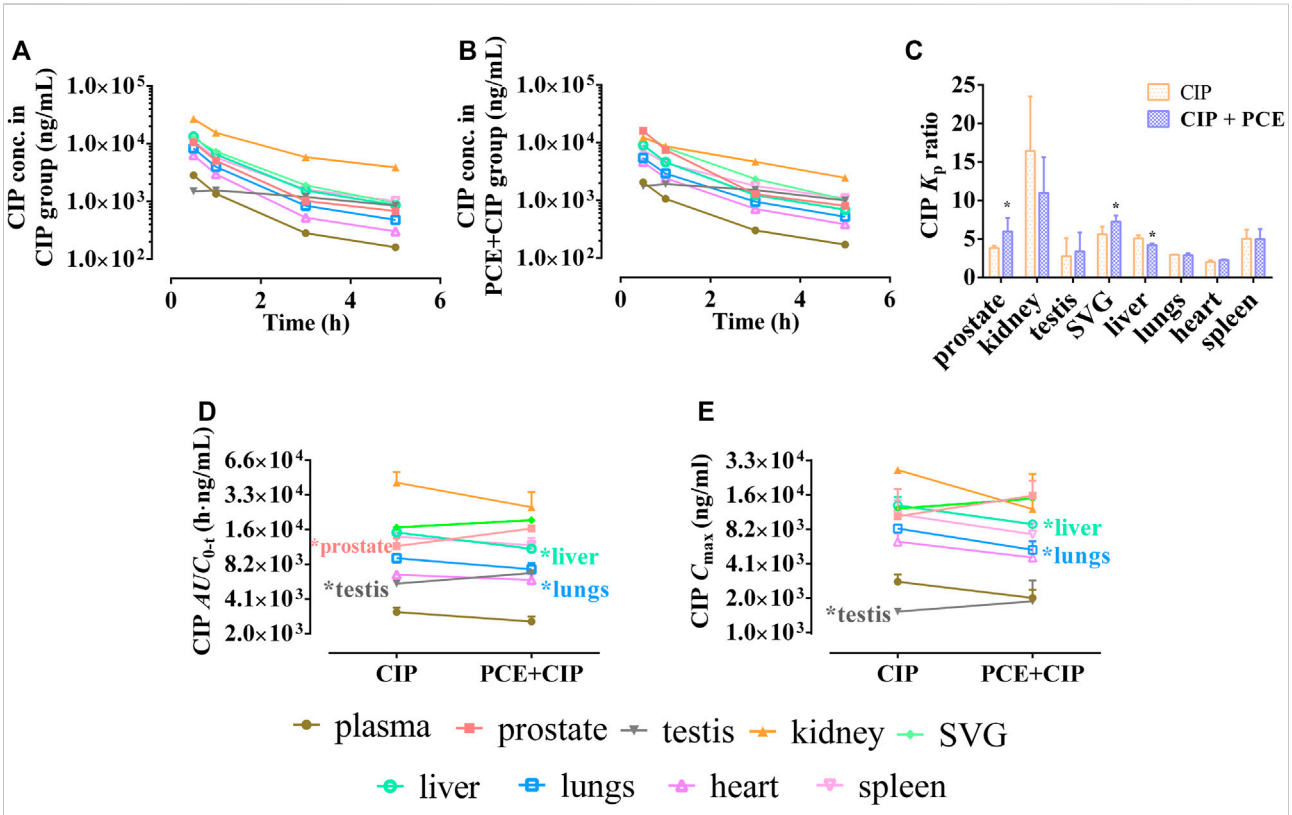

FIGURE 6
Tissue distribution profiles of ciprofloxacin (CIP) after intravenous administration of CIP in the absence **(A)** and presence **(B)** of PCE to rats, as well as the tissue to plasma distribution coefficients [K_p, **(C)**] and the distribution parameters $AUC_{0\text{-}t}$ **(D)** and C_{max} **(E)** of CIP (mean ± SD, n = 3).

The tissue distribution curves of PCA in the absence and| presence of CIP are shown in Figures 8A,B, respectively. CIP did not significantly alter the K_p of PCA in each tissue (p > 0.05, Figure 8C). Both $AUC_{0\text{-}t}$ and C_{max} of PCA in tissues were arranged as follows: SVG > kidney > prostate > testis > spleen in the PCE group, and prostate > SVG > kidney > testis > plasma in the CIP + PCE group (Figures 8D,E). CIP significantly increased the C_{max} of PCA in the prostate, but decreased its $AUC_{0\text{-}t}$ in the kidney (p < 0.05).

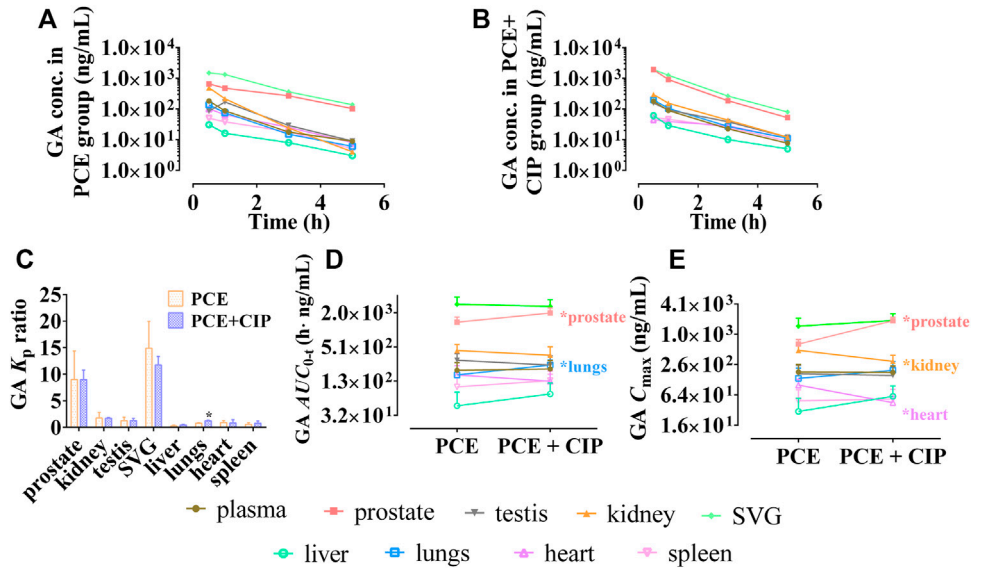

FIGURE 7
Tissue distribution profiles of gallic acid (GA) after oral administration of PCE in the absence **(A)** and presence **(B)** of ciprofloxacin, as well as the tissue to plasma distribution coefficients [K_p, **(C)**] and the distribution parameters including AUC_{0-t} **(D)** and C_{max} **(E)** of GA (mean ± SD, n = 3).

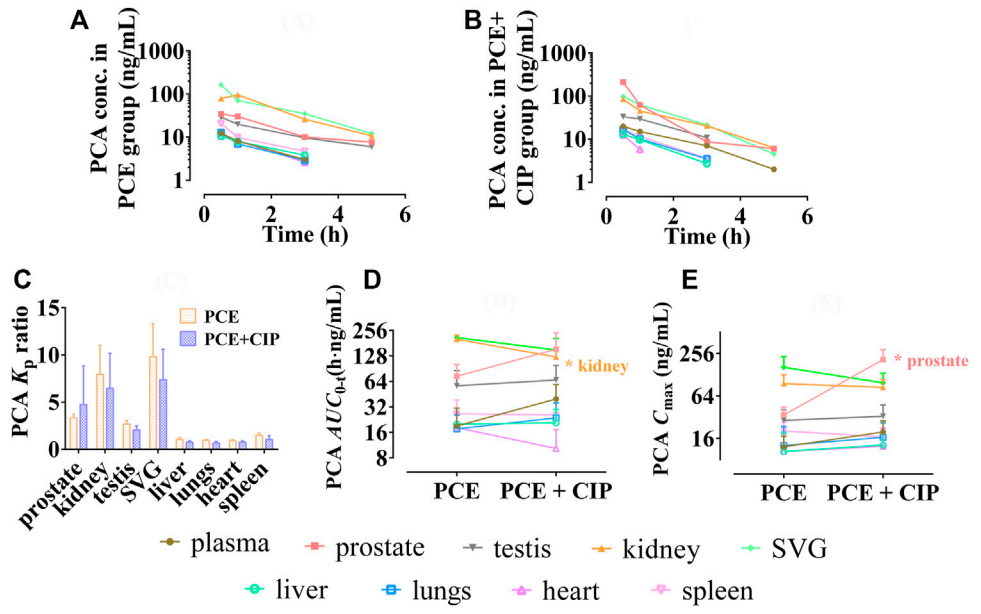

FIGURE 8
Tissue distribution profiles of protocatechuic acid (PCA) after oral administration of PCE in the absence **(A)** and presence **(B)** of ciprofloxacin, as well as the tissue to plasma distribution coefficients [K_p, **(C)**] and the distribution parameters AUC_{0-t} **(D)** and C_{max} **(E)** of PCA (mean ± SD, n = 3).

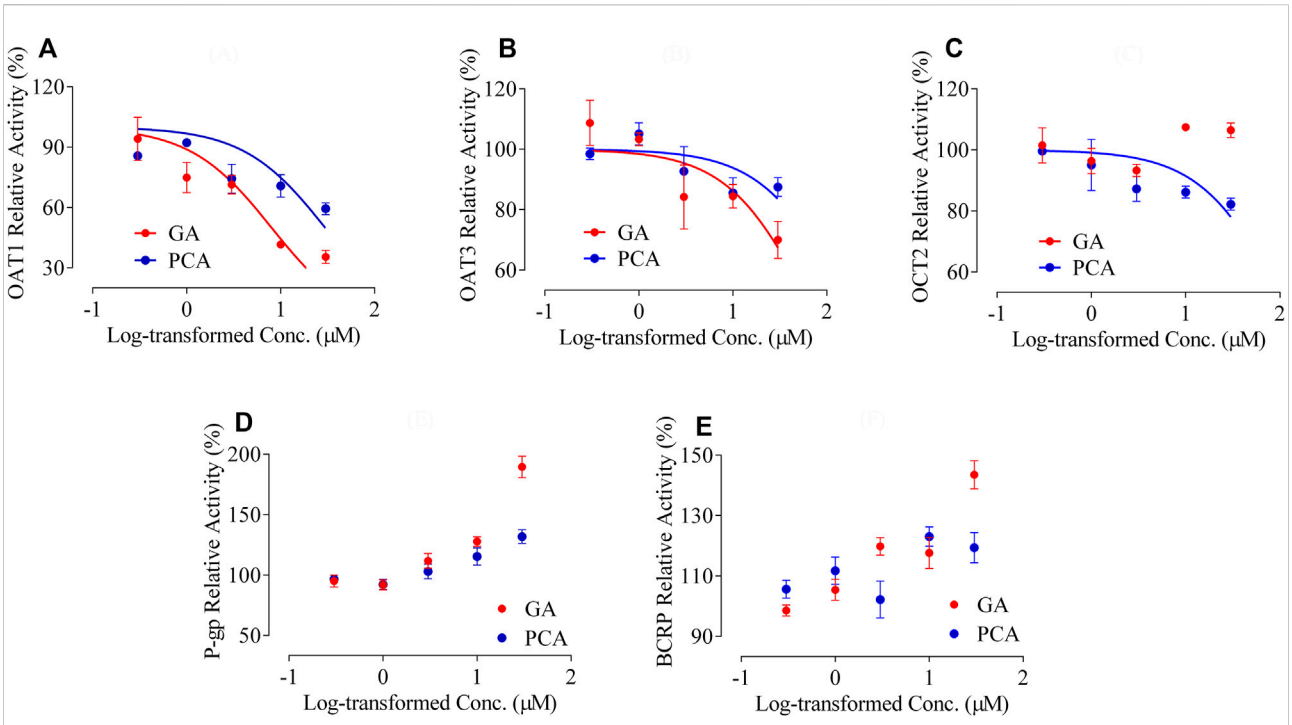

FIGURE 9
Inhibitory effects of GA and PCA on the activity of multiple transporters, including human organic anion transporter 1 [hOAT1, **(A)**], [hOAT3 **(B)**], human organic cation transporter 2 [hOCT2, **(C)**], human multidrug resistance protein 1 [hMDR1, **(D)**], and human breast cancer resistance protein [hBCRP, **(E)**] (mean ± SD, n = 3).

3.4 Effect of PCE on the transport of ciprofloxacin mediated by multiple transporters

3.4.1 Inhibitory effects of gallic acid and protocatechuic acid on the activity of multiple transporters

Significant inhibitory effects of the positive inhibitors of probenecid, cimetidine, rifampicin, verapamil, and cyclosporine were presented on the transporters hOAT1, hOAT3, hOCT2, hMDR1, and hBCRP, respectively (Supplementary Figure S2). A concentration-dependent inhibition type was observed on the transporters hOAT1 and hOAT3 for GA, as well as the transporters hOAT1, hOAT3 and hOCT2 for PCA (Figures 9A–C). GA and PCA presented significant inhibitory effects on the hOAT1-mediated uptake of ^{14}C-PAH with the IC_{50} values 8.01 and 29.73 μM, respectively (Figure 9A). Weak or ineffective inhibitions were observed on hOAT3 for GA (IC_{50} = 62.33 μM) and PCA (IC_{50} = 152.4 μM, Figure 9B), as well as hOCT2 for PCA (IC_{50} = 107.0 μM, Figure 9C). Meanwhile, no inhibitory effect was observed on MDR1 or BCRP′ activity after co-incubation with GA and PCA. Interestingly, it shows a concentration-dependent increase in the efflux of MDR1-mediated rhodamine 123 or BCRP-mediated lucifer yellow with the increased GA and PCA's concentration ranges from 0.3 to 30 μM (Figures 9D,E).

3.4.2 Effect of PCE on the bidirectional transport of ciprofloxacin in Caco-2 cells

In the bidirectional transport assay with Caco-2 cells, the net flux ratio of CIP after 0.5 and 1 h were 4.13 ± 0.76 and 3.48 ± 0.10, respectively. After co-incubation with GA, PCA and PCE, the net flux ratio of CIP showed varying degrees of enlargement (Figures 10A,B). A significant improvement was observed in the net efflux ratios after co-treatment with GA (50 μM), PCA (50 μM), and PCE (100 mg/ml) ($p < 0.05$). The increased net flux ratio facilitates the flow of CIP from the blood to the intestinal lumen, renal tubules or bile ducts, which may be related to the reduction of CIP systemic exposure.

3.4.3 Effect of PCE on the expressions of MDR1 and BCRP in Caco-2 cells

The effect of PCE on the expression of MDR1 and BCRP mRNAs are shown in Figures 10C,D, respectively. After pretreatment with bosentan, the expression of P-gp and BCRP mRNAs in Caco-2 cells were increased by 7.36- and 4.31-fold, respectively. After pretreatment with the investigated drugs, the expression of MDR1 and BCRP mRNAs increased 6.02- and 6.00-fold in cells treated with GA, 3.56- and 3.33-fold in cells

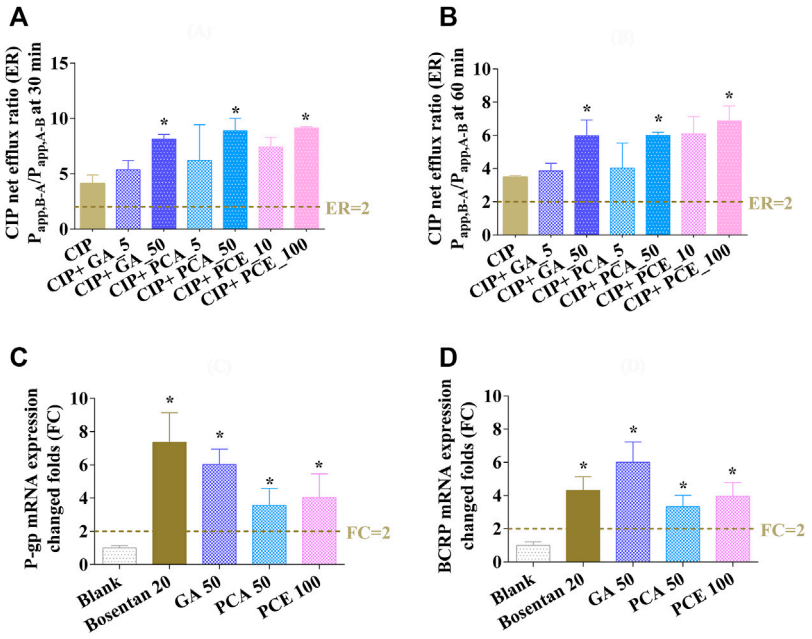

FIGURE 10
Effects of gallic acid (GA), protocatechuic acid (PCA) and PCE on the change of ciprofloxacin efflux ratios at 0.5 h **(A)** and 1 h **(B)**, and the mRNA expressions of MDR1 **(C)** and BCRP **(D)** in Caco-2 cells (mean ± SD, *n* = 3).

treated with PCA, and 4.04- and 3.95-fold in cells treated with PCE, respectively. The increased MDR1 and BCRP mRNA expressions may contribute to CIP efflux from the blood circulatory system.

4 Discussion

Herbal medicinal products are commonly used as a complementary or alternative treatment for a variety of diseases, rehabilitation and health care (Meng and Liu, 2014). Thereafter, due to the pharmacokinetic- and pharmacodynamic-based HDIs, the concurrent use of herbal medicinal products may mimic, magnify, or oppose the effects of medicinal products (Fugh-Berman, 2000). Pharmacokinetic HDIs may increase or decrease the systemic exposures of either component through multiple mechanisms, including drug-metabolizing enzymes (*e.g.*, CYP450s and UGTs), drug transporters (*e.g.*, P-gp and BCRP) and plasma protein (*e.g.*, albumin and globulin), which is basically similar to pharmacokinetic DDIs (Li et al., 2019). Nevertheless, the research of pharmacokinetic HDIs is generally more challenging than that of DDIs, given the complicated herbal components and the batch-to-batch variation of herbal medicines (Meng and Liu, 2014). This has led to a phenomenon that most of the current studies pay more attention to the unidirectional effect (herbs→drugs) than the bidirectional effect (herbs↔drugs). Even though, the pharmacokinetic HDIs between PCE and CIP were investigated on a bidirectional effect (PCE↔CIP) in this study. GA and PCA were identified as appropriate PK-marker components of *P. capitatum* because of 1) their extensive pharmacological activities consistent with *P. capitatum* (Liao et al., 2011; Khan et al., 2015; Choubey et al., 2018; Song et al., 2020; Bai et al., 2021), 2) their rich *in vitro* (Liao et al., 2013; Zhang et al., 2013a; Zhang et al., 2013b; Li et al., 2021b) and *in vivo* exposures (Ma et al., 2015, 2016; Huang et al., 2019; Li et al., 2021b; Guan et al., 2022), and 3) their acceptable pharmacokinetic properties (Ma et al., 2015; Li et al., 2021b) and targeted distribution in kidney tissue (Ma et al., 2016). However, there is a risk that the two compounds were possibly not the most critical compounds responsible for PCE's effect, and the use of any single compound of the two compounds in the study could not reflect the overall effect of PCE.

Since CIP is a substrate of multiple transporters, the drug-transporter mediated inhibition test was performed to study the responsibilities for the reduced CIP exposure. Although herbal crude extract has been used as perpetrator in some cell experiments, false positive or false negative results will inevitably occur (Ge et al., 2010). The main reasons include but are not limited to the following aspects. PCE addition can alter some extracellular characteristics, such as pH value and ionic strength. PCE contains some components that are not absorbed into blood when administered orally, which may

interfere with cultured cells. Despite serum pharmacological method can solve the above problems, preparation of test serum for cell experiment is a complicated process: Besides chemicals or heat pretreatment, it involves the proteolytic cascades of coagulation along with complement, fibrinolysis and kinin systems, as well as leukocyte and platelet activation resulting in release reactions (Ge et al., 2010). The pretreatment deviates serum sample elements away from the original *in vivo* state. The results obtained from the drug-containing serum are at least partially uncertain in its validity. Considering GA and PCA are highly exposed in plasma and urogenital system tissues, we examined the inhibitory effects of the two components on the activity of multiple transporters that mediate CIP transport. The shortcomings of using these two compounds are the same as those of using PK-markers.

Clinical evidence showed that combination of PCE and CIP could produce a better effect for the treatment of chronic prostatitis (Zhou et al., 2016) and urinary tract infections (Pu et al., 2016). However, since co-administration of PCE significantly reduces plasma CIP in human (Figure 2), the results seemed not to support such an effect. Interestingly, we found that the combined therapy significantly increased the exposure of CIP in the prostate (Figure 6), which may be the target tissue for the treatment of chronic prostatitis (Lipsky et al., 2010). In addition to CIP, GA and PCA (PCE PK-markers) presented high exposure in the urogenital system, such as prostate, kidney, and seminal vesicle gland (Figures 7, 8). The antibacterial, anti-inflammatory, antioxidant and analgesic activities of PCE, GA and PCA are helpful to improve the efficacy of CIP in the treatment of infectious diseases of urogenital system (Liao et al., 2011; Khan et al., 2015; Choubey et al., 2018; Song et al., 2020; Bai et al., 2021). The *in vitro* study proves that PCA increased up to 50% of the antibacterial activity, especially that of levofloxacin against *Staphylococcus aureus* and *Escherichia coli* (Fifere et al., 2022).

Concurrent use of PCE significantly reduced circulating CIP in humans and rats, consistent with previous reports (Lu et al., 2016). Considering the manner in which the drug is removed from the body, CIP is primarily cleared by active tubular secretion (up to 2/3 of the total clearance, Höffken et al., 1985; Mulgaonkar et al., 2012) and intestinal excretion (approximately 18%, Rohwedder et al., 1990). Since the liver metabolism (approximately 10%) and biliary excretion (approximately 1%) of the drug is relatively low (Vance-Bryan et al., 1990), the reduced circulating CIP in humans was mainly attributed to the change of CIP across the renal and intestinal epithelia. CIP is a known substrate of the ATP-binding cassette transporters BCRP (Alvarez et al., 2008; Haslam et al., 2011) and MDR1 (Brillault et al., 2010; Arakawa et al., 2012; Zhang et al., 2019; Zimmermann et al., 2019), both of which are located in the apical (luminal) membrane of kidney proximal tubules and intestinal epithelia (International Transporter Consortium, 2010). The reduced circulating CIP in humans may be attributed to the increased BCRP/MDR1-mediated CIP efflux from blood to feces and urine, as indicated by the effects of PCE, GA and PCA on CIP bidirectional transport and BCRP/MDR1 expressions in this study. Due to the zwitterionic nature, CIP is likely to interact with organic anion and cation transporters, such as OAT1, OAT3, and OCT2 (Dautrey et al., 1999; Vanwert et al., 2008; Arakawa et al., 2012; Mulgaonkar et al., 2012; Ong et al., 2013). But the inhibitory effects of GA and PCA on OAT1/3-mediated CIP secretion from blood to feces and urine did not contribute to the reduced circulating CIP in humans. That is, the decrease of CIP systematic exposure in the combined group was caused by the integrated effect of synergy/antagonism among multiple transporters. Additionally, the reduced circulating CIP may also come from other transporter-mediated interactions (eg., OATPs, MRPs, Wu et al., 2012; Marquez et al., 2009), drug metabolizing enzyme-mediated interactions (eg., CYP450, Zheng et al., 2014), and other PCE composition-perpetrated interactions (eg., flavonoids, An et al., 2014).

Tissue distribution-based HDI studies were also implemented to assess the effects of combination therapy on the altered distribution kinetics of CIP, GA, and PCA, which may directly or indirectly lead to changes in their therapeutic effect. The combined administration increased CIP exposure in the prostate, testis, and seminal vesicle gland, which may help to treat infectious diseases of the male reproductive system. As summarized by Obligacion et al. (2006), the human prostate tissue contains the multidrug resistance protein (MRP) transporters MRP1, MRP2, MRP3, and MRP4, and MDR1. Thus, the increased distribution of CIP in the prostate gland may be attributed to the activation of MRPs and MDR1 after treated with GA and PCA. Although no significant alteration in the circulating GA and PCA after combination therapy, there were some elevated distribution kinetics and tissue exposures in the prostate and lung. Interestingly, the exposures of CIP, GA, and PCA all showed an increase in the prostate tissue after combined administration, which will contribute to the treatment of chronic prostatitis. A meta-analysis of randomized controlled trials of combination therapy indicated that PCE-based products (Relinqing®) combined with fluoroquinolones can improve the total effective rate of chronic prostatitis compared with fluoroquinolones alone (Zhou et al., 2016). The accumulation of CIP and PCE PK-marker components in prostate tissue is helpful to explain the above clinical phenomenon.

In summary, we focused on the pharmacokinetic herb-drug interactions between PCE and CIP in humans, rats and cells. The effects of PCE↔CIP presented significantly reduced plasma exposure of CIP and almost unchanged exposure of PCE PK-markers (GA and PCA) in humans and rats. The reduced plasma CIP may be attributed to integrated routes mediated by multiple transporters, including BCRP, MDR1, and OAT1/3. GA and PCA were highly exposed to urogenital tissues after intragastric administration of PCE with or without CIP to rats. Although the

decreased circulating CIP seemed not to support the clinical synergism of CIP and PCE, the combined therapy increased the exposure of CIP, GA and PCA in the prostate gland. The enrichment of these drugs in prostate will be helpful to the treatment of chronic bacterial prostatitis. Additionally, the effect of combination therapy should pay attention to both the pharmacokinetic- and pharmacodynamic-based interactions, rather than unilaterally. Further in-depth research should be carried out in the future.

Data availability statement

The original contributions presented in the study are included in the article/Supplementary Material, further inquiries can be directed to the corresponding author.

Ethics statement

The studies involving human participants were reviewed and approved by the Second Affiliated Hospital of Tianjin University of Traditional Chinese Medicine. The patients/participants provided their written informed consent to participate in this study. The animal study was reviewed and approved by the Institutional Animal Care and Use Committee of Tianjin University of Traditional Chinese Medicine.

Author contributions

Conceptualization: ZL, BW, and YH. Methodology: ZL, XZ, SF, ST, and XD. Software: ZL and XD. Validation: ZL and XD. Formal analysis: ZL and ST. Investigation: ZL, XZ, SF, ST, XD, RW, and YL. Data curation: ZL, XZ, and SF. Writing—original draft preparation: ZL and ST. Writing—review and editing: YH. Visualization: ZL and ST. Supervision: YL, RW, and BW. Project administration: YH. Funding acquisition: ZL, YH, and BW. All authors have read and agreed to the published version of the manuscript.

Funding

The study was funded by the Scientific Research Project of Tianjin Municipal Education Commission (2021ZD017 and 2021ZD030), and the National Science and Technology Major Project of China under Grant number (2018ZX09734-002), Youth Qihuang Scholars Support Project of the National Administration of Traditional Chinese Medicine.

Conflict of interest

The authors declare that the research was conducted in the absence of any commercial or financial relationships that could be construed as a potential conflict of interest.

Publisher's note

All claims expressed in this article are solely those of the authors and do not necessarily represent those of their affiliated organizations, or those of the publisher, the editors and the reviewers. Any product that may be evaluated in this article, or claim that may be made by its manufacturer, is not guaranteed or endorsed by the publisher.

Supplementary material

The Supplementary Material for this article can be found online at: https://www.frontiersin.org/articles/10.3389/fphar.2022.1033667/full#supplementary-material

References

Alvarez, A. I., Pérez, M., Prieto, J. G., Molina, A. J., Real, R., and Merino, G. (2008). Fluoroquinolone efflux mediated by ABC transporters. *J. Pharm. Sci.* 97 (9), 3483–3493. doi:10.1002/jps.21233

An, G., Wang, X., and Morris, M. E. (2014). Flavonoids are inhibitors of human organic anion transporter 1 (OAT1)-mediated transport. *Drug Metab. Dispos.* 42 (9), 1357–1366. doi:10.1124/dmd.114.059337

Ando, T., Kusuhara, H., Merino, G., Alvarez, A. I., Schinkel, A. H., and Sugiyama, Y. (2007). Involvement of breast cancer resistance protein (ABCG2) in the biliary excretion mechanism of fluoroquinolones. *Drug Metab. Dispos.* 35 (10), 1873–1879. doi:10.1124/dmd.107.014969

Arakawa, H., Shirasaka, Y., Haga, M., Nakanishi, T., and Tamai, I. (2012). Active intestinal absorption of fluoroquinolone antibacterial agent ciprofloxacin by organic anion transporting polypeptide, Oatp1a5. *Oatp1a5. Biopharm. Drug Dispos.* 33 (6), 332–341. doi:10.1002/bdd.1809

Bai, J., Zhang, Y., Tang, C., Hou, Y., Ai, X., Chen, X., et al. (2021). Gallic acid: Pharmacological activities and molecular mechanisms involved in inflammation-related diseases. *Biomed. Pharmacother.* 133, 110985. doi:10.1016/j.biopha.2020.110985

Bonkat, G., Bartoletti, R., Bruyère, F., Cai, T., Geerlings, S. E., Köves, B., et al. (2022) "EAU guidelines on urological infections,". ISBN 978-94-92671-16-5 in *EAU guidelines, edition presented at the EAU annual congress amsterdam, The Netherlands 2022*. Arnhem: EAU Guidelines Office, Available at: http://uroweb.org/guidelines/compilations-of-all-guidelines/.

Brillault, J., De Castro, W. V., and Couet, W. (2010). Relative contributions of active mediated transport and passive diffusion of fluoroquinolones with various lipophilicities in a Calu-3 lung epithelial cell model. *Antimicrob. Agents Chemother.* 54 (1), 543–545. doi:10.1128/AAC.00733-09

Chinese Pharmacopoeia Commission (2010). *Pharmacopoeia of the people's Republic of China*. Beijing, China: China Chemical Industry Press, 1454.

Choubey, S., Goyal, S., Varughese, L. R., Kumar, V., Sharma, A. K., and Beniwal, V. (2018). Probing gallic acid for its broad spectrum applications. *Mini Rev. Med. Chem.* 18 (15), 1283–1293. doi:10.2174/1389557518666180330114010

Dautrey, S., Felice, K., Petiet, A., Lacour, B., Carbon, C., and Farinotti, R. (1999). Active intestinal elimination of ciprofloxacin in rats: Modulation by different substrates. *Br. J. Pharmacol.* 127 (7), 1728–1734. doi:10.1038/sj.bjp.0702703

Fifere, A., Turin-Moleavin, I. A., and Rosca, I. (2022). Does protocatechuic acid affect the activity of commonly used antibiotics and antifungals? *Life (Basel)* 12 (7), 1010. doi:10.3390/life12071010

Fugh-Berman, A. (2000). Herb-drug interactions. *Lancet* 355 (9198), 134–138. doi:10.1016/S0140-6736(99)06457-0

GBD Diseases and Injuries (2020). Global burden of 369 diseases and injuries in 204 countries and territories, 1990-2019: A systematic analysis for the global burden of disease study 2019. *Lancet* 396 (10258), 1204–1222. doi:10.1016/S0140-6736(20)30925-9

Ge, J., Wang, D., He, R., Zhu, H., Wang, Y., and He, S. (2010). Medicinal herb research: Serum pharmacological method and plasma pharmacological method. *Biol. Pharm. Bull.* 33 (9), 1459–1465. doi:10.1248/bpb.33.1459

International Transporter ConsortiumGiacomini, K. M., Huang, S. M., Tweedie, D. J., Benet, L. Z., Brouwer, K. L. R., Chu, X., et al. (2010). Membrane transporters in drug development. *Nat. Rev. Drug Discov.* 9 (3), 215–236. doi:10.1038/nrd3028

Guan, H., Li, P., Wang, Q., Zeng, F., Wang, D., Zhou, M., et al. (2022). Systematically exploring the chemical ingredients and absorbed constituents of *Polygonum capitatum* in hyperuricemia rat plasma using UHPLC-Q-Orbitrap HRMS. *Molecules* 27 (11), 3521. doi:10.3390/molecules27113521

Haslam, I. S., Wright, J. A., O'Reilly, D. A., Sherlock, D. J., Coleman, T., and Simmons, N. L. (2011). Intestinal ciprofloxacin efflux: The role of breast cancer resistance protein (ABCG2). *Drug Metab. Dispos.* 39 (12), 2321–2328. doi:10.1124/dmd.111.038323

Höffken, G., Lode, H., Prinzing, C., Borner, K., and Koeppe, P. (1985). Pharmacokinetics of ciprofloxacin after oral and parenteral administration. *Antimicrob. Agents Chemother.* 27 (3), 375–379. doi:10.1128/AAC.27.3.375

Huang, K., Zhang, P., Zhang, Z., Youn, J. Y., Wang, C., Zhang, H., et al. (2021). Traditional Chinese Medicine (TCM) in the treatment of COVID-19 and other viral infections: Efficacies and mechanisms. *Pharmacol. Ther.* 225, 107843. doi:10.1016/j.pharmthera.2021.107843

Huang, Y., Zhou, Z., Yang, W., Gong, Z., Li, Y., Chen, S., et al. (2019). Comparative pharmacokinetics of gallic acid, protocatechuic acid, and quercitrin in normal and pyelonephritis rats after oral administration of a *Polygonum capitatum* extract. *Molecules* 24 (21), 3873. doi:10.3390/molecules24213873

Khan, A. K., Rashid, R., Fatima, N., Mahmood, S., Mir, S., Khan, S., et al. (2015). Pharmacological activities of protocatechuic acid. *Acta Pol. Pharm.* 72 (4), 643–650.

Li, Y., Meng, Q., Yang, M., Liu, D., Hou, X., Tang, L., et al. (2019). Current trends in drug metabolism and pharmacokinetics. *Acta Pharm. Sin. B* 9 (6), 1113–1144. doi:10.1016/j.apsb.2019.10.001

Li, Z., Du, X., Li, Y., Wang, R., Liu, C., Cao, Y., et al. (2021b). Pharmacokinetics of gallic acid and protocatechuic acid in humans after dosing with Relinqing (RLQ) and the potential for RLQ-perpetrated drug-drug interactions on organic anion transporter (OAT)1/3. *Pharm. Biol.* 59 (1), 757–768. doi:10.1080/13880209.2021.1934039

Li, Z., Tian, S., Wu, Z., Xu, X., Lei, L., Li, Y., et al. (2021a). Pharmacokinetic herb-disease-drug interactions: Effect of ginkgo biloba extract on the pharmacokinetics of pitavastatin, a substrate of Oatp1b2, in rats with non-alcoholic fatty liver disease. *J. Ethnopharmacol.* 280, 114469. doi:10.1016/j.jep.2021.114469

Liao, S. G., Zhang, L. J., Sun, F., Wang, Z., He, X., Wang, A. M., et al. (2013). Identification and characterisation of phenolics in Polygonum capitatum by ultrahigh-performance liquid chromatography with photodiode array detection and tandem mass spectrometry. *Phytochem. Anal.* 24 (6), 556–568. doi:10.1002/pca.2432

Liao, S. G., Zhang, L. J., Sun, F., Zhang, J. J., Chen, A. Y., Lan, Y. Y., et al. (2011). Antibacterial and anti-inflammatory effects of extracts and fractions from Polygonum capitatum. *J. Ethnopharmacol.* 134 (3), 1006–1009. doi:10.1016/j.jep.2011.01.050

Lipsky, B. A., Byren, I., and Hoey, C. T. (2010). Treatment of bacterial prostatitis. *Clin. Infect. Dis.* 50 (12), 1641–1652. doi:10.1086/652861

Lu, Y., Gong, Z., Xie, Y., Pan, J., Sun, J., Li, Y., et al. (2016). Herb-drug interaction: Effects of Relinqing® granule on the pharmacokinetics of ciprofloxacin, sulfamethoxazole, and trimethoprim in rats. *Evid. Based. Complement. Altern. Med.* 2016, 6194206. doi:10.1155/2016/6194206

Ma, F., Deng, Q., Zhou, X., Gong, X., Zhao, Y., Chen, H., et al. (2016). The tissue distribution and urinary excretion study of gallic acid and protocatechuic acid after oral administration of polygonum capitatum extract in rats. *Molecules* 21 (4), 399–414. doi:10.3390/molecules21040399

Ma, F., Gong, X., Zhou, X., Zhao, Y., and Li, M. (2015). An UHPLC-MS/MS method for simultaneous quantification of gallic acid and protocatechuic acid in rat plasma after oral administration of Polygonum capitatum extract and its application to pharmacokinetics. *J. Ethnopharmacol.* 162, 377–383. doi:10.1016/j.jep.2014.12.044

Marquez, B., Caceres, N. E., Mingeot-Leclercq, M. P., Tulkens, P. M., and Van Bambeke, F. (2009). Identification of the efflux transporter of the fluoroquinolone antibiotic ciprofloxacin in murine macrophages: Studies with ciprofloxacin-resistant cells. *Antimicrob. Agents Chemother.* 53 (6), 2410–2416. doi:10.1128/AAC.01428-08

Meng, Q., and Liu, K. (2014). Pharmacokinetic interactions between herbal medicines and prescribed drugs: Focus on drug metabolic enzymes and transporters. *Curr. Drug Metab.* 15 (8), 791–807. doi:10.2174/1389200216666150223152348

Merino, G., Alvarez, A. I., Pulido, M. M., Molina, A. J., Schinkel, A. H., and Prieto, J. G. (2006). Breast cancer resistance protein (BCRP/ABCG2) transports fluoroquinolone antibiotics and affects their oral availability, pharmacokinetics, and milk secretion. *Drug Metab. Dispos.* 34 (4), 690–695. doi:10.1124/dmd.105.008219

Mulgaonkar, A., Venitz, J., and Sweet, D. H. (2012). Fluoroquinolone disposition: Identification of the contribution of renal secretory and reabsorptive drug transporters. *Expert Opin. Drug Metab. Toxicol.* 8 (5), 553–569. doi:10.1517/17425255.2012.674512

Obligacion, R., Murray, M., and Ramzan, I. (2006). Drug-metabolizing enzymes and transporters: Expression in the human prostate and roles in prostate drug disposition. *J. Androl.* 27 (2), 138–150. doi:10.2164/jandrol.05113

Ong, H. X., Traini, D., Bebawy, M., and Young, P. M. (2013). Ciprofloxacin is actively transported across bronchial lung epithelial cells using a Calu-3 air interface cell model. *Antimicrob. Agents Chemother.* 57 (6), 2535–2540. doi:10.1128/AAC.00306-13

Pu, X., Zhang, L., Yang, F., Xiang, D., and Zhang, J. (2016). Treatment of uncomplicated urinary tract infection by relinqing: A systematic review of randomized controlled trials of clinical studies. *Tianjin Med. J.* 44 (8), 1048–1052. doi:10.11958/20150252

Rohwedder, R., Bergan, T., Thorsteinsson, S. B., and Scholl, H. (1990). Transintestinal elimination of ciprofloxacin. *Chemotherapy* 36 (2), 77–84. doi:10.1159/000238751

Song, J., He, Y., Luo, C., Feng, B., Ran, F., Xu, H., et al. (2020). New progress in the pharmacology of protocatechuic acid: A compound ingested in daily foods and herbs frequently and heavily. *Pharmacol. Res.* 161, 105109. doi:10.1016/j.phrs.2020.105109

US FDA. *In Vitro*drug interaction studies—cytochrome P450 enzyme- and transporter-mediated drug interactions guidance for industry. 2020. 1.23. Available at: https://www.fda.gov/media/134582/download.

Van Giersbergen, P. L., Gnerre, C., Treiber, A., Dingemanse, J., and Meyer, U. A. (2002). Bosentan, a dual endothelin receptor antagonist, activates the pregnane X nuclear receptor. *Eur. J. Pharmacol.* 450 (2), 115–121. doi:10.1016/s0014-2999(02)02075-7

Vance-Bryan, K., Guay, D. R., and Rotschafer, J. C. (1990). Clinical pharmacokinetics of ciprofloxacin. *Clin. Pharmacokinet.* 19 (6), 434–461. doi:10.2165/00003088-199019060-00003

Vanwert, A. L., Srimaroeng, C., and Sweet, D. H. (2008). Organic anion transporter 3 (*Oat3/Slc22a8*) interacts with carboxyfluoroquinolones, and deletion increases systemic exposure to ciprofloxacin. *Mol. Pharmacol.* 74 (1), 122–131. doi:10.1124/mol.107.042853

WHO (2022), Traditional, complementary and integrative medicine. WHO Expert meeting on evaluation of traditional Chinese medicine in the treatment of COVID-19. Available at: http://www.wfcms.org/public/filespath/files/bd5a7ec0b29152ef509d04d97fdcda4f.pdf. [Accessed on August 10, 2022].

Wu, L. X., Guo, C. X., Chen, W. Q., Yu, J., Qu, Q., Chen, Y., et al. (2012). Inhibition of the organic anion-transporting polypeptide 1B1 by quercetin: An *in vitro* and *in vivo* assessment. *Br. J. Clin. Pharmacol.* 73 (5), 750–757. doi:10.1111/j.1365-2125.2011.04150.x

Zhang, K. X., Wang, Y. S., Jing, W. G., Zhang, J., and Liu, A. (2013a). Improved quality control method for prescriptions of *Polygonum capitatum* through simultaneous determination of nine major constituents by HPLC coupled with triple quadruple mass spectrometry. *Molecules* 18 (10), 11824–11835. doi:10.3390/molecules181011824

Zhang, K., Zhang, J., Wei, S., Jing, W., Wang, Y., and Liu, A. (2013b). Development and validation of HPLC coupled with triple quadrupole MS for the simultaneous determination of six phenolic acids, six flavonoids, and a lignan in Polygonum capitatum. *J. Sep. Sci.* 36 (15), 2407–2413. doi:10.1002/jssc.201300291

Zhang, Y., Guo, L., Huang, J., Sun, Y., He, F., Zloh, M., et al. (2019). Inhibitory effect of berberine on broiler P-glycoprotein expression and function: *In situ* and *in vitro* studies. *Int. J. Mol. Sci.* 20 (8), 1966. doi:10.3390/ijms20081966

Zheng, L., Lu, Y., Cao, X., Huang, Y., Liu, Y., Tang, L., et al. (2014). Evaluation of the impact of Polygonum capitatum, a traditional Chinese herbal medicine, on rat hepatic cytochrome P450 enzymes by using a cocktail of probe drugs. *J. Ethnopharmacol.* 158, 276–282. doi:10.1016/j.jep.2014.10.031

Zhou, X., Yang, J., Yang, G., Gong, J., and Xia, W. (2016). Meta Analysis of combined Relinqing randomized clinical trials in treating prostatitis. *J. Shanxi Univer. Chin. Med.* 17 (3), 1–4. doi:10.3969/j.issn.1000-7369.2016.03.001

Zimmermann, E. S., de Miranda Silva, C., Neris, C., Torres, B., Schmidt, S., and Dalla Costa, T. (2019). Population pharmacokinetic modeling to establish the role of P-glycoprotein on ciprofloxacin distribution to lung and prostate following intravenous and intratracheal administration to Wistar rats. *Eur. J. Pharm. Sci.* 27, 319–329. doi:10.1016/j.ejps.2018.11.007

frontiers | Frontiers in Pharmacology

TYPE Original Research
PUBLISHED 02 December 2022
DOI 10.3389/fphar.2022.1069704

OPEN ACCESS

EDITED BY
Simona Pichini,
National Institute of Health (ISS), Italy

REVIEWED BY
Xuehan Li,
Liaocheng People's Hospital, China
Wangliang Zhu,
The First Affiliated Hospital of Xi'an Jiaotong University, China

*CORRESPONDENCE
Jinxia Yuan,
yuanjinxia89@126.com
Guoliang Yuan,
yuanguoliang0815@126.com

†These authors have contributed equally to this work

SPECIALTY SECTION
This article was submitted to Drug Metabolism and Transport, a section of the journal Frontiers in Pharmacology

RECEIVED 14 October 2022
ACCEPTED 14 November 2022
PUBLISHED 02 December 2022

CITATION
Yuan J, Yan F, Li W and Yuan G (2022), Network pharmacological analysis of Xuefu Zhuyu decoction in the treatment of atherosclerosis.
Front. Pharmacol. 13:1069704.
doi: 10.3389/fphar.2022.1069704

Network pharmacological analysis of Xuefu Zhuyu decoction in the treatment of atherosclerosis

Jinxia Yuan[1*†], Fei Yan[2†], Wei Li[1†] and Guoliang Yuan[1*]

[1]Department of Cardiology, Shuyang Hospital of Traditional Chinese Medicine, Yangzhou University, Shuyang, Jiangsu, China, [2]School of Medicine, Yangzhou University, Yangzhou, Jiangsu, China

Objective: Using a network pharmacological approach, this study will evaluate the effect of Xuefu Zhuyu Decoction in the treatment of atherosclerosis.

Methods: The data were imported into the STRING database to construct a protein-protein interaction network, and the network topology was analysed with the Bisogenet plug-in by Cytoscape 3.7.2. Using the R language Bioconductor platform, Gene Ontology (GO) enrichment analysis and Kyoto Encyclopedia of Genes and Genomes (KEGG) enrichment analysis for potential targets of Xuefu Zhuyu Decoction in the treatment of atherosclerosis were performed, and import the results were imported into Cytoscape 3.7.2. To map the results and create a KEGG network diagram, we used Cytoscape 3.7.2 for analysis.

Results: A total of 91 chemical components and 1320 disease targets were obtained, including 138 cross-targets. TNF, AKT1 and ALB were identified as important targets, and Gene Ontology functional analysis indicated that biological process was the primary cause of oxidative stress. The primary action of molecular function is binding. KEGG has explored and enriched 149 signalling pathways, including the AGE-RAGE signalling system and the TNF signalling network. According to a study involving molecular docking, quercetin and β-carotene have a strong binding affinity for AKT1 and ALB.

Conclusion: The potential of Xuefu Zhuyu Decoction to treat atherosclerosis through multiple components and targets provides a way to further study its mechanism.

KEYWORDS

network pharmacology, molecular docking, xuefu zhuyu decoction, mechanism, atherosclerosis

Introduction

Atherosclerosis (AS) is characterized by the accumulation of fat and fibrous particles, as well as calcification, in the principal arteries (Wang and Bennett, 2012). The creation of atherosclerotic plaques is initiated by the activation of endothelial cells, which leads to the constriction of blood vessels and the activation of inflammatory pathways, resulting in the formation of atherosclerotic plaques (Wu et al., 2017; Jebari-Benslaiman et al., 2022). These processes lead to cardiovascular difficulties and remain the leading cause of death globally. Endothelial dysfunction, the creation of fatty streaks, the formation of fibrous plaques, and the rupture of plaques are all under investigation as potential causes of AS. Clinical medical research has demonstrated that traditional Chinese medicine has preventative and therapeutic effects on AS, and the physiopathological and clinical characteristics of AS distinguish it from several other conditions (Saigusa et al., 2020; Biros et al., 2022). Traditional Chinese medicine is increasingly used in the clinical adjuvant treatment of atherosclerosis. Although their mechanism of action is still unclear, it has been confirmed that Chinese herbal medicine can play a variety of anti-atherosclerotic roles by regulating ROS in cells (Zhang et al., 2022). Also, when atherosclerosis is caused by diabetes, traditional Chinese medicine works well to control the NLRP3 inflammatory response (Yuan et al., 2022).

Using network pharmacology to investigate the mechanisms of TCM-disease interactions has proven useful. Through advanced target-disease interaction networks and bioinformatics research, network pharmacology, which is coherent with TCM as a whole, can identify potential mechanisms of prescription effects in disease therapy. This is because TCM components are intricate and multipurpose. Due to its virtual screening properties, however, it must be confirmed in cellular and/or animal experiments (Hao and Xiao, 2014; Pangkanon et al., 2021).

Materials and methods

Screening of target components of Xuefu Zhuyu decoction

Identification of active chemical constituents of Chinese herbal medicines using TCM systems pharmacology platforms TCMSP and TCMID (Tao Ren, Hong Hua, Angelica sinensis, Sheng Di Huang, Niu Keng each, Chuan Xiong, Radix Platycodon, Citrus aurantium, *Glycyrrhiza* each, and Chai Hu). The active components of Xuefu Zhuyu Decoction were identified by screening in TCMSP, with an oral bioavailability (OB) of 30% and drug-likeness (DL) of 0.18. The likely protein targets were extracted from the Swiss target prediction database with conditional probability better than 0.1, and the screened protein targets were assigned standardized gene names in the UniProt database.

Screening for key atherosclerotic disease-related targets

By searching the Gene-Cards and OMIM databases using the term "atherosclerosis", atherosclerosis target genes were identified. Based on the score value, the number of targets was limited. Targets with scores greater than the median are often classified as potential targets for disease, and genes with scores greater than 5 in GeneCards were integrated with the OMIM database and deweighted as atherosclerosis-related targets. The stronger the correlation between goals and illness, the higher the score.

Target acquisition and venn diagramming

Using a Venn diagram, determining the intersection of the targets of Xuefu Zhuyu Decoction and the target points for atherosclerosis is the effective target point for Xuefu Zhuyu Decoction in the treatment of atherosclerosis.

Analysing the active ingredient-target network

The active ingredients and effective target genes were imported into Cytoscape 3.7.2 software for network construction, visualization, and a drug-active ingredient-target network diagram was obtained.

Construction of the protein network

The possible targets of the antiatherosclerotic effect of Xuefu Zhuyu decoction were entered into the GeneMANIA database (http://genemania.org), and their interactions were discovered. The indirect objectives were then acquired. The indirect targets have been added to the database of acting targets, which has been imported into the STRING database. To obtain the desired interaction network, *Homo sapiens*, who received a default score of 0.4, was utilized. Cytoscape 3. 7.2 was used to analyze the network topology once the TSV format was imported and saved. After calculating the degree, betweenness centrality (BC), topological coefficient (TC), and closeness centrality (CC) of each node, the top 3 targets were selected as key target proteins.

Analysis of target function enrichment and route expansion

Using R software (https://www.r-project.org) and its backend database org, gene IDs (entrezIDs) of possible targets were determined. The Hs.e.g.db database was utilized to perform GO functional enrichment analysis on these possible targets, followed by the Bioconductor tools DOSE, cluster Profiler, and path-view. The GO function enrichment analysis of these potential targets included three components: DOSE, cluster Profiler, and the path-view instrument (all from Bioconductor). We set *p* value Cutoff = 0.05 and q value Cutoff = 0.05 as appropriate for biological process (BP), cellular component (CC), and molecular function (MF). GO enrichment analysis revealed three fundamental categories: BP, MF and CC. The top ten items for enrichment are displayed as bar and bubble charts, with each category sorted in order of significance.

Molecular docking of Xuefu Zhuyu decoction's main active ingredient target

The targets of Xuefu Zhuyu Decoction acting on atherosclerosis were retrieved from the PDB database and saved in pdb format. After topological analysis, the compounds with the top 2 ligands in degree value were saved in mol2 format. The potential targets of Xuefu Zhuyu Decoction in atherosclerosis were molecularly docked with the main compounds of Xuefu Zhuyu Decoction using AutoDockTools-1.5.6.

Results

Obtaining the active components and objectives of Xuefu Zhuyu decoction

Xuefu Zhuyu Decoction includes 91 active constituents, as determined by screening criteria of OB 30% and DL 0.18, high GI absorption for pharmacokinetics, and over two "YESs" in druglikeness in TCMSP and TCMID. A total of 240 targets of Chinese medicine were retrieved by TCMSP and TCMID.

Atherosclerosis-related target acquisition

Following the discovery of disease genes using GeneCards and Omim, 1320 atherosclerosis-related targets were identified, and targets with scores above the median were empirically classified as potential disease targets. Then, these targets were added to relevant targets found through searches of the OMIM database, and duplicate values were eliminated.

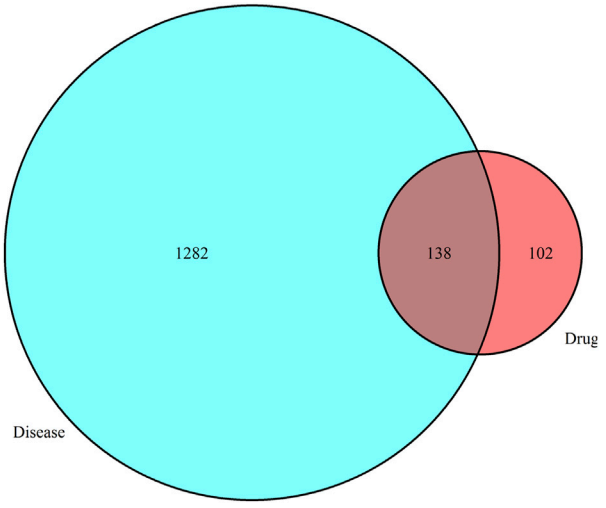

FIGURE 1
Venn diagram illustrating the overlap between Xuefu Zhuyu Decoction and atherosclerosis targets.

Venn diagrams

Using the Venn tool in TBtools, Figure 1 displays the intersection of the Xuefu Zhuyu Decoction and atherosclerosis targets.

Network diagram of active targets for Xuefu Zhuyu decoction

Cytoscape 3.7.2 Active ingredients and an efficient target network of Xuefu Zhuyu Decoction. Software was used to calculate the topological parameters of the Xuefu Zhuyu Decoction network for the treatment of atherosclerosis to analyze the importance of activity components and action goals. Based on the findings, quercetin, β-carotene, and kaempferol may be the primary active components in Xuefu Zhuyu Decoction that help treat atherosclerosis by acting on multiple targets Figure 2.

Construction of the protein network

We uploaded the intersection targets of Xuefu Zhuyu Decoction and atherosclerosis to the STRING database using the Venn tool, with the confidence level set to 0.90, and then built the PPI network map of targets. Cytoscape 3.7.2 was utilized to create the protein network relationship map. To decide network placement, the degree value size is used. The degree value is proportional to the size of the node. Haematopoeia deemed AKT1, ALB, IL6, TNF, TP53, and

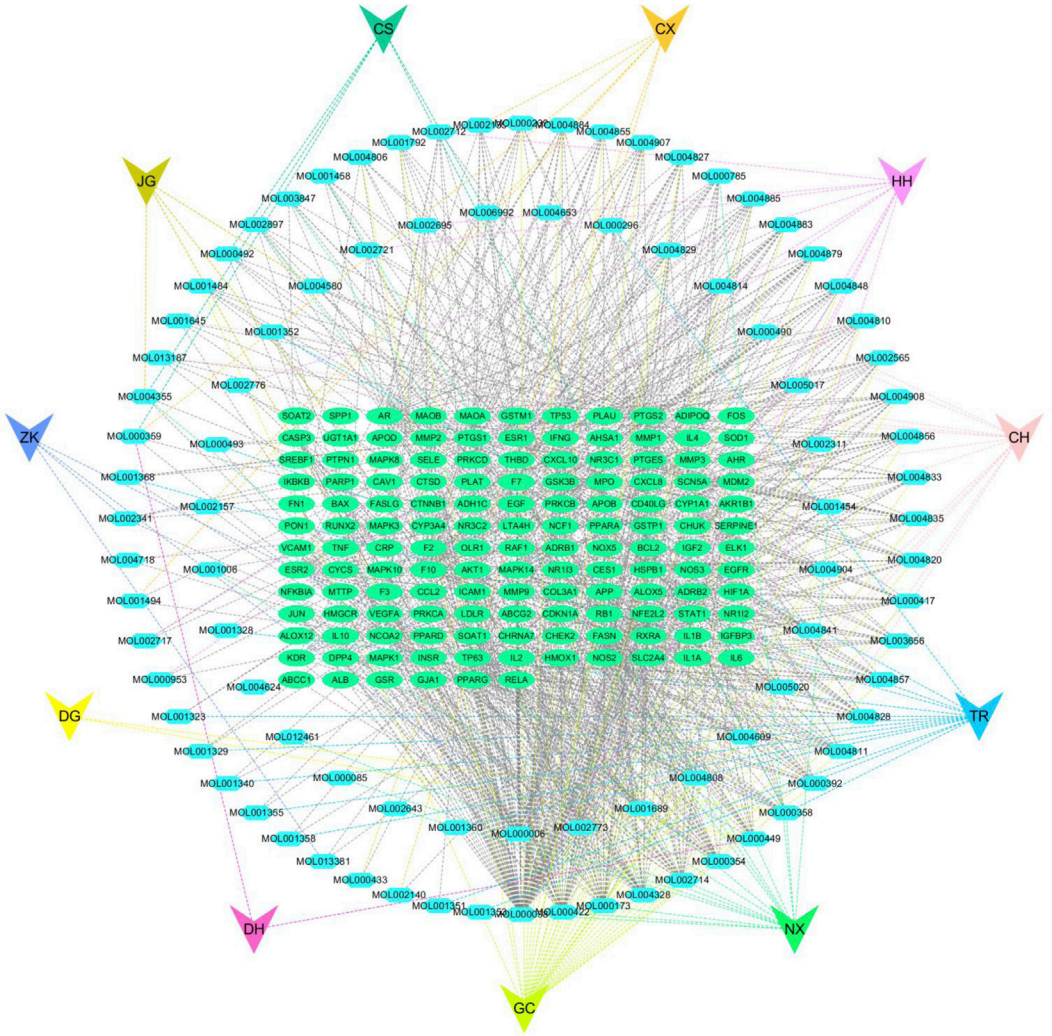

FIGURE 2
Active ingredient-active target network diagram of Xuefu Zhuyu Decoction.

other targets important targets for the treatment of atherosclerosis (Figure 3).

Results of an investigation of target pathway and function enrichment

GO annotation analysis of valid targets using R. The top ten results in BP, CC, and MF were selected, and oxidative stress was determined to be the major function of these target BPs. The primary functions of MF included binding activities. CC was predominantly active within the vesicle lumen, membrane raft, and microfilm areas. Figure 4A illustrates the results.

The top 20 KEGG-enriched signaling pathways visualized for analysis included the AGE-RAGE signaling route, the TNF signaling pathway, the IL-17 pathway, and others. Figure 4B demonstrates the outcomes.

Molecular docking results of the active ingredients of Xuefu Zhuyu decoction

The key components of Xuefu Zhuyu Decoction identified by topological analysis were molecularly docked with the probable targets of Xuefu Zhuyu Decoction in atherosclerosis using AutoDockTools-1.5.6. The likelihood of action increased as the ligand–receptor binding configuration became more stable, and the degree value was used to identify the most crucially important targets. A binding energy of -4.25 kcal/mol or less indicates some binding

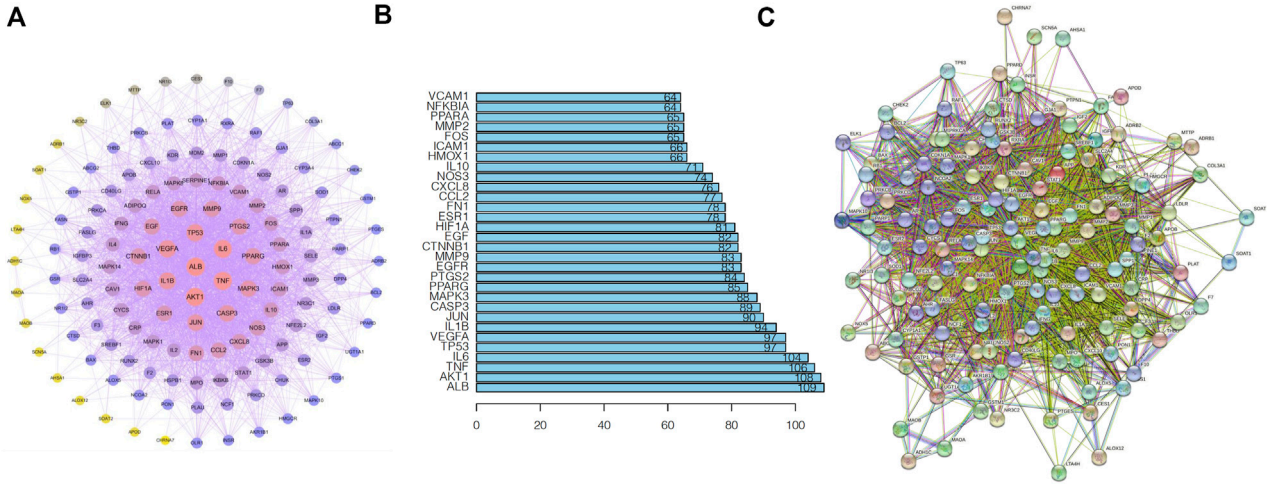

FIGURE 3
A schematic of the intersection target PPI network is shown. **(A)** PPI network map; **(B)** Core Gene Map; and **(C)** PPI Network Map.

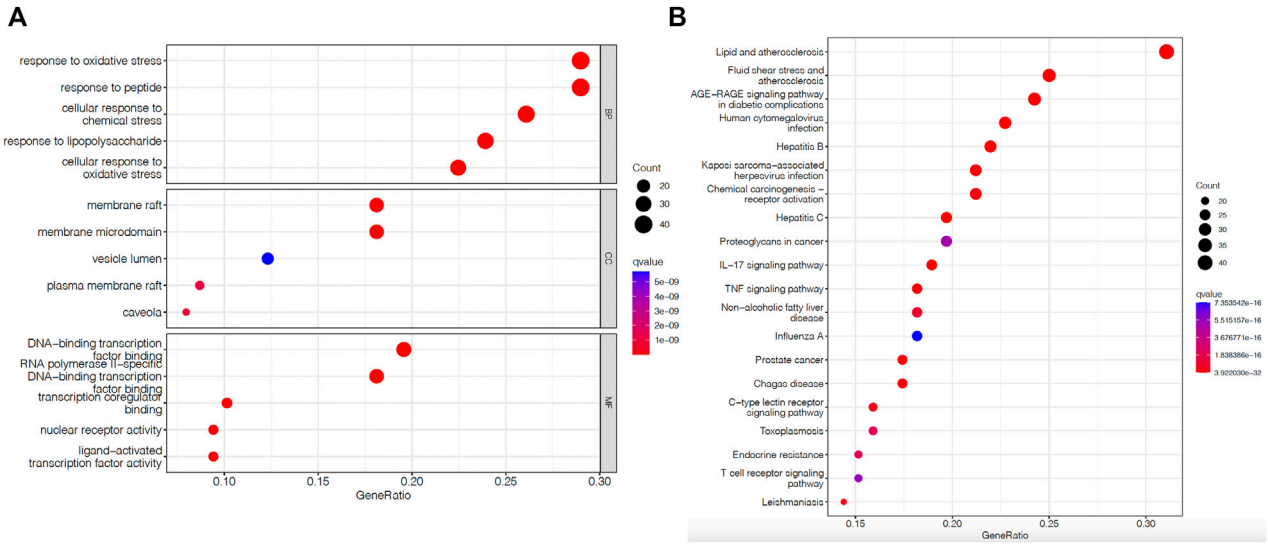

FIGURE 4
Enrichment analysis of Xuefu Zhuyu decoction in the treatment of atherosclerosis. **(A)** GO enrichment analysis; **(B)** KEGG enrichment analysis circle diagram.

activities between ligand small molecules and receptor proteins, 5.0 kcal/mol or greater indicates good binding activity between the two, and -7.0 kcal/mol or greater indicates robust conjugation activity between ligand and receptor. According to the docking results in Figure 5, the binding energies of quercetin and β-carotene with the AKT1 and ALB core targets were -9.9 and -10 kcal/mol, respectively, showing strong binding activity between the drug and target sections.

Discussion

Recent clinical research indicates that Chinese herbal medicine has special benefits for the development of anti-AS drugs and for enhancing the quality of patient survival. Several studies have already demonstrated the anti-inflammatory and antioxidant properties of herbal therapy in the aetiology of AS-7. Despite the fact that long-term use of statins can cause undesired side effects such as drug dependence and liver damage, oral

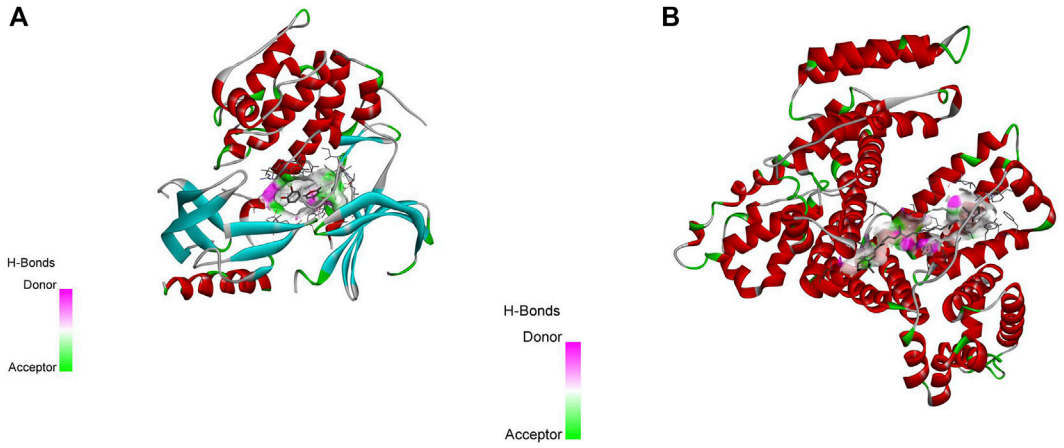

FIGURE 5
Diagram of Molecular docking model. **(A)** The docking diagram of quercetin and AKT1. **(B)** The docking diagram of β-carotene and ALB.

statins are commonly used in the prevention and treatment of atherosclerosis (Gotto, 2003). Xuefu Zhuyu Decoction can circulate Qi and alleviate pain, stimulate blood circulation and remove blood clots, and induce blood to self-settle by removing blood clots. However, due to the molecular complexity of medicine, it is challenging to develop a therapeutic mechanism utilising basic research approaches (Cao, 2022).

This study screened 91 active compounds using a combination of bioinformatics and network pharmacology, providing 240 active ingredient action targets. In addition, 1320 disease gene targets were intersected to produce a total of 138 common targets, among which active components such as quercetin, -carotene, and kaempferol were revealed. This study provides a molecular mechanism for the use of Xuefu Zhuyu Decoction in the treatment of atherosclerosis. The findings of this study provide a more detailed explanation of how Xuefu Zhuyu Decoction's can treat atherosclerosis at the molecular level and can be applied to make medicines to flight atherosclerotic-related illnesses.

A topological analysis of the ingredient-target-pathway network revealed that quercetin and β-carotene are key active ingredients in the treatment of atherosclerosis and correlate with more targets. It has been reported that quercetin, which blocked the Galectin-3-NLRP3 signaling pathway, reduced the inflammatory response caused by atherosclerosis (Li et al., 2021). Moreover, the transformation of beta-carotene into vitamin A slows down the evolution of atherosclerosis in mice by lowering the amount of hepatic lipid production (Zhou et al., 2020). According to the PPI network, ALB and AKT1 are the primary targets for Xuefu Zhuyu Decoction therapy to cure atherosclerosis.

AKT1 can participate in numerous signaling pathways, such as the cell cycle, inflammatory response, PI3K/Akt, MAPK, and AGE-RAGE signaling (Fernandez-Hernando et al., 2007; Hashimoto et al., 2017; Chen et al., 2019). Numerous studies have demonstrated that the NF-B pathway can regulate TNF and other inflammatory cytokines, enhancing endothelial function and reducing foam cell production and rupture, vascular smooth muscle cell proliferation, and atherosclerotic plaque growth (Ridker et al., 2017; Yang et al., 2019; Pangkanon et al., 2021). Interferon, a key immune function regulator, is highly expressed in atherosclerotic lesions, and mouse studies indicate that T and B-cell deficiency reduces the atherosclerotic burden during the development of atherosclerotic lesions and that regulation of the IL-17 signaling pathway may play a role in the pathogenesis of several inflammatory and autoimmune diseases, including atherosclerosis (Chen et al., 2010; Fan et al., 2016; Lu, 2017).

According to the results of the GO analysis, the therapy of the atherosclerotic pathway by Xuefu Zhuyu Decoction predominantly includes lipid metabolism and binding. Xuefu Zhuyu Decoction may aid in the treatment of AS by regulating the AGE-RAGE signaling cascade, TNF, and MAPK, according to a KEGG analysis.

A network pharmacology approach was utilized to evaluate the therapeutic targets and mechanisms of action of core Chinese herbal medicines on common-type atherosclerosis. Xuefu Zhuyu Decoction has anti-inflammatory and antioxidant properties *via* quercetin, β-carotene, kaempferol, and other flavonoid active component monomers. Consequently, it provides evidence to support its pharmacological impact. However, Network pharmacology is based on databases and analytical software, this study was analyzed through two databases, so the analysis results have limitations. The additional experimental validation is necessary to substantiate this assertion. In addition, the concentration used is not recorded in the database, but for the drug to work, it needs to be used at a certain concentration.

Data availability statement

The datasets presented in this study can be found in online repositories. The names of the repository/repositories and accession number(s) can be found in the article/Supplementary Material.

Author contributions

JY and GY designed the study and performed the experiments, FY collected the data, WL analyzed the data, JY and GY prepared the manuscript. All authors read and approved the final manuscript.

Conflict of interest

The authors declare that the research was conducted in the absence of any commercial or financial relationships that could be construed as a potential conflict of interest.

Publisher's note

All claims expressed in this article are solely those of the authors and do not necessarily represent those of their affiliated organizations, or those of the publisher, the editors and the reviewers. Any product that may be evaluated in this article, or claim that may be made by its manufacturer, is not guaranteed or endorsed by the publisher.

References

Biros, E., Reznik, J. E., and Moran, C. S. (2022). Role of inflammatory cytokines in Genesis and treatment of atherosclerosis. *Trends cardiovasc. Med.* 32 (3), 138–142. doi:10.1016/j.tcm.2021.02.001

Cao, R. (2022). Clinical observation on the prevention of deep vein thrombosis after total hip arthroplasty with the application of hemifu huang yu tang. *J. Pract. Chin. Med.*, 1281–1283.

Chen, L., Zheng, S. Y., Yang, C. Q., Ma, B. M., and Jiang, D. (2019). MiR-155-5p inhibits the proliferation and migration of VSMCs and HUVECs in atherosclerosis by targeting AKT1. *Eur. Rev. Med. Pharmacol. Sci.* 23 (5), 2223–2233. doi:10.26355/eurrev_201903_17270

Chen, S., Crother, T. R., and Arditi, M. (2010). Emerging role of IL-17 in atherosclerosis. *J. Innate Immun.* 2 (4), 325–333. doi:10.1159/000314626

Fan, Z., Yang, J., Yang, C., Yang, J., and Guo, X. (2016). IL-17: A promising therapeutic target for atherosclerosis. *Int. J. Cardiol.* 202, 930–931. doi:10.1016/j.ijcard.2015.08.195

Fernandez-Hernando, C., Ackah, E., Yu, J., Suarez, Y., Murata, T., Iwakiri, Y., et al. (2007). Loss of Akt1 leads to severe atherosclerosis and occlusive coronary artery disease. *Cell. Metab.* 6 (6), 446–457. doi:10.1016/j.cmet.2007.10.007

Gotto, A. M. (2003). Antioxidants, statins, and atherosclerosis. *J. Am. Coll. Cardiol.* 41 (7), 1205–1210. doi:10.1016/s0735-1097(03)00082-2

Hao, D. C., and Xiao, P. G. (2014). Network pharmacology: A rosetta stone for traditional Chinese medicine. *Drug Dev. Res.* 75 (5), 299–312. doi:10.1002/ddr.21214

Hashimoto, R., Kakigi, R., Nakamura, K., Itoh, S., Daida, H., Okada, T., et al. (2017). LPS enhances expression of CD204 through the MAPK/ERK pathway in murine bone marrow macrophages. *Atherosclerosis* 266, 167–175. doi:10.1016/j.atherosclerosis.2017.10.005

Jebari-Benslaiman, S., Galicia-Garcia, U., Larrea-Sebal, A., Olaetxea, J. R., Alloza, I., Vandenbroeck, K., et al. (2022). Pathophysiology of atherosclerosis. *Int. J. Mol. Sci.* 23 (6), 3346. doi:10.3390/ijms23063346

Li, H., Xiao, L., He, H., Zeng, H., Liu, J., Jiang, C., et al. (2021). Quercetin attenuates atherosclerotic inflammation by inhibiting galectin-3-NLRP3 signaling pathway. *Mol. Nutr. Food Res.* 65 (15), e2000746. doi:10.1002/mnfr.202000746

Lu, X. (2017). The impact of IL-17 in atherosclerosis. *Curr. Med. Chem.* 24 (21), 2345–2358. doi:10.2174/0929867324666170419150614

Pangkanon, W., Yenbutra, P., Kamanamool, N., Tannirandorn, A., and Udompataikul, M. (2021). A comparison of the efficacy of silicone gel containing onion extract and aloe vera to silicone gel sheets to prevent postoperative hypertrophic scars and keloids. *J. Cosmet. Dermatol.* 20 (4), 1146–1153. doi:10.1111/jocd.13933

Ridker, P. M., Everett, B. M., Thuren, T., MacFadyen, J. G., Chang, W. H., Ballantyne, C., et al. (2017). Antiinflammatory therapy with canakinumab for atherosclerotic disease. *N. Engl. J. Med.* 377 (12), 1119–1131. doi:10.1056/NEJMoa1707914

Saigusa, R., Winkels, H., and Ley, K. (2020). T cell subsets and functions in atherosclerosis. *Nat. Rev. Cardiol.* 17 (7), 387–401. doi:10.1038/s41569-020-0352-5

Wang, J. C., and Bennett, M. (2012). Aging and atherosclerosis: Mechanisms, functional consequences, and potential therapeutics for cellular senescence. *Circ. Res.* 111 (2), 245–259. doi:10.1161/CIRCRESAHA.111.261388

Wu, M. Y., Li, C. J., Hou, M. F., and Chu, P. Y. (2017). New insights into the role of inflammation in the pathogenesis of atherosclerosis. *Int. J. Mol. Sci.* 18 (10), E2034. doi:10.3390/ijms18102034

Yang, S., Li, J., Chen, Y., Zhang, S., Feng, C., Hou, Z., et al. (2019). MicroRNA-216a promotes M1 macrophages polarization and atherosclerosis progression by activating telomerase via the Smad3/NF-κB pathway. *Biochim. Biophys. Acta. Mol. Basis Dis.* 1865 (7), 1772–1781. doi:10.1016/j.bbadis.2018.06.016

Yuan, J. Y., Fu, Y., Feng, Z. H., Sang, F., Shao, M. Y., and Li, L. L. (2022). Potential mechanisms and effects of Chinese medicines in treatment of diabetic atherosclerosis by modulating NLRP3 inflammasome: A narrative review. *Chin. J. Integr. Med.* 28 (8), 753–761. doi:10.1007/s11655-022-3513-4

Zhang, L., Huang, J., Zhang, D., Lei, X., Ma, Y., Cao, Y., et al. (2022). Targeting reactive oxygen species in atherosclerosis via Chinese herbal medicines. *Oxid. Med. Cell. Longev.* 2022, 1852330. doi:10.1155/2022/1852330

Zhou, F., Wu, X., Pinos, I., Abraham, B. M., Barrett, T. J., von Lintig, J., et al. (2020). β-Carotene conversion to vitamin A delays atherosclerosis progression by decreasing hepatic lipid secretion in mice. *J. Lipid Res.* 61 (11), 1491–1503. doi:10.1194/jlr.RA120001066

frontiers | Frontiers in Pharmacology

TYPE Original Research
PUBLISHED 13 December 2022
DOI 10.3389/fphar.2022.1065130

OPEN ACCESS

EDITED BY
Simona Pichini,
National Institute of Health (ISS), Italy

REVIEWED BY
Jinping Gu,
Zhejiang University of Technology, China
Jiangeng Huang,
Huazhong University of Science and Technology, China

*CORRESPONDENCE
Dongyang Liu,
liudongyang@vip.sina.com
Yifan Zhai,
yzhai@ascentage.com

†These authors have contributed equally to this work and share first authorship

SPECIALTY SECTION
This article was submitted to Drug Metabolism and Transport, a section of the journal Frontiers in Pharmacology

RECEIVED 09 October 2022
ACCEPTED 23 November 2022
PUBLISHED 13 December 2022

CITATION
Yu Z, Lei Z, Yao X, Wang H, Zhang M, Hou Z, Li Y, Zhao Y, Li H, Liu D and Zhai Y (2022), Potential drug-drug interaction of olverembatinib (HQP1351) using physiologically based pharmacokinetic models. *Front. Pharmacol.* 13:1065130. doi: 10.3389/fphar.2022.1065130

Potential drug-drug interaction of olverembatinib (HQP1351) using physiologically based pharmacokinetic models

Zhiheng Yu[1†], Zihan Lei[2,3†], Xueting Yao[4†], Hengbang Wang[5†], Miao Zhang[3], Zhe Hou[3], Yafen Li[2,3], Yangyu Zhao[6], Haiyan Li[7], Dongyang Liu[4*] and Yifan Zhai[5*]

[1]Drug Clinical Trial Center, Department of Obstetrics and Gynecology, Peking University Third Hospital, Beijing, China, [2]Center of Drug Metabolism and Pharmacokinetics, School of Basic Medicine and Clinical Pharmacy, China Pharmaceutical University, Nanjing, China, [3]Drug Clinical Trial Center, Peking University Third Hospital, Beijing, China, [4]Drug Clinical Trial Center, Institute of Medical Innovation and Research, Peking University Third Hospital, Beijing, China, [5]Guangzhou Healthquest Pharma Co., Ltd, Guangzhou, China, [6]Department of Obstetrics and Gynecology, Peking University Third Hospital, Beijing, China, [7]Drug Clinical Trial Center, Department of Cardiology and Institute of Vascular Medicine, Institute of Medical Innovation and Research, Peking University Third Hospital, Beijing, China

Olverembatinib (HQP1351) is a third-generation BCR-ABL tyrosine kinase inhibitor for the treatment of chronic myeloid leukemia (CML) (including T315I-mutant disease), exhibits drug-drug interaction (DDI) potential through cytochrome P450 (CYP) enzymes CYP3A4, CYP2C9, CYP2C19, CYP1A2, and CYP2B6. A physiologically-based pharmacokinetic (PBPK) model was constructed based on physicochemical and *in vitro* parameters, as well as clinical data to predict 1) potential DDIs between olverembatinib and CYP3A4 and CYP2C9 inhibitors or inducers 2), effects of olverembatinib on the exposure of CYP1A2, CYP2B6, CYP2C9, CYP2C19, and CYP3A4 substrates, and 3) pharmacokinetics in patients with liver function injury. The PBPK model successfully described observed plasma concentrations of olverembatinib from healthy subjects and patients with CML after a single administration, and predicted olverembatinib exposure increases when co-administered with itraconazole (strong CYP3A4 inhibitor) and decreases with rifampicin (strong CYP3A4 inducer), which were validated by observed data. The predicted results suggest that 1) strong, moderate, and mild CYP3A4 inhibitors (which have some overlap with CYP2C9 inhibitors) may increase olverembatinib exposure by approximately 2.39-, 1.80- to 2.39-, and 1.08-fold, respectively; strong, and moderate CYP3A4 inducers may decrease olverembatinib exposure by approximately 0.29-, and 0.35- to 0.56-fold, respectively 2); olverembatinib, as a "perpetrator," would have no or limited impact on CYP1A2, CYP2B6, CYP2C9, CYP2C19, and CYP3A4 enzyme activity 3); systemic exposure of olverembatinib in liver function injury with Child-Pugh A, B, C may increase by 1.22-, 1.79-, and 2.13-fold, respectively. These simulations inform DDI risk for olverembatinib as either a "victim" or "perpetrator".

KEYWORDS

chronic myeloid leukemia, cytochrome P450, drug-drug interactions, modeling, physiologically based pharmacokinetics, tyrosine kinase inhibitor

1 Introduction

Olverembatinib (HQP1351) is a third-generation BCR-ABL1 tyrosine kinase inhibitor (TKI) (Ren et al., 2013). In 2020, the China National Medical Products Administration (NMPA) Center for New Drug Evaluation designated olverembatinib as a potential breakthrough therapy for treatment of patients with chronic myeloid leukemia (CML) that is resistant and/or intolerant to first- and second-generation TKI therapies (Center for Drug Evaluation, 1211). Shortly afterward, the NMPA approved conditional marketing authorization for olverembatinib (breakthrough therapy designation, 1211) at a dose of 40 mg orally every other day (QOD). Olverembatinib is currently approved by the US Food and Drug Administration as an orphan drug to treat CML, acute lymphoblastic leukemia, and acute myeloid leukemia (Orphan Drug Designations and Approvals).

Olverembatinib binds tightly to the ATP-binding sites of native BCR-ABL1 and multiple BCR-ABL1 mutants, including the most refractory ("gatekeeper") mutant T315I, and potently suppresses proliferation of leukemia cells expressing BCR-ABL1 (Ren et al., 2013). Compared with third-generation TKI inhibitor ponatinib, olverembatinib exhibited equivalent or more potent antiproliferative activity in both imatinib-resistant and imatinib-sensitive gastrointestinal stromal tumor cell lines (Liu et al., 2019). Clinical trials of olverembatinib have demonstrated preliminary safety and effectiveness in patients with T315I-mutated CML in the chronic phase (CML-CP) and accelerated phase (CML-AP). When administered at 40 mg QOD for 28 consecutive days per cycle over 24 months, olverembatinib elicited a major cytogenetic response (MCyR) in 79.3% patients with CML-CP (n = 121 without MCyR at baseline) and a major hematologic response (MaHR) in 78.4% patients with CML-AP (n = 37) without MaHR at baseline (Jiang et al., 2022).

Clinical pharmacokinetic data (data on file) have shown that olverembatinib is rapidly absorbed and slowly eliminated after oral administration in fasting and fed patients with CML. The median time to reach peak plasma concentration (T_{max}) for olverembatinib is 6 h, with a mean apparent terminal elimination half-life ($t_{1/2}$) of 32.7 h. There is no significant food effect; the maximum plasma concentration (C_{max}) and area under the plasma concentration-time curve from time 0 to infinity ($AUC_{0-\infty}$) ratio of fed to fasting is 1.28 and 1.17, respectively. After administration of a single radiolabeled dose of olverembatinib (30 mg) in healthy subjects, 87.68% of the dose was recovered in feces within 216 h, and 1.57% was recovered in urine within 96 h. About 23.95% of the cleared drug was unchanged in feces and 0.02% eliminated as the parent drug in urine.

Cytochrome P450 (CYP3A4 and CYP2C9)-mediated metabolism is a major clearance pathway. In the parlance of drug-drug interaction (DDI) studies, the "perpetrator" is the medication that affects the pharmacokinetics of another agent, whereas the "victim" is the medication whose pharmacokinetics are affected by the perpetrator. An olverembatinib clinical DDI study (data on file) showed that coadministration with itraconazole, a substrate for and inhibitor of CYP3A4, increased olverembatinib C_{max} by 1.74-fold and increased area under the concentration-time curve (AUC) by 2.63-fold. On the other hand, coadministration with CYP3A4 inducer rifampicin decreased the olverembatinib maximum concentration (C_{max}) and area under the concentration-time curve (AUC) by 0.36-fold and 0.24-fold, respectively. However, the potential for DDI between olverembatinib and other CYP3A4 inhibitors or inducers was not evaluated in DDI clinical trials. The DDI risk of olverembatinib in combine with CYP2C9 inhibitors or inducers was also not evaluated. Moreover, olverembatinib inhibits CYP2C9 and CYP2C19, and induces CYP1A2, CYP2B6, and CYP2C9, *in vitro*. The effect of olverembatinib as a perpetrator was also not evaluated in previous clinical DDI studies.

Increasingly, physiologically-based pharmacokinetic (PBPK) modeling applications have been used to facilitate the design of DDI studies, evaluate DDI potential *in lieu* of dedicated clinical studies in new drug applications (Zhao et al., 2011; Jones et al., 2015; Shebley et al., 2018). PBPK models that have been validated with clinical data have been increasingly used to predict the DDI potential for untested scenarios. To fully assess DDI risk, evaluate pharmacokinetic changes in patients with liver function injury, the primary objective of this study was to develop and verify a PBPK model for a comprehensive assessment of its clinical DDI and pharmacokinetics profiles in patients with liver function injury.

2 Methods

2.1 Modeling strategy

We formulated a overall strategy for qualification of the olverembatinib model and prediction of DDI (Figure 1). An olverembatinib PBPK model was constructed to simulate the plasma concentration-time profiles of olverembatinib after single-dose administration in healthy volunteers and patients with CML. To evaluate the ability of the model to predict DDI associated with olverembatinib, we conducted clinical DDI studies with strong CYP3A inhibitor and antifungal agent itraconazole and strong CYP3A inducer rifampicin to further

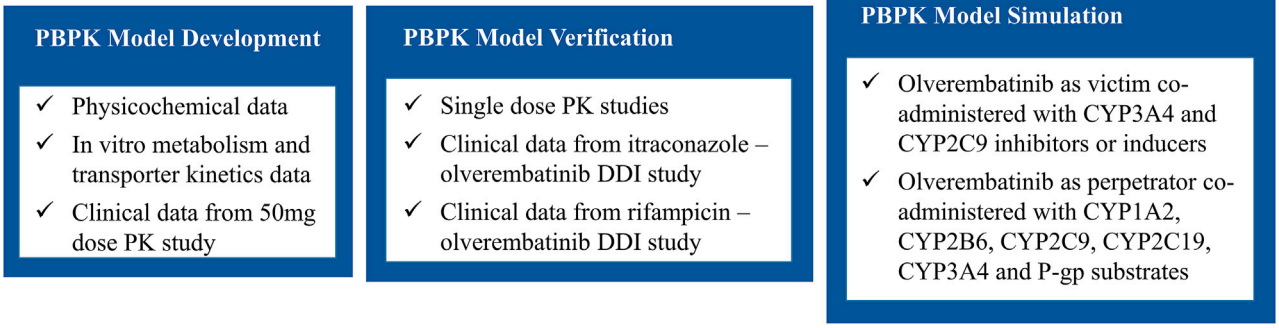

FIGURE 1
The overall model development, verification process, and simulation flow chart.

verify the base PBPK model. Prespecified acceptance criteria (0.5–2.0-fold of observed values) were used to guide model construction and validation.

2.2 Clinical data

All clinical pharmacokinetic data included in the modeling were obtained from three clinical studies (Supplementary Table S1). These studies were conducted in accordance with ethical standards of the institutional and/or national research committee, as well as the Declaration of Helsinki. Institutional review boards or equivalent ethics committees approved the study protocols, and all study participants provided written informed consent before any study-related procedures.

In the first study, on food effects, 12 Chinese patients with CML were randomly divided into two groups (A and B) and the experiments divided into two periods. In period 1, subjects in group A received 30 mg of oral olverembatinib under fasting conditions, while subjects in group B received the same oral dose 30 min after a high-fat meal. After a seven- day washout period, subjects in both groups took the drug interchangeably in period 2 (NCT03882281).

The second study was a single-center, open-label, single-dose phase 1 trial to investigate the absorption, metabolism, and excretion of [^{14}C]olverembatinib after a single oral 30 mg (100 μCi) dose in six healthy Chinese male subjects (NCT04126707). The third study was a phase 1, two-part trial designed to evaluate the interaction of olverembatinib and CYP3A4 perpetrators in healthy American subjects (n = 32). For uninhibited periods, subjects received one oral 20 mg dose of olverembatinib on Day 1. After a 3-day washout period, they were pretreated with 200 mg of oral itraconazole once daily for 4 days to inhibit CYP3A4 (Days 5–8). On Day 9, subjects received single oral 20-mg doses of olverembatinib and itraconazole, or itraconazole alone on Days 10 through12. For uninduced periods, subjects received one oral 40 mg dose of olverembatinib on Day 1. After a 3-day washout, subjects were pretreated with 600 mg of oral rifampicin once daily for 7 days to induce CYP3A4 (Days 5–11). On Day 12, they received single oral doses of olverembatinib at 40 mg and rifampicin at 600 mg, as well as rifampicin alone on Days 13 through15. Blood samples were collected immediately before and after drug administration at 0.5, 1, 2, 4, 6, 8, 12, 24, 48, 72, and 96 h.

2.3 Model construction

A minimal PBPK model with a first-order absorption model was used to construct the olverembatinib PBPK model, including model input parameters (Table 1). The first-order absorption model has different absorption rate constants (k_a) and fraction available from dosage form (f_a) to simulate absorption processes in fasting and fed states. The effective permeability of olverembatinib in the human jejunum was based on built-in predictive *in silico* tools (Sun et al., 2002) within the simulator and *in vitro* Caco-2 cell permeability data with correction by reference drugs (β-adrenoceptor blockers atenolol and propranolol). Caco-2 (human colorectal adenocarcinoma) cells are used to model the intestinal epithelial barrier. The Simcyp (Version 19.0, Certara Inc., Sheffield, UK) minimal PBPK, which treats all organs other than the intestine and liver as a single compartment (Rowland Yeo et al., 2010), was selected, along with a single adjusting compartment (SAC) distribution model. The SAC is a nonphysiologic compartment that permits adjustment to the drug concentration profile in the systemic compartment (Ke et al., 2016).

Final values of the apparent volume of SAC (V_{sac}), as well as the rate constants from systemic compartment to SAC (K_{in}) and from SAC compartment to the systemic compartment (K_{out}), were optimized based on observed pharmacokinetic data. The volume of distribution at steady state (V_{ss}) was predicted from

TABLE 1 Model development and model parameters.

Parameter	Value	Source
MW (g/mol)	532.56	Internal data
$f_{u,p}$	0.0005	Experimental data[a]
Log $P_{o:w}$	3.6	Experimental data[a]
pKa 1	2.90	Experimental data[a]
pKa 2	10.89	Experimental data[a]
B/P ratio	1.29	Experimental data[a]
Absorption model		
k_a (1/h)	0.136 (Fed)	Optimized based on observed data
	0.213 (Fasting)	
f_a	0.8 (Fed)	Optimized based on observed data
	0.574 (Fasting)	
P_{app} (10^{-6} cm/s) (HQP1351)	0.08	Experimental data[a]
P_{app} (10^{-6} cm/s) (Atenolol)	0.38	Experimental data[a]
P_{app} (10^{-6} cm/s) (Propranolol)	5.68	Experimental data[a]
Distribution model		
V_{sac} (L/kg)	38.02	Optimized based on observed data
SAC k_{in} (1/h)	0.0471	Optimized based on observed data
SAC k_{out} (1/h)	0.0177	Optimized based on observed data
K_p Scalar	6.01	Optimized based on observed data
Elimination model		
$CL_{int\ CYP2C9}$ (μL/min/pmol CYP)	0.022	Experimental data[a]
$CL_{int\ CYP3A4}$ (μL/min/pmol CYP)	0.2	Experimental data[a]
$CL_{int\ HLM}$ (μL/min/mg protein)	5.2559	Optimized based on liver microsomal enzyme phenotype study and human recombinant CYP enzyme study
$f_{u,mic}/f_{u,inc}$	0.0005	Assumed equal to fu,p
$ISEF_{CYP2C9}$	1.2938	Optimized based on fm_{CYP2C9} with liver microsomal enzyme phenotype study and human recombinant CYP2C9 study
$ISEF_{CYP3A4}$	0.7761	Optimized based on fm_{CYP3A4} with liver microsomal enzyme phenotype study and human recombinant CYP3A4 study
CLr (L/h)	0.132	Based on phase 1 dose escalation clinical study
Drug interaction		
Ki_{CYP2C9} (μM)	1.135	Calculated with $IC_{50,}$ substrate concentration[a], and substrate K_m[b]
$Ki_{CYP2C19}$ (μM)	1.924	Calculated with $IC_{50,}$ substrate concentration[a], and substrate K_m[c]
$Ind_{max\ CYP1A2}$	6.26	Experimental data[a]
$Ind_{max\ CYP2B6}$	17.900	Experimental data[a]
$Ind_{max\ CYP2C9}$	17.150	Experimental data[a]
$IndC_{50\ CYP1A2}$ (μM)	0.15	Experimental data[a]
$IndC_{50\ CYP2B6}$ (μM)	0.559	Experimental data[a]
$IndC_{50\ CYP2C9}$ (μM)	0.454	Experimental data[a]
$Ki_{P\text{-}gp}$ (μM)	2.23	Calculated with $IC_{50,}$ substrate concentration[a] and substrate Km[d]

[a]Internal data (fu, B/P ratio, CLintCYP, IndmaxCYP, and IndC50CYP, are summarized in Supplementary Tables S4-S7).
[b]Data were derived from Lee MY, Borgiani P, Johansson I, Oteri F, Mkrtchian S, Falconi M, et al. (Lee et al., 2014).
[c]Data were derived from Yang S, Qiu Z, Zhang Q, Chen J, Chen X (Yang et al., 2014).
[d]Data were derived from Troutman MD, Thakker DR. (Troutman and Thakker, 2003) MW, molecular weight; fu,p, fraction unbound in plasma; logP, log of the octanol-water partition coefficient for the neutral compound; pKa, acid dissociation constant; B/P, blood/plasma partition ratio; ka, first-order absorption rate constant; fa, fraction available from dosage form; Vsac, volume of the single adjusting compartment; SAC, single adjusting compartment; kp scalar, scalar applied to all predicted tissue kp values; CLint, intrinsic clearance; CYP, cytochrome P450; HLM, human liver microsome; fu,mic, microsomal protein binding; fmCYP2C9, fraction of drug metabolized by CYP2C9; fmCYP3A4, fraction of drug metabolized by CYP3A4; CLR, renal clearance; Ki, enzyme or transporter inhibition constant (concentration of inhibitor associated with half maximal inhibition); IC_{50}, half-maximal inhibitory concentration; Indmax, calibrated maximal fold induction over vehicle (1 = no induction); IndC50, calibrated inducer concentration that supports half-maximal induction (μM).

the steady-state tissue: plasma partition coefficient (K_p) calculated using mechanistic tissue distribution equations (Rodgers et al., 2005; Rodgers and Rowland, 2006). Intrinsic clearance values of 0.200 μL/min/pmol and 0.022 μL/min/pmol were assigned for CYP3A4 and CYP2C9, respectively, based on an *in vitro* human recombinant CYP isoenzyme study. Intersystem extrapolation factors for CYP3A4 and CYP2C9 were optimized based on clinical metabolism and excretion data in a mass balance study (NCT04126707). The mean value of renal clearance was confirmed by a phase 1 dose escalation study in 12 Chinese patients who received 50 mg of oral olverembatinib on Day 1.

Olverembatinib exhibits CYP2C9 and CYP2C19 inhibition and CYP1A2, CYP2B6 and CYP2C9 induction *in vitro*. The concentration of olverembatinib that supports half-maximum inhibition (K_i) was calculated using Eq. 1.

$$K_i = \frac{\mathrm{IC50}}{1 + [\mathrm{S}]/K_m} \quad (1)$$

Where IC_{50} signifies the half-maximum inhibitory concentration; S, the concentration of P450 marker substrate; and K_m, the Michaelis constant within the Michaelis-Menten equation, which is in turn used to characterize substrate-enzyme binding kinetics.

As a CYP2C9 probe substrate, the nonsteroidal anti-inflammatory drug diclofenac (2.5 μM) was incubated with human liver microsomes, nicotinamide adenine dinucleotide phosphate, and olverembatinib to obtain the IC_{50}. The Michaelis constant (K_m) of CYP2C9 incubated with diclofenac was obtained from reported data (Lee et al., 2014). Methods used to calculate the K_i of CYP2C19 and CYP2C9 were similar. The maximum fold induction (Ind_{max}) and half-maximum fold induction concentration ($IndC_{50}$) values of olverembatinib on CYP1A2, CYP2B6, and CYP2C9 were calculated by plotting mRNA fold induction *versus* olverembatinib concentration after *in vitro* incubation with human hepatocytes.

2.4 Model validation

The olverembatinib PBPK model was constructed and validated using Simcyp. Default virtual population models of healthy White and Chinese volunteers were used, except for demographic data noted in each clinical study. For model construction and validation, the virtual trials used in each simulation were based on corresponding doses used in each of the clinical studies (Supplementary Table S1). The constructed PBPK model was validated by comparing the predicted model and observed pharmacokinetic parameters and/or plasma concentration profiles. The PBPK model predictive performance was preliminarily evaluated by overlaying the observed concentration-time profile with the model-predicted profile and 90% predictive interval. The quantitative assessment was conducted by pharmacokinetic parameters (C_{max} and AUC), as represented by the ratio of the predicted to the observed value. The model performance success criterion was acceptable if it fell within the 0.5- to 2.0-fold range.

2.5 Model hypothesis

A food effect study (NCT03882281) was conducted in Chinese patients with CML, for whom there was no CML population library in Simcyp. As a result, a "Sim-Chinese healthy volunteers" simulated population was used for model verification under the assumption of equivalent pharmacokinetics in patients with CML and healthy volunteers.

2.6 Model simulation

After validation, the PBPK model was used to simulate untested clinical DDI scenarios for olverembatinib as either a victim or perpetrator (Zhang et al., 2022). As a victim, olverembatinib pharmacokinetics were simulated after coadministration with CYP3A4 and CYP2C9 perpetrators according to a prespecified dose scheme (Table 2). Substrate pharmacokinetics of CYP2C9, CYP2C19, CYP1A2, CYP2B6, and P-glycoprotein (P-gp) were simulated after coadministration with olverembatinib (as a perpetrator), also according to a protocol-based dose scheme (Table 2).

To evaluate the effect of liver function on olverembatinib pharmacokinetics, we performed the simulation in virtual patients with liver function injury classified as mild (A), moderate (B) and severe (C) by the Child-Pugh (CP) classification, including a prespecified dose scheme (Table 3. Ten virtual trials were simulated for each scenario to assess interstudy variability, and 10 subjects (aged 20–50 years and 50% female) participated in each simulated trial. All DDI model simulations were conducted with the virtual "Sim-Chinese healthy volunteers" population except for a P-gp-mediated DDI simulation, which was conducted with the representative population "Sim-Chinese healthy volunteers" population. All liver cirrhosis simulations were conducted with the default virtual population "Sim-Healthy volunteers, "Sim-Cirrhosis CP-A, "Sim-Cirrhosis CP-B," and "Sim-Cirrhosis CP-C″ populations. Except for olverembatinib, all compound files in Simcyp V.19 default were used.

TABLE 2 Simulated C_{max} and AUC ratios of olverembatinib (HQP1351) as victim in the presence and absence of CYP modulators and simulated C_{max} and AUC of CYP substrates when olverembatinib as CYP modulators.

Inhibitor/ inducer	Dose	Treatments days	HQP1351 dose	HQP1351 treatments	C_{max_inh} (ng/ml)	AUC_{96_inh} (h•ug/mL)	C_{max} ratio	AUC ratio
CYP3A4								
Itraconazole (strong inhibitor)	200 mg QD	8	40 mg	Coadministration on day 5	28.8	1.05	1.64	2.39
Verapamil (moderate inhibitor)	80 mg TID	8	40 mg	Coadministration on day 5	27.7	0.99	1.55	2.25
Fluconazole (moderate inhibitor)	200 mg QD	10	40 mg	Coadministration on day 7	24.9	0.79	1.42	1.80
Erythrocin (moderate inhibitor)	500 mg Q6h	8	40 mg	Coadministration on day 5	28.4	1.05	1.60	2.39
Fluvoxamine (mild inhibitor)	50 (36.65) mg QDd	10	40 mg	Coadministration on day 7	18.4	0.48	1.05	1.08
Cimetidine (mild inhibitor)	400 mg BID	10	40 mg	Coadministration on day 7	18.4	0.47	1.05	1.08
Rifampicin (strong inducer)[a]	600 mg QD	11	40 mg	Coadministration on day 8	7.56	0.13	0.43	0.29
Efavirenz (moderate inducer)	600 mg QD	11	40 mg	Coadministration on day 8	8.59	0.15	0.48	0.35
Phenobarbital (moderate inducer)[b]	100 mg QD	11	40 mg	Coadministration on day 8	11.7	0.24	0.67	0.56
CYP2C9								
Fluconazole (moderate inhibitor)	200 mg QD	10	40 mg	Coadministration on day 7	24.9	0.79	1.42	1.80
fluvoxamine (mild inhibitor)	50 (36.65) mg QD[c]	10	40 mg	Coadministration on day 7	18.4	0.48	1.05	1.08
Substrates	Dose	Treatments	HQP1351 dose	HQP1351 treatments (days)	C_{max_inh} (ug/mL)	AUC_{360_inh} (h•ug/L)	C_{max} ratio	AUC ratio
CYP2C9								
Tolbutamide	500 mg	Coadministration on day 13	40 mg QOD	27	44.0	0.82	0.92	0.71
(S)-Warfarin	10 mg	Coadministration on day 13	40 mg QOD	27	1.20	0.06	0.98	0.72
CYP2C19								
Omeprazole	20 mg	Coadministration on day 13	40 mg QOD	27	0.32	0.002	1.01	1.02
CYP1A2								
Caffeine	150 mg	Coadministration on day 13	40 mg QOD	27	3.99	0.03	0.93	0.69
CYP2B6								
Bupropion	150 (130.2) mg[d]	Coadministration on day 13	40 mg QOD	27	0.104	0.002	0.95	0.91
P-gp								
Dabigatran etexilate	150 mg	Coadministration on day 13	40 mg QOD	27	2.63	14.4	1.00	1.00
Digoxin	0.5 mg	Coadministration on day 13	40 mg QOD	27	1.77	28.3	1.00	1.00

Cmax_inh: Maximum plasma substrates concentration following coadministration with modulators; $AUC_{96_}$inh: Area under the plasma substrates concentration curve from 0 to 96 h following coadministration with modulators; $AUC_{360_}$inh: Area under the plasma concentration curve from 0 to 360 h following coadministration with modulators.

[a]Rifampicin is also a moderate inducer of CYP2C9.

[b]Phenobarbital is the Simcyp default drug model, which also induced CYP2C9.

[c]Fluvoxamine maleate dose is 50 mg, which contains fluvoxamine 36.65 mg.

[d]Bupropion hydrochloride sustained-release tablets dose is 150 mg, which contains fluvoxamine 130.2 mg. BID, two times a day; QD, every day; QOD, every other day; TID, three times a day.

TABLE 3 Simulated C_{max} and AUC_{0-96} of olverembatinib (HQP1351) in different liver cirrhosis populations.

Population	Description	HQP1351 dose	C_{max} (ng/ml)	AUC_{0-96} (h•ng/mL)	C_{max} ratio	AUC_{0-96} ratio
Healthy Caucasian population	Caucasian healthy population	40 mg SD	15.2	292	NA	NA
Sim-cirrhosis CP-A	Caucasian mild cirrhosis population	40 mg SD	17.6	356	1.16	1.22
Sim-cirrhosis CP-B	Caucasian moderate cirrhosis population	40 mg SD	24.2	522	1.59	1.79
Sim-cirrhosis CP-C	Caucasian severe cirrhosis population	40 mg SD	28.4	621	1.87	2.13

C_{max} ratio: The ratio of the Cmax in the liver cirrhosis population and Cmax in Caucasian healthy population; AUC, ratio: The ratio of the area under the curve (AUC) in the liver cirrhosis population and AUC, in Caucasian healthy population; CP, Child-Pugh; NA, not applicable; SD, single dose.

3 Results

3.1 Model construction

Absorption and distribution behaviors of olverembatinib were effectively predicted using first-order absorption kinetics with a minimal PBPK model. Using the same dose regimen as in dosed patients, a simulation was performed. The predicted plasma concentration profiles after single oral 30 mg doses (fasting or fed) were consistent with observed profiles in Chinese patients with CML in the food effect study (Figure 2). C_{max} ratios (predicted/observed) in fasting and fed conditions were 1.13 and 1.02, respectively. AUC ratios (predicted/observed) in fasting and fed conditions were 0.95 and 1.12, respectively. Similarly, predicted concentration profiles after a single oral dose of 20 or 40 mg were consistent with those observed data in healthy American volunteers. The C_{max} and AUC ratio (predicted/observed) ranges were 0.88–1.06 and 0.88 to 1.03, respectively. In the mass balance study, the observed olverembatinib concentration in healthy Chinese volunteers were within the prediction interval. The C_{max} and AUC ratios (predicted/observed) were 0.76 and 1.12, respectively.

3.2 Model validation

The applicability of the PBPK model to assess the magnitude of drug interactions between olverembatinib and CYP3A4 perpetrators was verified. The model simulated the concentration-time profiles of 20 mg of olverembatinib administered with CYP3A4 inhibitor itraconazole in the clinical DDI study (Figure 3). Itraconazole's effect on olverembatinib was simulated in profiles for changes in C_{max} and AUC (Supplementary Table S3). The observed C_{max} and AUC ratios of olverembatinib in the presence or absence of itraconazole were 1.74 and 2.63, respectively. The corresponding PBPK model predicted C_{max} and AUC ratios of 1.69 and 2.22, respectively, which were consistent with observed values in the clinical DDI study.

3.3 Model simulation

The effect of CYP3A4 inducer rifampicin on olverembatinib was demonstrated by simulating the pharmacokinetic profiles of the TKI when coadministered with the antibiotic. The simulation was acceptable when compared with the observed concentration-time profiles of olverembatinib among healthy American volunteers in the rifampicin DDI study (Figure 3). Observed C_{max} and AUC ratios of olverembatinib in the presence and absence of rifampicin were 0.36 and 0.24, respectively, compared to predicted ratios of 0.38 and 0.27, respectively. The PBPK model-predicted mean C_{max} and AUC ratios of olverembatinib (at 40 mg) with or without rifampicin were less than 1.5 times the observed values (Supplementary Table S3).

3.3.1 Simulation of olverembatinib as a DDI victim

The constructed PBPK model was used to simulate other untested clinical DDI scenarios for olverembatinib during coadministration with CYP3A4 and CYP2C9 inhibitors and inducers in healthy Chinese volunteers. Simulated olverembatinib pharmacokinetic parameters and corresponding ratios with and without coadministration of CYP3A4 and CYP2C9 modulators are outlined (Table 2).

PBPK simulations indicated that olverembatinib AUC_{0-96h} (area under the plasma drug concentration-time curve from 0 to 96 h) may increase by approximately 2.39- and by 1.80- to 2.39-fold during coadministration with strong and moderate CYP3A4 inhibitors, respectively. Simulations suggested that the strong and moderate CYP3A4 inducers may decrease the AUC_{0-96h} of olverembatinib by 0.29- and 0.56- to 0.35-fold, respectively. Based on the PBPK model simulations, predicted ratios of olverembatinib AUC_{0-96h} in the presence or absence of moderate and mild CYP2C9 inhibitors were 1.80 and 1.08, respectively.

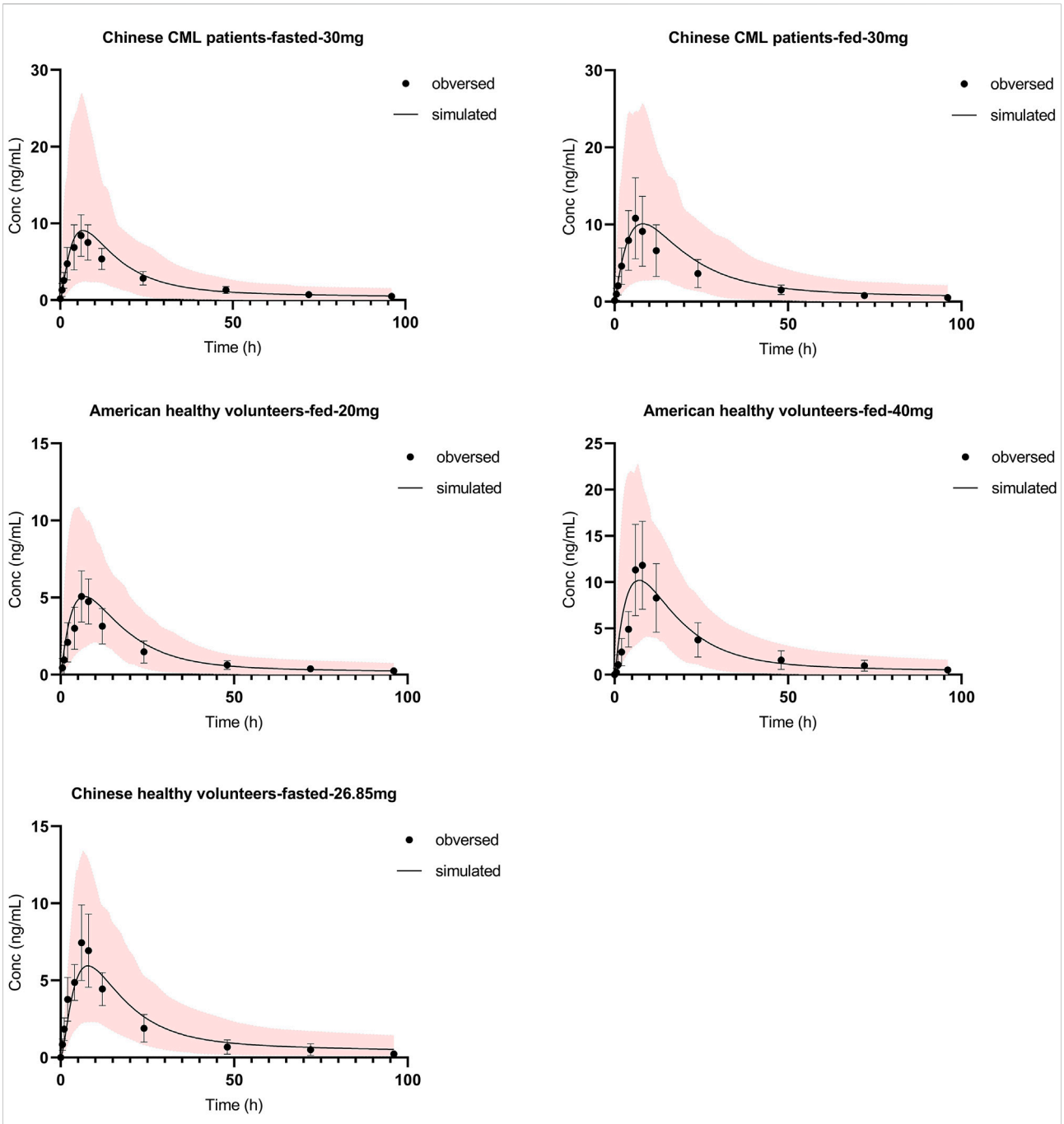

FIGURE 2
Olverembatinib PBPK model verification. Observed (mean and standard deviation, dots and bar) and simulated (solid lines) mean plasma concentration-time profiles of olverembatinib in different populations following single oral doses of olverembatinib (30, 20, 40 or 26.85 mg). The shaded area is the 5–95% range in concentrations from 1,000 simulated healthy Chinese or American adult subjects.

3.3.2 Simulation of olverembatinib as a DDI perpetrator

To assess the potential effects of olverembatinib on the pharmacokinetics of CYP2C9, CYP2C19, CYP1A2, CYP2B6, and CYP3A4 substrate drugs, the predicted pharmacokinetic parameters and mean C_{max} and AUC ratios of substrate drugs with or without olverembatinib were simulated (Table 2).

Tolbutamide (which interferes with binding of anticoagulant warfarin enantiomers) and (S)-warfarin are substrates of CYP2C9. PBPK simulations indicate that tolbutamide and (S)-

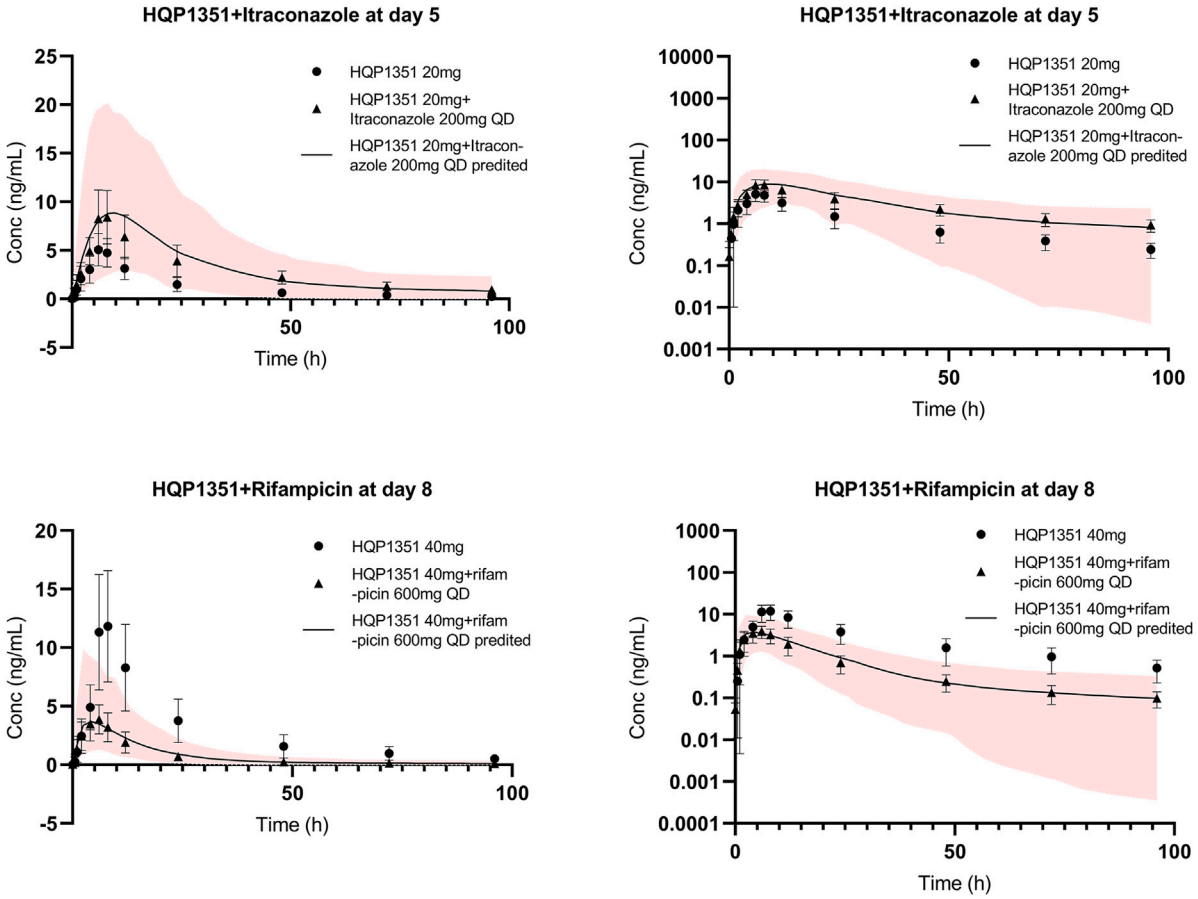

FIGURE 3
Further verification of olverembatinib PBPK model. Observed (mean and standard deviation, dots for single dose, triangle for coadministration and bar) and simulated (solid lines for coadministration) mean plasma concentration-time profiles of olverembatinib in healthy American volunteers following oral doses of olverembatinib (left panels = linear scale; right panels = semi-log scale). The shaded area is the 5%–95% range in concentrations from 1,000 simulated healthy American adult subjects.

warfarin AUC_{0-360h} (area under the plasma drug concentration-time curve from 0 to 360 h) may decrease by approximately 0.71- and 0.72-fold, respectively during coadministration with olverembatinib. Similarly, simulations suggested that olverembatinib may increase the AUC_{0-360h} of CYP2C19 substrate and proton pump inhibitor omeprazole by 1.02-fold and decrease the AUC_{0-360h} of CYP1A2 substrate of caffeine (anaesthetic) and CYP2B6 substrate and antidepressant bupropion by 0.69- and 0.91-fold, respectively.

As a DDI perpetrator, olverembatinib has no or limited impact on the enzyme activity of CYP2C9, CYP2C19, CYP1A2, or CYP2B6. Finally, we assessed the potential effects of olverembatinib on the pharmacokinetics of P-gp substrates dabigatran etexilate (low-molecular-weight prodrug of the direct thrombin inhibitor) and the cardiac glycoside digoxin. The AUC_{0-360h} ratio for dabigatran etexilate or digoxin in the presence or absence of olverembatinib was 1.0 each.

3.3.3 Simulation of olverembatinib in liver cirrhosis populations

In this simulation, we used a liver cirrhosis population model based on Caucasian people. The ratio of the AUC in liver cirrhosis and healthy populations was assumed to be equal in both Caucasian and Chinese people. PBPK simulations indicated that predicted ratios of olverembatinib AUC_{0-96h} among patients in cirrhosis CP-A, CP-B, and CP-C, relative to healthy volunteers, were 1.22, 1.79, and 2.13, respectively. For C_{max}, the model-predicted ratios in patients with CP-A, CP-B, and CP-C cirrhosis, relative to healthy volunteers, were 1.16, 1.59, and 1.87, respectively (Table 3).

4 Discussion

This study developed a model-based approach for comprehensive evaluation of olverembatinib DDI profiles,

including evaluation of its potential as a victim of CYP3A4 and CYP2C9 and as a perpetrator for CYP2C9, CYP2C19, CYP1A2, CYP2B6, and P-gp substrates. PBPK modeling was used to assess metabolic DDI risks as part of the clinical pharmacology strategy for the development of olverembatinib. Robustness of the current PBPK model was demonstrated by the similarity of model predictions with observed clinical data after a single dose of olverembatinib across various drug interaction pathways. Because hepatic metabolism is the principal pathway governing elimination of olverembatinib, the effect of liver function injury on exposure to olverembatinib was evaluated by simulating pharmacokinetic profiles in patients with liver cirrhosis.

Olverembatinib is metabolized by multiple CYP isozymes, with higher relative contributions with CYP3A4 and CYP2C9 (60.0% and 21.6%; data from human liver microsome study). The clinical DDI study indicated that the AUC of olverembatinib (20 or 40 mg single dose) increased 2.61-fold (or by 163%) after itraconazole treatment (200 mg daily [QD]) and decreased 0.24-fold (or by 76%) after rifampicin administration. In addition, a PBPK modeling simulation demonstrated that a strong CYP3A4 inhibitor increased olverembatinib AUC by 139%. Moderate and mild CYP3A4 inhibitors (some of which overlap as CYP2C9 inhibitors) increased olverembatinib exposures by 80%–139% and 8%, respectively.

Strong and moderate CYP3A4 inducers (some of which overlap as CYP2C9 inducers) decreased olverembatinib exposure by 44%–71%. In our study, moderate CYP3A4 inhibitor and antibiotic erythromycin was administered at a higher-than-routine dose (500 mg every 6 h) and hence showed an inhibitory effect similar to that with strong CYP3A4 inhibitor itraconazole. After adjustment of the erythromycin dose to 500 mg 3 times a day, the mean C_{max} and AUC_{0-t} ratios for olverembatinib in the presence or absence of erythrocin were 1.60 and 2.39, respectively. Both CYP3A4 and CYP2C9 were inhibited by fluconazole and antidepressant fluvoxamine and induced by rifampicin and the barbiturate phenobarbital. Olverembatinib exposures changed significantly after coadministration with these drugs. Based on the clinical DDI study and predictions of the PBPK model, coadministration of olverembatinib with strong and moderate CYP3A4 inhibitors or inducers is not recommended.

In vitro studies suggested that olverembatinib is a weak CYP2C9 and CYP2C19 inhibitor, and a weak CYP1A2, CYP2B6 and CYP2C9 inducer. The PBPK model was used to evaluate the DDI potential of olverembatinib and CYP/P-gp substrates. Olverembatinib decreased tolbutamide and (S)-warfarin (CYP2C9 substrates), caffeine (CYP1A2 substrate), and bupropion (CYP2B6 substrate) exposures by 28%–29%, 31%, and 9%, respectively. Olverembatinib increased omeprazole (CYP2C19 substrate) exposure by 2% but did not change exposures of dabigatran etexilate and digoxin (P-gp substrates). As a DDI perpetrator, olverembatinib had no or limited impact on activities of CYP1A2, CYP2B6, CYP2C9, CYP2C19, and P-gp.

In addition, olverembatinib is neither a substrate nor inhibitor of OATP1B1 (organic anion transporting polypeptide 1B1), OATP1B3 (organic anion transporting polypeptide 1B3), OAT1 (organic anion transporter 1), OAT3 (organic anion transporter 3), OCT2 (organic cation transporter 2), MATE1 (multidrug and toxin extrusion 1), or MATE2K (multidrug and toxin extrusion 2). Olverembatinib also showed no obvious *in vivo* inhibition on P-gp and BCRP (breast cancer resistance protein) and exerted a negligible perpetrator effect on substrates of common CYP enzymes and transporters. However, these findings will need to be further validated by additional clinical studies.

Hepatic elimination is an important mechanism that regulates overall clearance of olverembatinib. In the current simulation, we show that respective exposures of olverembatinib in Caucasian populations with mild, moderate, and severe cirrhosis were 22%, 79%, and 113% higher than in healthy volunteers. Because no clinical data were obtained before this study, the olverembatinib pharmacokinetic assessment in liver function injury populations was not validated. The simulation results indicate that patients with mild liver injury can receive the same dose of olverembatinib as those with normal liver function. An appropriate dose adjustment should be considered for patients with moderate liver injury by weighing the benefits and risks. However, in patients with severe cirrhosis, olverembatinib is not recommended. Additional clinical studies in patients with liver cirrhosis are needed to optimize the dose regimen.

A limitation of this study is that the transporters mediated disposition was not integrated in PBPK model since olverembatinib is a substrate of P-gp, BCRP (breast cancer resistance protein). The effects of transporters expressed on the gut and liver have not been investigated.

Besides, the B/P ratio was obtained from healthy volunteer blood, however, in patients with CML, too many myeloid cells become granulocytes (red blood cells, platelets and several white blood cell types). So, red blood cell count might change B/P ratio in CML patients. The B/P ratio of olverembatinib in CML patients need a further study. Furthermore, the model simulation for liver cirrhosis patients was not validated by clinical data. We believe that further research is needed on this point.

5 Conclusion

A robust PBPK model of olverembatinib was constructed and validated to predict CYP3A4-and CYP2C9-mediated drug interactions. The validated PBPK model was utilized to forecast DDI risks where no clinical data were available. Simulations suggested that no dose adjustment for

olverembatinib is required when the TKI is coadministered with mild CYP3A4 and CYP2C9 inhibitors. With moderate and strong CYP3A4 or CYP2C9 inhibitors and inducers, coadministration is not recommended. Dose adjustment might be not needed in light liver cirrhosis patients with CP-A. Moderated liver cirrhosis patients should use olverembatinib with caution and are suggested to monitor liver function. But the severe liver cirrhosis patients are not suggested to use olverembatinib.

Data availability statement

The original contributions presented in the study are included in the article/Supplementary Material, further inquiries can be directed to the corresponding authors.

Ethics statement

The studies involving human participants were reviewed and approved by 1) Frontage Clinical Services, Inc. 2) Medical ethics committee of peking university people's hospital. 3) Ethics Committee of the First Affiliated Hospital of Nanjing Medical University. The patients/participants provided their written informed consent to participate in this study. The animal study was reviewed and approved by Shanghai Medicilon Inc.

Author contributions

ZY performed the PBPK modeling and simulation and conducted statistical and graphical analysis. ZL drafted this manuscript and was responsible for article revision. HW and YZ provided funding and supervised this study. MZ and ZH assisted the PBPK modeling and simulation and quality control. YL assisted the paper quality control. HW contributed the *in vivo* and *in vitro* data of olverembatinib. HL and YZ supervised the study. XY guided the modeling operation and optimization, and prepared original draft. DL conceived the study conceptualization and methodology.

Funding

The research was funded by Guangzhou Healthquest Pharma Co., Ltd and Bill and Melinda Gates Foundation (No. INV-007625).

Acknowledgments

We thank Ashutosh K. Pathak, MD, PhD, MBA, FRCP (Edin.), Stephen W. Gutkin, Paul O. Fletcher, PhD, and Ndiya Ogba, PhD, with Guangzhou Healthquest for providing editorial assistance and substantive input in manuscript preparation. This study and its report were supported by Guangzhou Healthquest Pharma group Corp Ltd. (Hong Kong).

Conflict of interest

Authors HW and YZ were employed by the company Guangzhou Healthquest Pharma Inc.

The remaining authors declare that the research was conducted in the absence of any commercial or financial relationships that could be construed as a potential conflict of interest.

Publisher's note

All claims expressed in this article are solely those of the authors and do not necessarily represent those of their affiliated organizations, or those of the publisher, the editors and the reviewers. Any product that may be evaluated in this article, or claim that may be made by its manufacturer, is not guaranteed or endorsed by the publisher.

Supplementary material

The Supplementary Material for this article can be found online at: https://www.frontiersin.org/articles/10.3389/fphar.2022.1065130/full#supplementary-material

References

breakthrough therapy designation. NMPA [Available at: https://www.cde.org.cn/main/xxgk/listpage/da6efd086c099b7fc949121166f0130c.

Center for Drug Evaluation, NMPA. Breakthrough therapy designation. Available at: https://www.cde.org.cn/main/xxgk/listpage/da6efd086c099b7fc949121166f0130c

Jiang, Q., Li, Z., Qin, Y., Li, W., Xu, N., Liu, B., et al. (2022). Olverembatinib (HQP1351), a well-tolerated and effective tyrosine kinase inhibitor for patients with T315I-mutated chronic myeloid leukemia: Results of an open-label, multicenter phase 1/2 trial. *J. Hematol. Oncol.* 15 (1), 113. doi:10.1186/s13045-022-01334-z

Jones, H. M., Chen, Y., Gibson, C., Heimbach, T., Parrott, N., Peters, S. A., et al. (2015). Physiologically based pharmacokinetic modeling in drug discovery and development: A pharmaceutical industry perspective. *Clin. Pharmacol. Ther.* 97 (3), 247–262. doi:10.1002/cpt.37

Ke, A., Barter, Z., Rowland-Yeo, K., and Almond, L. (2016). Towards a best practice approach in PBPK modeling: Case example of developing a unified efavirenz model accounting for induction of CYPs 3A4 and 2B6. *CPT. Pharmacometrics Syst. Pharmacol.* 5 (7), 367–376. doi:10.1002/psp4.12088

Lee, M. Y., Borgiani, P., Johansson, I., Oteri, F., Mkrtchian, S., Falconi, M., et al. (2014). High warfarin sensitivity in carriers of CYP2C9*35 is determined by the

impaired interaction with P450 oxidoreductase. *Pharmacogenomics J.* 14 (4), 343–349. doi:10.1038/tpj.2013.41

Liu, X., Wang, G., Yan, X., Qiu, H., Min, P., Wu, M., et al. (2019). Preclinical development of HQP1351, a multikinase inhibitor targeting a broad spectrum of mutant KIT kinases, for the treatment of imatinib-resistant gastrointestinal stromal tumors. *Cell Biosci.* 9, 88. doi:10.1186/s13578-019-0351-6

Orphan Drug Designations and Approvals. FDA [Available from: https://www.accessdata.fda.gov/scripts/opdlisting/oopd/listResult.cfm.

Ren, X., Pan, X., Zhang, Z., Wang, D., Lu, X., Li, Y., et al. (2013). Identification of GZD824 as an orally bioavailable inhibitor that targets phosphorylated and nonphosphorylated breakpoint cluster region-Abelson (Bcr-Abl) kinase and overcomes clinically acquired mutation-induced resistance against imatinib. *J. Med. Chem.* 56 (3), 879–894. doi:10.1021/jm301581y

Rodgers, T., Leahy, D., and Rowland, M. (2005). Physiologically based pharmacokinetic modeling 1: Predicting the tissue distribution of moderate-to-strong bases. *J. Pharm. Sci.* 94 (6), 1259–1276. doi:10.1002/jps.20322

Rodgers, T., and Rowland, M. (2006). Physiologically based pharmacokinetic modelling 2: Predicting the tissue distribution of acids, very weak bases, neutrals and zwitterions. *J. Pharm. Sci.* 95 (6), 1238–1257. doi:10.1002/jps.20502

Rowland Yeo, K., Jamei, M., Yang, J., Tucker, G. T., and Rostami-Hodjegan, A. (2010). Physiologically based mechanistic modelling to predict complex drug-drug interactions involving simultaneous competitive and time-dependent enzyme inhibition by parent compound and its metabolite in both liver and gut - the effect of diltiazem on the time-course of exposure to triazolam. *Eur. J. Pharm. Sci.* 39 (5), 298–309. doi:10.1016/j.ejps.2009.12.002

Shebley, M., Sandhu, P., Emami Riedmaier, A., Jamei, M., Narayanan, R., Patel, A., et al. (2018). Physiologically based pharmacokinetic model qualification and reporting procedures for regulatory submissions: A consortium perspective. *Clin. Pharmacol. Ther.* 104 (1), 88–110. doi:10.1002/cpt.1013

Sun, D., Lennernas, H., Welage, L. S., Barnett, J. L., Landowski, C. P., Foster, D., et al. (2002). Comparison of human duodenum and Caco-2 gene expression profiles for 12, 000 gene sequences tags and correlation with permeability of 26 drugs. *Pharm. Res.* 19 (10), 1400–1416. doi:10.1023/a:1020483911355

Troutman, M. D., and Thakker, D. R. (2003). Efflux ratio cannot assess P-glycoprotein-mediated attenuation of absorptive transport: Asymmetric effect of P-glycoprotein on absorptive and secretory transport across caco-2 cell monolayers. *Pharm. Res.* 20 (8), 1200–1209. doi:10.1023/a:1025049014674

Yang, S., Qiu, Z., Zhang, Q., Chen, J., and Chen, X. (2014). Inhibitory effects of calf thymus DNA on metabolism activity of CYP450 enzyme in human liver microsomes. *Drug Metab. Pharmacokinet.* 29 (6), 475–481. doi:10.2133/dmpk.DMPK-13-RG-131

Zhang, M., Yu, Z., Yao, X., Lei, Z., Zhao, K., Wang, W., et al. (2022). Prediction of pyrotinib exposure based on physiologically-based pharmacokinetic model and endogenous biomarker. *Front. pharmacol.* 13, 972411. doi:10.3389/fphar.2022.972411

Zhao, P., Zhang, L., Grillo, J. A., Liu, Q., Bullock, J. M., Moon, Y. J., et al. (2011). Applications of physiologically based pharmacokinetic (PBPK) modeling and simulation during regulatory review. *Clin. Pharmacol. Ther.* 89 (2), 259–267. doi:10.1038/clpt.2010.298

frontiers | Frontiers in Pharmacology

TYPE Original Research
PUBLISHED 15 December 2022
DOI 10.3389/fphar.2022.1076266

OPEN ACCESS

EDITED BY
Simona Pichini,
National Institute of Health (ISS), Italy

REVIEWED BY
Eric F. Egelund,
University of Florida, United States
Thaigarajan Parumasivam,
Universiti Sains Malaysia (USM), Malaysia

*CORRESPONDENCE
Sandra Grañana-Castillo,
S.Granana-Castillo@liverpool.ac.uk

SPECIALTY SECTION
This article was submitted to Drug Metabolism and Transport, a section of the journal Frontiers in Pharmacology

RECEIVED 21 October 2022
ACCEPTED 28 November 2022
PUBLISHED 15 December 2022

CITATION
Grañana-Castillo S, Montanha MC, Bearon R, Khoo S and Siccardi M (2022), Evaluation of drug-drug interaction between rilpivirine and rifapentine using PBPK modelling.
Front. Pharmacol. 13:1076266.
doi: 10.3389/fphar.2022.1076266

Evaluation of drug-drug interaction between rilpivirine and rifapentine using PBPK modelling

Sandra Grañana-Castillo[1]*, Maiara Camotti Montanha[1], Rachel Bearon[2], Saye Khoo[1] and Marco Siccardi[1]

[1]Department of Pharmacology and Therapeutics, University of Liverpool, Liverpool, United Kingdom, [2]Department of Mathematical Sciences, University of Liverpool, Liverpool, United Kingdom

Tuberculosis remains the leading cause of death among people living with HIV. Rifapentine is increasingly used to treat active disease or prevent reactivation, in both cases given either as weekly or daily therapy. However, rifapentine is an inducer of CYP3A4, potentially interacting with antiretrovirals like rilpivirine. This *in silico* study investigates the drug-drug interaction (DDI) magnitude between daily oral rilpivirine 25 mg with either daily 600 mg or weekly 900 mg rifapentine. A physiologically based pharmacokinetic (PBPK) model was built in Simbiology (Matlab R2018a) to simulate the drug-drug interaction. The simulated PK parameters from the PBPK model were verified against reported clinical data for rilpivirine and rifapentine separately, daily rifapentine with midazolam, and weekly rifapentine with doravirine. The simulations of concomitant administration of rifapentine with rilpivirine at steady-state lead to a maximum decrease on $AUC_{0\text{-}24}$ and C_{trough} by 83% and 92% on day 5 for the daily rifapentine regimen and 68% and 92% for the weekly regimen on day 3. In the weekly regimen, prior to the following dose, $AUC_{0\text{-}24}$ and C_{trough} were still reduced by 47% and 53%. In both simulations, the induction effect ceased 2 weeks after the interruption of rifapentine's treatment. A daily double dose of rilpivirine after initiating rifapentine 900 mg weekly was simulated but failed to compensate the drug-drug interaction. The drug-drug interaction model suggested a significant decrease on rilpivirine exposure which is unlikely to be corrected by dose increment, thus coadministration should be avoided.

KEYWORDS

drug interaction (DI), PBPK, antiretroviral therapy, tuberculosis, rilpivirine, rifapentine

Introduction

Tuberculosis affects one-fourth of the world-wide population (WHO, 2021c). People with *tuberculosis* have 5–10% life-time risk of falling ill and without treatment there is a 45% risk of death (WHO, 2021c). Among people living with HIV, *tuberculosis* remains a primary cause of death as without adequate treatment nearly all die (WHO, 2021a,c).

Rilpivirine is a NNRTI drug to treat HIV infection, and alongside other antiretrovirals it increases the life expectancy of people living with HIV to similar levels of their HIV negative peers. Rilpivirine is commercially available combined with emtricitabine and tenofovir, or combined with dolutegravir (Drugbank Rilpivirine, 2022). Additionally, it is approved as the first long-acting intramuscular HIV treatment when given together with cabotegravir; oral cabotegravir and rilpivirine are given during lead-in therapy, or for bridging specific clinical scenarios (FDA, 2022).

Rifapentine can be given daily as substitution for rifampicin, to treat active *tuberculosis* (WHO, 2021b; Dorman et al., 2021; CDC, 2022) and as prophylaxis in combination with isoniazid weekly for 3 months (3HP) or daily for a month (1HP) (FDA, 2010; WHO, 2020). 3HP and 1HP shortens the treatment of latent *tuberculosis* and decreases pill burden compared to the six or 9 months of daily isoniazid (6H/9H) or 3-month daily isoniazid with rifampicin (3HR).

Rifamycins (rifampicin, rifapentine, rifabutin) are antibiotics to treat *tuberculosis*. However, they are metabolic inducers that can potentially interact with some antiretrovirals. Rifapentine promotes the synthesis of enzymes, namely CYP3A4, which is the primary metabolising enzyme of rilpivirine, leading to a potential drug-drug interaction (DDI) if taken together (FDA, 2011a; Williamson et al., 2013).

Physiologically based pharmacokinetic (PBPK) modelling is a mathematical approach that aims to predict the potential magnitude of DDIs prior or, in some occasions, as replacement of clinical trials, among other applications (FDA, 2018). PBPK modelling mechanistically describes a drug's pharmacokinetic behaviour by combining physiology, population, and drug properties (FDA, 2020). It comprises of multiple compartments each representing a primary body organ which are then interconnected by the arterial and venous systems, mimicking the physiological composition (Nestorov, 2003). This technique permits exploring potential scenarios that otherwise would not be feasible due to ethical or logistical constraints (Zhuang and Lu, 2016).

In this *in silico* study, we aimed to investigate the DDI magnitude between daily oral rilpivirine 25 mg with either daily 600 mg or weekly 900 mg rifapentine.

Materials and methods

A cohort of 100 adults (50% female) was generated between the age of 18 and 60. No ethic approval was required as this study was based on virtual patients. The PBPK model was designed in Simbiology (Matlab version 2018a). The following assumptions were made: 1) well-stirred compartments with instant distribution of the drug; 2) no drug absorption from the colon; and 3) the model drug transport into tissues was blood-flow limited.

Anthropometry

Anatomical properties were randomised following a normal distribution using the height from CDC (2020) and BMI from de la Grandmaison et al. (2001). From these predefined characteristics, weight was the product of BMI divided by height square and body surface area was calculated with the Du Bois formula. Organ volumes were the product of organ density (Brown et al., 1997) and organ weight (Bosgra et al., 2012). Blood flows connected the organ compartments and they were derived from the total cardiac output (Brown et al., 1997).

Intestinal absorption

A previously defined compartmental absorption and transit model were used to represent the oral absorption (Yu and Amidon, 1999). The drug absorption rate constant (K_a) was either derived from clinical data, retrograde calculation from effective permeability (P_{eff}) or using Caco-2 cells. The parameters are described in Table 1. Additionally, a tablet disintegration rate (K_{disin}) was included in rifapentine's absorption.

Intestinal metabolism

Intestinal clearance (L/h) was implemented using Eq. 1 for rilpivirine, midazolam and doravirine, the latter two drugs are used for the model qualification, and using Eq. 2 for rifapentine.

$$CL_{gut} = CL_{int,3A4} \cdot Ab_{3A4,intestines} \cdot MPPGI \cdot WT_{intestines} \cdot \frac{10^3 \cdot 60}{10^6} \cdot EnzAct_{3A4} \quad (1)$$

$$CL_{gut} = CL_{int,HLM} \cdot MPPGI \cdot WT_{intestines} \cdot \frac{10^3 \cdot 60}{10^6} \cdot AutoInd_{HLM} \quad (2)$$

Where $CL_{int,3A4}$ is the intrinsic clearance for CYP3A4, and $CL_{int,HLM}$ is the intrinsic clearance for rifapentine. $Ab_{3A4,intestines}$ is the abundance of CYP3A4 in the intestine (43 ± 8.6 pmol enzyme/mg microsome) (Paine et al., 1997), MPPGI is the microsomal protein per Gram of intestine (2.7 ± 0.49 mg microsome/g protein) (Paine et al., 1997), $WT_{intestines}$ is the intestine weight in kilograms, and $EnzAct_{3A4}$ and $AutoInd_{HLM}$ are the relative increases in enzyme activity.

Hepatic metabolism

CYP3A4 contributed to rilpivirine, midazolam and doravirine metabolism. Hepatic metabolism (CL_{hep}) was calculated considering the CYP3A4 *in vitro* intrinsic clearance ($CL_{int,3A4}$) (Eq. 3) and was scaled to the whole liver. When

TABLE 1 Summary of physicochemical and *in vitro* data for rilpivirine, rifapentine, midazolam and doravirine.

Property	Rilpivirine	Rifapentine	Midazolam	Doravirine
Physicochemical properties				
MW (g/mol)	366.4 (NCBI, 2022b)	877.04 (FDA, 2010)	325.6 (NCBI, 2022a)	425.7 (FDA, 2016)
$LogP_{o:w}$	4.86 (Drugbank Rilpivirine, 2022)	4 (DrugBank Rifapentine, 2022)	3.89 (DrugBank Midazolam, 2022)	3.51 (DrugBank Doravirine, 2022)
f_u	0.003 (FDA, 2011b)	0.023 (FDA, 2010)	0.031 (Gertz et al., 2010)	0.24 (FDA, 2016)
pKa1	5.6 (Drugbank Rilpivirine, 2022)	6.99 (DrugBank Rifapentine, 2022)	6.57 (DrugBank Midazolam, 2022)	9.47 (FDA, 2016)
pKa2	NA	7.88 (DrugBank Rifapentine, 2022)	NA	NA
R	0.7 (FDA, 2011b)	0.56 (Reith et al., 1998)	0.55 (Gertz et al., 2010)	1 (FDA, 2016)
Caco-2 permeability (10^{-6} cm/s)	12 (FDA, 2011b)	NA	NA	NA
P_{eff} (10^{-4} cm/s)	NA	NA	NA	3.11 (FDA, 2016)
K_a (h^{-1})	NA	2 (Savic et al., 2014)	3.18 (van Rongen et al., 2015)	NA
Solubility (mg/L)	18.5 (kommavarapu et al., 2015)	213 (Dooley et al., 2012)*	NA	58.8 (Zhang and Pike, 2021)*
K_{disin} (h^{-1})	NA	0.5	NA	NA
Bioavailability (%)	NA	NA	45 (DrugBank Midazolam, 2022)	64 (FDA, 2016)
Metabolism, elimination and induction data				
$CL_{int,3A4}$ CYP3A4 (uL/min/pmol)	6.81 (Aouri et al., 2017)** $_{liver}$	NA	1.7 $_{gut}$ 2.73 $_{liver}$ (Gertz et al., 2010)	1.5 (Khalilieh et al., 2020)** $_{gut}$ 0.03** $_{liver}$ (Khalilieh et al., 2020)
$CL_{int,HLM}$ (uL/min/mg)	NA	6.9 $_{liver\ and\ gut}$ (Nakajima et al., 2011)	NA	NA
CL_R (L/h)	NA	NA	NA	0.57 (FDA, 2016)
$EC_{50,3A4}$ (mg/L)	NA	0.8 (McGinnity et al., 2009)	NA	NA
$E_{max,3A4}$ (fold)	NA	13 (McGinnity et al., 2009)	NA	NA
$K_{deg,3A4}$ (h^{-1})	NA	0.024 (Ramsden et al., 2015)	NA	NA
$EC_{50,HLM}$ (mg/L)	NA	4.27 (Hibma et al., 2020)	NA	NA
$E_{max,HLM}$ (fold)	NA	0.73 (Hibma et al., 2020)	NA	NA
γ	NA	10 (Hibma et al., 2020)	NA	NA
$K_{deg,HLM}$ (h^{-1})	NA	0.00587 (Hibma et al., 2020)	NA	NA
Distribution data				
$V_{d,CF}$	NA	0.16	0.2	0.05

CL_{int}, intrinsic clearance; CL_R, renal clearance; CYP, cytochrome P450; EC_{50}, half maximum effect concentration; E_{max}, maximum attainable effect; f_u, fraction unbound in plasma; γ, Hill coefficient; HLM, human liver microsomes (rifapentine's clearance autoinduction); K_a, absorption rate; K_{deg}, degradation rate; K_{disin}, disintegration rate; log $P_{o:w}$, partition coefficient between octanol and water; MW, molecular weight; NA, not applicable; P_{eff}, effective permeability; pK_a, logarithmic value of the dissociation constant; R, blood-to-plasma drug ratio; $V_{d,CF}$, volume of distribution correction factor.

*Rifapentine's solubility has been increased by x10 (original data 21.3 mg/L) and doravine's solubility has been increased by x3 (original data 19.6 mg/L) to fit the PK, profile.

**Retrograde calculation.

$CL_{int,3A4}$ data was unavailable, the hepatic metabolism was estimated using a retrograde calculation from the systemic clearance and absolute bioavailability.

$$CL_{hep} = CL_{int,3A4} \cdot Ab_{3A4,liver} \cdot MPPGL \cdot WT_{liver} \cdot \frac{10^3 \cdot 60}{10^6} \cdot EnzAct_{3A4} \quad (3)$$

Where $Ab_{3A4,liver}$ is the abundance of CYP3A4 in the liver (138.92 ± 27.78 pmol/mg microsomes) (Barter et al., 2006), MPPGL is the microsomal protein per gram of liver, and WT_{liver} is the liver weight in kilograms. MPPGL was normally distributed using Eq. 4 and a standard deviation of ± 4 mg microsome/g protein (Barter et al., 2008), where age is expressed in years.

$$MPPGL = 10^{1.407+0.0158 \cdot Age - 0.00038 \cdot Age^2 + 0.0000024 \cdot Age^3} \quad (4)$$

The CYP3A4 induction was represented as a relative increase of enzyme activity ($EnzAct_{3A4}$), considering the differential rate of synthesis and degradation of CYP3A4 ($K_{deg,3A4}$) using Eq. 5:

$$\frac{d(EnzAct_{3A4})}{dt} = K_{deg,3A4} \cdot (1 + INDSYN_{3A4}) - K_{deg,3A4} \cdot EnzAct_{3A4} \quad (5)$$

Where $K_{deg,3A4}$ is 0.024 h^{-1} (Ramsden et al., 2015), and $INDSYN_{3A4}$ is the induction of CYP3A4 enzyme synthesis (Eq. 6):

$$INDSYN_{3A4} = \frac{E_{max} \cdot C_p \cdot f_u}{EC_{50} + (C_p \cdot f_u)} \quad (6)$$

Where E_{max} is the maximum fold effect, EC_{50} is the rifapentine's concentration that elicits half of the maximum effect (McGinnity et al., 2009), C_p is the plasma concentration and f_u is the fraction unbound in plasma.

The Arylacetamide Deacetylase (AADAC) was the primary metabolising enzyme for rifapentine. Hepatic metabolism (CL_{hep}) was calculated considering the deacetylase activity in human liver microsomes ($CL_{int,HLM}$) using Eq. 7 (Nakajima et al., 2011).

$$CL_{hep} = CL_{int,HLM} \cdot MPPGL \cdot WT_{Liver} \cdot \frac{10^3 \cdot 60}{10^6} \cdot AutoInd_{HLM} \quad (7)$$

Where $AutoInd_{HLM}$ is the relative increase in the acetylase enzyme according to Hibma et al. (2020) The model consisted of an indirect response semi-mechanistic enzyme-turnover model, where the synthesis deacetylase rate was affected by $INDSYN_{HLM}$ (Eq. 8).

$$\frac{d(AutoInd_{HLM})}{dt} = K_{deg,HLM} \cdot (1 + INDSYN_{HLM}) - K_{deg,HLM} \cdot AutoInd_{HLM} \quad (8)$$

Where K_{deg} is the enzyme degradation rate (K_{deg} 0.00587 h^{-1}) and $INDSYN_{HLM}$ is the induction of rifapentine's metabolism (Eq. 9) and γ is the Hill coefficient:

$$INDSYN_{HLM} = \frac{E_{max} \cdot C_p{}^{\gamma}}{EC_{50}{}^{\gamma} + C_p{}^{\gamma}} \quad (9)$$

The total systemic clearance was the sum of the hepatic metabolism (CL_{hep}) limited by the hepatic blood flow and renal clearance (CL_R).

Distribution

The total volume of distribution (V_{ss}) was calculated following Poulin and Theil (2002) work. However, rifapentine, midazolam and doravirine needed a correction factor applied to the volume of distribution ($V_{d,CF}$) to match the clinical parameter; $V_{d,CF}$ was identified *via* fitting the observed PK profile.

Model qualification: PK simulations

The PK profiles of rilpivirine and rifapentine were simulated to verify the performance of the PBPK models. Clinically relevant doses for each drug were simulated: once daily oral rilpivirine 25 mg, once daily oral rifapentine 600 mg and once weekly oral rifapentine 900 mg. The predicted PK values of the PBPK model were compared to the typical population estimates from clinical studies (Aouri et al., 2017; Hibma et al., 2020). If the PK parameters were not reported, these were extracted from PK graphs using the Plot Digitizer Tool (plotdigitizer.sourceforge.net). The model performance was successfully verified if the simulated values were within 2-fold range of the reported clinical values and the absolute average-fold error (AAFE) was below 2 (Eq. 10).

$$AAFE = 10^{\left|\frac{\sum \log \frac{Predicted}{Observed}}{N}\right|} \quad (10)$$

Model qualification: DDI simulations

4The rifapentine model was verified against clinical DDI data with CYP3A4 sensitive substrates, midazolam and doravirine. The DDI model was validated using two studies: one using daily rifapentine at ascending doses (5, 10, 15, and 20 mg/kg) with a single dose of midazolam 15 mg and the other using weekly rifapentine 900 mg and isoniazid 900 mg with doravirine 100 mg twice daily (Dooley et al., 2012; Lam et al., 2020). To verify the simulations, the dose and schedule were matched to the DDI study design, with the exception of the daily rifapentine, which was simulated as a 600 mg fixed-dose instead of multiple doses dependant on weight. This is because the daily rifapentine study showed a similar decrease of AUC and Cmax of midazolam across the four escalating doses of rifapentine which ranged from 91 to 93% and 82–87%, respectively (Dooley et al., 2012). In addition, the dose was fixed because most studies with rifapentine do not show a body weight dependency (Savic et al., 2017; Hibma et al., 2020; Pham et al., 2022). Therefore, to verify the midazolam-rifapentine DDI, a fixed dose of 600 mg was used for simplicity. Isoniazid was omitted in the validation of the doravirine-rifapentine DDI model (vide discussion). The DDI model performance was evaluated by comparing the observed and simulated PK parameter values of the substrate with the CYP3A4 modulator, and the observed and simulated percentage decrease resulting from the PK fold of rilpivirine with and without rifapentine. Similarly, to the PK simulations, the DDI simulations were successfully validated if the values were within 2-fold range of the reported clinical values and if the AAFE was equal or below 2.

Model application: DDI prediction of rilpivirine with rifapentine

The verified model was used to predict the effect of either daily or weekly rifapentine on daily rilpivirine in a virtual population. The protocol consisted of 14 days daily dose of rilpivirine alone to reach steady state concentrations, followed by 14 days of daily dose of rilpivirine with either daily or weekly dose of rifapentine and 14 days

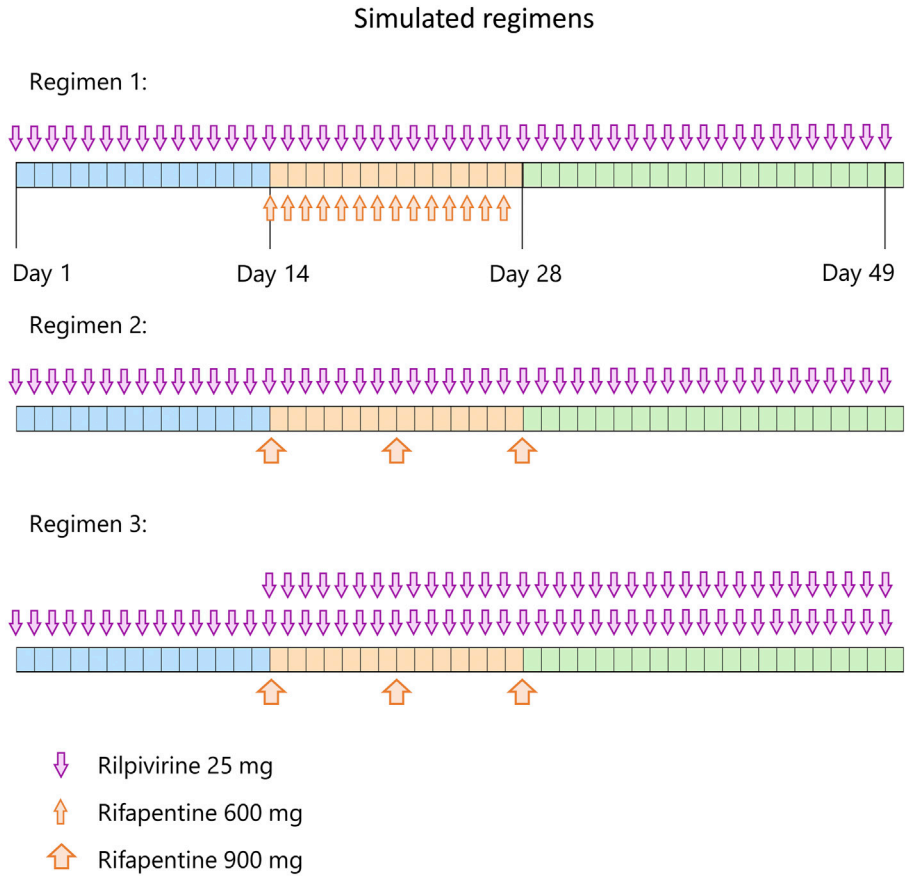

FIGURE 1
Simulated regimens. Each regimen starts with 14 days of rilpivirine 25 mg once daily (blue period), followed by 14 days (orange period) of rilpivirine 25 mg once daily and 600 mg rifapentine once daily on regimen 1, rilpivirine 25 mg once daily and once weekly 900 mg rifapentine on regimen 2, and rilpivirine 50 mg once daily and once weekly 900 mg rifapentine on regimen 3. On the third period (green), rifapentine's administration is ceased but rilpivirine is maintained with the same dose strategy as the previous period during 21 days.

more of daily dose of rilpivirine alone. To further evaluate treatment options, an additional 25 mg daily dose adjustment on rilpivirine was simulated right after the initiation of the weekly rifapentine's regimen to identify if it could be an alternative to circumvent the potential DDI (Figure 1).

Results

Model qualification

The PBPK model was qualified successfully against clinical data for rifapentine 600 mg daily and 900 mg weekly with an average (min-max) AAFE of 1.20 (1.00–1.59) for AUC, C_{max}, C_{trough}, CL/F, $t_{1/2}$, and V_{ss}/F (Hibma et al., 2020). The rifapentine model included the autoinduction of its own metabolism. In line with the literature, the simulations showed a clearance increase of 71% in the daily regimen, where it reached its maximum potential, and minimal increase of clearance (30%) in the weekly regimen (Hibma et al., 2020).

Rilpivirine was qualified against clinical data for rilpivirine 25 mg daily at steady state (Aouri et al., 2017). All parameters were within the acceptance criteria with an AAFE of 1.12 (1.04–1.22).

To qualify the induction of CYP3A4 by rifapentine, midazolam was used as a single 15 mg dose with and without rifapentine daily 600 mg steady state and doravirine 100 mg twice daily alone and also after co-administration of weekly 900 mg rifapentine. The midazolam-rifapentine yielded an AAFE of 1.25 (1.00–1.74) and the doravirine-rifapentine of 1.27 (1.04–1.89), all in agreement with the acceptance criteria.

The validation is outlined in Supplementary Tables S1–S9 and Supplementary Figures S1–S7, available as Supplementary data.

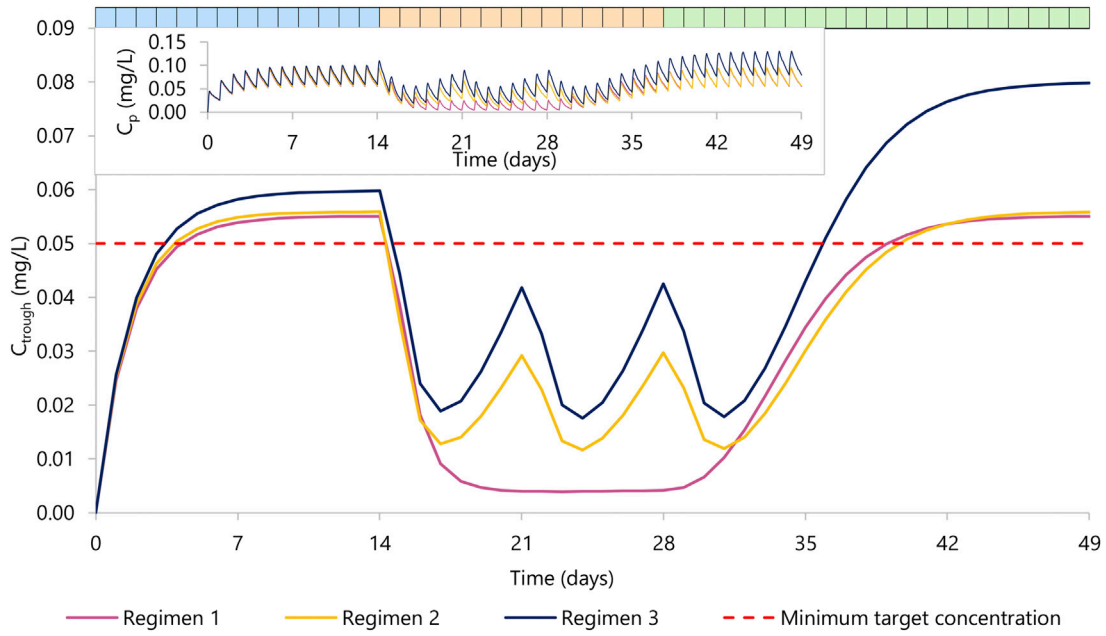

FIGURE 2
Rilpivirine C_{trough} concentration over time. Regimen 1 (violet) represents 14 days of rilpivirine 25 mg daily dose (period one in blue), 14 days of rilpivirine 25 mg daily dose with rifapentine 600 mg daily dose (period two in orange), and 21 days of rilpivirine 25 mg daily dose (period three in green). Regimen 2 (yellow) represents 14 days of rilpivirine 25 mg daily dose (period 1), 14 days of rilpivirine 25 mg daily dose with rifapentine 900 mg weekly dose, a total of three doses) (period 2), and 21 days of rilpivirine 25 mg daily dose (period 3). Regimen 3 (dark blue) represents 14 days of rilpivirine 25 mg daily dose (period 1), 14 days of rilpivirine 50 mg daily dose with rifapentine 900 mg weekly dose a total of three doses (period 2), and 21 days of rilpivirine 50 mg daily dose (period 3). The red dashed line represents the minimum target concentration for rilpivirine. The top left corner contains the mean plasma concentration PK profile for rilpivirine for each regimen.

TABLE 2 Predicted PK parameters of orally administered rilpivirine with and without rifapentine in multiple dosing regimens.

	RPV 25 mg q24 h alone	Regimen 1		Regimen 2				Regimen 3			
PK parameter	Steady state	Day 5		Day 3		Day 7		Day 3		Day 7	
	Mean	Mean	% Change	Mean	% Change	Mean	% Change	Mean	% Change	Mean	% Change
$AUC_{0\text{-}24h}$ (mg/L·h)	1.93	0.32	−83	0.62	−68	0.87	-55	1.03	−47	1.42	−26
C_{max} (mg/L)	0.10	0.027	−73	0.044	−57	0.058	-43	0.060	−41	0.081	−21
C_{trough} (mg/L)	0.06	0.005	−92	0.014	−78	0.020	-68	0.030	−51	0.043	−30
CL/F (L/h)	29.0	77.7	168	40.0	38	57.7	99	24.3	−16	35.1	21
$t_{1/2}$ (h)	12.9	8.3	−36	11.8	−9	12.5	-3	20.2	56	21.2	64
V_{ss}/F (L)	540	928	72	683	26	1,039	92	708	31	1,076	99

Regimen 1: RPV, 25 mg q24 h + RFP, 600 mg q24 h.
Regimen 2: RPV, 25 mg q24 h + RFP, 900 mg q7d.
Regimen 3: RPV, 50 mg q24 h + RFP, 900 mg q7d.
AUC_{0-24h}, the area under the curve over 24 h; C_{max}, maximum plasma concentration; C_{trough}, plasma concentration before dose; CL/F, apparent clearance; $t_{1/2}$, half-life; V_{ss}/F, apparent volume of distribution. RPV, rilpivirine; RFP, rifapentine. Day 5 after RFP, dose is the nadir for regimen 1 and day 3 is the nadir for regimen 2 and 3. Day 7 corresponds to the day before administering weekly rifapentine. Percentage change is compared to rilpivirine 25 mg q24 h alone.

Model predictions

Results are summarized in Figure 2 and Table 2.

In the regimen 1, we simulated the administration of rilpivirine 25 mg daily for 14 days (period 1), followed by the concomitant administration of daily rifapentine 600 mg for 14 days (period 2), and on day 28, we ceased the administration of rifapentine and continued with rilpivirine 25 mg once daily alone for 21 additional days (period 3). Within the first 3 days of concomitant administration of daily rifapentine 600 mg, rilpivirine's plasma concentration (C_p) showed a linear but steep decrease. After the first dose of rifapentine, the values of $AUC_{0\text{-}24}$ and C_{trough} for rilpivirine were reduced by 18% and 37%, by day 2 they were reduced by 51% and 71%, and by day 3 72% and 85%, respectively. On the fifth day, the plateau maximum effect was observed, with reductions in $AUC_{0\text{-}24}$ and C_{trough} of 83% and 92% (C_{trough} = 0.005 mg/L), respectively and remained similar until the cease of rifapentine at the start of period 3. In period 3, the plasma concentrations of rilpivirine slowly recovered over time, with more than 95% restored after 14 days of the last rifapentine dose.

In the regimen 2, a similar decrease was observed on the simulated weekly rifapentine 900 mg with rilpivirine. Period one consisted of once daily 25 mg rilpivirine, period two of once daily 25 mg rilpivirine with once weekly 900 mg rifapentine, a total of three doses, and period three of once daily 25 mg rilpivirine. The maximum effect was achieved on day 3 with reductions on the $AUC_{0\text{-}24}$ and C_{trough} by 68% and 92% (C_{trough} = 0.013 mg/L). Shortly after, as rifapentine's C_p declined, rilpivirine's C_p slowly recovered; but prior to the following weekly dose, $AUC_{0\text{-}24}$ and C_{trough} were still reduced by 47% and 53% (C_{trough} = 0.029 mg/L). After the second dose, rilpivirine reached its maximum induction at day 3 after rifapentine's dose. Analogously to regimen 1, rilpivirine C_p was restored to more than 95% its original C_p after the last rifapentine dose.

Regimen three evaluated a double dose administration of rilpivirine; identical to regimen two except for an additional 25 mg rilpivirine daily dose on period two and 3. The PK profile was comparable to regimen 2, with $AUC_{0\text{-}24}$ and C_{trough} slightly higher due to the increase of dose. Maximum induction was also reached on day 3 after rifapentine's first dose, with a simulated $AUC_{0\text{-}24}$ and C_{trough} reduced by 66% and 69% (C_{trough} = 0.019 mg/L) compared to the standard regimen. Considering that in period three rilpivirine is still administered as a double dose, minimum target concentration is reached earlier on day 8 after rifapentine's cessation.

Discussion

The DDI between rilpivirine and rifapentine has not yet been clinically studied, although it has been with rifampicin and rifabutin, two other rifamycins (FDA, 2011a). Rifapentine is a stronger CYP3A4 inducer than rifabutin but weaker than rifampicin; for example, rifapentine decreases indinavir's AUC by 70%, rifampicin by 92% while rifabutin by 34% (Burman et al., 2001). This PBPK model suggests an AUC and C_{trough} decrease of rilpivirine by 83 and 92% at its maximum induction when administered with daily oral rifapentine. These findings are comparable to the rifampicin-rilpivirine interaction, where the AUC and C_{trough} decreased by 80% and 89%, respectively (Ford et al., 2011). Considering the clinical data provided by the FDA, rifampicin and rifabutin coadministration with rilpivirine is contraindicated (FDA, 2011a). However, a double dose of rilpivirine might be sufficient to overcome the DDI with rifabutin, with rilpivirine doubled at least 2 weeks after rifabutin's cessation (Liverpool HIV Drug Interactions, 2022b).

In this PBPK study we aimed to identify the DDI magnitude between rilpivirine and rifapentine. The PBPK model showed a strong DDI between rilpivirine and daily rifapentine and less prominent DDI when rifapentine was administered weekly. However, the decrease on key PK parameters were very significant in both scenarios, including when rilpivirine dose was virtually doubled. In this case, the PBPK model suggested that the coadministration of rilpivirine and rifapentine, either daily or weekly, is contraindicated.

There has been an increased interest in studying DDIs *via* PBPK modelling as it allows the simulation of multiple scenarios with the ultimate goal of informing regulatory agencies, prioritise and design clinical trials, as well as informing healthcare professionals on how to manage DDIs. However, some parameters are not yet fully described, making it difficult to mathematically characterise them. In this model, we considered that all rilpivirine was cleared due to CYP3A4 metabolism without inclusion of renal clearance, as there is limited information on drug metabolism. In the same way, rilpivirine bioavailability was assumed to be 100% due to lack of clinical data. Because some physiological processes are not well understood, *in vitro* data occasionally did not match the PK profile accurately, and data had to be fitted or calculated in retrograde. This model captured the DDI mechanistically and in a time dependant manner, including the synthesis and degradation of CYP3A4 as well as the autoinduction of rifapentine's clearance although it did not account for potential interaction with transporters. An *in vitro* study showed a 3-fold increase in ABCB1 relative gene expression at the highest rifapentine concentration (10 uM), which encodes for p-glycoprotein, while no change for OATP1B1 and OATP1B3 transporters (Williamson

et al., 2013). A DDI between moxifloxacin and three times weekly rifapentine 900 mg showed a decrease on the moxifloxacin's AUC by 17.2%, the authors suggested that transporters could have played a role as moxifloxacin is not metabolised by CYP P450 isoforms but that was not assessed (Dooley et al., 2008). There is little evidence that transporters play an important role on rifapentine's DDI. Genetic polymorphisms were not assessed in this PBPK model, although Aouri et al. (2017) demonstrated that CYP3A4*22 polymorphism among others did not affect rilpivirine's pharmacokinetics.

While 1HP and 3HP treatments include isoniazid and rifapentine, the DDI model omitted isoniazid PK. Isoniazid presents an *in vitro* inhibition constant (Ki) of 51.8–75.9 μmol/L (7.1–10.4 mg/L) (Desta et al., 2001; Wen et al., 2002) and desirable C_p levels range between 3 and 6 mg/L (Huerta-García et al., 2020). At therapeutic concentrations, theoretically 40% of the CYP3A activity is inhibited (Desta et al., 2001). Considering that rifapentine is a moderate to strong CYP3A inducer with a C_{max} more than ten times higher than its CYP3A EC_{50}, the overall DDI between isoniazid, rifapentine and a substrate is driven by the rifapentine induction effect.

Antiretroviral therapy (ART) including rilpivirine is highly advantageous as the fixed-dose combined pills are relatively small compared to the alternatives as well as the oral-lead in or substitute for missed doses of long-acting injectables antiretrovirals (Bennet, 2020). Nonetheless, rilpivirine presents higher rates of virologic failure in patients with high viral load (>100,000 copies/mL) or ≤95% adherence, relative to patients taking efavirenz (Bennet, 2020). Maintenance of adequate plasma concentrations is essential for optimal antiretroviral therapy. Current target trough concentration (C_{trough}) for rilpivirine is 0.05 mg/L (Néant et al., 2020), which is suggested as four times the concentration required for 90% inhibition (IC_{90} 0.012 mg/L) (Margolis et al., 2015). However, a recent study with rilpivirine based regimen have highlighted that the current C_{trough} target might need to be reassessed (Néant et al., 2019) and an optimal target C_{trough} of 0.07 mg/L is required to achieve virologic response, especially in pre-treated patients (Néant et al., 2020). This is further complicated considering that 11% of a population in Aouri et al. study did not reach a C_{trough} of 0.05 mg/L (Aouri et al., 2017). Considering the repurposed target concentration, many more would fall in subtherapeutic concentrations. Dose increase is usually done by 25 mg, as rilpivirine is only available in this dose (EMC, 2021). A practical example is the management of the DDIs with rifabutin where rilpivirine dose can be doubled to overcome the DDI (EMC, 2021). However, increasing the dose even further (x3-12 times) increases the risk of QTc prolongation as this phenomenon is dose dependant and should be avoided (Aouri et al., 2017).

This *in silico* study, suggests that co-administration of rifapentine with rilpivirine is contraindicated and replacement or inclusion of an additional antiretroviral therapy is recommended. Currently, 3HP is only recommended with raltegravir 400 mg twice daily or efavirenz 600 mg once daily for treatment of latent *tuberculosis* infection in people living with HIV (WHO, 2020). These drugs are good substitute candidates as raltegravir is primarily metabolised by UGT1A1 and efavirenz by CYP2B6 with marginal contribution of CYP3A4 (Ogburn et al., 2010). A study in 2014 showed a 71% AUC_{0-12} increase of raltegravir after 900 mg weekly rifapentine, which was tolerated and safe (Weiner et al., 2014). Differently, daily rifapentine treatment decreased raltegravir's C_{min} by 41%, which requires more clinical investigation (Weiner et al., 2014; Liverpool HIV Drug Interactions, 2022a). Podany et al. (2015) observed that 88% of participants taking efavirenz with 1HP maintained the minimum target concentration ≥1 mg/L and viral suppression. Recently, dolutegravir twice daily has proven safe and well tolerated with 3HP and 1HP. Dolutegravir's AUC decreased by 26% when co-administered with 3HP, suggesting that dolutegravir could be administered without dose adjustments but a double dose is recommended in individuals at risk of treatment failure or blips (Dooley et al., 2020). A double dose of dolutegravir with 1HP showed concentrations higher than dolutegravir once daily alone and was suggested to be safe (Imperial et al., 2022). As seen in the validation study of weekly rifapentine, doravirine 100 mg twice daily could potentially be used with 3HP (Lam et al., 2020). On the other hand, bictegravir is contraindicated (Arora et al., 2021; Liou et al., 2021) and there is no data with protease inhibitors or darunavir yet.

Conclusion

This modelling approach provides a potential tool to study the magnitude of DDIs of daily and weekly regimens which can help designing clinical trials when necessary or avoid them when the interaction is unmanageable. This PBPK study suggests that rilpivirine antiretroviral therapy does not reach sufficient exposure to be managed with 3HP or 1HP on its own and potentially an additional antiretroviral regimen should be included. Alternatively, some antiretrovirals are manageable both with 3HP and 1HP, and others can only be managed with 3HP as the DDI is less marked. 3HP is preferred if it does not require switching therapies and 1HP if it does and it is a suitable regimen. This PBPK model is characterised by some limitations including *in vitro* data availability and description of processes involved in drug disposition such as drug transport that can hinder the ability to accurately predict complex scenarios. Nonetheless, it is based on a detailed description of the human physiology, drug metabolism, and PK processes representing a powerful tool to explore different scenarios and aid clinicians on how to manage DDIs.

Data availability statement

The raw data supporting the conclusion of this article will be made available by the authors, without undue reservation.

Author contributions

All authors contributed to the overall concept and design. SG-C performed the modelling analysis. SG-C wrote the manuscript with support from MM, RB, SK, and MS. All authors reviewed and contributed to the final manuscript.

Funding

This project is funded by Engineering and Physical Sciences Research Council (EPSRC).

Acknowledgments

This work has been presented at the American Conference of Pharmacometrics 13, Denver, CO, United States, 2022 (Poster T-058).

Conflict of interest

The authors declare that the research was conducted in the absence of any commercial or financial relationships that could be construed as a potential conflict of interest.

Publisher's note

All claims expressed in this article are solely those of the authors and do not necessarily represent those of their affiliated organizations, or those of the publisher, the editors and the reviewers. Any product that may be evaluated in this article, or claim that may be made by its manufacturer, is not guaranteed or endorsed by the publisher.

Supplementary material

The Supplementary Material for this article can be found online at: https://www.frontiersin.org/articles/10.3389/fphar.2022.1076266/full#supplementary-material

References

Aouri, M., Barcelo, C., Guidi, M., Rotger, M., Cavassini, M., Hizrel, C., et al. (2017). Population pharmacokinetics and Pharmacogenetics analysis of rilpivirine in HIV-1-Infected individuals. *Antimicrob. Agents Chemother.* 61. doi:10.1128/aac.00899-16

Arora, P., Collins, S., Martin, H., Zhang, X., Mak, L., Ling, J., et al. (2021). "Drug interactions with once-daily B F/TAF in combination with once-weekly rifapentine," in *Virtual conference on retroviruses and opportunistic infections*.

Barter, Z. E., Chowdry, J. E., Harlow, J. R., Snawder, J. E., Lipscomb, J. C., and Rostami-Hodjegan, A. (2008). Covariation of human microsomal protein per gram of liver with age: Absence of influence of operator and sample storage may justify interlaboratory data pooling. *Drug Metab. Dispos.* 36 (12), 2405–2409. doi:10.1124/dmd.108.021311

Barter, Z. E., Rowland Yeo, K., Tucker, G. T., and Rostami-Hodjegan, A. (2006). *A meta-analysis of CYP3A4 abudance in human liver: Use of different standards contributes to apparent heterogeneity in reported values*. [Online]. Available: https://www.certara.com/app/uploads/Resources/Posters/Barter_2006_ACCP_CYP3A4.pdf (Accessed 05 13, 2022).

Bennet, J. E. (2020). *Principles and practice of infectious diseases, chapter 128: Antiretroviral therapy for human immunodeficiency virus infection. Ninth Edition ed.* Elsevier, 1739–1760.

Bosgra, S., van Eijkeren, J., Bos, P., Zeilmaker, M., and Slob, W. (2012). An improved model to predict physiologically based model parameters and their inter-individual variability from anthropometry. *Crit. Rev. Toxicol.* 42 (9), 751–767. doi:10.3109/10408444.2012.709225

Brown, R. P., Delp, M. D., Lindstedt, S. L., Rhomberg, L. R., and Beliles, R. P. (1997). Physiological parameter values for physiologically based pharmacokinetic models. *Toxicol. Ind. Health* 13 (4), 407–484. doi:10.1177/074823379701300401

Burman, W. J., Gallicano, K., and Peloquin, C. (2001). Comparative pharmacokinetics and pharmacodynamics of the rifamycin antibacterials. *Clin. Pharmacokinet.* 40 (5), 327–341. doi:10.2165/00003088-200140050-00002

CDC (2020). *Anthropometric reference data for children and adults: United States, 2015–2018*. [Online]. Available: https://www.cdc.gov/nchs/fastats/body-measurements.htm (Accessed 05 11, 2022).

CDC (2022). *Treatment for TB disease*. [Online]. Available: https://www.cdc.gov/tb/topic/treatment/tbdisease.htm (Accessed 11 16, 2022).

de la Grandmaison, G. L., Clairand, I., and Durigon, M. (2001). Organ weight in 684 adult autopsies: New tables for a caucasoid population. *Forensic Sci. Int.* 119 (2), 149–154. doi:10.1016/s0379-0738(00)00401-1

Desta, Z., Soukhova, N. V., and Flockhart, D. A. (2001). Inhibition of cytochrome P450 (CYP450) isoforms by isoniazid: Potent inhibition of CYP2C19 and CYP3A. *Antimicrob. Agents Chemother.* 45 (2), 382–392. doi:10.1128/aac.45.2.382-392.2001

Dooley, K., Flexner, C., Hackman, J., Peloquin, C. A., Nuermberger, E., Chaisson, R. E., et al. (2008). Repeated administration of high-dose intermittent rifapentine reduces rifapentine and moxifloxacin plasma concentrations. *Antimicrob. Agents Chemother.* 52 (11), 4037–4042. doi:10.1128/aac.00554-08

Dooley, K. E., Bliven-Sizemore, E. E., Weiner, M., Lu, Y., Nuermberger, E. L., Hubbard, W. C., et al. (2012). Safety and pharmacokinetics of escalating daily doses of the antituberculosis drug rifapentine in healthy volunteers. *Clin. Pharmacol. Ther.* 91 (5), 881–888. doi:10.1038/clpt.2011.323

Dooley, K. E., Savic, R., Gupte, A., Marzinke, M. A., Zhang, N., Edward, V. A., et al. (2020). Once-weekly rifapentine and isoniazid for tuberculosis prevention in patients with HIV taking dolutegravir-based antiretroviral therapy: A phase 1/2 trial. *Lancet. HIV* 7 (6), e401–e409. doi:10.1016/s2352-3018(20)30032-1

Dorman, S. E., Nahid, P., Kurbatova, E. V., Phillips, P. P. J., Bryant, K., Dooley, K. E., et al. (2021). Four-month rifapentine regimens with or without moxifloxacin for tuberculosis. *N. Engl. J. Med.* 384 (18), 1705–1718. doi:10.1056/NEJMoa2033400

DrugBank Doravirine (2022). *DrugBank doravirine*. [Online]. Available: https://go.drugbank.com/drugs/DB12301 (Accessed September 12, 2022).

DrugBank Midazolam (2022). *DrugBank midazolam*. [Online]. Available: https://go.drugbank.com/drugs/DB00683 (Accessed September 12, 2022).

DrugBank Rifapentine (2022). *DrugBank rifapentine*. [Online]. Available: https://go.drugbank.com/drugs/DB01201 (Accessed May 19, 2022).

Drugbank Rilpivirine (2022). *Rilpivirine*. [Online]. Available: https://go.drugbank.com/drugs/DB08864 (Accessed October 19, 2022).

EMC (2021). *Edurant 25 mg film-coated tablets*.

FDA (2010). *Priftin (rifapentine) Tablets label*. [Online]. Available: https://www.accessdata.fda.gov/drugsatfda_docs/label/2010/021024s009lbl.pdf (Accessed 05 19, 2022).

FDA (2011a). *Edurant (rilpivirine) tablets label*. [Online]. Available: https://www.accessdata.fda.gov/drugsatfda_docs/label/2011/202022s000lbl.pdf (Accessed 07 25, 2022).

FDA (2011b). *Rilpivirine: Clinical pharmacology and biopharmaceutics review(s)*. [Online]. Available: https://www.accessdata.fda.gov/drugsatfda_docs/nda/2011/202022Orig1s000ClinPharmR.pdf (Accessed 05 19, 2022).

FDA (2016). *NDA multi-disciplinary review and evaluation – NDA 210806 and NDA 210807 doravirine (DOR) and DOR/3TC/DOR*. [Online]. Available: https://

www.accessdata.fda.gov/drugsatfda_docs/nda/2018/210806Orig1s000,%20210807Orig1s000MultidisciplineR.pdf (Accessed 09 15, 2022).

FDA (2018). *Program of physiologically-based pharmacokinetic and pharmacodynamic modeling (PBPK Program)*. [Online]. Available: https://www.fda.gov/about-fda/center-drug-evaluation-and-research-cder/program-physiologically-based-pharmacokinetic-and-pharmacodynamic-modeling-pbpk-program#:~:text=On%20August%2031%2C%202018%2C%20FDA%20issued%20the%20%E2%80%9C,applications%20%28BLAs%29%2C%20or%20abbreviated%20new%20drug%20applications%20%28ANDAs%29 (Accessed 06 16, 2022).

FDA (2020). *The use of physiologically based pharmacokinetic analyses - biopharmaceutics applications for oral drug product development, manufacturig changes, and controls guidance for industry*. C.f.D.E.a.R. (CDER).

FDA (2022). *CABENUVA (cabotegravir extended-release injectable suspension; rilpivirine extended-release injectable suspension), co-packaged for intramuscular use*. [Online]. Available: https://www.accessdata.fda.gov/drugsatfda_docs/label/2022/212888s003lbl.pdf (Accessed 06 22, 2022).

Ford, N., Lee, J., Andrieux-Meyer, I., and Calmy, A. (2011). Safety, efficacy, and pharmacokinetics of rilpivirine: Systematic review with an emphasis on resource-limited settings. *HIV AIDS (Auckl)* 3, 35–44. doi:10.2147/hiv.S14559

Gertz, M., Harrison, A., Houston, J. B., and Galetin, A. (2010). Prediction of human intestinal first-pass metabolism of 25 CYP3A substrates from *in vitro* clearance and permeability data. *Drug Metab. Dispos.* 38 (7), 1147–1158. doi:10.1124/dmd.110.032649

Hibma, J. E., Radtke, K. K., Dorman, S. E., Jindani, A., Dooley, K. E., Weiner, M., et al. (2020). Rifapentine population pharmacokinetics and dosing recommendations for latent tuberculosis infection. *Am. J. Respir. Crit. Care Med.* 202 (6), 866–877. doi:10.1164/rccm.201912-2489OC

Huerta-García, A. P., Medellín-Garibay, S. E., Ortiz-Álvarez, A., Magaña-Aquino, M., Rodríguez-Pinal, C. J., Portales-Pérez, D. P., et al. (2020). Population pharmacokinetics of isoniazid and dose recommendations in Mexican patients with tuberculosis. *Int. J. Clin. Pharm.* 42 (4), 1217–1226. doi:10.1007/s11096-020-01086-1

Imperial, M. Z., Luetkemeyer, A., Dawson, R., Cramer, Y., Rosenkranz, S., Swindells, S., et al. (2022). "Dolutegravir pharmacokinetics in people with HIV receiving daily 1HP for latent tuberculosis treatment (ACTG A5372) - abstract 78," in *Conference on retroviruses and opportunistic infections*.

Khalilieh, S., Yee, K. L., Sanchez, R., Stoch, S. A., Wenning, L., and Iwamoto, M. (2020). Clinical pharmacokinetics of the novel HIV-1 non-nucleoside reverse transcriptase inhibitor doravirine: An assessment of the effect of patient characteristics and drug-drug interactions. *Clin. Drug Investig.* 40 (10), 927–946. doi:10.1007/s40261-020-00934-2

kommavarapu, P., Maruthapillai, A., Palanisamy, K., and Sunkara, M. (2015). Preparation and characterization of rilpivirine solid dispersions with the application of enhanced solubility and dissolution rate. *Beni-Suef Univ. J. Basic Appl. Sci.* 4 (1), 71–79. doi:10.1016/j.bjbas.2015.02.010

Lam, E., Schaefer, J., Zheng, R., Zhan, T., and Kraft, W. K. (2020). Twice-daily doravirine overcomes the interaction effect from once-weekly rifapentine and isoniazid in healthy volunteers. *Clin. Transl. Sci.* 13 (6), 1244–1250. doi:10.1111/cts.12810

Liou, B. H., Cheng, C. N., Lin, Y. T., Lin, Y. J., Chuang, Y. C., Lin, K. Y., et al. (2021). Short-course daily isoniazid and rifapentine for latent tuberculosis infection in people living with HIV who received coformulated bictegravir/emtricitabine/tenofovir alafenamide. *J. Int. AIDS Soc.* 24 (11), e25844. doi:10.1002/jia2.25844

Liverpool HIV Drug Interactions (2022a). *Raltegravir with rifapentine interaction*. [Online]. Available: https://www.hiv-druginteractions.org/checker (Accessed 06 23, 2022).

Liverpool HIV Drug Interactions (2022b). *Rilpivirine with rifapentine*. [Online]. Available: https://www.hiv-druginteractions.org/checker (Accessed 06 24, 2022).

Margolis, D. A., Brinson, C. C., Smith, G. H. R., de Vente, J., Hagins, D. P., Eron, J. J., et al. (2015). Cabotegravir plus rilpivirine, once a day, after induction with cabotegravir plus nucleoside reverse transcriptase inhibitors in antiretroviral-naive adults with HIV-1 infection (LATTE): A randomised, phase 2b, dose-ranging trial. *Lancet. Infect. Dis.* 15 (10), 1145–1155. doi:10.1016/s1473-3099(15)00152-8

McGinnity, D. F., Zhang, G., Kenny, J. R., Hamilton, G. A., Otmani, S., Stams, K. R., et al. (2009). Evaluation of multiple *in vitro* systems for assessment of CYP3A4 induction in drug discovery: Human hepatocytes, pregnane X receptor reporter gene, and Fa2N-4 and HepaRG cells. *Drug Metab. Dispos.* 37 (6), 1259–1268. doi:10.1124/dmd.109.026526

Nakajima, A., Fukami, T., Kobayashi, Y., Watanabe, A., Nakajima, M., and Yokoi, T. (2011). Human arylacetamide deacetylase is responsible for deacetylation of rifamycins: Rifampicin, rifabutin, and rifapentine. *Biochem. Pharmacol.* 82 (11), 1747–1756. doi:10.1016/j.bcp.2011.08.003

NCBI (2022a). PubChem database, midazolam, CID = 4192 [Online]. Available at: https://pubchem.ncbi.nlm.nih.gov/compound/4192 (Accessed October 20, 2022).

NCBI (2022b). PubChem database, rilpivirine, CID = 6451164 [Online]. Available at: https://pubchem.ncbi.nlm.nih.gov/compound/rilpivirine (Accessed October 20, 2022).

Néant, N., Solas, C., Bouazza, N., Lê, M. P., Yazdanpanah, Y., Dhiver, C., et al. (2019). Concentration-response model of rilpivirine in a cohort of HIV-1-infected naive and pre-treated patients. *J. Antimicrob. Chemother.* 74 (7), 1992–2002. doi:10.1093/jac/dkz141

Néant, N., Lê, M. P., Bouazza, N., Gattacceca, F., Yazdanpanah, Y., Dhiver, C., et al. (2020). Usefulness of therapeutic drug monitoring of rilpivirine and its relationship with virologic response and resistance in a cohort of naive and pretreated HIV-infected patients. *Br. J. Clin. Pharmacol.* 86 (12), 2404–2413. doi:10.1111/bcp.14344

Nestorov, I. (2003). Whole body pharmacokinetic models. *Clin. Pharmacokinet.* 42 (10), 883–908. doi:10.2165/00003088-200342100-00002

Ogburn, E. T., Jones, D. R., Masters, A. R., Xu, C., Guo, Y., and Desta, Z. (2010). Efavirenz primary and secondary metabolism *in vitro* and *in vivo*: Identification of novel metabolic pathways and cytochrome P450 2A6 as the principal catalyst of efavirenz 7-hydroxylation. *Drug Metab. Dispos.* 38 (7), 1218–1229. doi:10.1124/dmd.109.031393

Paine, M. F., Khalighi, M., Fisher, J. M., Shen, D. D., Kunze, K. L., Marsh, C. L., et al. (1997). Characterization of interintestinal and intraintestinal variations in human CYP3A-dependent metabolism. *J. Pharmacol. Exp. Ther.* 283 (3), 1552–1562.

Pham, M. M., Podany, A. T., Mwelase, N., Supparatpinyo, K., Mohapi, L., Gupta, A., et al. (2022). Population pharmacokinetic modeling and simulation of rifapentine supports concomitant antiretroviral therapy with efavirenz and non-weight based dosing. *Antimicrob. Agents Chemother.* 66 (9), e0238521. doi:10.1128/aac.02385-21

Podany, A. T., Bao, Y., Swindells, S., Chaisson, R. E., Andersen, J. W., Mwelase, T., et al. (2015). Efavirenz pharmacokinetics and pharmacodynamics in HIV-infected persons receiving rifapentine and isoniazid for tuberculosis prevention. *Clin. Infect. Dis.* 61 (8), 1322–1327. doi:10.1093/cid/civ464

Poulin, P., and Theil, F. P. (2002). Prediction of pharmacokinetics prior to *in vivo* studies. 1. Mechanism-based prediction of volume of distribution. *J. Pharm. Sci.* 91 (1), 129–156. doi:10.1002/jps.10005

Ramsden, D., Zhou, J., and Tweedie, D. J. (2015). Determination of a degradation constant for CYP3A4 by direct suppression of mRNA in a novel human hepatocyte model, HepatoPac. *Drug Metab. Dispos.* 43 (9), 1307–1315. doi:10.1124/dmd.115.065326

Reith, K., Keung, A., Toren, P. C., Cheng, L., Eller, M. G., and Weir, S. J. (1998). Disposition and metabolism of 14C-rifapentine in healthy volunteers. *Drug Metab. Dispos.* 26 (8), 732–738.

Savic, R. M., Lu, Y., Bliven-Sizemore, E., Weiner, M., Nuermberger, E., Burman, W., et al. (2014). Population pharmacokinetics of rifapentine and desacetyl rifapentine in healthy volunteers: Nonlinearities in clearance and bioavailability. *Antimicrob. Agents Chemother.* 58 (6), 3035–3042. doi:10.1128/aac.01918-13

Savic, R. M., Weiner, M., MacKenzie, W. R., Engle, M., Whitworth, W. C., Johnson, J. L., et al. (2017). Defining the optimal dose of rifapentine for pulmonary tuberculosis: Exposure-response relations from two phase II clinical trials. *Clin. Pharmacol. Ther.* 102 (2), 321–331. doi:10.1002/cpt.634

van Rongen, A., Kervezee, L., Brill, M., van Meir, H., den Hartigh, J., Guchelaar, H. J., et al. (2015). Population pharmacokinetic model characterizing 24-hour variation in the pharmacokinetics of oral and intravenous midazolam in healthy volunteers. *CPT. Pharmacometrics Syst. Pharmacol.* 4 (8), 454–464. doi:10.1002/psp4.12007

Weiner, M., Egelund, E. F., Engle, M., Kiser, M., Prihoda, T. J., Gelfond, J. A., et al. (2014). Pharmacokinetic interaction of rifapentine and raltegravir in healthy volunteers. *J. Antimicrob. Chemother.* 69 (4), 1079–1085. doi:10.1093/jac/dkt483

Wen, X., Wang, J. S., Neuvonen, P. J., and Backman, J. T. (2002). Isoniazid is a mechanism-based inhibitor of cytochrome P450 1A2, 2A6, 2C19 and 3A4 isoforms in human liver microsomes. *Eur. J. Clin. Pharmacol.* 57 (11), 799–804. doi:10.1007/s00228-001-0396-3

WHO (2020). *WHO operational handbook on tuberculosis (Module 1 – prevention): Tuberculosis preventive treatment*. [Online]. Available: https://www.who.int/publications/i/item/9789240001503 (Accessed 06 23, 2022).

WHO (2021a). *HIV and tuberculosis*. [Online]. Available: https://www.who.int/westernpacific/health-topics/hiv-aids/hiv-and-tuberculosis (Accessed 09 17, 2022).

WHO (2021b). Treatment of drug-susceptible tuberculosis: Rapid communication [Online]. Available at: https://www.who.int/publications/i/item/9789240028678 (Accessed November 16, 2022).

WHO (2021c). Tuberculosis [Online]. Available at: https://www.who.int/news-room/fact-sheets/detail/tuberculosis (Accessed June 16, 2022).

Williamson, B., Dooley, K. E., Zhang, Y., Back, D. J., and Owen, A. (2013). Induction of influx and efflux transporters and cytochrome P450 3A4 in primary human hepatocytes by rifampin, rifabutin, and rifapentine. *Antimicrob. Agents Chemother.* 57 (12), 6366–6369. doi:10.1128/aac.01124-13

Yu, L. X., and Amidon, G. L. (1999). A compartmental absorption and transit model for estimating oral drug absorption. *Int. J. Pharm.* 186 (2), 119–125. doi:10.1016/s0378-5173(99)00147-7

Zhang, Y., and Pike, A. (2021). Pyridones in drug discovery: Recent advances. *Bioorg. Med. Chem. Lett.* 38, 127849. doi:10.1016/j.bmcl.2021.127849

Zhuang, X., and Lu, C. (2016). PBPK modeling and simulation in drug research and development. *Acta Pharm. Sin. B* 6 (5), 430–440. doi:10.1016/j.apsb.2016.04.004

frontiers | Frontiers in Pharmacology

TYPE Original Research
PUBLISHED 30 January 2023
DOI 10.3389/fphar.2022.1042756

OPEN ACCESS

EDITED BY
Simona Pichini,
National Institute of Health (ISS), Italy

REVIEWED BY
Rong Shi,
Shanghai University of Traditional Chinese Medicine, China
Annagiulia Di Trana,
Marche Polytechnic University, Italy

*CORRESPONDENCE
Xiu-Min Li,
XiuMin_Li@NYMC.edu

†These authors have contributed equally to this work

SPECIALTY SECTION
This article was submitted to Drug Metabolism and Transport, a section of the journal Frontiers in Pharmacology

RECEIVED 13 September 2022
ACCEPTED 23 December 2022
PUBLISHED 30 January 2023

CITATION
Li K, Yu X-H, Maskey AR, Musa I, Wang Z-Z, Garcia V, Guo A, Yang N, Srivastava K, Dunkin D, Li J-X, Guo L, Cheng Y-C, Yuan H, Tiwari R and Li X-M (2023), Cytochrome P450 3A4 suppression by epimedium and active compound kaempferol leads to synergistic anti-inflammatory effect with corticosteroid. *Front. Pharmacol.* 13:1042756. doi: 10.3389/fphar.2022.1042756

Cytochrome P450 3A4 suppression by epimedium and active compound kaempferol leads to synergistic anti-inflammatory effect with corticosteroid

Ke Li[1,2†], Xiu-Hua Yu[2,3†], Anish R. Maskey[2], Ibrahim Musa[2], Zhen-Zheng Wang[2,4], Victor Garcia[5], Austin Guo[5], Nan Yang[2,6], Kamal Srivastava[2,6], David Dunkin[7], Jun-Xiong Li[1], Longgang Guo[8], Yung-Chi Cheng[9], Haoliang Yuan[10], Raj Tiwari[2] and Xiu-Min Li[2,11]*

[1]Guangdong Hospital of Integrated Traditional Chinese and Western Medicine, Guangzhou University of Chinese Medicine, Foshan, China, [2]Department of Pathology, Microbiology and Immunology, New York Medical College, Valhalla, NY, United States, [3]Central Laboratory, Affiliated Hospital, Changchun University of Chinese Medicine, Changchun, China, [4]Academy of Chinese Medical Science, Henan University of Chinese Medicine, Zhengzhou, China, [5]Department of Pharmacology, New York Medical College, Valhalla, NY, United States, [6]General Nutraceutical Technology, Elmsford, NY, United States, [7]Department of Pediatrics, Division of Gastroenterology, Icahn School of Medicine at Mount Sinai, New York, NY, United States, [8]Guangzhou ImVin Pharmaceutical Co., Ltd., Guangzhou, China, [9]Department of Pharmacology, School of Medicine, Yale University, New Haven, China, [10]Jiangsu Key Laboratory of Drug Discovery for Metabolic Disease and State Key Laboratory of Natural Medicines, China Pharmaceutical University, Nanjing, China, [11]Department of Otolaryngology, Westchester Medical Center New York Medical College, Valhalla, NY, United States

Introduction: Cytochrome P450 (CYP) 3A4 is a major drug metabolizing enzyme for corticosteroids (CS). Epimedium has been used for asthma and variety of inflammatory conditions with or without CS. It is unknown whether epimedium has an effect on CYP 3A4 and how it interacts with CS. We sought to determine the effects of epimedium on CYP3A4 and whether it affects the anti-inflammatory function of CS and identify the active compound responsible for this effect.

Methods: The effect of epimedium on CYP3A4 activity was evaluated using the Vivid CYP high-throughput screening kit. CYP3A4 mRNA expression was determined in human hepatocyte carcinoma (HepG2) cells with or without epimedium, dexamethasone, rifampin, and ketoconazole. TNF-α levels were determined following co-culture of epimedium with dexamethasone in a murine macrophage cell line (Raw 264.7). Active compound (s) derived from epimedium were tested on IL-8 and TNF-α production with or without corticosteroid, on CYP3A4 function and binding affinity.

Results: Epimedium inhibited CYP3A4 activity in a dose-dependent manner. Dexamethasone enhanced the expression of CYP3A4 mRNA, while epimedium inhibited the expression of CYP3A4 mRNA and further suppressed dexamethasone enhancement of CYP3A4 mRNA expression in HepG2 cells ($p < 0.05$). Epimedium and dexamethasone synergistically suppressed TNF-α production

Abbreviations: CS, Corticosteroids; CKZ, Chuan Ke Zhi; CYP450, Cytochrome P450; CYP3A4, Cytochrome P450 3A4; DL, Drug-likeness; DMSO, Dimethyl sulfoxide; IL-1β, Interleukin-1β; IL-8, Interleukin-8; LPS, Lipopolysaccharide; OB, Oral bioavailability; TCMSP, Traditional Chinese Medicine Systems Pharmacology; TNF-α, Tumor Necrosis Factor.

by RAW cells ($p < 0.001$). Eleven epimedium compounds were screened by TCMSP. Among the compounds identified and tested only kaempferol significantly inhibited IL-8 production in a dose dependent manner without any cell cytotoxicity ($p < 0.01$). Kaempferol in combination with dexamethasone showed complete elimination of TNF-α production ($p < 0.001$). Furthermore, kaempferol showed a dose dependent inhibition of CYP3A4 activity. Computer docking analysis showed that kaempferol significantly inhibited the catalytic activity of CYP3A4 with a binding affinity of −44.73kJ/mol.

Discussion: Inhibition of CYP3A4 function by epimedium and its active compound kaempferol leads to enhancement of CS anti-inflammatory effect.

KEYWORDS

epimedium, CYP3A4, drug-drug interaction (DDI), anti-inflammation, kaempferol

1 Introduction

The impact of a drug on the efficacy, toxicity, or metabolism of another commonly referred to as drug-drug interaction, has presented a challenge in managing patient's healthcare around the world (Tornio et al., 2019). Better understanding of the combination of Chinese herbal medicines and synthetic drugs could improve the efficacy of clinical medications and reduce the occurrence of adverse reactions. Drug-metabolizing enzymes are the main component of human detoxification and bioavailability systems, with several hundred types having been identified to date (Preissner et al., 2013). Among these, cytochrome P450(CYP) proteins have been shown to be involved in most drug metabolism reactions, with CYP3A4 being the most important in the human liver where it facilitates 30%–40% of drug metabolization (Shimada et al., 1994; Paine et al., 2006; Zanger and Schwab, 2013). Some drugs, such as dexamethasone (Dex), metabolized by CYP3A4, are known to enhance CYP3A4 activity and accelerate drug metabolism, which may reduce the efficacy of drugs and lead to disappointing anti-inflammatory effects (Pascussi et al., 2001).

Corticosteroids (CS) are the most widely used benchmark anti-inflammatory medication and the first line of therapy for a variety of chronic inflammatory autoimmune and allergic disorders such as asthma, lupus, Crohn's disease, and atopic dermatitis (Chong and Fonacier, 2016; Adcock and Mumby, 2017). While extremely efficacious, prolonged use of CS to control chronic symptoms and the necessity of using it in long-term or at high doses for the management of difficult-to-control diseases is problematic due to the high risk of serious adverse effects. The side-effects of high-dose CS use include global immune suppression, disruption of the hypothalamic pituitary adrenal (HPA) axis, loss of bone density, increased water retention, dyslipidemia, and dermal thinning (Yasir et al., 2022). Chuan Ke Zhi (CKZ) is a China Food and Drug Administration approved medication (Imvin Pharmaceutical LTD., Guangzhou, China) comprised of epimedium and Morinda officinalis (Ba Ji Tian) (Zhao et al., 2013). *Epimedium sagittatum* is a key herbal constituent from CKZ that has been approved by the China FDA for treating osteoporosis, sexual dysfunction, hypertension, and common inflammatory diseases, such as chronic obstructive pulmonary disease and asthma particularly steroid-resistant asthma (Zhao et al., 2013; Xu et al., 2016). Yet, it is unknown whether epimedium can influence CYP3A4 or how it interacts with CS. We tested 141 TCM natural products using Vivid® CYP high-throughput screening kit (Invitrogen Corporation; Carlsbad, CA). Epimedium is one of the natural products that showed over 90% inhibition of CYP3A4 (Yu et al. manuscript in preparation). Consequently, an increased understanding of these interactions will ensure appropriate prescription medicines for long-term treatments and appropriate dosing, especially for the use of CS.

The objective of this study was to determine the effects of epimedium on CYP3A4 function and mRNA expression. Moreover, we sought to determine the relationship between epimedium and dexamethasone with regards to changes in CYP3A4 mRNA expression and its anti-inflammatory effects. To this end, we accessed epimedium's effect on CYP3A4 activity, as well as its effect on CYP3A4 mRNA expression and on the production of the inflammatory cytokine, TNF-α with or without dexamethasone. We further identified bioavailable compounds based on the traditional Chinese medicine system pharmacology database and analysis platform (TCMSP) and tested their anti-IL-8 and anti- TNF-α effects in a human liver cell line and mouse macrophage cell line with or without dexamethasone. The most effective compound, kaempferol was further subjected to assessment of CYP3A4 function by Vivid assay and molecular binding to the CYP3A4 protein structure by computational docking. We, for the first time, demonstrated that epimedium and its active compound kaempferol exhibit an inhibitory effect on CYP3A4, the key CS drug metabolizing enzyme, leading to a synergistic anti-inflammatory effect with dexamethasone.

2 Materials and methods

2.1 Sources of *epimedium sagittatum* extract, active compounds, solvents, and cell lines

According to FDA, the impurity for extract from the natural source means "elemental impurities" (FDA. Botanical, 2016). The powdered water extract of *epimedium sagittatum* (Yin Yang Huo) used in our *in vitro* experiments was made by ImVin Pharmaceutical Co., Ltd. (Guangzhou, China). Epimedium extract was produced in a good manufacturing practice (GMP) facility (Epimedium processing method is shown in Supplementary Method S1). The quality was monitored by high-performance liquid chromatography (HPLC) and thin layer chromatography (Supplementary Figure S1; Supplementary Figure S2), and the heavy metal content, pesticide residual and microbial levels all meet FDA standards. Epimedium extract was

dissolved in corning phosphate buffered saline (PBS, Fisher scientific, MA, United States) for cell culture experiments. The pure compounds, Icariin, anhydroicaritin, quercetin, and kaempferol (Chengdu Herbpuritfy Co., Sichuan, China) with a purity >98% were generous gifts from United States Time Technology Inc. (Elmsford, NY). Compounds were dissolved in dimethyl sulfoxide (DMSO, Fisher Scientific) for *in vitro* cell culture. The concentration of DMSO used in the final culture concentration is less than .1%. This method has been widely used in previous publications including ours (Lopez-Exposito et al., 2011; Yang et al., 2014; Srivastava et al., 2020). HepG2 cells and RAW264.7 cells were purchased from American Tissue Culture Company (Manassas, Virginia).

2.2 Measurement of CYP3A4 activity by Vivid CYP450 assay kits

Vivid CYP450 assay kits were purchased from Thermo Fisher Scientific, Waltham, Massachusetts. This kit has been widely used to measure CYP3A4 activity. The stock solution of epimedium (100 mg/mL) was prepared in methanol and diluted to final concentrations of epimedium (500 μg/mL) with P450 reaction buffer. The positive control compound was ketoconazole (final concentration was 10 μM). In each well, 40 μL of epimedium, solvent or a positive inhibitor control were incubated with 50 μL of pre-mixture at room temperature (25°C) for 20 min. The reaction was initiated by the addition of 10 μL/well of a mixture of substrate and NADP (+) with the appropriate concentration of the vivid substrate. The plate was read immediately for fluorescence changes every 2 min for 60 min using a Spectra Max iD5 Multi-Mode Micro plate Reader (Molecular Devices; San Jose, CA, United States) with appropriate excitation and emission wavelengths for 490 nm and 520 nm. Based on the Vivid CYP450 kits user guide, we used the below formula to calculate percent inhibition.

$$\%\text{Inhibition} = \left(1 - \frac{X - B}{A - B}\right) \times 100\%$$

Where X is the rate observed in the presence of test compound, A is the rate observed in the presence of inhibitor (solvent control or no inhibitor control, as appropriate), and B the rate observed in the presence of the positive inhibition control, ketoconazole. In aspirate experiment, the active compound (kaempferol at the concentrations of 5, 10, 20, and 40 μg/mL) from epimedium was measured for its effect on CYP3A4 activity by Vivid CYP450 assay kits following the same method as per manufacturer's instruction, (Themo Fisher Scientific, Waltham, Massachusetts) and previous publication (Li et al., 2013). All experiments were replicated at least three times.

2.3 HepG2 cell culture and quantitative reverse transcription polymerase chain reaction (qRT-PCR) assay to determine CYP3A4 mRNA expression

HepG2 cells, an immortalized cell line consisting of human liver carcinoma cells, derived from the liver tissues of a 15-year-old Caucasian male who had a well-differentiated hepatocellular carcinoma, were cultured in Dulbecco's Modified Eagle's Medium (DMEM) containing 10% Fetal Bovine Serum (FBS), 100 U/m L Penicillin and 100 μg/mL Streptomycin. Cell cultures were maintained in a humidified 37°C, 5% CO_2 incubator. In-order to measure CYP3A4 expression, HepG2 cells (5×10^5 cells/mL) were added in a 6-well tissue culture plate. After 24 h of incubation at 37°C in 5% CO_2, the cells were treated with vehicle (0.1% DMSO), rifampin(10 μM), ketoconazole(10 μM), dexamethasone(10 μM), epimedium (125 μg/mL), and dexamethasone (10 μM) in combination with epimedium (125 μg/mL) in 1 mL of medium for 48 h. RNA was extracted using AllPrep DNA/RNA Mini Kit (QIAGEN company) according to the manufacturer's recommended protocol. Total RNA was subjected to reverse transcription using RevertAid RT Kit (Themofisher Scientific) and the following primer pairs: CYP3A4, forward 5′-TGGAAGAGATTACGATCATTGCT-3′ and reverse 5′-AGTCGATGTTCACTCCAAATGAT-3′ was used to perform q-RT PCR using SYBR® Green PCR Master Mix (Themofisher Scientific). All experiments were replicated at least three times. A similar experiment was performed using kaempferol. HepG2 cells (5×10^5 cells/mL) were cultured with vehicle (0.1%DMSO), dexamethasone(0.1 μM), dexamethasone(0.1 μM), kaempferol (40 μg/mL), dexamethasone (0.1 μM) combined with kaempferol (40 μg/mL), and dexamethasone (1 μM) combined with kaempferol (40 μg/mL) for 48 h after which RNA was extracted and expression of CYP3A4 was determined using the same qRT-PCR kit and primers as described above. All experiments were replicated at least three times.

2.4 Western blotting

In order to measure CYP3A4 protein expression, HepG2 cells, were cultured in Dulbecco's Modified Eagle's Medium (DMEM) containing 10% Fetal Bovine Serum (FBS), 100 U/m L Penicillin and 100 μg/mL Streptomycin. Cell cultures were maintained in a humidified 37°C, 5% CO_2 incubator. HepG2 cells at 3×10^6 cells/mL were added in a 6-well tissue culture plate. After 24 h of incubation at 37°C in 5% CO_2, the cells were treated with vehicle (0.1%DMSO), epimedium(125 μg/mL) for 48 h. After the culture time point the cells were harvested, centrifuged at 3,000 rpm for 5 min and the supernatant discarded. The cell suspension was washed with PBS and centrifuged at 3,000 rpm for 5 min. Then the cell lysis was done for protein extraction using 100–200 μL of RIPA lysis buffer, with intermittent vigorous vortexing and incubating on ice for about 1 h. After completion of lysis, the tubes were spined in centrifuge at 14,000 rpm for 20 min at 4°C. The supernatant was collected and transferred to another tube to measure the protein concentration. Electrophoresis was done at 90 V for 15 min followed by 100–110 V for the remaining time and transferred to a PVDF membrane. The membrane was incubated with primary antibodies of the CYP3A4, β-actin overnight. The next day, the membrane was washed with PBST and incubated with secondary antibody for 2 h and after the membrane was washed with PBST 4 times before adding the chemiluminescence substrate and imaging. The primary antibodies of CYP3A4 and β-actin were ordered from Cell Signaling (Danvers, MA, United States) and were used at a 1:1,000 dilution, the secondary antibody was used at a 1:10,000 dilution.

2.5 Cell proliferation and viability

HepG2 cells at the concentration of 5×10^3cells/well/100 μL were added in a 96-well tissue culture plate to adhere and incubated at 37°C with 5% CO_2 for 24 h. Cells were treated with different concentrations

of epimedium (500 μg/mL, 250 μg/mL, 125 μg/mL, 62.5 μg/mL, 31.25 μg/mL) for 48 h 20μL of MTT 3-(4,5-Dimethylthiazol-2-yl)-2,5-Diphenyltetrazolium Bromide, 5ug/mL, Thermofisehr, NJ, United States) was added to each well and incubated for 4 h after which the supernatants were discarded and replaced with 150 μL of DMSO. The plate was placed in an orbital shaker at room temperature for 10 mins and absorbance was read at 595 nm using Vmax Kinetic ELISA Micro plate Reader. The percentage of cell proliferation was calculated by comparison with the vehicle (0.1% DMSO) which was set at 100%.

In a separate experiment, HepG2 cells (6.5×10^3 cells/well/100 μL) were added in a 96-well tissue culture plate to adhere for 24 h (37°C with 5% CO_2). Then cells were incubated with different treatments (dexamethasone at 0.1 μM, 1 μM, kaempferol at 40 μg/mL, kaempferol at 40 μg/mL combined with 0.1 μM and 1 μM dexamethasone) for 48 h 10 μL of CCK8 was added in each well. After 4 h of incubation at 37°C, absorbance was read at 450 nm using a Micro plate Reader. All experiments were replicated at least three times.

2.6 TNF-α measurement

RAW264.7 cells are murine macrophage cells that produce TNF-α and have been used to measure changes in TNF-α production after treatments (Liu et al., 2015). RAW264.7 growth medium is composed of DMEM with 10% FBS and 1% penicillin/streptomycin and was changed every 3–4 days or at 75% confluency. Raw 264.7 cells were diluted to a concentration of 2×10^5 cells/mL and plated with 250 μL in 48-well plates. The cells were incubated at 37°C with 5% CO2 for 1 h to allow their attachment to the bottom of the wells. Treatments of epimedium at 125 μg/mL and prescribed concentrations of 10^{-6} M or 10^{-7} M dexamethasone (Sigma Aldrich, St. Louis, MO), were added in volumes of 200 μL. .5 μg/mL of LPS (Escherichia coli0111: B4, Sigma Aldrich, St. Louis, MO) were also added for stimulation. The cells were then incubated at 37°C with 5% CO2 for 24 h and the supernatants were subsequently collected for TNF- α quantification using a mouse TNF- α ELISA kit (BD Biosciences). The dilution of TNF-α measurement was 1:30. All experiments were replicated at least three times with duplicate ELISA measurements of each sample.

2.7 Screening for epimedium active compounds using the TCMSP data base

TCMSP is a unique systems pharmacology platform of Chinese herbal medicines that captures the relationships between drugs, targets, and diseases. Oral bioavailability (OB) is one of the most crucial pharmacokinetic properties frequently evaluated in early drug screening which represents the percentage of an orally administered dose of a given compound that delivers to the systemic circulation to produce a pharmacological effect in the organism. High OB is a pivotal factor in determining bioactive molecules as a potential therapeutic agent. Drug-likeness (DL) is a qualitative means of analysis used in drug design for determining the drug ability of a given molecule, which is an important consideration in guiding the design and selection of compounds during the early stages of drug discovery and development.

2.8 IL-8 measurement

HepG2 cells were diluted to a concentration of 5×10^5 cells/mL and plated with 1 mL in 12-well plates. The cells were incubated at 37°C with 5% CO_2 for 1 h to attach to the bottom of the wells. Kaempferol at 40 μg/mL and prescribed concentrations of 10^{-6} M or 10^{-7} M dexamethasone (Sigma Aldrich, St. Louis, MO), were added in volumes of 500 μL. After pre-treatment for 48 h, 5 ng/mL of IL-1β was added to pre-treatment groups for stimulation. The cells were incubated at 37°C with 5% CO_2 for 6 h and the supernatants were subsequently collected for IL-8 quantification using a human IL-8 ELISA kit (BD Biosciences). The dilution of IL-8 measurement was 1:1. All experiments were replicated at least three times with duplicate ELISA measurements of each sample.

2.9 Computer docking for kaempferol and CYP3A4

The crystal structure of P450 3A4 (PDB ID: 2V0M) was obtained from the protein data bank (http://www.rcsb.org/). CDOCKER implemented in Discovery Studio 3.0 has been used for molecular docking. The force field has been applied to the crystal structure. All the other molecules, including water, were removed. The crystal ligand was used as the reference to define the binding site with the coordinate of 18.9801, 8.89066, 61.9966. The size of site sphere was defined with a radius of 12 Å. All the compounds were prepared using the Prepare Ligands protocol. Finally, the docking poses for each compound were outputted based on the docking score.

The crystal structure of P450 3A4 (PDB ID: 2V0M) was obtained from the protein data bank (http://www.rcsb.org/). CDOCKER implemented in Discovery Studio 3.0 has been used for molecular docking. The force field has been applied to the crystal structure. All the other molecules, including water, were removed. The crystal ligand was used as the reference to define the binding site with the coordinate of 18.9801, 8.89066, 61.9966. The size of site sphere was defined with a radius of 12 Å. The molecular structures of Epimedium components were obtained from NCBI and their SDF file format were downloaded from TCMSP. All the compounds were prepared using the Prepare Ligands protocol. Finally, the docking poses for each compound were determined based on the docking score.

3 Results

3.1 Epimedium's dose-dependent inhibition of CYP3A4 activity

To determine if epimedium inhibits CYP3A4 activity, a Vivid CYP450 kit was used to measure the effect of different concentrations of epimedium. Results showed that epimedium suppressed CYP3A4 activity in a dose-dependent manner. The inhibition rate was 33.5%, 45.5%, 76.3%, 93.2%, and 98% at an incremental concentration of 31.25, 62.5, 125, 250, and 500 μg/mL, respectively (Figure 1A). According to the epimedium inhibition of CYP3A4, the calculated IC50 and IC90 was 95.74 μg/mL and 216.1 ug/mL, respectively (Figures 1B, C). These results demonstrate that epimedium exhibits a potent inhibitory effect on CYP3A4 activity.

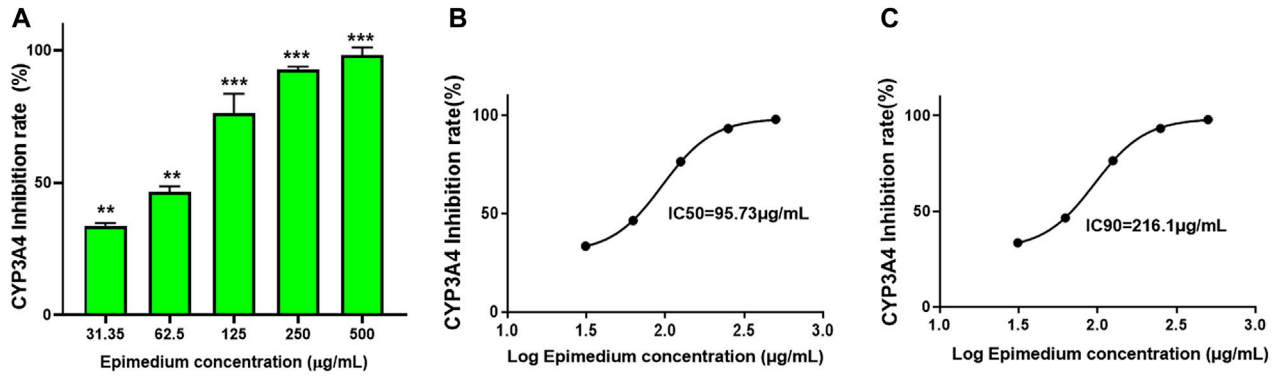

FIGURE 1
Epimedium inhibition of CYP3A4 activity: The inhibition of CYP3A4 was measured by commercially available Vivid assay kit as per manufacturers instruction. Epimedium showed dose-dependent suppression of CYP3A4 enzyme activity **(A)**. The IC_{50} and IC_{90} were calculated to be 95.73 pg/mL and 216.1 pg/mL respectively **(B,C)**. Data represents triplicate experiments and expressed as mean ± SD. np < 0.01; ***p < 0.001 *vs.* control.

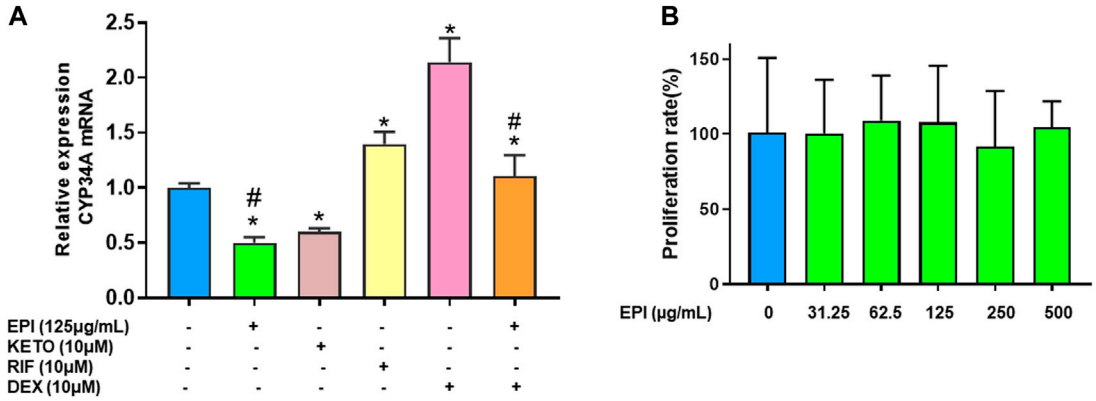

FIGURE 2
Epimedium suppressed CYP3A4 mRNA expression in human liver cell lines: HepG2 cells were cultured with Epimedium (EPI) and Dexamethasone (DEX) either alone or in combination. Rifampin (RI F)was used as a CYP3A4 enhancer whereas Ketoconazole (KETO) as a CYP3A4 inhibitor. The expression levels were determined by qRT-PCR. EPI alone inhibited CYP3A4 mRNA expression comparable to KETO whereas DEX enhanced CYP3A4 mRNA levels comparable to RIF. Coculture EPI and DEX remarkably reduced DEX enhancement of CYP3A4 mRNA levels **(A)**. Cell proliferation assay measured using MTT assay showed no different in proliferation between groups **(B)**. Data represents triplicate experiments and expressed as mean ± SD. *p < .05 *vs.* control (0.1%DMS0), #p < 0.05 *vs.* DEX.

3.2 Epimedium suppressed CYP3A4 mRNA expression and reduced dexamethasone enhancement of CYP3A4 mRNA expression without cytotoxicity in a human liver carcinoma cell line (HepG2)

To determine if epimedium suppresses CYP3A4 mRNA expression, we conducted quantitative PCR in HepG2 cells (liver carcinoma cell line). Epimedium, like ketoconazole, significantly inhibited CYP3A4 gene expression by 50% and 40% respectively (Figure 2A, p < 0.05 *vs.* DMSO control). In contrast, rifampin, and dexamethasone alone significantly increased CYP3A4 mRNA level by 39% and 114% respectively (p < 0.05 *vs.* DMSO control). However, when epimedium was used in combination with dexamethasone, we saw a 50% suppression of the CYP3A mRNA expression in HepG2 cells (p < 0.05). We next conducted an MTT assay to examine whether epimedium inhibition of CYP3A4 expression is linked to a cytotoxic effect. MTT is a well accepted colorimetric assay to determine cell proliferation, viability, and cytotoxicity. We observed that there was no significant difference in the rate of proliferation/viability in HepG2 cells at 31.25, 62.5, 125, 250 and 500 μg/mL concentration (Figure 2B). Taken together, this data demonstrates that epimedium inhibits CYP3A4 mRNA expression, and counter-regulates the dexamethasone paradoxical enhancement of CYP3A4 in a non-cytotoxic manner.

3.3 Epimedium suppressed CYP3A4 protein expression in a human liver carcinoma cell line (HepG2)

Epimedium suppressed CYP3A4 mRNA expression, therefore we used western blotting to measure the protein expression of CYP3A4.

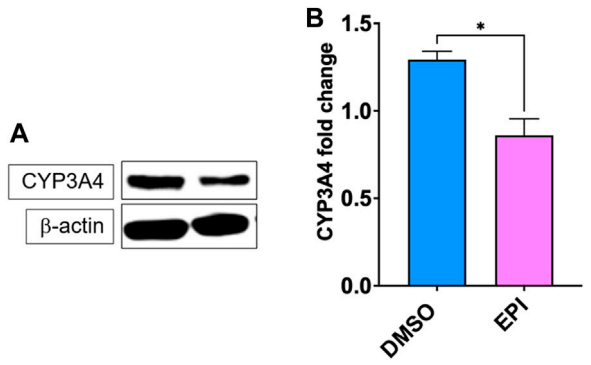

FIGURE 3
Epimedium inhibits CYP3A4 protein expression. HepG2 cells were cultured with Epimedium for 48 h and protein expression was determined using western blotting. **(A)**. Western Bands **(B)**. CYP3A4 protein expression. Data represents triplicate experiments and expressed as mean ± SD. *$p < .05$ *vs.* control (0.1%DMS0).

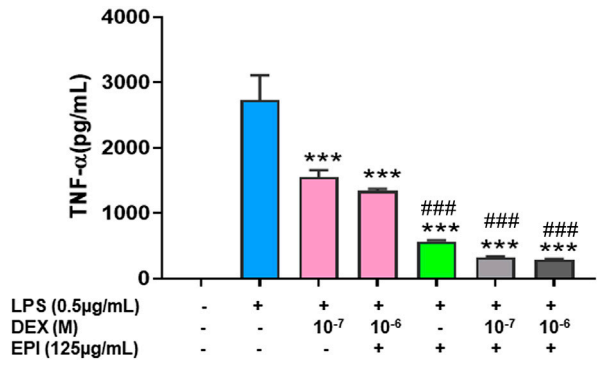

FIGURE 4
Epimedium and dexamethasonesynergistically suppressed TNF-α production: RAW cells were cultured with Epimedium either alone or in combination with Dexamethasone for 24 h. The cells were stimulated with LPS (0.5 pg/mL). The supernatant were harvested and TNF-a levels were measured by ELISA. **(A)** Dexamethasone (10^{-6} M, 10^{-7} M) and Epimedium (125 pg/m1) significantly reduced TNF-α levels. When Epimedium was added to dexamethasone, the TNF-α levels were suppressed by 88%. Data represents triplicate experiments and expressed as mean ± SD. ***$p < 0.001$ *vs.* control (0.1%DMS0),"#$p <$ 0.001 *vs.* Dex (10−7 M).

Our results showed that epimedium significantly inhibited CYP3A4 protein expression (Figure 3, $p < 0.05$).

3.4 Epimedium and dexamethasone synergistically suppressed TNF-α production by murine macrophage cell line (Raw 264.7)

TNF-α is a master pro-inflammatory cytokine and plays a major pathological role in corticosteroid resistant asthma, inflammatory bowel disease, psoriasis, rheumatoid arthritis and COVID-19 cytokine storm among others (Russell et al., 2020). Since we observed that dexamethasone upregulated CYP3A4 mRNA expression and that may be counterproductive to its anti-inflammatory effect, and epimedium reduced this unwanted effect of dexamethasone on CYP3A4 mRNA, we hypothesize that epimedium may enhance the anti-inflammatory effect of dexamethasone. To test this possibility, we used murine macrophage cell line, Raw 264.7 cells. Our results showed that dexamethasone at 10^{-7} M only inhibited TNF-α by 20.4%, compared with that in the untreated cells. Co-treatment of dexamethasone (10^{-6} M) and epimedium (125 μg/mL) significantly decreased TNF-α level (stimulated by LPS (500 ng/mL)) by 63.2% and 78.3% respectively (Figure 4, $p < 0.01$). Interestingly, when epimedium (125 μg/mL) was added to dexamethasone at either 10^{-7} M or 10^{-6} M, we observed that the TNF-α levels were significantly lower than either dexamethasone or epimedium alone ($p < 0.001$). These data clearly demonstrates that epimedium provided synergistic effect with dexamethasone on inhibition of TNF-α production.

3.5 Screening bioavailable active compounds from epimedium *via* TCMSP database

We used the TCMSP database to filter potential bioavailable active components in epimedium (Ru et al., 2014). The screening criteria were oral bioavailability (OB) > 40% and drug like (DL) index>0.18, as previously described (Ru et al., 2014; Wang et al., 2021a; Wang et al., 2021b). Eleven potential compounds were identified. The molecular names of these compounds are magnograndiolide, olivil, Yinyanghuo A, 1,2-diguaiacylpropane-1,3-diol, Yinyanghuo E, quercetin, Yinyanghuo C, anhydroicaritin, linoleyl acetate, kaempferol and icariin. The molecular weight of all potential epimedium compounds identified fall between 250–500 g/mol except for Icariin which was around 676.73 g/mol (Table 1).

3.6 Effect of 4 epimedium candidate compounds on IL-8 production by HepG2 cells

Next, we tested epimedium derived compounds from the TCMSP screening results and focused on four commercially available compoundsicariin, anhydroicaritin, quercetin, and kaempferol. We tested these compounds at a concentration of 40 μg/mL against IL-1β-stimulated HepG2 cells and determined levels of the of the inflammatory cytokine IL-8. We found that quercetin enhanced IL-8 levels, opposite to the parent extract (Figure 5A). Icariin and anhydroicaritin did not reduce IL-8 production at the tested doses. Only kaempferol showed significant inhibition of IL-8 production ($p < 0.01$). We further showed a dose dependent reduction of IL-8 production by kaempferol (Figure 5B, $p < 0.01$–0.001) with no cytotoxicity (Figure 5C).

3.7 Kaempferol and dexamethasone combined effects onTNF-α production in the murine macrophage cell line (Raw264.7)

Based on kaempferol's pharmacological profile, we then tested the effects of combining kaempferol with dexamethasone on TNF-α

TABLE 1 Active compounds from Epimedium.

Index	Molecule name	Molecule wt. (g/Mol)	OB(%)>40	DL > .18
1	Magnograndiolide	266.37	63.71	.19
2	olivil	376.44	62.23	.41
3	Yinyanghuo A	420.49	56.96	.77
4	1,2-diguaiacylpropane-1,3-diol	320.37	52.31	.22
5	Yinyanghuo E	352.36	51.63	.55
6	quercetin	302.25	46.43	.28
7	Yinyanghuo C	336.36	45.67	.5
8	Anhydroicaritin	368.41	45.41	.44
9	Linoleyl acetate	308.56	42.1	0.2
10	Kaempferol	286.25	41.88	.24
11	Icariin	676.73	41.58	.61

Screening active compounds from Epimedium using TCMSP, database: The screening criteria were OB>40% and DL > 0.18. We found 11 active compounds of Epimedium. All the molecule weights were between 250 and 676.73 (g/Mol). TCMSP.

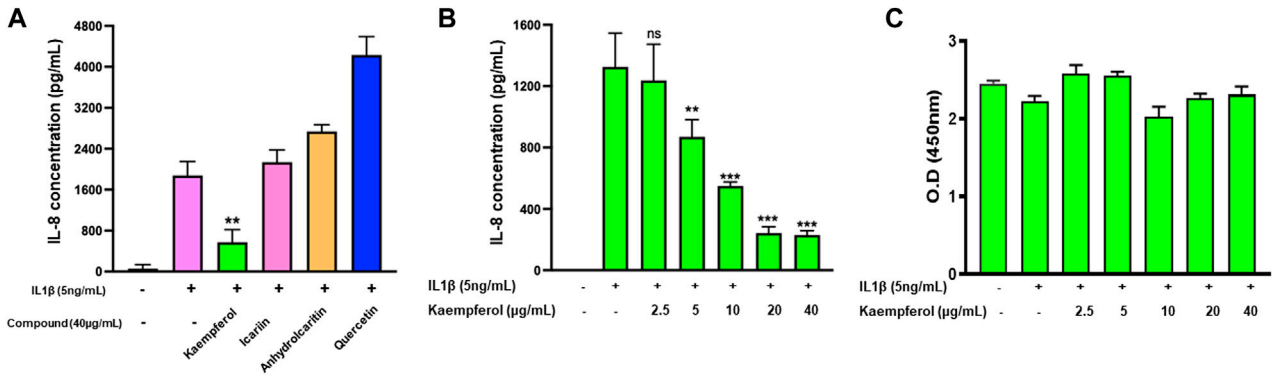

FIGURE 5
Effect of four epimedium candidate compounds on IL-8 production: HepG2 cells were cultured in presence of four main Epimedium candidate compound for 48 h. After which cells were stimulated with IL-1 β (5 ng/m1). The supernatant were harvest and IL-8 levels were measured by ELISA. **(A)** Out of four main candidates, Kaempferol significantly reduced IL-8 levels. **(B)** Kaempferol showed a dose dependent inhibition of IL-8 production by stimulated HepG2 cells. **(C)** No cell cytotoxicity was observed with Kaempferol at different doses. Data represents triplicate experiments and expressed as mean ± SD. "$p < 0.01$; $p < 0.001$; *vs.* control (0.1%DMSO). 0.D; optical density.

production. Dexamethasone and kaempferol each showed significant suppression of TNF-α production, respectively compared with untreated cells (Figure 6A $p < 0.001$). Interestedly, TNF-α production was further reduced and approached baseline levels when dexamethasone and kaempferol were used in combination ($p < 0.001$ *vs.* dexamethasone alone, kaempferol alone treated cells). This inhibition did not cause any sign of cytotoxicity (Figure 6B).

3.8 Kaempferol inhibits CYP3A4 activity in a dose-dependent manner

To determine if kaempferol inhibited CYP3A4 activity, a Vivid CYP450 kit was used to measure CYP3A4 activity at different concentrations of kaempferol. Kaempferol dose-dependently suppressed CYP3A4 activity (Figure 7A, $p < 0.01$). The inhibition rate was 58.0%, 74.1%, 89.9%, and 97.4% at an incremental concentration of 5.0, 10.0, 20.0, 40.0 μg/mL respectively (Figure 7A). Based on the kaempferol inhibition of CYP3A4, we calculated a IC50 and IC90 of 9.8 μg/mL and 29.54 μg/mL, respectively (Figures 7B, C).

3.9 Computer docking of kaempferol and CYP3A4

To further understand how kaempferol interacts with the CYP3A4 protein structure, we conducted *in silico* molecular docking/modeling. The docking score is −44.7332 kcal/mol,

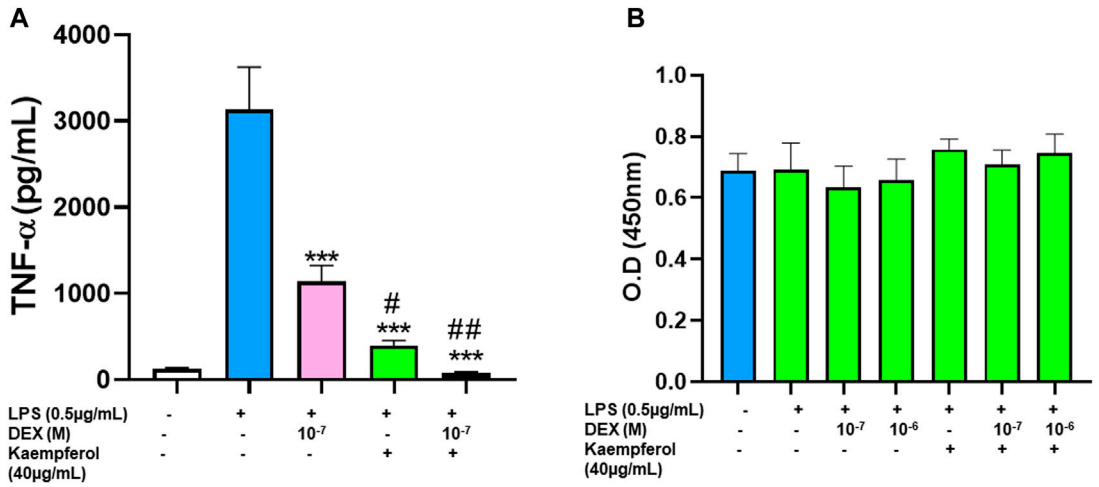

FIGURE 6
Effect of Kaempferol and dexamethasone co-culture on TNF- α production by RAW cells: Epimedium and dexamethasone synergistically suppressed TNF-α production RAW cells were cultured with Epimedium either alone or in combination with Dexamethasone for 24 h. The cells were stimulated with LPS (0.5 pg/m1). The supernatant were harvested and TNF-α levels were measured by ELISA. **(A)** Dexamethasone (10^{-7},10^{-6} M) and Kaempferol (40 pg/m1) significantly reduced TNF-α levels. When Kaempferol and dexamethasone was added together, the TNF-α levels were suppressed by 97%. **(B)** Cell viability with CCK8 assay showed no cell cytotoxicity. Data represents triplicate experiments and expressed as mean ± SD. "'$p < 0.001$ *vs.* control (without LPS), "$p < 0.05$; "$p < 0.01$ *vs.* Dex (10^{-7} M).

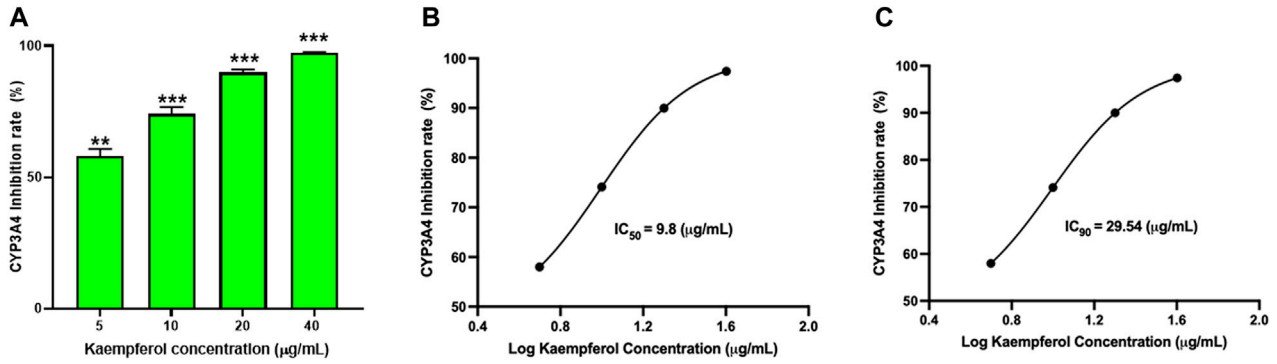

FIGURE 7
Kaempferol dose dependent inhibition of CYP3A4 activity: The inhibition of CYP3A4 was measured by commercially available Vivid assay kit as per manufacturers instruction. **(A)** Kaempferol showed dose-dependent suppression of CYP3A4 enzyme activity. The IC_{50} and IC_{90} were calculated to be 9.8 pg/mL and 29.54 pg/mL respectively **(B,C)**. Data represents triplicate experiments and expressed as mean ± SD. "$p < 0.01$; "'$p < 0.001$ *vs.* control.

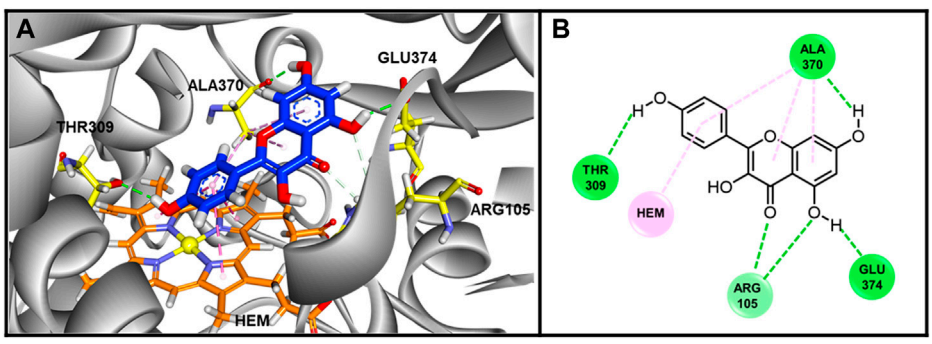

FIGURE 8
The Binding conformations of compound Kaempferol with enzyme CYP3A4. **(A)** 3D Binding pose of Kaempferol in inhibited binding domain of CYP450 3A4. For Kaempferol, carbon and oxygen are highlighted in blue and red, respectively. For amino acids of protein, carbon, oxygen and nitrogen are displayed by yellow, red and blue, respectively. For HEM molecule, the orange, blue and yellow color stand for carbon, nitrogen and iron ion. **(B)** Binding interactions between Kaempferol with residues of CYP450 3A4. The green and pink lines stand for hydrogen bonds and hydrophobic interactions. The docking score was −44.7332 kJ/md, showing good binding affinity between kaempferol and CYP3A4.

implying strong binding affinity between kaempferol with CYP3A4. The binding conformation was illustrated in Figure 8. Hydrogen bonds between kaempferol and THR390, ALA370, ARG105 and GLU 374 were formed, which stabilize the configuration of kaempferol. There is π-π stacking interaction between benzene group of kaempferol with HEM molecule in CYP450 3A4. The hydrophobic interactions were found between kaempferol with ALA370. The kaempferol completely occupied the catalytic sites of CYP450 3A4, preventing enzyme binding with its substrates, which likely explains part of the mechanism of how kaempferol influences CYP450 3A4.

4 Discussion

Corticosteroids are a mainstream anti-inflammatory class of drugs and CYP3A4 is the major drug metabolizing enzyme of corticosteroids. Studies have shown that dexamethsone paradoxically enhances CYP3A4 gene expression (Pascussi et al., 2001), consequently reducing the anti-inflammatory capacity of corticosteroids. Therefore, a natural product that enhances the anti-inflammatory capability of corticosteroids by modulation of CYP3A4 will be an important strategy to enhance the anti-inflammatory effects of corticosteroids. Previous studies have investigated the effects of natural products including drug interactions however there were no reports on potential therapeutic implications of these interactions (Mahgoub, 2002; Melillo de Magalhães et al., 2012; Huang et al., 2013). CYP3A4 is the dominant CYP3A family enzyme expressed in the human liver and gastrointestinal tract (Horsmans, 1997). Pharmacogenomic variations of CYP3A4 in human have been implicated in the metabolism of many drugs and in drug-drug interactions which could have important implications for the clinical use of drugs in combination therapy (Gurley et al., 2002; Delgoda and Westlake, 2004). *In vivo* studies have shown that Panax ginseng (Malati et al., 2012) and, Angelica (Ishihara et al., 2000) respectively induces and inhibits CYP 3A in the liver and gastro intestinal tract, therefore patients taking them in combination with other substrates that are metabolized by CYP3A must be closely monitored for adequate therapeutic response to the substrate medication. Therefore, due to the wide spectrum of substances processed by CYP3A4, interferences and interactions are not uncommon.

In this study, we demonstrated for the first time that epimedium dose-dependently inhibited the CYP3A4 enzymes with IC50 value of 95.73 μg/mL and an IC90 value of 216 μg/mL, respectively. Due to its inhibitory effect on the CYP3A4 enzyme, we hypothesized that epimedium would regulate CYP3A4 mRNA expression in the presence of dexamethasone. Therefore we measured the effect of epimedium alone and in combination with dexamethasone on the mRNA expression of CYP3A4 using an HepG2 cell line because it is a suitable surrogate of primary human hepatocytes to determine changes in CYP3A4 expression in the human body (Li et al., 2013). The results showed that epimedium inhibited CYP3A4 transcription without any cytotoxicity. Dexamethasone alone at a low concentration of 10 μM induced CYP3A4 mRNA, similar to rifampin (a CYP3A4 enhancer (Kobayashi et al., 2019)). However, in combination with epimedium, we observed 50% less suppression of CYP3A4 mRNA expression. This suggests that epimedium strongly inhibits CYP3A4 activity and would potentially influence the metabolism and increase the bioavailability of dexamethasone, providing a synergistic anti-inflammatory effect. To confirm this synergistic effect, we measured TNF- α production when epimedium is combined with dexamethasone. Thus, we tested the ability of epimedium to suppress LPS-induced TNF-α in macrophages. First, we showed that dexamethasone at 10^{-7} M caused a 20.4% inhibition of TNF-α and at a higher concentration of 10^{-6} M it caused a 63.2% inhibition of TNF-α. While epimedium at 125 μg/mL resulted in a 78.3% inhibition. In combining epimedium with dexamethasone at 10^{-7} M and at 10^{-6} M, we observed further suppression of TNF-α regardless of the difference in concentrations. Thus, our results confirmed the synergistic anti-inflammatory effect of epimedium in combination with dexamethasone. This implies that dexamethasone can be used at a lower dose with epimedium to achieve a more potent inhibition of TNF-α, which is clinically significant. The combination might serve to reduce the potential side effects of corticosteroids while maintaining or even enhancing its anti-inflammatory effects, this warrant further clinical investigation.

Furthermore, we used TCSMP database to screen bioactive compounds of epimedium. We identified 11 candidates based on the criteria of oral bioavailability and drug like index. We selected the commercially available compounds icariin, anhydroicaritin, kaempferol, and quercetin from the 11 compounds to measure their anti-inflammatory effect on IL-8. Out of the four compounds tested, only kaempferol significantly reduced the expression of IL-8 and did so in a dose dependent and non-toxic manner. In addition, kaempferol in combination with dexamethasone synergistically suppressed TNF-α production in macrophage cell line supporting that kaempferol is one of the epimedium active compounds. Furthermore, we showed that kaempferol inhibited CYP3A4 activity and in a dose dependent fashion with an IC50 of 9.8 mg/mL and IC90 of 29.54 mg/mL, which is approximately 10 X more potent than its parent extract epimedium. Using molecular docking we showed that kaempferol binds strongly to CYP3A4 by occupying the catalytic sites of CYP450 3A4, preventing enzyme binding with its substrates.

Human studies evaluating the bioavailability of kaempferol shows that the conjugated forms of kaempferol have a higher bioavailability than the free forms (Hollman et al., 1995; Hollman et al., 1996). Upon absorption, kaempferol is rapidly metabolized in the liver to form glucuronide methyl, and sulfate metabolites which are detected in blood and urine. Few studies that have investigated kaempferol have shown that the most available forms of kaempferol are–kaempferol glucoside and rutinoside in tea (Dabeek and Marra, 2019). Studies conducted by De Vries et al. (de Vries et al., 1998) examined the digestion and absorption of kaempferol from black tea in 15 participants. It was shown that urinary excretion of kaempferol was 2.5% of the amount ingested. The digestion and absorption of kaempferol were also assessed after an intake of 12.5 mg kaempferol from broccoli for 12 days, it was shown that the urinary excretion was 0.9%. There are limited clinical studies on the bioavailability of kaempferol and as such more studies are needed to investigate the bioavailability in a clinical setting. Our studies on kaempferol therefore provide an *in vitro* data of its effects on CYP3A4 and the

results in this study will need to be further validated in a clinical setting.

Flavonoids are generally extensively metabolized by the liver (Mullen et al., 2006). There are few studies evaluating the bioavailability of kaempferol. In the study by (DuPont et al., 2004) the metabolites of kaempferol were assessed in plasma and urine after ingesting kaempferol-containing leafy vegetable endive. It was shown that kaempferol-3-glucuronide was the major metabolite of kaempferol found in both urine and plasma. 40% of total kaempferol was detected in plasma while 14% was detected in urine. This shows that kaempferol has the potential to reach inhibitory concentration. However, this area needs to be further explored. More studies need to be carried out to further understand the metabolism and bioavailability of kaempferol in the human body.

5 Conclusion

In conclusion, this study reveals, to the best of our knowledge for the first time, that epimedium suppresses CYP3A4 level, and thus enhance the dexamethasone effect on LPS-induced TNF-α production, probably through inhibition of CYP3A4 activity and upregulation of dexamethasone utilization. Our data illustrates the potential therapeutic value of epimedium in treating steroid-refractory diseases. Kaempferol is an effective candidate for the downregulation of IL-8 expression. Further studies using epimedium and kaempferol on HepG2 cell lines may provide relevant additional data on anti-inflammation, and *in vivo* study of dexamethasone in the presence of epimedium or kaempferol is warranted.

Data availability statement

The datasets presented in this study can be found in online repositories. The names of the repository/repositories and accession number(s) can be found in the article/Supplementary Material.

Author contributions

X-ML designed the experiment. KL, X-HY, Z-ZW, AM, LG, and IM conducted the research work, wrote, and contributed to the writing of the manuscript. KS and HY wrote up the data analysis. IM and X-ML contributed to the discussion. AG, NY, DD, Y-CC, VG, RT, LG, J-XL, and X-ML revised the manuscript.

Funding

This work is supported by Integrative medicine Study (ORA LOG NO: 012874-101) to X-ML at New York Medical College; International exchange program in 2018 of Guangzhou University of Chinese Medicine as well as Guangzhou Science and Technology Plan Project (706086293043) to KL.

Acknowledgments

We thank ImVin Pharmaceutical Co., Ltd. (Guangzhou, China for providing the powdered water extract of epimedium sagittatum (Yin Yang Huo) used in our *in vitro* experiments.

Conflict of interest

X-ML received research support to her institution from the National Institutes of Health (NIH)/National Center for Complementary and Alternative Medicine (NCCAM) # 1P01 AT002644725-01 "Center for Chinese Herbal Therapy (CHT) for Asthma", and grant #1R01AT001495-01A1 and 2R01 AT001495-05A2, NIH/NIAID R43AI148039, Food Allergy Research and Education (FARE), Winston Wolkoff Integrative Medicine Fund for Allergies and Wellness, the Parker Foundation and Henan University of Chinese Medicine; received consultancy fees from FARE and Johnson & Johnson Pharmaceutical Research & Development, L.L.C. Bayer Global Health LLC; received royalties from Up To Date; is an Honorary Professor of Chinese Medical University, Taichung, Taiwan; Henan University of Chinese Medicine Zhenzhou, China, and Professorial Lecture at Icahn School of Medicine at Mount Sinai, New York, NY, US; received travel expenses from the NCCAM and FARE; share US patent US7820175B2 (FAHF-2), US10500169B2 (XPP), US10406191B2 (S. Flavescens), US10028985B2 (WL); US11351157B2 (nanoBBR): take compensation from her practice at Center for Integrative Health and Acupuncture PC; US Times Technology Inc is managed by her related party; is a member of General Nutraceutical Technology LLC and Health Freedom LLC.Nan Yang received research support from the National Institutes of Health (NIH)/National Center for Complementary and Alternative Medicine (NCCAM), NIH/NIAID R43AI148039; shares US patent: US10500169B2 (XPP), US10406191B2 (S. Flavescens), US10028985B2 (WL); and is a member of General Nutraceutical Technology LLC and Health Freedom LLC. Kamal Srivastava share PCT/US2017/056822.

The remaining authors declare that the research was conducted in the absence of any commercial or financial relationships that could be construed as a potential conflict of interest.

Publisher's note

Supplementary material

The Supplementary Material for this article can be found online at: https://www.frontiersin.org/articles/10.3389/fphar.2022.1042756/full#supplementary-material

References

Adcock, I. M., and Mumby, S. (2017). Glucocorticoids. *Handb. Exp. Pharmacol.* 237, 171–196. doi:10.1007/164_2016_98

Chong, M., and Fonacier, L. (2016). Treatment of eczema: Corticosteroids and beyond. *Clin. Rev. Allergy Immunol.* 51 (3), 249–262. doi:10.1007/s12016-015-8486-7

Dabeek, W. M., and Marra, M. V. (2019). Dietary quercetin and kaempferol: Bioavailability and potential cardiovascular-related bioactivity in humans. *Nutrients* 11 (10), 2288. doi:10.3390/nu11102288

de Vries, J. H., Hollman, P. C., Meyboom, S., Buysman, M. N., Zock, P. L., van Staveren, W. A., et al. (1998). Plasma concentrations and urinary excretion of the antioxidant flavonols quercetin and kaempferol as biomarkers for dietary intake. *Am. J. Clin. Nutr.* 68 (1), 60–65. doi:10.1093/ajcn/68.1.60

Delgoda, R., and Westlake, A. C. (2004). Herbal interactions involving cytochrome p450 enzymes: A mini review. *Toxicol. Rev.* 23 (4), 239–249. doi:10.2165/00139709-200423040-00004

DuPont, M. S., Day, A. J., Bennett, R. N., Mellon, F. A., and Kroon, P. A. (2004). Absorption of kaempferol from endive, a source of kaempferol-3-glucuronide, in humans. *Eur. J. Clin. Nutr.* 58 (6), 947–954. doi:10.1038/sj.ejcn.1601916

Fda. Botanical (2016). Drug development guidance for industry. Available at https://www.fda.gov/downloads/Drugs/GuidanceComplianceRegulatoryInformation/Guidances/UCM458484.pdf.

Gurley, B. J., Gardner, S. F., Hubbard, M. A., Williams, D. K., Gentry, W. B., Cui, Y., et al. (2002). Cytochrome P450 phenotypic ratios for predicting herb-drug interactions in humans. *Clin. Pharmacol. Ther.* 72 (3), 276–287. doi:10.1067/mcp.2002.126913

Hollman, P. C., de Vries, J. H., van Leeuwen, S. D., Mengelers, M. J., and Katan, M. B. (1995). Absorption of dietary quercetin glycosides and quercetin in healthy ileostomy volunteers. *Am. J. Clin. Nutr.* 62 (6), 1276–1282. doi:10.1093/ajcn/62.6.1276

Hollman, P. C., vd Gaag, M., Mengelers, M. J., van Trijp, J. M., de Vries, J. H., and Katan, M. B. (1996). Absorption and disposition kinetics of the dietary antioxidant quercetin in man. *Free Radic. Biol. Med.* 21 (5), 703–707. doi:10.1016/0891-5849(96)00129-3

Horsmans, Y. (1997). Georges brohee prize 1996. Major cytochrome P-450 families: Implications in health and liver diseases. *Acta Gastroenterol. Belg* 60 (1), 2–10.

Huang, J., Li, J., Zheng, S., Wu, J., Zhang, W., Sun, T., et al. (2013). Epimedium flavonoids counteract the side effects of glucocorticoids on hypothalamic-pituitary-adrenal axis. *Evid. Based Complement. Altern. Med.* 2013, 938425. doi:10.1155/2013/938425

Ishihara, K., Kushida, H., Yuzurihara, M., Wakui, Y., Yanagisawa, T., Kamei, H., et al. (2000). Interaction of drugs and Chinese herbs: Pharmacokinetic changes of tolbutamide and diazepam caused by extract of Angelica dahurica. *J. Pharm. Pharmacol.* 52 (8), 1023–1029. doi:10.1211/0022357001774750

Kobayashi, T., Sugaya, K., Onose, J. I., and Abe, N. (2019). Peppermint (Mentha piperita L.) extract effectively inhibits cytochrome P450 3A4 (CYP3A4) mRNA induction in rifampicin-treated HepG2 cells. *Biosci. Biotechnol. Biochem.* 83 (7), 1181–1192. doi:10.1080/09168451.2019.1608802

Li, M., Chen, P. Z., Yue, Q. X., Li, J. q., Chu, R. a., Zhang, W., et al. (2013). Pungent ginger components modulates human cytochrome P450 enzymes *in vitro*. *Acta Pharmacol. Sin.* 34 (9), 1237–1242. doi:10.1038/aps.2013.49

Liu, C., Yang, N., Song, Y., Wang, L., Zi, J., Zhang, S., et al. (2015). Ganoderic acid C1 isolated from the anti-asthma formula, ASHMI™ suppresses TNF-α production by mouse macrophages and peripheral blood mononuclear cells from asthma patients. *Int. Immunopharmacol.* 27 (2), 224–231. doi:10.1016/j.intimp.2015.05.018

Lopez-Exposito, I., Castillo, A., Yang, N., Liang, B., and Li, X. M. (2011). Chinese herbal extracts of Rubia cordifolia and Dianthus superbus suppress IgE production and prevent peanut-induced anaphylaxis. *Chin. Med.* 6, 35. doi:10.1186/1749-8546-6-35

Mahgoub, A. A. (2002). Grapefruit juice potentiates the anti-inflammatory effects of diclofenac on the carrageenan-induced rat's paw oedema. *Pharmacol. Res.* 45 (1), 1–4. doi:10.1006/phrs.2001.0856

Malati, C. Y., Robertson, S. M., Hunt, J. D., Chairez, C., Alfaro, R. M., Kovacs, J. A., et al. (2012). Influence of Panax ginseng on cytochrome P450 (CYP)3A and P-glycoprotein (P-gp) activity in healthy participants. *J. Clin. Pharmacol.* 52 (6), 932–939. doi:10.1177/0091270011407194

Melillo de Magalhães, P., Dupont, I., Hendrickx, A., Joly, A., Raas, T., Dessy, S., et al. (2012). Anti-inflammatory effect and modulation of cytochrome P450 activities by Artemisia annua tea infusions in human intestinal Caco-2 cells. *Food Chem.* 134 (2), 864–871. doi:10.1016/j.foodchem.2012.02.195

Mullen, W., Edwards, C. A., and Crozier, A. (2006). Absorption, excretion and metabolite profiling of methyl-glucuronyl-glucosyl- and sulpho-conjugates of quercetin in human plasma and urine after ingestion of onions. *Br. J. Nutr.* 96 (1), 107–116. doi:10.1079/bjn20061809

Paine, M. F., Hart, H. L., Ludington, S. S., Haining, R. L., Rettie, A. E., and Zeldin, D. C. (2006). The human intestinal cytochrome P450 "pie. *Drug Metab. Dispos.* 34 (5), 880–886. doi:10.1124/dmd.105.008672

Pascussi, J. M., Drocourt, L., Gerbal-Chaloin, S., Fabre, J. M., Maurel, P., and Vilarem, M. J. (2001). Dual effect of dexamethasone on CYP3A4 gene expression in human hepatocytes. Sequential role of glucocorticoid receptor and pregnane X receptor. *Eur. J. Biochem.* 268 (24), 6346–6358. doi:10.1046/j.0014-2956.2001.02540.x

Preissner, S. C., Hoffmann, M. F., Preissner, R., Dunkel, M., Gewiess, A., and Preissner, S. (2013). Polymorphic cytochrome P450 enzymes (CYPs) and their role in personalized therapy. *PLoS One* 8 (12), e82562. doi:10.1371/journal.pone.0082562

Ru, J., Li, P., Wang, J., Zhou, W., Li, B., Huang, C., et al. (2014). TCMSP: A database of systems pharmacology for drug discovery from herbal medicines. *J. Cheminform* 6, 13. doi:10.1186/1758-2946-6-13

Russell, B., Moss, C., George, G., Santaolalla, A., Cope, A., Papa, S., et al. (2020). Associations between immune-suppressive and stimulating drugs and novel COVID-19-a systematic review of current evidence. *Ecancermedicalscience* 14, 1022. doi:10.3332/ecancer.2020.1022

Shimada, T., Yamazaki, H., Mimura, M., Inui, Y., and Guengerich, F. P. (1994). Interindividual variations in human liver cytochrome P-450 enzymes involved in the oxidation of drugs, carcinogens and toxic chemicals: Studies with liver microsomes of 30 Japanese and 30 caucasians. *J. Pharmacol. Exp. Ther.* 270 (1), 414–423.

Srivastava, K., Fidan, O., Shi, Y., Yang, N., Liu, C., Song, Y., et al. (2020). Berberine-containing natural medicine confers sustained peanut tolerance associated with distinct microbiota signature. *J. Allergy Clin. Immunol.* 145 (2), AB84. (Abstract). doi:10.1016/j.jaci.2019.12.037

Tornio, A., Filppula, A. M., Niemi, M., and Backman, J. T. (2019). Clinical studies on drug-drug interactions involving metabolism and Transport: Methodology, pitfalls, and interpretation. *Clin. Pharmacol. Ther.* 105 (6), 1345–1361. doi:10.1002/cpt.1435

Wang, Z. Z., Jia, Y., Srivastava, K. D., Huang, W., Tiwari, R., Nowak-Wegrzyn, A., et al. (2021). Systems pharmacology and in silico docking analysis uncover association of CA2, PPARG, RXRA, and VDR with the mechanisms underlying the shi zhen tea formula effect on eczema. *Evid. Based Complement. Altern. Med.* 2021, 8406127. doi:10.1155/2021/8406127

Wang, Z. Z., Li, K., Maskey, A. R., Huang, W., Toutov, A. A., Yang, N., et al. (2021). A small molecule compound berberine as an orally active therapeutic candidate against COVID-19 and sars: A computational and mechanistic study. *Faseb J.* 35 (4), e21360. doi:10.1096/fj.202001792R

Xu, S., Yu, J., Yang, L., Zhu, Y., Sun, S., and Xu, Z. (2016). Comparative pharmacokinetics and bioavailability of epimedin C in rat after intramuscular administration of epimedin C, a combination of four flavonoid glycosides and purified herba epimedii extract. *J. Anal. Methods Chem.* 2016, 5093537. doi:10.1155/2016/5093537

Yang, N., Wang, J., Liu, C., Song, Y., Zhang, S., Zi, J., et al. (2014). Berberine and limonin suppress IgE production by human B cells and peripheral blood mononuclear cells from food-allergic patients. *Ann. Allergy Asthma Immunol.* 113 (5), 556–564. e4. doi:10.1016/j.anai.2014.07.021

Yasir, M., Goyal, A., and Sonthalia, S. (2022). *Corticosteroid adverse effects*. Florida, United States: StatPearls. StatPearls Publishing Copyright © 2022, StatPearls Publishing LLC.

Zanger, U. M., and Schwab, M. (2013). Cytochrome P450 enzymes in drug metabolism: Regulation of gene expression, enzyme activities, and impact of genetic variation. *Pharmacol. Ther.* 138 (1), 103–141. doi:10.1016/j.pharmthera.2012.12.007

Zhao, J. J., Pan, K., Wang, Q. J., Xu, Z. D., Weng, D. S., Li, J. J., et al. (2013). Effect of anti-asthma Chinese medicine Chuankezhi on the anti-tumor activity of cytokine-induced killer cells. *Chin. J. Cancer* 32 (10), 553–560. doi:10.5732/cjc.012.10249

Frontiers in Pharmacology

Explores the interactions between chemicals and living beings

The most cited journal in its field, which advances access to pharmacological discoveries to prevent and treat human disease.

Discover the latest Research Topics

See more →

Frontiers

Avenue du Tribunal-Fédéral 34
1005 Lausanne, Switzerland
frontiersin.org

Contact us

+41 (0)21 510 17 00
frontiersin.org/about/contact